Technical University of Catalonia

Department of Strength of Materials and Structural Engineering

University of Ferrara

Department of Engineering

Continuum Damage Model for Nonlinear Analysis of Masonry Structures

Luca Pelà

2009

Look ahead,
and even when you think
you are looking ahead,
look even more ahead.

Robert Baden Powell

Doctoral Thesis submitted in fulfilment of the requirements for the Degree of Doctor of Philosophy

International Ph.D. Program:

Universitat Politècnica de Catalunya

Departament de Resistència de Materials i Estructures a l'Enginyeria

Doctorat en Análisi Estructural

Università degli Studi di Ferrara

Dipartimento di Ingegneria

Dottorato di Ricerca in Scienze dell'Ingegneria Civile

Thesis Supervisors:

Prof. Miguel Cervera - Universitat Politècnica de Catalunya, Spain

Prof. Alessandra Aprile - Università degli Studi di Ferrara, Italy

Public Defence: Ferrara, Italy, March 26, 2009

Board of Examiners:

Prof. Antonio Tralli - Università degli Studi di Ferrara, Italy

Prof. Miguel Cervera - Universitat Politècnica de Catalunya, Spain

Prof. Pere Roca - Universitat Politècnica de Catalunya, Spain

Prof. Andrea Benedetti - Alma Mater Studiorum Università di Bologna, Italy

Prof. Giorgio Vassena - Università degli Studi di Brescia, Italy

European Referees (for the Doctor Europaeus Mention)**:**

Prof. Sergio Oller - Universitat Politècnica de Catalunya, Spain

Prof. Rui Faria - Universidade do Porto, Portugal

Acknowledgments

The research reported in this thesis has been carried out at the Department of Strength of Materials and Structural Engineering (RMEE) of the Technical University of Catalonia and at the Department of Engineering (ENDIF) of the University of Ferrara. The aforementioned Universities subscribed a co-tutoring agreement, with the aim of formalising the international co-tutorship of this Doctoral Thesis.

The work reported in this thesis has been possible thanks to the scholarship made available by the University of Ferrara. Additional financial support by the same University is gratefully acknowledged.

The work was performed under the guidance of Prof. Miguel Cervera and the supervision of Prof. Pere Roca and Prof. Andrea Benedetti.

I am very grateful to Prof. Cervera for his continuous helpfulness, his wise advice and his sincere incitement during all the research. Thanks also for proposing me the opportunity to do a prestigious international Ph.D.

I would like to thank Prof. Roca for the workstation he provided me at the UPC and for all the helpful support he gave me during my long stay in Barcelona.

I gratefully acknowledge the invaluable help of Prof. Andrea Benedetti and Prof. Alessandra Aprile, expressed in the form of so many suggestions and fruitful discussions. Moreover, they gave me the precious opportunity to continue my studies. This led me to a memorable international experience. Their friendship and support are definitely very important for me.

I would like to thank Prof. Antonio Tralli, for interesting discussions and for the fellowship he provided me to support my stay in Barcelona.

I gratefully acknowledge the always helpful suggestions contributed by Prof. Sergio Oller on many occasions.

I would like to record my thanks to Prof. Evelina Lamma and to Lena Fabbri, who devoted a lot of energies to define the co-tutoring agreement between the UNIFE and the UPC. I would like also to acknowledge Rosa Maria Olea and Felicidad Leiva of the UPC, as well as the coordinator of the Ph.D. Program of the Engineering Department of Ferrara, Prof. Stefano Trillo.

I am grateful to all my kind colleagues of the Department of Construction Engineering of Barcelona, in particular to Cristian, Alvaro and Guillermo for their support and sincere friendship.

I must acknowledge Roberto Clemente for all the material provided in order to help me to handle the tracking algorithm. Thanks also to Michele Chiumenti for providing me the COMET package.

A special thanks goes out to my friends and colleagues of the Department of Engineering of Ferrara, Monia, Stefania, Marco, Valerio, Anna, Alessio, Giovanni, Chiara, Agnese, Tommaso, Sara, Stefano, Alessandro and Luisfilippo.

I have no words to thank my best friends in Barcelona, Beniamino, Rubén, Flaminio, Marc and Hiram. Although I met them only 2 years ago, today they are definitely like brothers for me. I doubt that I will ever be able to convey my gratitude fully. Thanks also to Marina and his family, Alberto and Anna, Sergio and Teresa, Cristina, Sonia, Elvira, Leo, Guillermo, Miriam, Luisa, Gerard and Jordi.

A very special thanks goes out to all my Italian friends, in particular to Enrico, Alessandro, Alessio and Davide. They have always been beside me, even when I was so far. We have always shared good times and unforgettable happy moments.

Finally, a very special thanks goes out to my family, Mario, Marisa, Claudia, Tina and Isolda. Thanks God for giving me such a beautiful family. They gave me the education and handed down the most important life values. They taught me the love of knowledge. They have always encouraged and helped me a lot, even when I was far from home. I love you.

My gratitude to Chiara, my girlfriend, cannot be expressed in few words. Her love, patience and support in whatever I do are things that I will never forget…

Abstract

The present work focuses on the formulation of a Continuum Damage Mechanics model for nonlinear analysis of masonry structural elements. The material is studied at the macro-level, i.e. it is modelled as a homogeneous orthotropic continuum.

The orthotropic behaviour is simulated by means of an original methodology, which is based on nonlinear damage constitutive laws and on the concept of *mapped tensors* from the anisotropic real space to the isotropic fictitious one. It is based on establishing a one-to-one mapping relationship between the behaviour of an anisotropic real material and that of an isotropic fictitious one. Therefore, the problem is solved in the isotropic fictitious space and the results are transported to the real field. The application of this idea to strain-based Continuum Damage Models is rather innovative.

The proposed theory is a generalization of classical theories and allows us to use the models and algorithms developed for isotropic materials. A first version of the model makes use of an isotropic scalar damage model. The adoption of such a simple constitutive model in the fictitious space, together with an appropriate

definition of the mathematical transformation between the two spaces, provides a damage model for orthotropic materials able to reproduce the overall nonlinear behaviour, including stiffness degradation and strain-hardening/softening response. The relationship between the two spaces is expressed in terms of a *transformation tensor* which contains all the information concerning the real orthotropy of the material. A major advantage of this working strategy lies in the possibility of adjusting an arbitrary isotropic criterion to the particular behaviour of the orthotropic material. Moreover, orthotropic elastic and inelastic behaviours can be modelled in such a way that totally different mechanical responses can be predicted along the material axes.

The aforementioned approach is then refined in order to account for different behaviours of masonry in tension and compression. The aim of studying a real material via an equivalent fictitious solid is achieved by means of the appropriate definitions of two transformation tensors related to tensile or compressive states, respectively. These important assumptions permit to consider two individual damage criteria, according to different failure mechanisms, i.e. cracking and crushing. The constitutive model adopted in the fictitious space makes use of two scalar variables, which monitor the local damage under tension and compression, respectively. Such a model, which is based on a stress tensor split into tensile and compressive contributions that allows the model to contemplate orthotropic induced damage, permits also to account for masonry unilateral effects. The orthotropic nature of the Tension-Compression Damage Model adopted in the fictitious space is demonstrated. This feature, both with the assumption of two distinct damage criteria for tension and compression, does not permit to term the fictitious space as “isotropic”. Therefore, the proposed formulation turns the original concept of “mapping the real space into an *isotropic* fictitious one” into the innovative and more general one of “mapping the real space into a *favourable*

(or *convenient*) fictitious one". Validation of the model is carried out by means of comparisons with experimental results on different types of orthotropic masonry.
The model is fully formulated for the 2-dimensional case. However, it can be easily extended to the 3-dimensional case. It provides high algorithmic efficiency, a feature of primary importance when analyses of even large scale masonry structures are carried out. To account for this requisite it adopts a strain-driven formalism consistent with standard displacement-based finite element codes. The implementation in finite element programs is straightforward.
Finally, a *localized damage model for orthotropic materials* is formulated. This is achieved by means of the implementation of a crack tracking algorithm, which forces the crack to develop along a single row of finite elements. Compared with the smeared cracking approach, such an approach shows a better capacity to predict realistic collapsing mechanisms. The resulting damage in the ultimate condition appears localized in individual cracks. Moreover, the results do not suffer from spurious mesh-size or mesh-bias dependence. The numerical tool is finally validated via a finite element analysis of an in-plane loaded masonry shear wall.

Resumen

En el presente trabajo se plantea la formulación de un modelo basado en la Mecánica del Daño Continuo aplicado al análisis no lineal de estructuras de obra de fábrica. El material se estudia a nivel macroscópico y se modela como un continuo homogéneo y ortótropo.

La ortotropía del comportamiento se simula por medio de una metodología original, basada en leyes constitutivas no lineales y en el concepto de *tensores transformados* desde el espacio real anisótropo a un espacio ficticio isótropo. En detalle, se establece una transformación entre el comportamiento de un sólido real anisótropo y el de un sólido ficticio isótropo. De esta manera el problema se resuelve en el espacio ficticio isótropo y los resultados se retraen al espacio real. La aplicación de dicho planteamiento a Modelos de Daño Continuo basados en deformaciones es muy innovadora.

La teoría propuesta es una generalización de las teorias clásicas y permite utilizar modelos y algoritmos formulados para materiales isótropos. Una primera versión del modelo considera un modelo de daño escalar e isótropo. La adopción de este modelo simple en el espacio ficticio, junto a la apropriada definición de la

transformación matemática entre los dos espacios, conduce a un modelo de daño para materiales ortótropos capaz de reproducir el comportamiento no lineal global, incluyendo degradación de rigidez y leyes de endurecimiento/ablandamiento. La relación entre los dos espacios está expresada en términos de un *tensor de transformación* que contiene toda la información sobre la real ortotropía del material. Una ventaja muy importante de esta estrategía reside en la posibilidad de ajustar cualquier criterio de daño al comportamiento particular del material ortótropo. Además, se pueden modelar comportamientos elásticos e inelásticos totalmente diferentes a lo largo de los ejes del material.

El procedimiento mencionado anteriormente se refina después para reproducir los diferentes comportamientos a tracción y a compresión. El objetivo de estudiar un material real por medio de un sólido equivalente ficticio se logra a través de las definiciones de dos tensores de transformación relacionados a estados de tensión y compresión, respectivamente. Estos importantes supuestos permiten considerar dos criterios de daño distintos de acuerdo con diferentes mecanismos de fallo, es decir fisuración y aplastamiento. El modelo constitutivo contemplado en el espacio ficticio considera dos variables para controlar respectivamente el daño local a tracción y compresión. Dicho modelo, que está basado en una descomposición del tensor de tensión en componentes positivas y negativas que hace que el modelo induzca una degradación ortótropa, permite también representar el caracter unilateral del daño. El proceso de validación del modelo se lleva a cabo mediante la comparación con resultados experimentales de diversos ensayos sobre obra de fábrica ortótropa.

El modelo está formulado para el caso bidimensional. Sin embargo, es posible su extensión al caso 3D. Se observa una considerable eficiencia computacional, muy importante para el análisis de estructuras complejas de obra de fábrica. Este requisito se debe al favorable formato en deformaciones, compatible con

programas de elementos finitos estándar basados en desplazamientos. La implementación en codigos de elementos finitos es relativamente simple.

Finalmente, se plantea la formulación de un *modelo de daño localizado para materiales ortótropos*. Se utiliza un algoritmo de rastreo de fisuras, que fuerza la fisura a desarrollarse a lo largo de una fila singular de elementos finitos. Su comparación con el enfoque de fisura distribuida evidencia una mejor capacidad de predecir mecanismos de fallo realistas. El daño correspondiente a condiciones últimas se modela mediante fisuras localizadas. Además, los resultados no dependen ni del tamaño de los elementos finitos utilizados en la discretización espacial, ni de la orientación de la malla. El proceso de validación de la herramienta numérica se lleva a cabo mediante el análisis por el método de elementos finitos de una pared de obra de fábrica sometida a cargas verticales y horizontales.

Sommario

Questo lavoro presenta la formulazione di un modello basato sulla Meccanica del Danneggiamento dei Solidi Continui, finalizzato all'analisi non lineare di elementi strutturali in muratura. Il materiale viene studiato da un punto di vista macroscopico e modellato come un continuo omogeneo ortotropo.

Il comportamento ortotropo viene simulato per mezzo di una metodologia originale, basata su leggi costitutive non lineari e sul concetto di *tensore mappato* dallo spazio reale anisotropo ad uno spazio fittizio isotropo. In pratica, si stabilisce una trasformazione tra il comportamento di un solido reale anisotropo e di uno fittizio isotropo. Di conseguenza, il problema viene risolto nello spazio fittizio isotropo e i risultati ricondotti al campo reale. L'applicazione di questa idea a modelli di danno continuo formulati in deformazioni è piuttosto innovativa.

La teoria proposta è una generalizzazione delle teorie classiche e permette l'utilizzo di modelli e algoritmi sviluppati per materiali isotropi. Una prima versione del modello utilizza una legge costitutiva di danno isotropo scalare. Tale semplice assunzione nello spazio fittizio, assieme ad un'appropriata definizione della trasformazione matematica tra i due spazi, fornisce un modello di danno per

materiali ortotropi in grado di riprodurre il comportamento non lineare globale, tenendo in conto la degradazione della rigidezza e leggi di hardening/softening non lineari. La relazione tra i due spazi si esprime per mezzo di un *tensore di trasformazione* che contiene tutta l'informazione sull'ortotropia reale del materiale. Uno dei vantaggi principali di tale metodologia risiede nella possibilità di aggiustare un qualsiasi criterio di danno isotropo al comportamento particolare del materiale ortotropo. In aggiunta, è possibile modellare il comportamento elastico ed anelastico in modo tale da riprodurre risposte meccaniche completamente differenti lungo gli assi del materiale.

L'approccio summenzionato viene successivamente raffinato, in maniera tale da includere la descrizione del diverso comportamento a trazione e a compressione. L'obiettivo di studiare un materiale reale per mezzo di un solido equivalente fittizio viene raggiunto mediante l'appropriata definizione di due tensori di trasformazione relazionati, rispettivamente, a stati di trazione e compressione. Tali importanti assunzioni permettono di considerare due criteri di danno indipendenti, coerentemente a due diversi meccanismi di rottura, ossia fessurazione e schiacciamento. Il modello costitutivo adottato nello spazio fittizio è caratterizzato dall'uso di due variabili scalari che controllano, rispettivamente, il danno locale a trazione e compressione. Tale modello, basato su una decomposizione del tensore degli sforzi nelle sue componenti di trazione e compressione che permette di contemplare l'anisotropia indotta per danneggiamento, include anche la descrizione del carattere unilaterale del danno. La validazione del modello viene eseguita attraverso un attento confronto con risultati sperimentali su differenti tipi di murature, caratterizzate anche da elevati gradi di ortotropia.

La formulazione completa del modello viene presentata per il caso bidimensionale; ciononostante, è facilmente possibile estrapolare quella tridimensionale. Il modello è caratterizzato da un'alta efficienza computazionale, una caratteristica di primaria importanza nel campo dell'analisi di strutture in muratura anche complesse. A tal

fine, viene adottato un vantaggioso formato in deformazioni, pienamente compatibile con i programmi ad elementi finiti standard. L'implementazione del modello in codici ad elementi finiti è relativamente semplice e viene descritta in dettaglio.

Infine, si presenta la formulazione di un *modello di danno localizzato per materiali ortotropi*, ottenuta per mezzo dell'implementazione di un algoritmo di *crack-tracking*, che forza la fessura a localizzarsi lungo una singola fila di elementi finiti. Confrontato con il tradizionale approccio alle fessure distribuite, il modello proposto presenta una maggiore capacità di prevedere meccanismi di collasso realistici: il danno risultante in condizioni ultime appare localizzato in fessure discrete. Inoltre, i risultati sono oggettivi al variare delle dimensioni degli elementi finiti e dell'inclinazione della mesh adottata nel problema discreto. La validazione del modello numerico viene condotta per mezzo dell'analisi agli elementi finiti di una parete a taglio in muratura caricata nel piano.

Contents

Chapter 1.
Introduction

Masonry has always been one of the basic building materials. Important new developments in the materials and applications occurred in the last decades but the techniques to assemble bricks or blocks are essentially the same as the ones developed thousands of years ago.

In many European countries, the existing building heritage is mainly constituted by masonry structures, including monuments of huge architectural and historical value. In a great number of cases, such buildings are also located in earthquake prone sites. Exceptional events such as earthquakes are often the most evident cause of damage on the buildings, and even of their collapse. For instance, the Umbria-Marche earthquake (1997) damaged important historical heritage buildings in Italy, such as the Basilica of Saint Francis in Assisi and more than 200 ancient churches. In the former case, the partial collapse of the transept vault caused 4 persons to die and reduced some Giotto's and Cimabue's frescos to a huge jigsaw puzzle, see Figure 1.1.

Figure 1.1 Photo sequence of the transept vault partial collapse occurred in the Basilica of Saint Francis in Assisi, Italy, during the Umbria-Marche earthquake (1997).

Therefore, it is evident the importance of the structural evaluation of existing masonry buildings, in order not only to guarantee the architectural heritage conservation, but also people safety.

The engineer participation in the conservation projects is twofold. Firstly, it is necessary to assess the structural safety of the construction. Secondly, the designer must provide the strengthening solutions, if they are necessary. In both cases the engineer needs adequate structural analysis tools.

The analysis of masonry structures is a complex task. The material presents a very particular mechanical behaviour, which is principally due the lack of homogeneity and standardization. The structural response of such a composite material derives from the complex interaction between units and mortar joints.

The traditional simplified analysis methods are not able to contemplate all the inherent complex phenomena, such as cracks opening, compression crushing and

shear slip. The incompatibilities between observed real structural behaviour and the predictions stemming from conventional analysis methods led to the need for using refined and advanced computational strategies.

The numerical approach seems to be an effective possibility to deal with such a complicated problem. Several methods and computational tools are available for the assessment of the mechanical behaviour. The approaches use different theories, resulting in different levels of complexity and cost. Such analysis strategies are still in an experimental phase, hence the problem is still open.

Nowadays, a significant effort is carried out to develop computational models of analysis that can be successfully used to determine the structural capacity and expected damage attained by masonry structures under different actions, including earthquakes. In this particular instance, the determination of the capacity should consider accurately the development of localized damage such as the individual large cracks normally experienced by masonry structures in the ultimate condition. The analysis of the cracking phenomenon is also useful to understand the causes of the existing cracks actually visible on historical structures, due for instance to construction phases, foundations settlements, previous earthquakes, etc.

1.1 Overview of Computational Modelling of Masonry Structures

In the last decades, the masonry research community has been showing a great interest in sophisticated numerical tools, being in opposition to the prevailing tradition of rules-of-thumb and empirical formulae. Several difficulties arose from adopting existing numerical tools from more advanced research fields, namely the mechanics of concrete, rock and composite materials, because of the very particular features of masonry. All the aforementioned factors led to the need for developing appropriate and specific tools for the analysis of masonry structures.

The large number of modern research studies concerning this issue emphasizes the little importance given in the past to the numerical aspects.

Several numerical models have been proposed for the structural analysis of masonry constructions. Such models are characterized by different theoretical backgrounds and levels of detail. The cause of these differences is the large variety of the objects which could be studied. Masonry involves building techniques which may considerably differ for materials, texture and structural details. Therefore, trying to individuate a unique model of absolute applicability and general validity is not realistic.

Several ways are practicable and the choice of the analyst depends on the searched information (serviceability, damage, collapse, failure mechanisms, etc.), the required level of accuracy (local or global behaviour of the structure), the necessary input data (detailed or rough information about material characteristics) and the costs (principally the time permissible for the analysis).

The simplest approach to the modelling of masonry constructions is based on representing the structure as a combination of structural elements, such as truss, beam, plate or shell elements. This is the case of the *simplified methods via macro-elements*. Several approaches based on the concept of the equivalent frame method are found in the literature (Magenes and Dalla Fontana, 1998; Roca *et al.*, 2005), in which the building walls are idealized as equivalent frames made by pier elements, spandrel beam elements and joint elements (Figure 1.2). Research efforts were also devoted to the development of two-dimensional macro-elements (Brencich and Lagomarsino, 1998, see Figure 1.3). All the cited simplified approaches are characterized by a very low computational cost, since each macro-element represents an entire wall or masonry panel, reducing drastically the number of degrees of freedom of the structure. Nevertheless, such simplified elements usually provide a coarse description of the real masonry element behaviour.

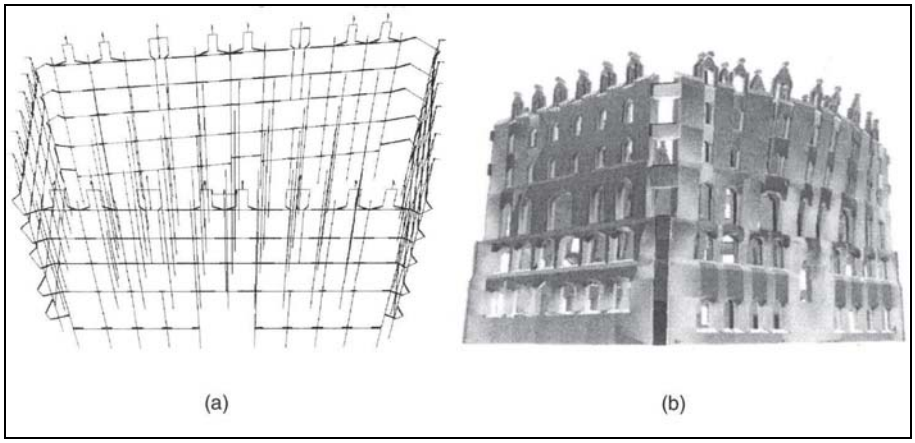

Figure 1.2 Application of the simplified method proposed by Roca *et al.* (2005) to the study of the Gaudí's Casa Botines.

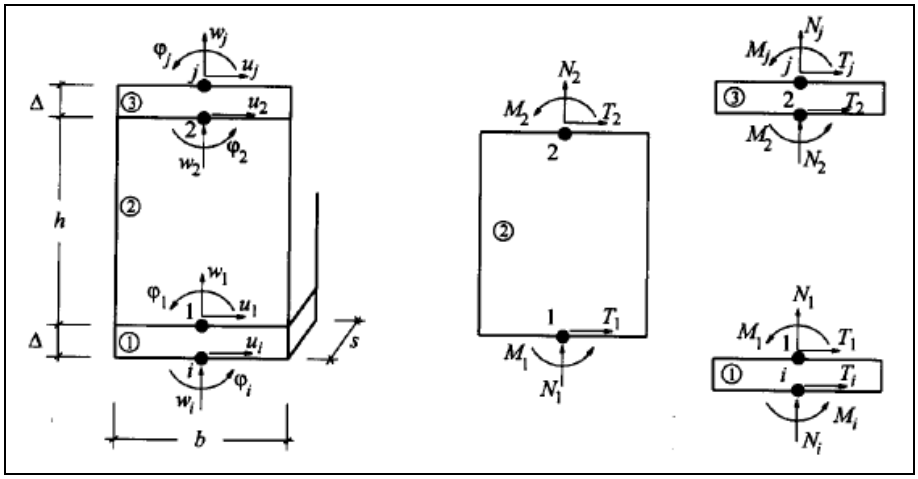

Figure 1.3 Macro-elements proposed by Brencich and Lagomarsino (1998).

Masonry is a composite material that consists of units and mortar joints. In general, the approach towards a better numerical representation can focus on the micro-modelling of the individual components, viz. unit (brick, block, etc.) and mortar, or the macro-modelling of masonry as a composite, see Figure 1.4.

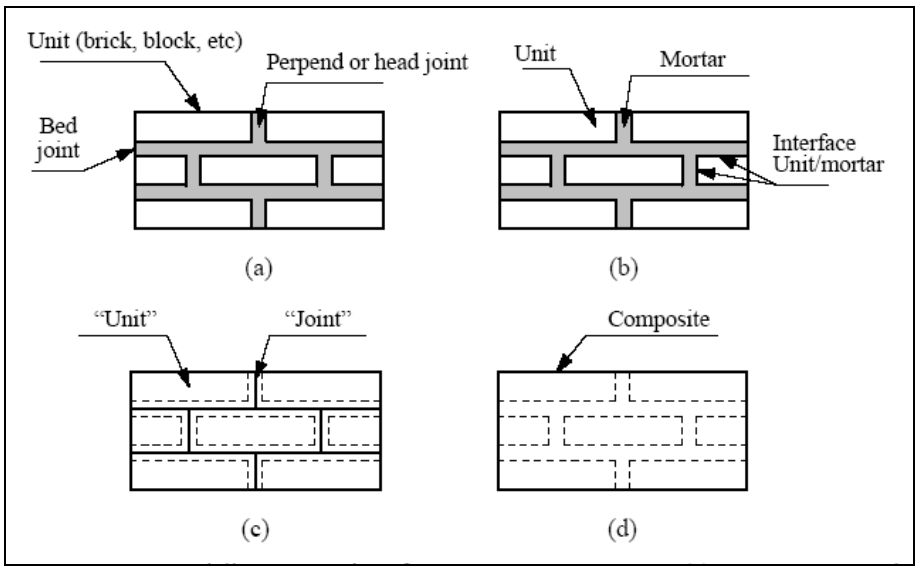

Figure 1.4 Modelling strategies for masonry structures (from Lourenço, 1996): masonry sample (a); detailed (b) and simplified (c) micro-modelling; macro-modelling (d).

Micro-modelling is probably the best tool available to analyse and understand the real behaviour of masonry, particularly concerning its local response. Such an approach includes distinct representations of units, mortar and the unit/mortar interface. The *detailed* micro-models represent units and mortar in the joints with continuum elements, whereas the unit-mortar interface is represented by discontinuous elements (Figure 1.4b). Elastic and inelastic properties of both unit and mortar can be taken into account. The interface represents a potential crack/slip plane. Such a modelling procedure leads to very accurate results, but requires an intensive computational effort. This drawback is partially overcome by the *simplified* micro-models (Lofti and Shing, 1994; Tzamtzis, 1994; Lourenço and Rots, 1996; Gambarotta and Lagomarsino, 1997; Sutcliffe *et al.*, 2001), where expanded units are represented by continuum elements while the behaviour of the mortar joints and unit-mortar interface is lumped in discontinuous elements (Figure

1.4c). Masonry is thus considered as a set of elastic blocks bonded by potential fracture/slip lines at the joints (Figures 1.5-1.6).

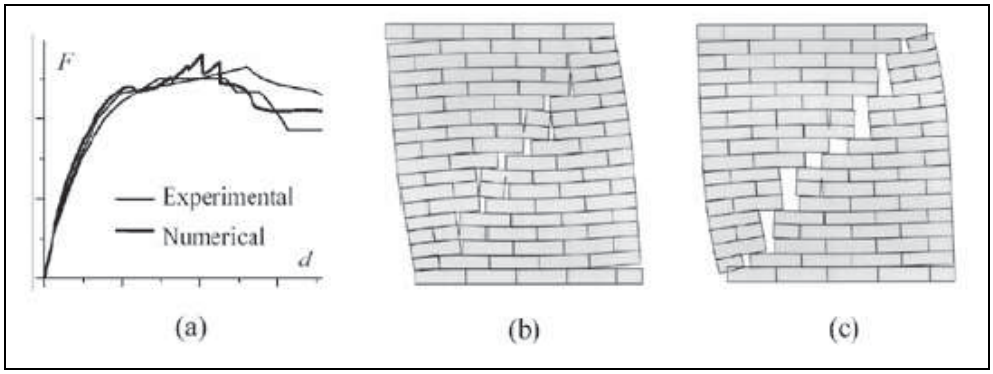

Figure 1.5 Micro-modelling of masonry shear walls (from Lourenço, 1996): load-displacement diagrams (a); deformed mesh at peak load (b); deformed mesh at collapse (c).

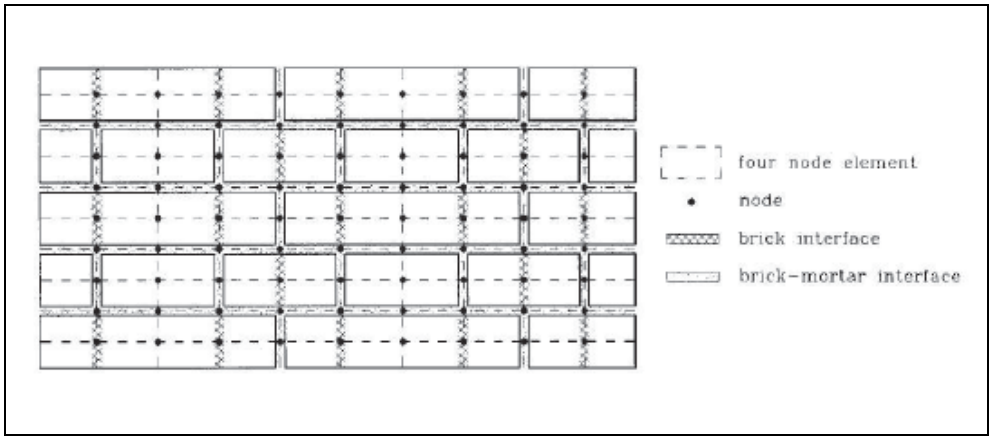

Figure 1.6 Micro-modelling of masonry, from Gambarotta and Lagomarsino (1997).

The micro-modelling approaches are suitable for small structural elements with particular interest in strongly heterogeneous states of stress and strain. The primary aim is to closely represent masonry from the knowledge of the properties of each constituent and the interface. The necessary experimental data must be obtained from laboratory tests in the constituents and small masonry samples. Nevertheless,

the high level of refinement required for obtaining accurate results means an intensive computational effort (i.e. great number of degrees of freedom of the numerical model), which limits micro-models applicability to the analysis of small elements (e.g. laboratory specimens) or, at least, to small structural details.

Midway between micro-modelling and macro-modelling we recognize the *homogenized modelling*. Several homogenization techniques have been developed to obtain macro-constitutive laws starting from the micro-constitutive laws of the constituents and the texture of the masonry (Luciano and Sacco, 1997; Gambarotta and Lagomarsino, 1997; Zucchini and Lourenço, 2002; Massart *et al.* 2004, Milani *et al.*, 2006). Such methodologies consist in identifying an elementary cell, which generates an entire panel by regular repetition. In this way, a field problem can be written on the unit cell in order to achieve average values for the homogenized masonry material, starting from the knowledge of the mechanical properties of the constituents and the geometry of the elementary cell (Figure 1.7). Recently, homogenization techniques have been effectively applied to upper and lower bound limit analyses (Milani *et al.*, 2006; Cecchi *et al.*, 2007; Milani *et al.*, 2007; Milani *et al.*, 2008), see Figure 1.8. Recent advances in terms of sophisticated analysis homogenisation tools are discussed in Lourenço *et al.* (2007).

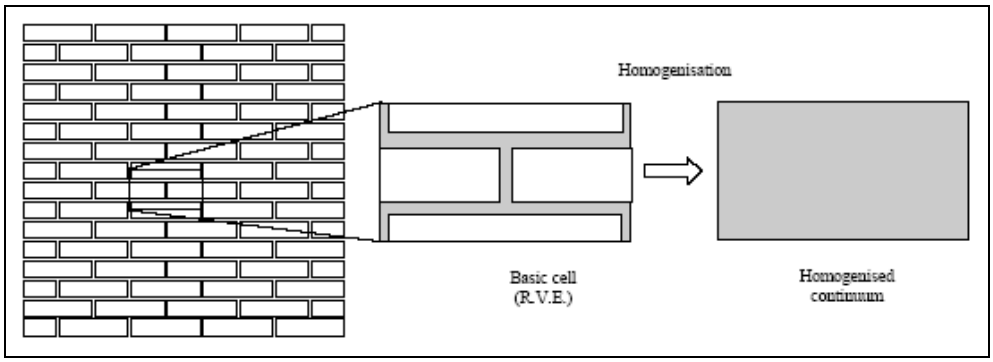

Figure 1.7 Basic cell for masonry and objective of homogenization.

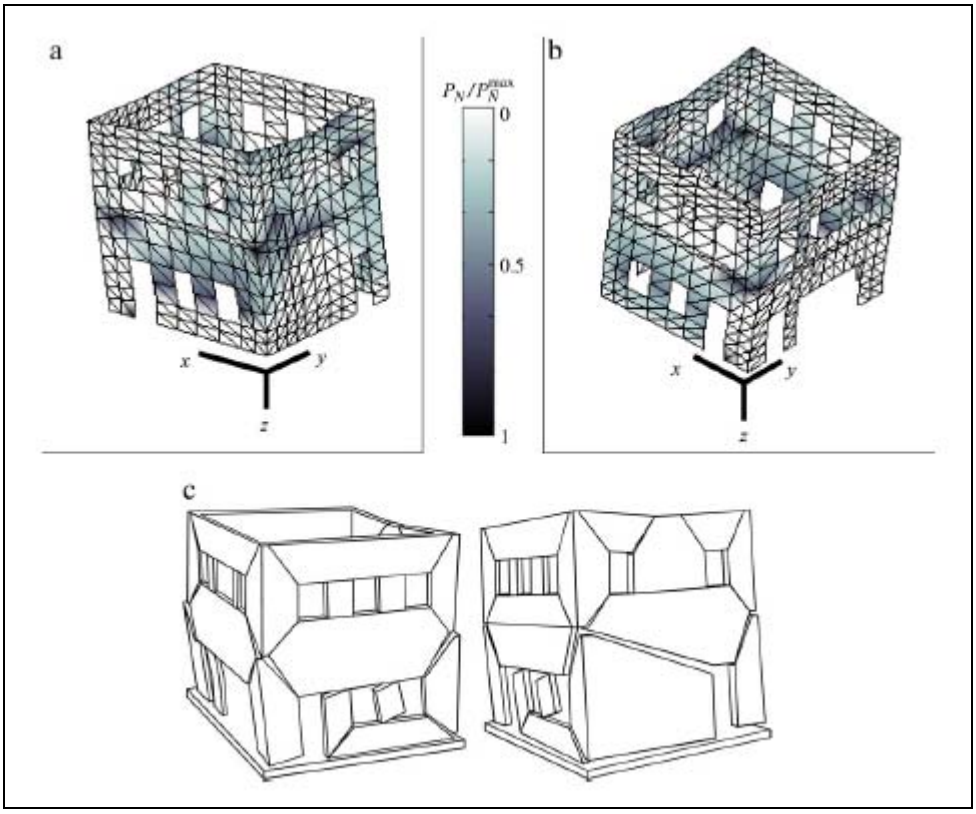

Figure 1.8 3-D homogenized limit analysis of a masonry building, from Milani *et al.* 2007.

In large and practice-oriented analyses the knowledge of the interaction between units and mortar is, generally, negligible for the global structural behaviour. In these cases a different approach can be used, namely the *macro-modelling* (Figure 1.4d), which does not make any distinction between units and joints. The material is regarded as a fictitious homogeneous orthotropic continuum. An appropriate relationship is established between average masonry strains and average masonry stresses. A complete macro-model must account for different tensile and compressive strengths along the material axes as well as different inelastic behaviour for each material axis. This is clearly a phenomenological approach, meaning that the continuum parameters must be assessed by means of tests on

specimens of sufficiently large size, under homogeneous states of stress. As an alternative to difficult experimental tests, it is possible to assess experimentally the individual components (or simple wallets and cores, see Benedetti *et al.* 2008) and consider the obtained data as input parameters for the following numerical homogenization technique. Clearly, macro-modelling is more practice oriented due to the reduced time and memory requirements as well as a user-friendly mesh generation. The computational advantage is considerable, since the mesh discretization does not have to accurately describe the internal structure of masonry and the finite elements can have dimensions greater than the single brick units. This type of modelling is most valuable when a compromise between accuracy and efficiency is needed.

The macro-models, also termed *Continuum Mechanics finite element models*, can be related to plasticity or damage constitutive laws.

An example of the former approach is the work of Lourenço *et al.* (1997 and 1998, see Figure 1.9), which proposed a non-linear constitutive model for in-plane loaded walls based on the plasticity theory, for which the material admissible field is bounded by a Hill-type yield criterion for compression and a Rankine-type yield criterion for tension.

The latter approach, which is based on Continuum Damage Mechanics, is the one that will be considered in the thesis.

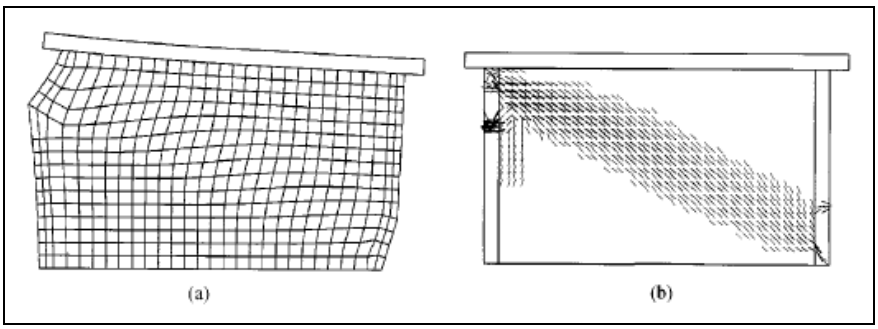

Figure 1.9 Analysis of a shear wall with the plasticity model of Lourenço *et al.* (1997): deformed mesh (a) and cracks (b).

Among the Damage Mechanics-based macro-models we cite the work of Papa (1996), which consists in an unilateral damage model for masonry deriving from the extension of a damage model originally developed for isotropic material to the orthotropic case and including a homogenization technique to keep into account the texture of brick and mortar. Berto *et al.* (2002) developed a specific damage model for orthotropic brittle materials with different elastic and inelastic properties along the two material directions. The basic assumption of the model is the acceptance of the natural axes of the masonry (i.e. the bed joints and the head joints directions) also as principal axes of the damage, see Figure 1.10.

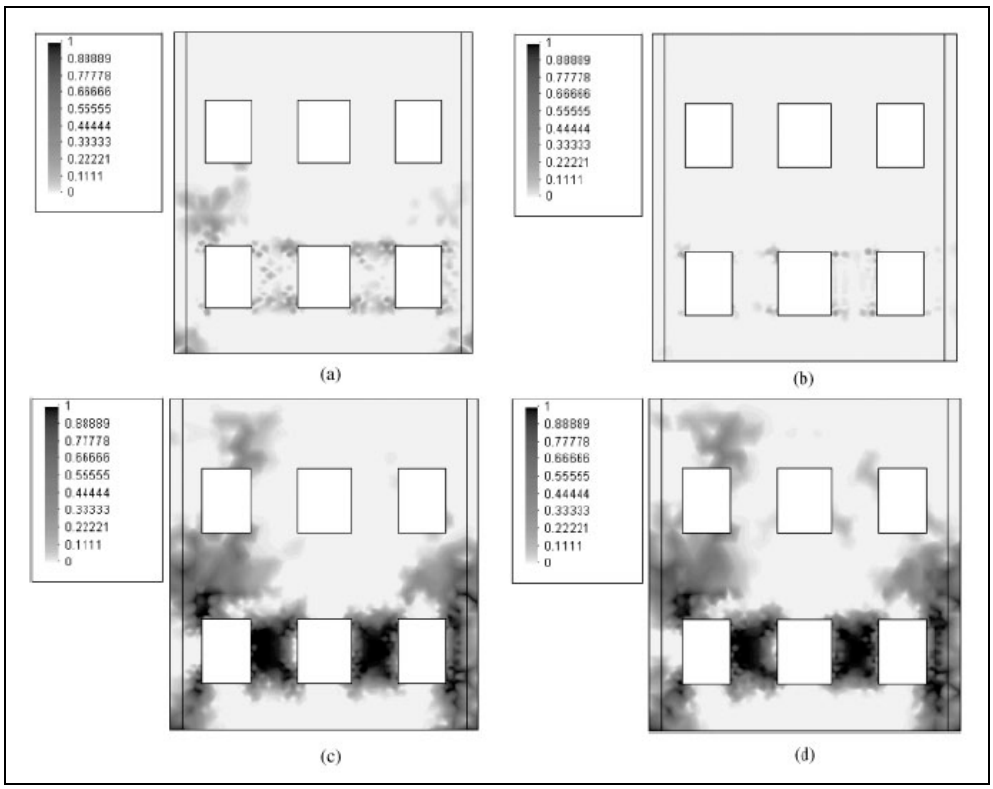

Figure 1.10 Analysis of a cyclically-loaded wall with openings (from Berto *et al.* 2002): (a) d_x^- , (b) d_y^- , (c) d_x^+ and (d) d_y^+ numerical damage contours.

The macro-models have been extensively used with the aim of analyzing the seismic response of complex masonry structures, such as arch bridges (Pelà *et al.*, 2009), historical buildings (Mallardo *et al.*, 2007), mosques and cathedrals (Massanas *et al.*, 2004; Martínez *et al.*, 2006; Murcia, 2008), see Figures 1.11-1.12.

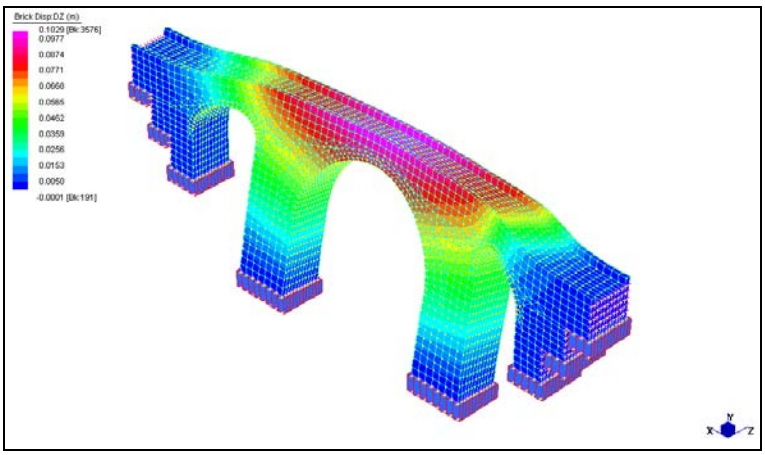

Figure 1.11 Pushover analysis of a masonry arch bridge, from Pelà *et al.* (2009).

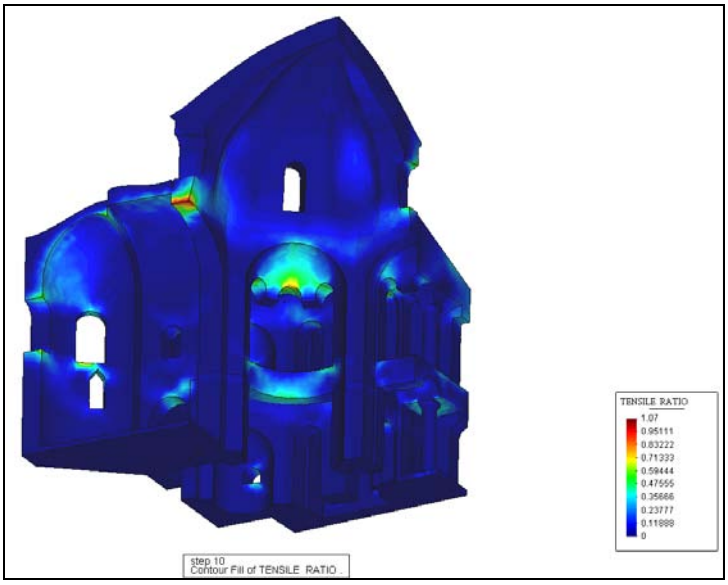

Figure 1.12 Analysis of Küçük Ayasofya Mosque in Istanbul, from Massanas *et al.* (2004).

In the case of Continuum Damage finite element models, isotropic criteria are usually preferred because of their simplicity, hence the need for only few material parameters. Moreover, smeared damage models are generally adopted even if they only provide general information about the level of damage expected on the

structure. In fact, the damage is simulated in an unrealistic way, involving significant volumes and spreading over large regions of the structure.

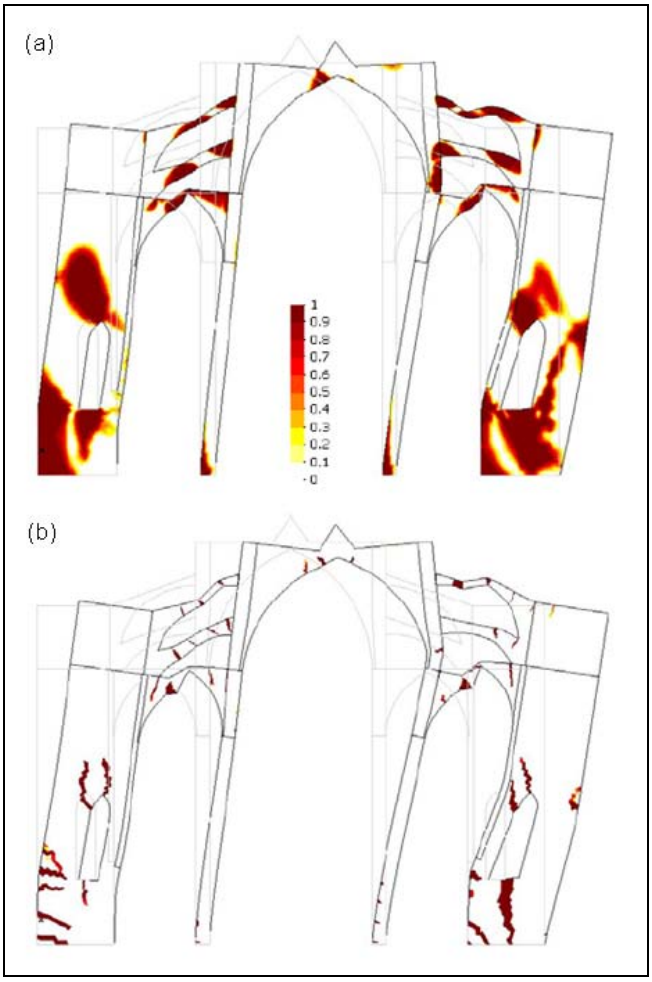

Figure 1.13 Seismic analysis of Mallorca Cathedral: smeared damage approach (a) versus localized damage approach (b), from Clemente *et al.* (2006).

An interesting enhancement of the traditional smeared damage approaches was proposed by Clemente *et al.* (2006). The model is based on the so-called smeared-crack scalar damage model, modified in such a way that it can reproduce localized

individual (discrete) cracks. This is achieved by means of a local crack-tracking algorithm. The crack tracking model enables the simulation of more realistic damage distributions than the original smeared-crack model. The localized cracks predicted by the crack tracking model reproduce consistently a set of expectable plastic hinges developing gradually in the structure and leading to the full collapsing mechanism. The model has been used to analyze the response of the structure of Mallorca Cathedral under gravity and seismic forces, see Figure 1.13.

1.2 Masonry Material: Principal Features

Masonry is a heterogeneous material that consists of units and joints. The huge number of possible combinations (see Figure 1.14) generated by the geometry, nature and arrangement of units as well as the characteristics of mortars raises doubts about the accuracy of the generic term “masonry”. Despite the large number of typologies, the overall mechanical behaviour presents several peculiar features. A complete description of the material is not pursued in this study and the reader is referred to Drysdale *et al.* (1994) and Hendry (1990).

From a phenomenological point of view, masonry is a composite material with an overall orthotropic behaviour. Such an anisotropy arises from the geometrical arrangements of units and mortar, even if the properties of these constituents are isotropic. The orthotropy in the elastic response is related to the different elastic properties of mortar and units. Moreover, the constituents are arranged in such a way that the horizontal and vertical directions are obviously not equivalent.

The mortar joints act as planes of weakness. Therefore, structural response is strongly dependent on the orientations of the bed joints.

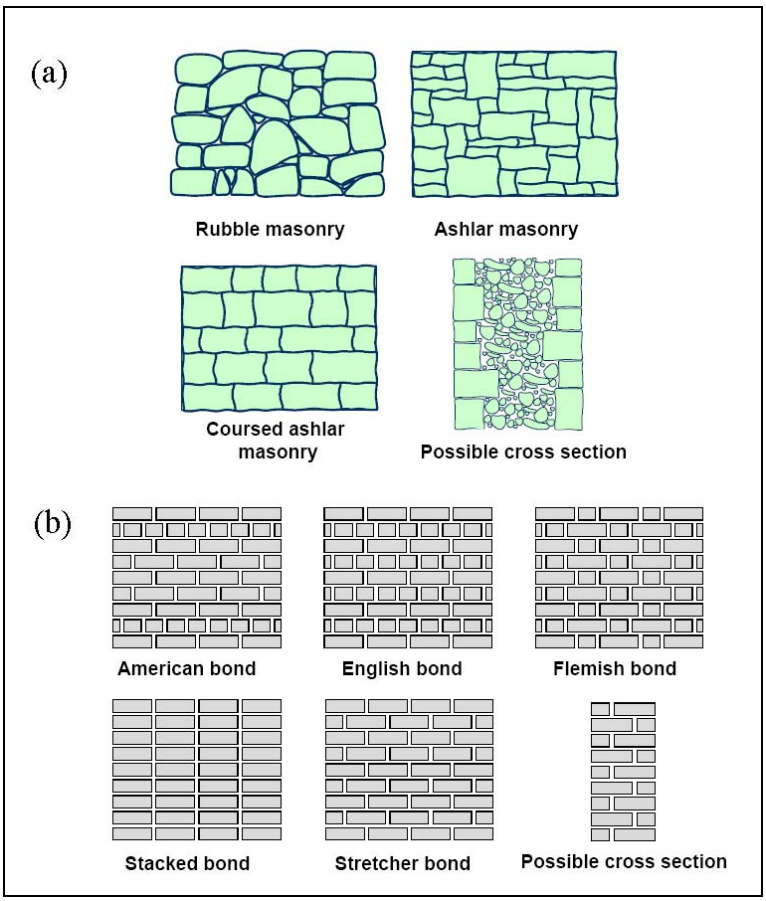

Figure 1.14 Variability of masonry: stone masonry (a), brick masonry (b).

The uniaxial compressive strength of masonry in the direction normal to the bed joints has been traditionally regarded as the most relevant structural material property. Uniaxial compression tests in the direction parallel to the bed joints have received substantially less attention from the masonry community. However, masonry is an anisotropic material and, particularly in the case of low longitudinal compressive strength of the units due to high perforation, the resistance to compressive loads parallel to the bed joints can have a decisive effect on the load bearing capacity.

Hilsdorf (1969) demonstrated that the difference in elastic properties of the unit and mortar is the precursor of failure. In fact, units are normally stiffer than mortar and the difference is more pronounced in ancient masonry, built with lime mortar. Uniaxial compression of masonry in direction perpendicular to bed joints leads to a state of triaxial compression in the mortar and of compression/biaxial tension in the unit, see Figure 1.15. In practice, the unit confines the mortar and avoids its lateral extension. As a consequence, vertical cracks appear in the units. Upon increasing deformation, additional vertical cracks appear, until the failure.

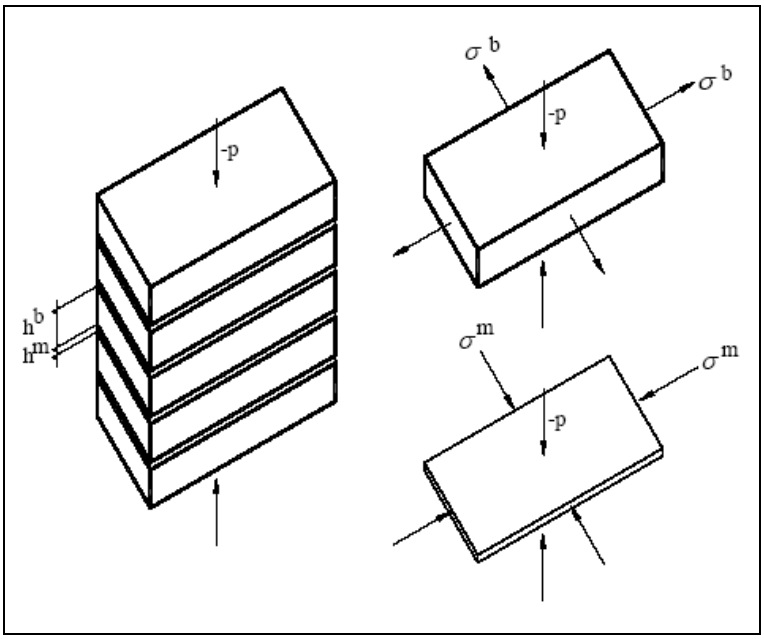

Figure 1.15 Local state of stress in masonry prisms under uniaxial vertical compression.

The strength and the failure mode change when different inclinations of bed joints are considered (Samarasinghe and Hendry, 1980; Page, 1981, 1983) because of the anisotropic nature of the material. If loading direction is parallel to bed joints, the splitting of the bed joints in tension occurs. For intermediate inclinations, we find a mixed mechanism, see Figure 1.16.

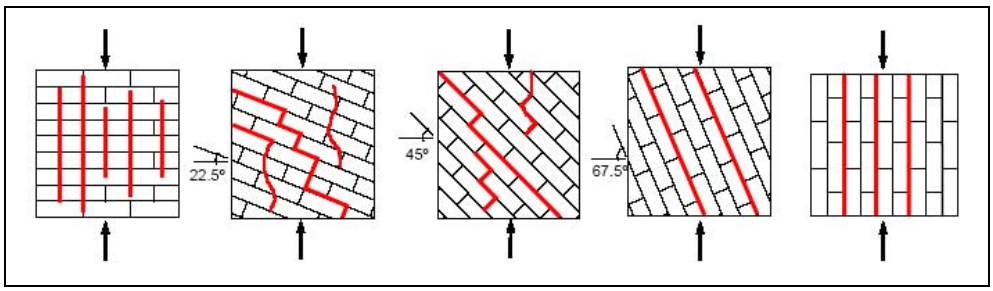

Figure 1.16 Modes of failure of solid clay units masonry under uniaxial compression, from Page (1981, 1983).

For tensile loading perpendicular to the bed joints, failure is generally caused by debonding between the bed joint and the unit. As a rough approximation, the masonry tensile strength can be equated to the tensile bond strength between the joint and the unit. In masonry with low strength units and greater tensile bond strength between the bed joint and the unit, e.g. high-strength mortar and units with numerous small perforations, which produce a dowel effect, failure may occur as a result of stresses exceeding the unit tensile strength. As a rough approximation, the masonry tensile strength in this case can be equated to the tensile strength of the unit.

For tensile loading parallel to the bed joints a complete test program was set-up by Backes (1985). The author tested masonry wallets under direct tension and he found that tension failure was affected by the type of the mortar and the masonry units. For stronger mortar and weaker masonry units, the tension cracks passed along the head mortar joints and through the centre of the bricks at the intervening courses, as shown in Figure 1.17a. For weaker mortar joints and stronger masonry units, the tension crack passed along the head joints of the masonry units and the length of bed joints between staggered head joints, as shown in Figure 1.17b.

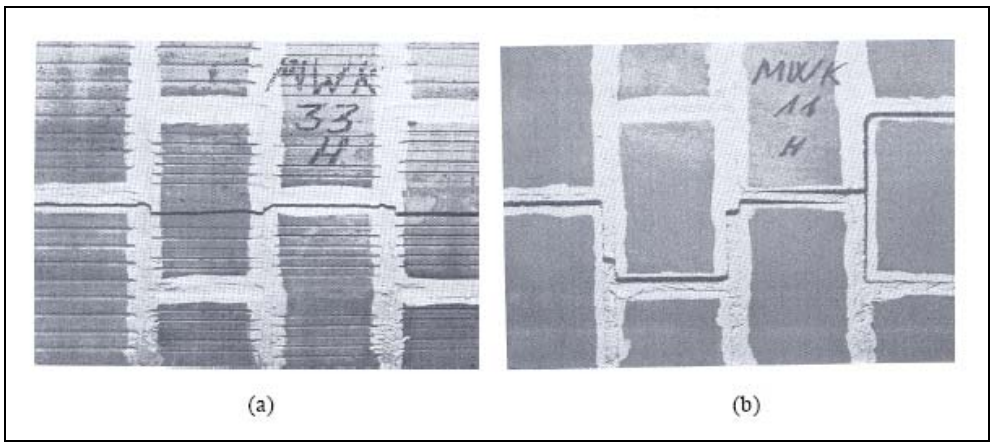

Figure 1.17 Modes of tension failure of masonry walls under direct tension, from Backes (1985): through type (a), zigzag type (b).

Figure 1.18 shows different modes of failure observed by Page (1983) on solid clay units masonry walls subjected to uniaxial tension. As can be seen, for intermediate inclinations of the bed joints, the failure is concentrated on joints.

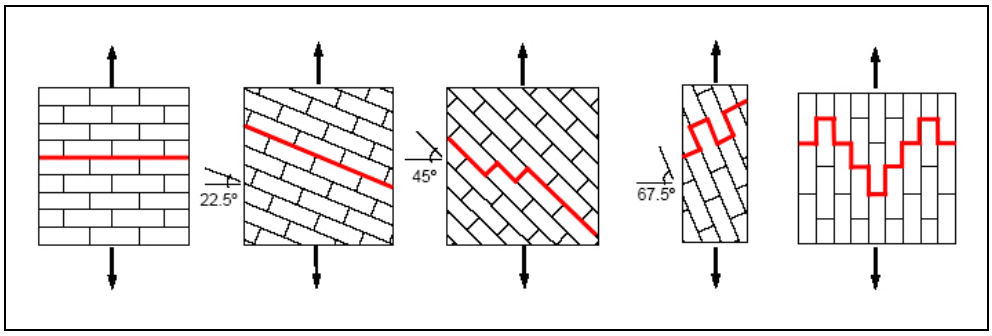

Figure 1.18 Modes of failure of solid clay units masonry under uniaxial tension, from Page (1983).

The constitutive behaviour of masonry under biaxial states of stress cannot be completely described from the constitutive behaviour under uniaxial loading conditions. The biaxial strength envelope cannot be described solely in terms of principal stresses, because masonry is an anisotropic material. Therefore, the

biaxial strength envelope of masonry must be either described in terms of the full stress vector in a fixed set of material axes or, in terms of principal stresses and the rotation angle θ between the principal stresses and the material axes. The most complete set of experimental data of masonry subjected to proportional biaxial loading was provided by Page (1981, 1983), see Figure 1.19. The tests were carried out with half scale solid clay units. Both the orientation of the principal stresses with regard to the material axes and the principal stress ratio considerably influence the failure mode and strength.

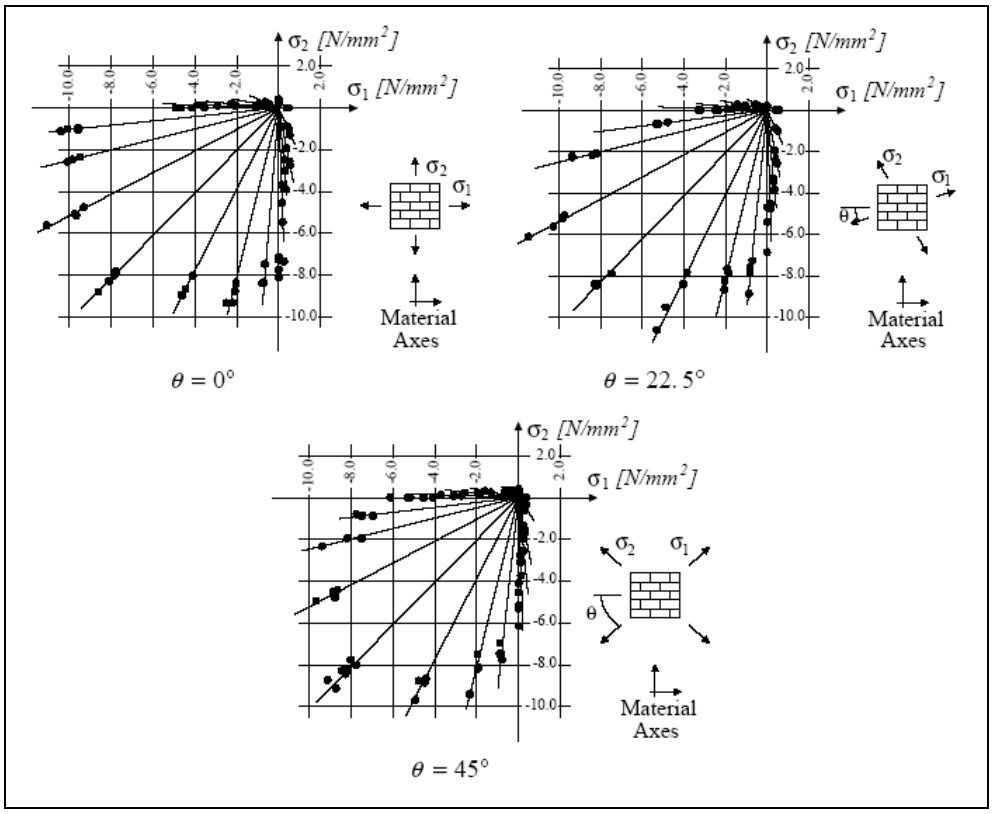

Figure 1.19 Biaxial strength of solid clay units masonry, from Page (1981, 1983).

The influence of the lateral tensile stress in the tensile strength is not known because no experimental results are available. A lateral compressive stress decreases the tensile strength. The minimum value is achieved when tension direction is perpendicular to the bed joints. In tension-compression (Page, 1983), the failure occurs either by cracking and sliding of the joints or in a combined mechanism involving both units and joints, see Figure 1.20.

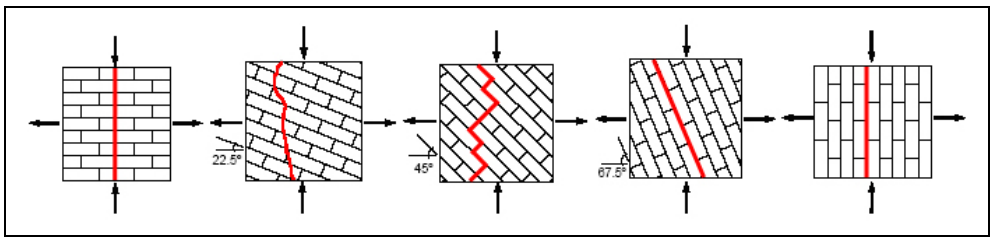

Figure 1.20 Modes of failure of solid clay units masonry under biaxial tension-compression, from Page (1983).

In biaxial compression failure typically occurs by splitting of the specimen at mid-thickness, in a plane parallel to its free surface, regardless of the orientation of the principal stresses, see Figure 1.21. The orientation plays a significant role when the compression in one direction is much greater than the perpendicular one. In this case, failure occurs in a combined mechanism involving both joint failure and lateral splitting. The increase of compressive strength under biaxial compression can be explained by friction in the joints and internal friction in the units and mortar.

It is further noted that the strength envelope shown in Figure 1.19 is of limited applicability for other types of masonry. Different strength envelopes and different failure modes are likely to be found for different materials, unit shapes and geometry. Comprehensive programs to characterize the biaxial strength of different masonry types were carried using full scale specimens, see Ganz and Thürlimann (1982) for hollow clay units masonry, Guggisberg and Thürlimann (1987) for clay

and calcium-silicate units masonry and Lurati et al. (1990) for concrete units masonry.

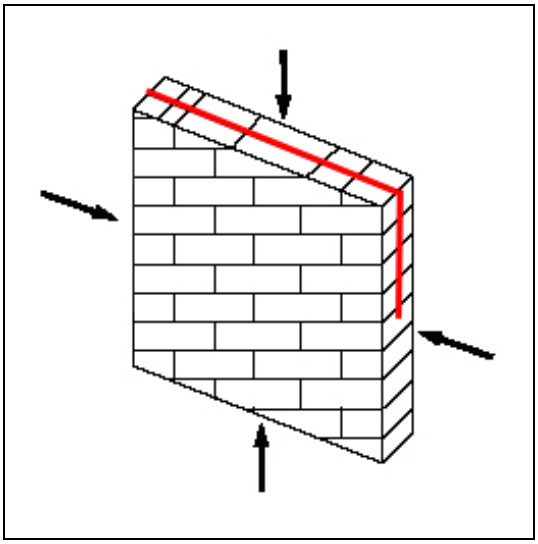

Figure 1.21 Mode of failure of solid clay units masonry under biaxial compression-compression, from Page (1981).

Concerning the shear capacity of masonry, we observe that the determination of the shear response of masonry joints is a complex task, since it depends on the ability of the test set-up to generate a uniform state of stress in the joints. Different test configurations are possible and the reader is referred to van der Pluijm (1983, 1998), Hofmann and Stockl (1986) and Atkinson *et al.* (1989). Obviously, the shear strength increases with the confining compression stress, because of the frictional behaviour of masonry in shear. Moreover, the real behaviour of a joint is generally non-associative, i.e. $\delta_n \neq \delta_t \tan\phi$, where δ_n and δ_t are respectively the normal (dilatant) and tangential relative displacements between sliding surfaces at a masonry joint, and ϕ is the angle of friction. Whilst in practice some dilatancy will be likely to occur when two rough blocks pass over each other, experimental evidence indicates that real joint behaviour is quite complex, with the amount of

dilatancy being dependent on the micro-scale geometrical and mechanical features of the masonry joint (van Zijl, 2004). Also, it is found that the angle of dilatant friction tends to reduce both with increasing relative tangential displacement and also under the action of increasing normal stresses, see Figure 1.22.

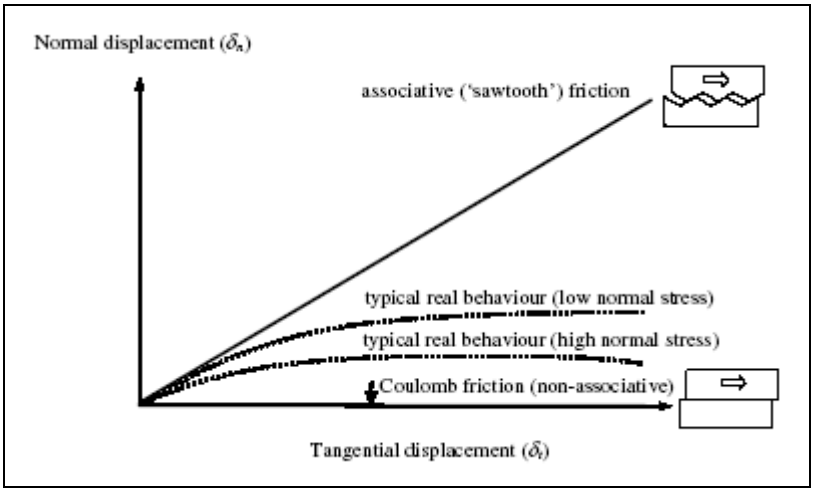

Figure 1.22 Masonry joint behaviour: associative, Coulomb friction (non-associative) idealisations and typical real behaviours.

A salient feature of masonry is the softening behaviour, which is typical of quasi-brittle materials. Softening is a gradual decrease of mechanical resistance under a continuous increase of deformation and it is due to a process of progressive internal crack growth. Such mechanical behaviour is commonly attributed to the heterogeneity of the material, due to the presence of different phases and material defects, like flaws and voids. Even prior to loading, mortar contains microcracks due to the shrinkage during curing and the presence of the aggregate. The clay brick contains inclusions and microcracks due to the shrinkage during the burning process. The initial stresses and cracks as well as variations of internal stiffness and strength cause progressive crack growth when the material is subjected to progressive deformation. Initially, the microcracks are stable which means that

they grow only when the load is increased. Around peak load an acceleration of crack formation takes place and the formation of macrocracks starts. The macrocracks are unstable, which means that the load has to decrease to avoid an uncontrolled growth. In a deformation controlled test the macrocrack growth results in softening and localization of cracking in a small zone while the rest of the specimen unloads. Figure 1.23 shows characteristic stress-displacement diagrams for quasi-brittle materials in uniaxial tension, uniaxial compression and pure shear.

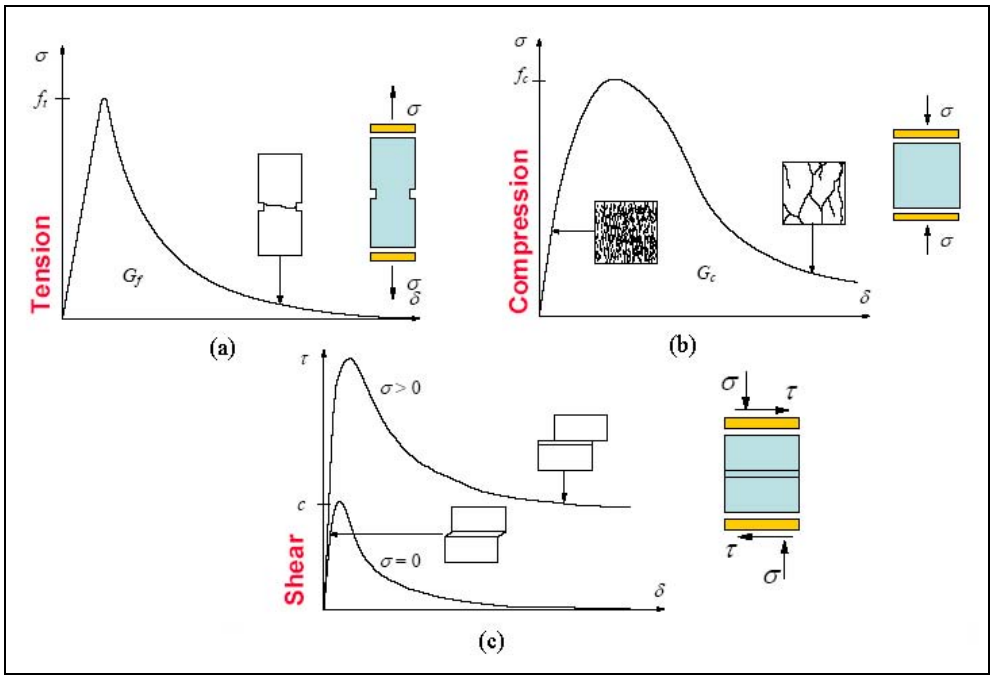

Figure 1.23 Typical behaviour of quasi-brittle materials and definition of fracture energy: uniaxial tensile loading (a); uniaxial compressive loading (b); pure shear (c).

The integral of the $\sigma-\delta$ diagram is the *fracture energy* , denoted by G_f and G_c, for tension and compression, respectively. In case of mode II failure mechanism, i.e. slip of the unit-mortar interface under shear loading, the inelastic behaviour in shear can be described by the mode II fracture energy $G_{II,f}$, defined by the integral

of the $\tau-\delta$ diagram. Figure 1.23c shows brittle behaviours in shear. The value of the fracture energy depends on the level of the confining stress.

Shear failure is a salient feature of masonry behaviour which must be incorporated in a micro-modelling strategy. However, for continuum macro-models, this failure cannot be directly included because the unit and mortar geometries are not discretized. Shear failure is then associated with tension and compression modes in a principal stress space.

1.3 Aim and Objectives of the Thesis

The main aim of this thesis is to provide a non linear model, based on the Continuum Damage Mechanics, devoted to the finite element analysis of masonry structures. The work consists in developing a robust and accurate numerical tool for the analysis even of large and complex constructions.

The study focuses on two-dimensional structures, which can be approximated as being in a state of plane stress, such as panels, shear walls and arched structures. The material is studied at the macro-level, i.e. it is modelled as a homogeneous orthotropic continuum without making any distinction between units and joints.

This aim will be achieved through the following enabling objectives:

- To gather information on the existing knowledge about Continuum Damage Mechanics models, through a comprehensive literature review.
- To develop an efficient model capable of predicting the behaviour of masonry structures, which includes orthotropic elastic as well as orthotropic inelastic behaviour and incorporates the knowledge of concepts used in crack propagation problems.
- To validate the model by comparing the predicted behaviour with the behaviour observed in experiments on different types of masonry. The

developed model should be able to predict the failure mode and the ultimate load with reasonable agreement with the experimental evidence.

- To apply the validated model to engineering practice case-studies.

It is further noted that the model developed and the discussion carried out in this study has a much broader applicability than masonry structures. In fact, the proposed model could be utilized for most anisotropic materials such as plastics, wood and fibre-reinforced composite materials.

1.4 Outline of the Thesis

This thesis consists of six Chapters.

Chapter 1 provides an introduction and states the aim and objectives of the research. A brief overview on the mechanical behaviour of the material and computational modelling of masonry structures is also included.

Chapter 2 reports a review of the most known Continuum Damage Mechanics models. The aspects related to their numerical implementation are also discussed.

Chapter 3 presents the formulation of a scalar damage model for orthotropic materials. An original methodology is presented, which is a generalization of the classical theories and allows one to use the models and algorithms developed for isotropic materials. Such a methodology is based on establishing a one-to-one mapping relationship between the behaviour of an anisotropic real material and that of an isotropic fictitious one. Therefore, the problem is solved in the isotropic fictitious space and the results are transported to the real field. Orthotropic elastic and inelastic behaviours of the material are taken into account, in such a way that totally different responses can be predicted along the material axes. The proposed tool is able to reproduce the mechanical degradation of the material and to predict the potential collapse under given load conditions.

Chapter 4 presents the formulation of a two-parameters damage model for masonry. Such a model is more sophisticated than the one described in the previous chapter. In fact, it accounts for different orthotropic behaviours in tension and compression. Individual damage criteria are considered for tension and compression, according to different failure mechanisms. The former is associated with cracking phenomenon, while the latter is associated with the crushing of the material. Totally different elastic and inelastic behaviours can be predicted along the material axes, both in tension and compression. The resulting formulation is easily implemented in a non linear finite element code. Validation of the model is performed by means of a comparison between the calculated numerical results and the experimental results available in the literature for different types of orthotropic masonry.

Chapter 5 validates the damage model developed in Chapter 4 by means of the FE analysis of an engineering practice case study, i.e. a shear wall with openings. A localized-cracks approach is considered instead of the traditional smeared one, in order to obtain more accurate and mesh-objective results. The description of the adopted local crack-tracking algorithm is also provided.

Chapter 6 presents an extended summary and the final conclusions which can be derived from this study. Suggestions for future work are also pointed out.

Chapter 2.
Overview of Continuum Damage Mechanics and Damage Models

The mechanical behaviour of many materials is complex and highly nonlinear, even for moderate stress levels. The available literature on material modelling includes models based on the theories of Hypoelasticity, Hyperelasticity, Plasticity, Fracture Mechanics, Plastic-Fracture or Continuum Damage Mechanics. *Continuum Damage Mechanics* provides a powerful and general framework for the derivation of consistent material models suitable for many engineering fields. This theory was firstly introduced by Kachanov (1958) in the context of creep related problems. It has been accepted afterwards as a valid tool to deal with complex material behaviour. Continuum Damage Mechanics covers a broad range of applications nowadays. It is used for materials so different as metals, ceramics, rock, concrete and masonry. Such a large acceptance is due to several important factors, namely:

- The *simplicity* of the approach, which is totally based on Continuum Mechanics Theory. This is a major difference with Fracture Mechanics and leads to a much simpler formulation and interpretation. The damaged material is assumed to remain a continuum and the collective effect of cracks is modelled by modifying the mechanical properties, i.e. stiffness and strength. One or more, scalar or tensorial, field quantities are introduced into the constitutive equations as measures of the degradation of the material.
- The *consistency* of the theory, which is formulated in a rigorous framework, i.e. the Thermodynamics of irreversible processes.
- The *versatility* of the approach, which can deal with a large number of problems, e.g. creep, fatigue, brittle or ductile failure, etc.
- The *compatibility* with other theories. For instance, the combination of Damage Mechanics Theory with Plasticity is straightforward. In addition, it is possible to include thermal and rate dependent effects in the formulation.

This Chapter presents some approaches to this branch of Continuum Mechanics. Basic concepts are defined, together with the theoretical formulation. Then, a comparative discussion concerning some damage models is carried out, in order to emphasize the implications arising from the different backgrounds. In particular, the attention is paid mainly to the models in which the damage is described by one or two scalar variables. A large number of studies deals with such approaches to characterize the mechanical behaviour of materials. The principal features of these approaches will be pointed out, in order to better understand the models that will be formulated in the following Chapters of the thesis.

2.1 Continuum Damage Mechanics: Background and Basics

All real materials deform when loaded. The deformation may be elastic or inelastic. It may be time independent or dependent. Occasionally rupture may occur, being either ductile or brittle. The deformational properties are described by constitutive equations, which are either derived from micromechanical or statistical considerations or even postulated to fit measurements test specimens.

In general, constitutive equations relate to the material modelled as a *continuum*. The deformation is described by a field variable, the *strain*. The distribution of internal forces in the material is described by another field variable, the *stress*. These concepts are useful in analyzing the behaviour of load carrying structures in spite of the fact that they do not account for the discrete structure of real materials.

Under certain load conditions the material structure may begin to disintegrate. Small cracks may form, voids and other forms of small cavities may appear in highly stressed parts. Such deterioration weakens the material and lowers its load carrying capacity. Because of their nature, these defects are discrete entities. An accurate analysis of their influence would have to consider them as discrete disturbances of the material continuum. This is definitely a prohibitive task.

In a pioneering paper Kachanov (1958) proposed to describe the collective effect of such deterioration by means of a field variable termed *continuity*. Therefore, an inherently discrete process was modelled by a continuous variable. What was lost in accuracy in modelling the deterioration was then gained in computational simplicity.

The state of the material with regard to deterioration was characterized by a dimensionless scalar field variable ψ denoted continuity. To a completely defect free material was ascribed the condition $\psi = 1$, whereas $\psi = 0$ was defined to characterize a completely destroyed material with no remaining load carrying

capacity. Kachanov also postulated a law according to which ψ changes with time in a material subjected to stress at elevated temperature during extended times. For further details on Kachanov's analysis of brittle creep rupture the reader is referred to Kachanov (1958, 1986).

The continuity Ψ quantifies the absence of the material deterioration. The complementary quantity $D = 1 - \psi$ is therefore a measure of the state of deterioration or *damage* (Odqvist and Hult, 1962; Rabotnov, 1963). For a completely undamaged material $D = 0$ whereas $D = 1$ corresponds to a state of complete loss of integrity of the material structure. The designation D as field variable to describe the degree of material damage has lately come into a widespread use and will be used in the sequel of the work.

Although Kachanov assumed Ψ to be a scalar field variable, later developments have led to the study of tensorial quantities to describe damage, see Krajcinovic and Lemaitre (1987) and the references therein.

Even though the Kachanov model was entirely phenomenological, micromechanical studies lent support to this model, see Jansson and Stigh (1985). Such results led to increasing interest in damage analyses based on Mechanics principles.

The term *Continuum Damage Mechanics* was coined by Janson and Hult (1977). The aim of such a theory is to develop methods for the prediction of the load carrying capacity of structures subjected to material damage evolution. It is a counterpart of Fracture Mechanics, which deals with structures containing one or several cracks of finite size. In this latter approach, the cracks are usually assumed to be embedded in a non-deteriorating material. However, Fracture Mechanics and Continuum Damage Mechanics may be combined to predict the damage growth and the resulting decrease of load carrying capacity (Janson and Hult, 1977; Krajcinovic, 1985).

2.1.1 Damage Variable

Damage in solid materials is the creation and growth of microvoids or microcracks, which are discontinuities in a medium considered as continuous at a larger scale. In engineering, the mechanics of continuous media introduces a Representative Volume Element (RVE) on which all properties are described by homogenized variables. To give an order of magnitude, its size can vary from about 0.1 mm^3 for metals and ceramics to about 100 mm^3 for concrete. The damage discontinuities are small with respect to the size of the RVE but of course large compared to the atomic spacing, see Figure 2.1.

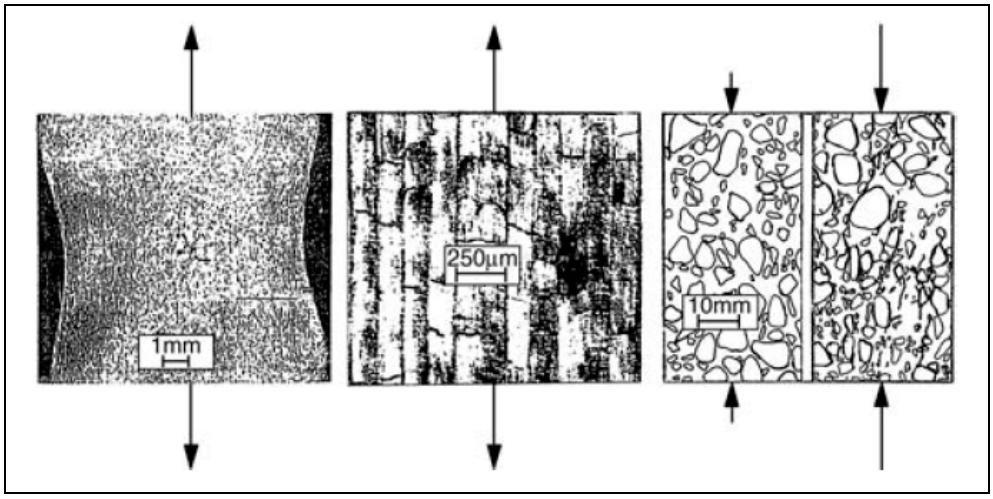

Figure 2.1 Examples of damage in a metal (microcavities in copper), in a composite (microcracks in carbon-fiber/epoxy resin laminate), and in concrete (crack pattern). From Lemaitre and Desmorat (2005).

From a physical point of view, damage is always related to plastic or irreversible strains and more generally to a strain dissipation either on the mesoscale, the scale of the RVE, or on the microscale, the scale of the discontinuities.

In the first case (*mesolevel*), the damage is called *ductile damage* if it is nucleation and growth of cavities in a mesofield of plastic strains under static loadings; it is

called *creep damage* when it occurs at elevated temperature and is represented by intergranular decohesions in metals; it is called *low cycle fatigue damage* when it occurs under repeated high level loadings, inducing mesoplasticity.

In the second case (*microlevel*), it is called brittle failure, or *quasi-brittle damage*, when the loading is monotonic; it is called *high cycle fatigue damage* when the loading is a large number of repeated cycles. Ceramics, concrete, and metals under repeated loads at low level below the yield stress are subjected to quasi-brittle damage.

Consider a damaged solid in which a characteristic element of finite volume has been isolated, i.e. the RVE, see Figure 2.2.

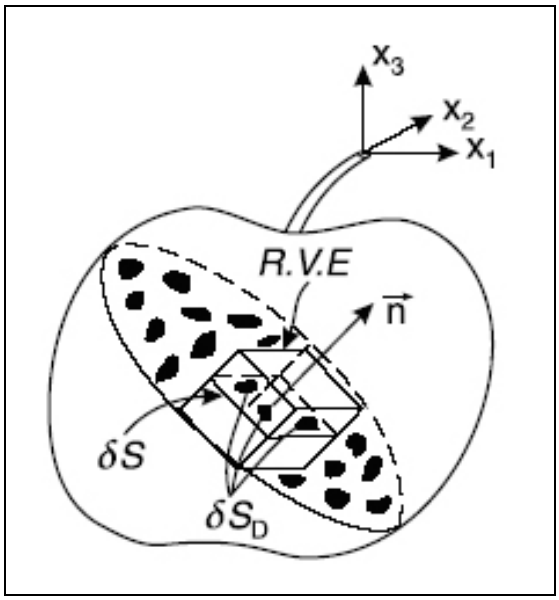

Figure 2.2 Damaged element and interpretation of the damage variable.

Let δS be the area of the section of the volume element identified by its normal $\vec{n}$. On this section, cracks and cavities which constitute the damage leave traces of different forms. Let $\delta \overline{S}$ be the effective area of resistance $\left(\delta \overline{S} < \delta S\right)$ taking

account of the area of these traces, stress concentrations in the neighbourhood of geometric discontinuities and the interactions between the neighbouring defects. Let δS_D be the difference

$$\delta S_D = \delta S - \delta \overline{S} \tag{2.1}$$

i.e. the total area of the defect traces corrected for stress concentrations and interactions. We will see in Section 2.1.2 that the concept of effective stress associated with the hypothesis of strain-equivalence enables us to avoid the calculations of δS_D. In fact, it would be extremely difficult to do because of the lack of knowledge of the precise geometry of the defects and because of the doubts regarding the applicability of Continuum Mechanics on this scale.

By definition (Lemaitre and Chaboche, 1985), the damage variable is physically defined by the surface density of microcracks and intersections of microvoids lying on a plane cutting the RVE of cross section δS (Fig. 2.2):

$$D(\vec{n}) = \frac{\delta S_D}{\delta S} \tag{2.2}$$

Expression (2.2) provides the mechanical measure of local damage relative to the direction $\vec{n}$. It is evident that:

- $D(\vec{n}) = 0$ corresponds to the undamaged or virgin state;
- $D(\vec{n}) = 1$ corresponds to the totally damaged material, hence breaking of the RVE into two parts;
- $0 \le D(\vec{n}) \le 1$ characterizes the damaged state.

If the damage is *isotropic*, it consists of cracks and cavities with an orientation distributed uniformly in all directions. In this case, the variable $D(\vec{n})$ does not

depend on the normal and the damaged state is completely characterized by the scalar intrinsic variable *d*:

$$D(\vec{n}) = d \qquad \forall \vec{n} \tag{2.3}$$

However, experimental evidence proves that during the loading history, the microcracks undergo irreversible growth mainly "in the direction perpendicular to the maximum tensile strain" (Krajcinovic and Fonseka, 1981). Therefore, in the general case of anisotropic damage, the value of the variable $D(\vec{n})$ depends on the orientation of the normal. It will be seen afterwards that the corresponding intrinsic variable can be represented by a vector or a tensor.

2.1.2 Effective Stress Concept and Principle of Strain-Equivalence

The introduction of a damage variable which represents a surface density of discontinuities leads directly to the concept of effective stress, i.e. the stress calculated over the section which effectively resists to the forces.

For simplicity, we consider the uniaxial case. If *F* is the applied force on a section of the representative volume element, $\sigma = F/S$ is the usual stress satisfying the equilibrium equation. In the presence of isotropic damage *d*, the effective area of resistance is

$$\bar{S} = S - S_D = S(1-d) \tag{2.4}$$

and by definition the *effective stress* $\bar{\sigma}$ is defined as

$$\bar{\sigma} = \sigma \frac{S}{\bar{S}} = \frac{\sigma}{(1-d)} \tag{2.5}$$

Evidently it results that $\bar{\sigma} \geq \sigma$. For a virgin material $\bar{\sigma} = \sigma$, whereas at the moment of fracture $\bar{\sigma} \to \infty$.

In the case of multiaxial isotropic damage, the ratio $S/\overline{S}$ does not depend on the orientation of the normal and the operator $(1-d)$ can be applied to all components. As a consequence, we can consider the tensorial form

$$\overline{\boldsymbol{\sigma}} = \frac{\boldsymbol{\sigma}}{(1-d)} \tag{2.6}$$

or the inverse expression

$$\boldsymbol{\sigma} = (1-d)\overline{\boldsymbol{\sigma}} \tag{2.7}$$

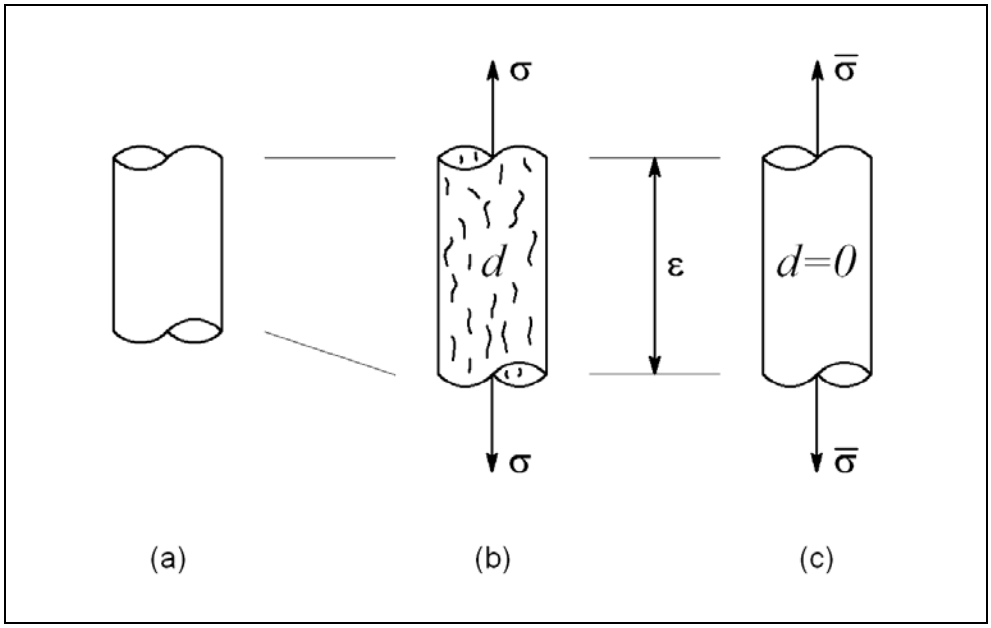

Figure 2.3 Effective stress and equivalence in strain: virgin material (a), damaged material (b) and equivalent virgin material (c).

The definition of the effective stress is introduced in connection with the *hypothesis of strain equivalence* (Lemaitre and Chaboche, 1978):

the strain associated with a damaged state under the applied stress $\boldsymbol{\sigma}$ *is equivalent to the strain associated with its undamaged state under the effective stress* $\overline{\boldsymbol{\sigma}}$ (Figure 2.3).

We assume that the deformation behaviour of the material is only affected by damage in the form of the effective stress. Any deformation behaviour, whether uniaxial or multiaxial, of a damaged material is represented by the constitutive law of the virgin material in which the usual stress is replaced by the effective stress. For example, the uniaxial linear elastic law of a damaged material is written as

$$\sigma = (1-d)\,\overline{\sigma} = (1-d)\,E\,\varepsilon \tag{2.8}$$

In which E is the Young's modulus. This constitutes a non-rigorous hypothesis which assumes that all the different behaviours accompanying damage (elasticity, plasticity, viscoplasticity) are affected in the same way by the surface density of the damage defects. However, its simplicity allows the establishment of a coherent and efficient formalism.

From Equation (2.8) it derives that the macroscopic (or apparent) tension σ is related to the strain by means of a damaged Young's modulus:

$$E_d = (1-d)\,E \tag{2.9}$$

The damage is irreversible, so

$$\dot{S}_d \geq 0, \quad \dot{d} \geq 0 \quad \rightarrow \quad \dot{E}_d \leq 0 \tag{2.10}$$

The damage is initiated when the strain (or stress) exceeds the initial *damage threshold* ε_0 (or σ_0):

$$d = 0 \quad if \quad \begin{cases} \sigma < \sigma_0 \\ \varepsilon < \varepsilon_0 \end{cases} \tag{2.11}$$

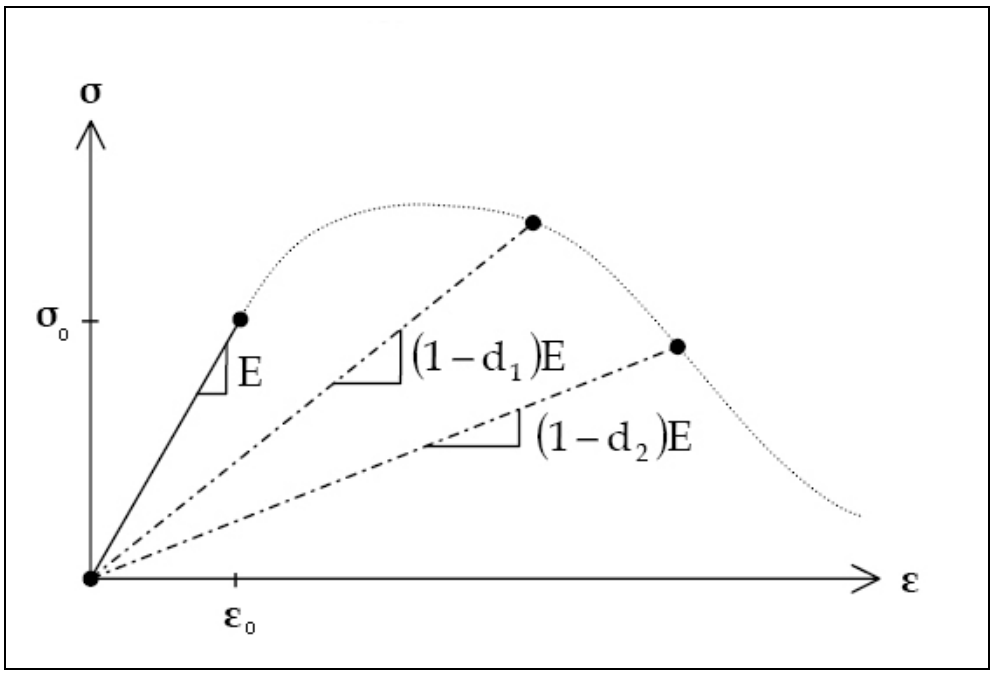

Figure 2.4 Damaged Young's modulus during increasing uniaxial load.

In case of unloading we have

$$\dot{\varepsilon} < 0 \quad \rightarrow \quad \dot{S}_d = 0 \quad \textit{and} \quad \dot{d} = 0 \tag{2.12}$$

and, therefore,

$$\dot{\sigma} = \left(1 - d\right) E\, \dot{\varepsilon} - \dot{d}\, E\, \varepsilon = E_d \dot{\varepsilon} \tag{2.13}$$

In case of unloading the damage does not increase and, consequently, unloading occurs until the origin according to a damaged stiffness, see Figure 2.4. A successive reloading follows the same unloading branch, until the damage threshold is reached again. The damage constitutive law differs from the plasticity constitutive law in that no plastic irreversible deformation occurs: all the deformation is recovered during the unloading, hence the unloading/reloading paths are not parallel.

2.1.3 Thermodynamic Framework

Continuum Damage Mechanics is formulated in a rigorous framework (Maugin, 1992). The general structure of the classical theory is furnished by the consolidate Thermodynamics Theory of irreversible process with internal variables (Coleman and Gurtin, 1967).

The constitutive relationship is obtained by writing the dissipation of the thermo-mechanical process. The dissipation expression is obtained taking into account the first and second principles of thermodynamics (Lemaitre and Chaboche, 1985). The first principle postulates the balance of the energy, demanding the conservation of the total internal energy of the system:

$$\rho \dot{e} = \boldsymbol{\sigma} : \dot{\boldsymbol{\varepsilon}} + \rho r - div\, \vec{q} \tag{2.14}$$

where e is the specific internal energy, $\boldsymbol{\sigma}$ the Cauchy stress tensor, $\dot{\boldsymbol{\varepsilon}}$ is the rate of deformation (under the hypothesis of small strains), r is the specific density of the internal heat production, $\vec{q}$ is the heat flux vector.

The second principle of thermodynamics establishes that for an irreversible process the change in the internal production of entropy should be bigger or the same than the change of introduced entropy:

$$\rho \dot{s} - \frac{r}{T} + div \frac{\vec{q}}{T} \geq 0 \tag{2.15}$$

where s is the specific entropy and T is the absolute temperature. The fundamental inequality containing the first and second principles is obtaining by replacing r in (2.15) with the expression resulting from the equation of conservation of energy (2.14). By introducing another variable, i.e. the specific free energy

$$\psi = e - Ts \tag{2.16}$$

after simple calculations, we finally obtain the Clausius-Duhem inequality:

$$D = \boldsymbol{\sigma} : \dot{\boldsymbol{\varepsilon}} - \rho\left(\dot{\psi} + s\dot{T}\right) - \vec{q} \cdot \frac{\vec{grad}\, T}{T} \geq 0 \tag{2.17}$$

The *method of local state* postulates that the thermodynamic state of a material medium at a given point and instant is completely defined by the knowledge of the values of a certain number of variables at that instant, which depend only upon the point considered (Lemaitre and Chaboche, 1985). Physical phenomena can be described with a precision which depends on the choice of the nature and number of variables. The processes defined in this way will be thermodynamically admissible if, at any instant of evolution, the Clausius-Duhem inequality is satisfied. The variables of the thermodynamical problem are the free variables and the internal variables.

The *free variables* are also termed *state variables*, since the value they assume define the state of the problem. We limit ourselves to the two observable variables which occur in damage phenomena

$$\mathcal{F} = \left\{\boldsymbol{\varepsilon},\, T\right\} \tag{2.18}$$

assuming small strains. For reversible phenomena, at every instant of time, the state depends uniquely on these variables.

For dissipative phenomena, the current state depends also on the past history which is represented by the values at each instant of other variables, called *internal variables*:

$$\mathcal{G} = \left\{\boldsymbol{\varepsilon}^p, \boldsymbol{\varepsilon}^e, V_k\right\} \tag{2.19}$$

The plastic strains $\boldsymbol{\varepsilon}^p$ are required as internal variables in plasticity and viscoplasticity problems. For small strains, the plastic strains is the permanent strain associated to the relaxed configuration, given by the decomposition $\boldsymbol{\varepsilon}^p = \boldsymbol{\varepsilon} - \boldsymbol{\varepsilon}^e$. The thermoelastic strains $\boldsymbol{\varepsilon}^e$ are also internal variables and they

include, as well, the possibility of thermal dilatation. Other phenomena such as damage, hardening etc. require the introduction of other internal variables, which in (2.19) are termed V_k. The values assumed by all the internal variables are described by opportune evolution laws.

Once all the variables of the mechanical problem have been defined, we postulate the existence of a thermodynamical potential from which the state laws can be derived. Without entering into details, the specification of a function with scalar value, concave with respect to the temperature and convex with respect to other variables, allows us to satisfy a priori the conditions of thermodynamic stability imposed by the inequalities that can be derived from the second principle (Maugin, 1992; Lemaitre and Chaboche, 1985). It is possible to work with different potentials. Here we choose the free specific energy potential

$$\psi = \psi\left(\boldsymbol{\varepsilon},\ T, \boldsymbol{\varepsilon}^p, \boldsymbol{\varepsilon}^e, V_k\right) \tag{2.20}$$

In elastoplasticity or viscoplasticity the strains appear only in the form of their additive decomposition $\boldsymbol{\varepsilon}^e = \boldsymbol{\varepsilon} - \boldsymbol{\varepsilon}^p$, hence we can write $\psi = \psi\left(T, \boldsymbol{\varepsilon}^e, V_k\right)$. We now use the Clausius-Duhem inequality with

$$\dot{\psi} = \frac{\partial \psi}{\partial \boldsymbol{\varepsilon}^e} : \dot{\boldsymbol{\varepsilon}}^e + \frac{\partial \psi}{\partial T}\dot{T} + \frac{\partial \psi}{\partial V_k}\dot{V}_k \tag{2.21}$$

to obtain

$$D = \left(\boldsymbol{\sigma} - \rho\frac{\partial \psi}{\partial \boldsymbol{\varepsilon}^e}\right) : \dot{\boldsymbol{\varepsilon}}^e + \boldsymbol{\sigma} : \dot{\boldsymbol{\varepsilon}}^p - \rho\left(s + \frac{\partial \psi}{\partial T}\right)\dot{T} - \rho\frac{\partial \psi}{\partial V_k}\dot{V}_k - \vec{q}\cdot\frac{\vec{grad}\,T}{T} \geq 0 \tag{2.22}$$

Since the Clausius-Duhem inequality holds regardless of any particular $\dot{\boldsymbol{\varepsilon}}^e$ or $\dot{T}$, it necessarily follows that (Coleman and Gurtin, 1967):

$$\boldsymbol{\sigma} = \rho \frac{\partial \psi}{\partial \boldsymbol{\varepsilon}^e}$$
$$s = -\frac{\partial \psi}{\partial T} \qquad (2.23a,b)$$

In an analogous manner, we define the thermodynamic forces associated with the internal variables by

$$A_k = \rho \frac{\partial \psi}{\partial V_k} \qquad (2.24)$$

Equations (2.23a), (2.23b) and (2.24) constitute the *state laws*. In particular, the first one defines the *constitutive law*.

In the following Sections, some damage models will be discussed. As it will be seen, all the models present a formulation consistent with the thermodynamical framework that it has been presented. In particular, the constitutive laws are all consistent with (2.23a) and have been obtained by assuming a free specific energy potential in compliance with (2.20).

2.2 Brief Overview of Damage Models

In Section 2.1 we have presented the basics of the classical theory of Continuum Damage Mechanics. The concepts related to the original formulation of Kachanov (1958) have been emphasized, such as the effective stress and the strain-equivalence (Rabotnov, 1969; Lemaitre and Chaboche, 1978; Lemaitre, 1984; Krajcinovic, 1984; Chaboche, 1988; Murakami, 1988).

Since the pioneering paper of Kachanov, a great effort has been devoted to the research on Continuum Damage Mechanics. Completely different approaches at the theory have been presented, even concerning the basic hypotheses to describe the damage phenomenon. In Section 2.1.2 we have discussed the classical approach consisting in the strain-equivalent relationship between the real physic space and

an effective undamaged one (Kachanov, 1958; Lemaitre, 1978; Simó and Ju, 1987). Other hypotheses have been formulated to define the transformation between the real damaged space and the effective undamaged one. For instance, the concept of *effective strain* has been proposed in connection with the *hypothesis of stress equivalence* (Simó and Ju, 1987). Other researches (Krajcinovic and Fonseka, 1981; Dragon and Mroz, 1979; Carol *et al.*, 2001; Luccioni and Oller, 2003) have considered the *hypothesis of energy equivalence*.

In the literature we find different approaches to describe the damage from the phenomenological point of view. In addition to the models based on the assumption of one or more scalar damage variables (Simó and Ju, 1987; Faria and Oliver, 1993; Faria *et al.*, 1998, 2000, 2004; Cervera et al. 1995, 1996, 1999; Cervera, 2003), models which employ vectorial damage variables (Krajcinovic and Fonseka, 1981; Talreja, 1985) have been proposed. In addition, models with second order tensors (Dragon and Mroz, 1979; Murakami and Ohno, 1980; Lemaitre *et al.*, 2000; Carol *et al.*, 2001), fourth-order tensors (Chaboche, 1979; Ortiz, 1985; Lemaitre and Chaboche, 1985; Simó and Ju, 1987; Ju, 1990; Lubarda *et al.*, 1994; Govindjee *et al.*, 1995) or even eighth-order damage tensors (Chaboche, 1988) can also be found in the literature. In fact, the surface microcracks and the volume cavities that make up damage usually have preferred orientations (Krajcinovic and Fonseka, 1981). This leads to the so-called *damage induced anisotropy*, which can be described only via second or even higher order tensors. However, probably due to the difficulties in postulating appropriate evolution laws for higher order tensors, the second-order tensor is preferred in the modelling of damage induced anisotropy, though only damage not higher than orthotropy can be described. Nevertheless, we recognize that the more the model is sophisticated, the more the number of parameters must be experimentally evaluated to formulate the model. Moreover, it is very difficult to compare the experimental

evidence with the induced anisotropic damage predicted by the related models, with the aim of choosing the most proper damage variable.

In addition, the differences between the great number of models reported in the literature are due to the aim of the analysis. Consequently, we will find different damage variable laws depending on the mechanical phenomenon considered. For instance, different theories are available for creep damage (Kachanov 1958; Rabotnov, 1963; Murakami and Ohno, 1980), fatigue damage (Lemaitre, 1985; Lemaitre and Chaboche, 1985), ductile damage (Lemaitre, 1985; Dragon, 1985), brittle and quasi-brittle damage (Simó and Ju, 1987; Faria and Oliver, 1993; Govindjee *et al.*, 1995; Cervera et al. 1995, 1996, 1999; Faria et al., 1998, 2000, 2004).

One of the critical issues associated with damage models is the selection of a proper damage criteria. This aspect is strictly related to the particular material investigated. For instance, in case of concrete several different criteria have been adopted, such as the equivalent strain-based (Mazars and Pijaudier-Cabot, 1989) and the stress-based approaches (Ortiz, 1985), as well as the damage energy release rate-based proposals (Simó and Ju, 1987; Ju, 1989) and the empirical criteria (Faria *et al.* 1998; Comi and Perego, 2001).

In addition to the classical elastic-damage models (Mazars and Pijaudier-Cabot, 1989; Lubarda *et al.*, 1994; Cervera *et al.*, 1995, 2003; Comi and Perego, 2001; Faria *et al.* 2004), we can also find models which account for the irreversible strains due to plastic flow, e.g. Ortiz (1985), Lemaitre (1985), Dragon (1985), Resende (1987), Simó and Ju (1987), Lubliner *et al.* (1989), Yazdani and Schreyer (1990), di Prisco and Mazars (1996), Lee and Fenves (1998), Faria *et al.* (2000), Hansen *et al.* (2001). Other models account also for rate dependent effects, i.e. viscosity (Simó and Ju, 1987; Cervera *et al.*, 1996, 1999 ; Cervera, 2003), or even plasticity coupled with viscous damage (Simó and Ju, 1987; Faria and Oliver 1993; Faria *et al.*, 1998).

A complete review of the available damage models is not pursued in this study and the reader is referred to Oller (2001), Luccioni (2003), Lemaitre and Desmorat (2005). In the following sections, we will focus on some damage models which present concepts and features very useful to fully understand the models presented in Chapters 3 and 4. We will delve into their formulations in order to emphasize the main hypotheses together with the computational aspects related to their numerical implementation.

2.3 Scalar Damage Models

The simplest models are the scalar damage ones, in which the stiffness degradation is described by a single scalar variable *d* which affects in the same measure all the components of the elastic constitutive tensor.

The formulation that will be principally detailed herein is the strain-based damage model proposed by Simó and Ju (1987). It provides a simple constitutive model which, nevertheless, is able to reproduce the overall nonlinear behaviour including stiffness degradation, strain-hardening/softening response and rate dependency.

2.3.1 Thermodynamic Formulation

The crucial idea underlining the strain-based isotropic continuum damage model formulated by Simó and Ju is the hypothesis that damage in the material is directly linked to the history of total strain. Therefore, the *free* (or *state*) variable of the thermodynamic problem is the strain tensor $\boldsymbol{\varepsilon}$. In addition, we consider an internal strain-like variable $r = r(\boldsymbol{\varepsilon})$ which can be interpreted as the current damage threshold. The scalar damage variable is a function of the internal variable, i.e $d = d(r)$. The following form of the free energy potential is assumed

$$\psi(\boldsymbol{\varepsilon}, r) = \left[1 - d(r)\right]\psi_0 \tag{2.25}$$

Where d is the damage variable (see Section 2.1.1), $\psi_0(\boldsymbol{\varepsilon})$ is the initial elastic stored energy function of the undamaged (virgin) material. It is a convex function that in the linear case assumes the form

$$\psi_0(\boldsymbol{\varepsilon}) = \frac{1}{2}\boldsymbol{\varepsilon} : \mathbf{C} : \boldsymbol{\varepsilon} \geq 0 \tag{2.25}$$

where **C** denotes the usual (fourth-order) isotropic linear-elastic constitutive tensor. From (2.25) and recalling that $0 \leq d(r) \leq 1$, it derives that $\psi(\boldsymbol{\varepsilon}, r) \geq 0$.

According to the Clausius-Duhem inequality, see Equation (2.22), the dissipation for an isothermic elasto-damageable process takes the form

$$D = -\dot{\psi} + \boldsymbol{\sigma} : \dot{\boldsymbol{\varepsilon}} = \left(-\frac{\partial \psi}{\partial \boldsymbol{\varepsilon}} + \boldsymbol{\sigma} \right) : \dot{\boldsymbol{\varepsilon}} + \psi_0 \dot{d} \geq 0 \tag{2.26}$$

Applying the Coleman's method (Coleman and Gurtin, 1967) to guarantee the condition of positive dissipation in (2.26), the constitutive equation is obtained as

$$\boldsymbol{\sigma} = \frac{\partial \psi}{\partial \boldsymbol{\varepsilon}} = \left[1 - d(r)\right] \mathbf{C} : \boldsymbol{\varepsilon} \tag{2.27}$$

The notion of effective stress both with the hypothesis of strain equivalence follow from the assumed form of the free energy. In fact:

$$\overline{\boldsymbol{\sigma}} = \mathbf{C} : \boldsymbol{\varepsilon} \tag{2.28}$$

Therefore, we finally obtain

$$\boldsymbol{\sigma} = \left[1 - d(r)\right] \overline{\boldsymbol{\sigma}} \tag{2.29}$$

According to (2.26) and (2.27), the dissipation can be expressed as

$$D = \psi_0 \dot{d} \geq 0 \tag{2.30}$$

provided that, in view of (2.25), the scalar damage variable increases monotonically, i.e. $\dot{d} \geq 0$.

2.3.2 Damage Threshold Function

Simó and Ju (1987) characterized the progressive degradation of mechanical properties of the material due to damage by means of a simple isotropic damage mechanism. For this aim, they introduced the concept of *equivalent strain* $\bar{\tau}$, which is the (undamaged) energy norm of the strain tensor:

$$\bar{\tau} = \sqrt{2\psi_0(\boldsymbol{\varepsilon})} = \sqrt{\boldsymbol{\varepsilon} : \mathbf{C} : \boldsymbol{\varepsilon}} \tag{2.31}$$

Such a scalar positive quantity, is defined in order to identify 'loading', 'unloading' or 'reloading' situations for a general 3D stress state. We then characterize the state of damage in the material by means of a damage criterion formulated in the strain space, with the following functional form

$$g(\bar{\tau}_t, r_t) = \bar{\tau}_t - r_t \leq 0 \tag{2.32}$$

Here, the subscript *t* refers to value at current time, and r_t is the damage threshold at current time *t*. If r_0 denotes the initial damage threshold before any loading is applied, a property characteristic of the material, we must have that $r_t \geq r_0$. Equation (2.32) states that damage in the material is initiated when the energy norm of the strain tensor $\bar{\tau}_t$ exceeds the initial damage threshold r_0.

Expression (2.31) is the equation of an ellipsoid. Figures 2.5 and 2.6 show the shape of the damage threshold surface in the principal strain space and in the principal stress space for a Poisson's ratio equal to 0.2.

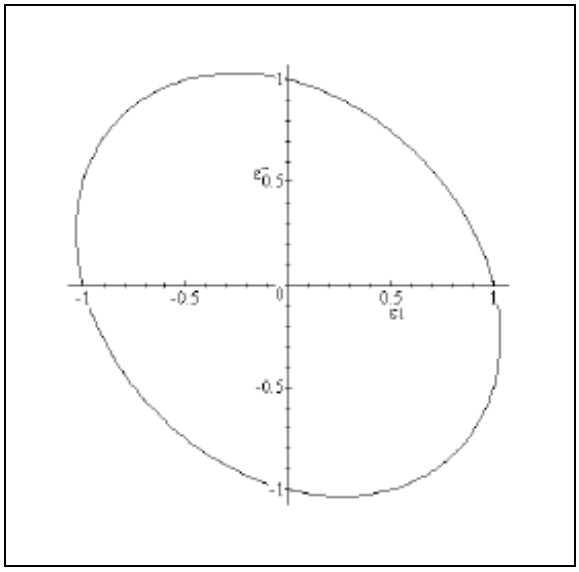

Figure 2.5 Damage threshold surface in the principal strain space, with $\varepsilon_3 = 0$, according to Simó an Ju (1987).

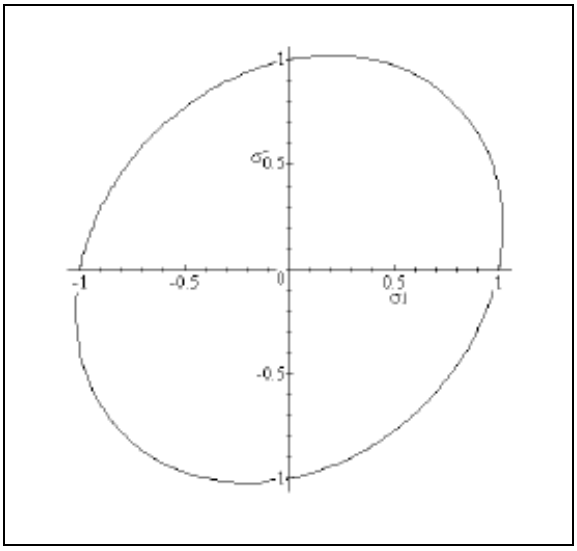

Figure 2.6 Damage threshold surface in the principal stress space, with $\sigma_3 = 0$, according to Simó an Ju (1987).

2.3.3 Damage Evolution Law

For the isotropic case, the evolution of the damage variable *d* is defined by the rate equation

$$\dot{d}_t = \dot{\mu}\, H\left(\overline{\tau}_t, d_t\right) \tag{2.33}$$

in which

$$\dot{r} = \dot{\mu} \tag{2.34}$$

and function $H\left(\overline{\tau}_t, d_t\right)$ relates its arguments to the damage variable. It is possible to consider an explicit damage evolution law in the form

$$d_t = G\left(\overline{\tau}_t\right) \tag{2.35}$$

Several forms of the damage accumulation function $G\left(\overline{\tau}_t\right)$ are available in literature (Mazars, 1982; Oliver *et al.*, 1990; Cervera *et al.*, 1999; Oller, 2001).

The term $\dot{\mu}$ is a damage consistency parameter that defines damage loading/unloading conditions to the Kuhn-Tucker relations

$$\dot{\mu} \geq 0 \quad g\left(\overline{\tau}_t, r_t\right) \leq 0 \quad \dot{\mu}\, g\left(\overline{\tau}_t, r_t\right) = 0 \tag{2.36}$$

Conditions (2.36) are standard for problems involving unilateral constraint. If $g\left(\overline{\tau}_t, r_t\right) < 0$, the damage criterion is not satisfied and by condition $(2.36)_3$ $\dot{\mu} = 0$; hence, the damage rule (2.33) implies that $\dot{d}_t = 0$ and no further damage takes place. If, on the other hand, $\dot{\mu} > 0$, that is, further damage ("loading") is taking place, condition $(2.36)_3$ now implies that $g\left(\overline{\tau}_t, r_t\right) = 0$. In this event the value of $\dot{\mu}$ is determined by the damage consistency condition, i.e.

$$g\left(\overline{\tau}_t, r_t\right) = \dot{g}\left(\overline{\tau}_t, r_t\right) = 0 \quad \rightarrow \quad \dot{\mu} = \dot{\overline{\tau}}_t \tag{2.37}$$

So that r_t is given by the expression

$$r_t = \max\left[r_0, \max\left(\overline{\tau}_t\right)\right] \tag{2.38}$$

2.3.4 Tangent Constitutive Tensor

Time differentiation of (2.27) along with the damage rule (2.33) and the damage consistency condition (2.37) then yields

$$\dot{\boldsymbol{\sigma}}\left(\boldsymbol{\varepsilon}, d\right) = \left(1-d\right)\frac{\partial \psi_0^2}{\partial \boldsymbol{\varepsilon}^2} : \dot{\boldsymbol{\varepsilon}} - H\left(\overline{\tau}_t, d_t\right)\dot{\overline{\tau}}_t \overline{\boldsymbol{\sigma}} \tag{2.39}$$

since $\overline{\boldsymbol{\sigma}} = \partial \psi_0 / \partial \boldsymbol{\varepsilon}$. By recalling that $\mathbf{C} = \partial \psi_0^2 / \partial \boldsymbol{\varepsilon}^2$ we obtain

$$\dot{\boldsymbol{\sigma}}\left(\boldsymbol{\varepsilon}, d\right) = \left(1-d\right)\mathbf{C} : \dot{\boldsymbol{\varepsilon}} - H\left(\overline{\tau}_t, d_t\right)\dot{\overline{\tau}}_t \overline{\boldsymbol{\sigma}} \tag{2.40}$$

By taking the time derivative of (2.31), we obtain $\dot{\overline{\tau}} = \left(1/\overline{\tau}\right)\overline{\boldsymbol{\sigma}} : \dot{\boldsymbol{\varepsilon}}$. Substitution into (2.40) then yields

$$\dot{\boldsymbol{\sigma}}\left(\boldsymbol{\varepsilon}, d\right) = \mathbf{C}^{\tan} : \dot{\boldsymbol{\varepsilon}} \tag{2.41}$$

In which

$$\mathbf{C}^{\tan} = \left(1-d\right)\mathbf{C} - \frac{H\left(\overline{\tau}_t, d_t\right)}{\overline{\tau}_t}\overline{\boldsymbol{\sigma}} \otimes \overline{\boldsymbol{\sigma}} \tag{2.42}$$

Note that $\mathbf{C}^{\tan}$ is a symmetric and rank-four tensor. The symmetry of the tangent stiffness tensor is due to the opportune definition of the equivalent strain $\overline{\tau}$ given by Equation (2.31).

2.3.5 Numerical Implementation

The damage model proposed by Simó and Ju (1987) permits to evaluate the damage variable in an explicit way without any iterative procedure. The constitutive law integration algorithm is given in the following Table 2.1.

Table 2.1 Algorithm for the implementation of the damage model of Simó and Ju (1987).

1. Compute the displacement increment for step n from the equilibrium equation

   $\Delta \mathbf{u}_n$

2. Compute the strain increment and update the strain

   $\boldsymbol{\varepsilon}_n = \boldsymbol{\varepsilon}_{n-1} + \Delta \boldsymbol{\varepsilon}_n$

3. Impose

   $d_n = d_{n-1}$

   $r_n = r_{n-1}$

4. Compute the current equivalent strain

   $\bar{\tau}_n = \sqrt{2\psi_0(\boldsymbol{\varepsilon}_n)} = \sqrt{\boldsymbol{\varepsilon}_n : \mathbf{C} : \boldsymbol{\varepsilon}_n}$

5. Check damage criterion

   $g(\bar{\tau}_n, r_n) = \bar{\tau}_n - r_n \leq 0$

   Yes: elastic behaviour, no further damage. Go to 9.

   No: proceed to 6.

6. Compute the damage variable

   $d_n = G(\bar{\tau}_n)$

7. Update the damage threshold

   $r_n = \bar{\tau}_n$

8. Compute the tangent constitutive tensor

$$\mathbf{C}^{\tan} = \left(1 - d_n\right)\mathbf{C} - \frac{H\left(\overline{\tau}_n, d_n\right)}{\overline{\tau}_n}\overline{\boldsymbol{\sigma}}_n \otimes \overline{\boldsymbol{\sigma}}_n$$

9. Update the stress

$$\boldsymbol{\sigma}^n = \left(1 - d^n\right)\mathbf{C} : \boldsymbol{\varepsilon}^n$$

10. End

The formulation presented is characterized by a particular versatility, which permits to include rate dependent effects and also the plastic strains. For further details on the corresponding numerical algorithms, the reader is referred to Simó and Ju (1987), Oller (2001), Luccioni (2003) and Cervera (2003).

2.3.6 Different Damage Criteria

Several damage threshold functions different than (2.31) have been proposed in literature. The choice is strictly linked to the type of material to be analyzed.
Mazars (1982) proposed the following form

$$\overline{\tau} = \sqrt{\boldsymbol{\varepsilon} : \boldsymbol{\varepsilon}} \tag{2.43}$$

Figures 2.7 and 2.8 show the shape of the damage threshold surface in the principal strain space and in the principal stress space for a Poisson's ratio equal to 0.2.
This choice leads to a non-symmetric tangent constitutive tensor (Mazars, 1982)

$$\mathbf{C}^{\tan} = \left(1 - d\right)\mathbf{C} - \frac{H\left(\overline{\tau}_t, d_t\right)}{\overline{\tau}_t}\overline{\boldsymbol{\sigma}} \otimes \boldsymbol{\varepsilon} \tag{2.44}$$

Therefore, it is evident that the symmetry of the tangent constitutive tensor depends crucially on the form of the damage threshold function, namely the equivalent strain.

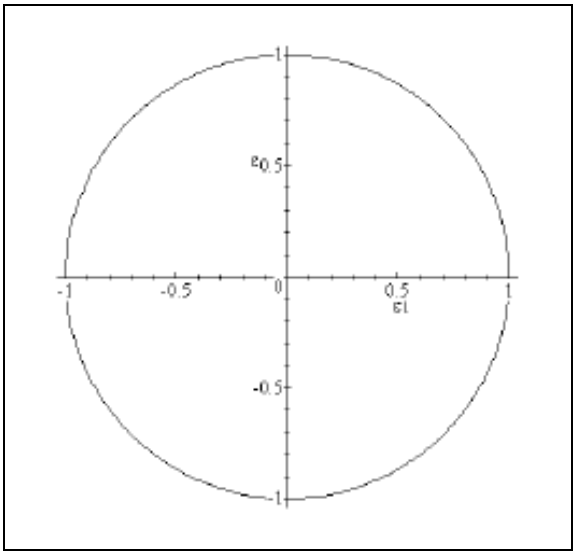

Figure 2.7 Damage threshold surface in the principal strain space, with $\varepsilon_3 = 0$, according to Mazars (1982).

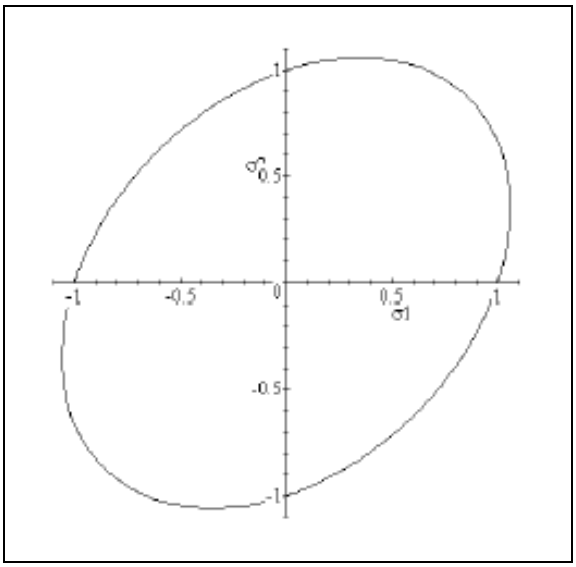

Figure 2.8 Damage threshold surface in the principal stress space, with $\sigma_3 = 0$, according to Mazars (1982).

The damage criteria described by Equations (2.31) and (2.43) are suitable for materials which exhibit similar behaviour in tension and compression, such as metals. Nevertheless, the geomaterials are characterized by different damage thresholds in tension and compression. In this case, the damage threshold surface should account for this phenomenon, like the one proposed by Oliver *et al.* (1990)

$$\bar{\tau} = \left(\theta + \frac{1-\theta}{n} \right) \sqrt{2\psi_0} \tag{2.45}$$

in which n is the ratio between the compression and tension damage thresholds and

$$\theta = \frac{\sum_{i=1}^{3} \langle \bar{\sigma}_i \rangle}{\sum_{i=1}^{3} |\bar{\sigma}_i|} \tag{2.46}$$

The symbols $\langle \cdot \rangle$ are the Macauley brackets $\left(\langle x \rangle = x, \, if \; x \geq 0, \langle x \rangle = 0, \, if \; x < 0 \right)$.

Figures 2.9 and 2.10 show the shape of the damage threshold surface in the principal strain space and in the principal stress space for a Poisson's ratio equal to 0.2.

Expression (2.45) is inadequate for geomaterials, such as concrete, since the strength enhancement observed in the compression–compression domain cannot be predicted.

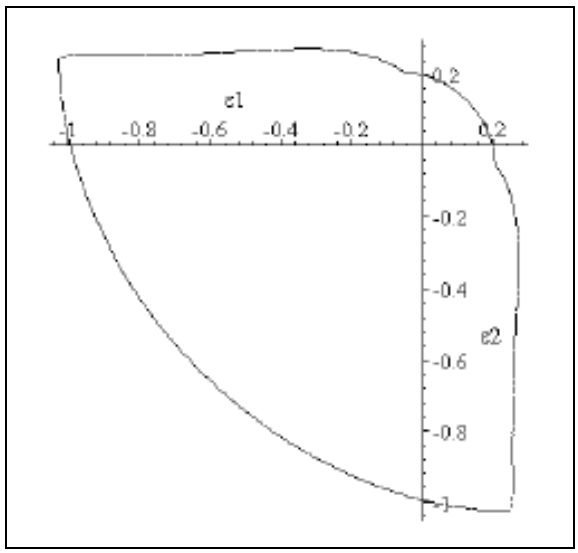

Figure 2.9 Damage threshold surface in the principal strain space, with $\varepsilon_3 = 0$, according to Oliver *et al.* (1990).

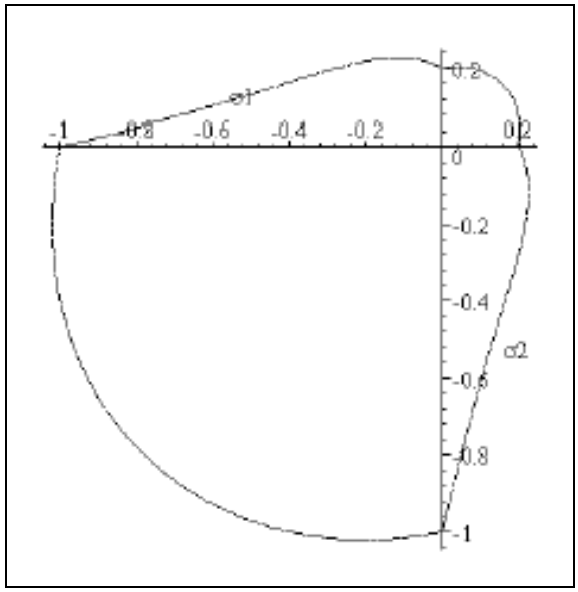

Figure 2.10 Damage threshold surface in the principal stress space, with $\sigma_3 = 0$, according to Oliver *et al.* (1990).

2.4 Unilateral Effect and Damage Models

The unilateral nature of damage is related to the fact that damage, though irreversible, can be active or not, depending on load conditions. For instance, in geomaterials, the stiffness degradation in tension is due to formation and propagation of microcracks. In addition, experimental tests emphasize the phenomenon of crack closure upon loading reversal, with consequent stiffness recovery.

The mechanical behaviour which can be described by a unilateral damage model is represented in Figure 2.11.

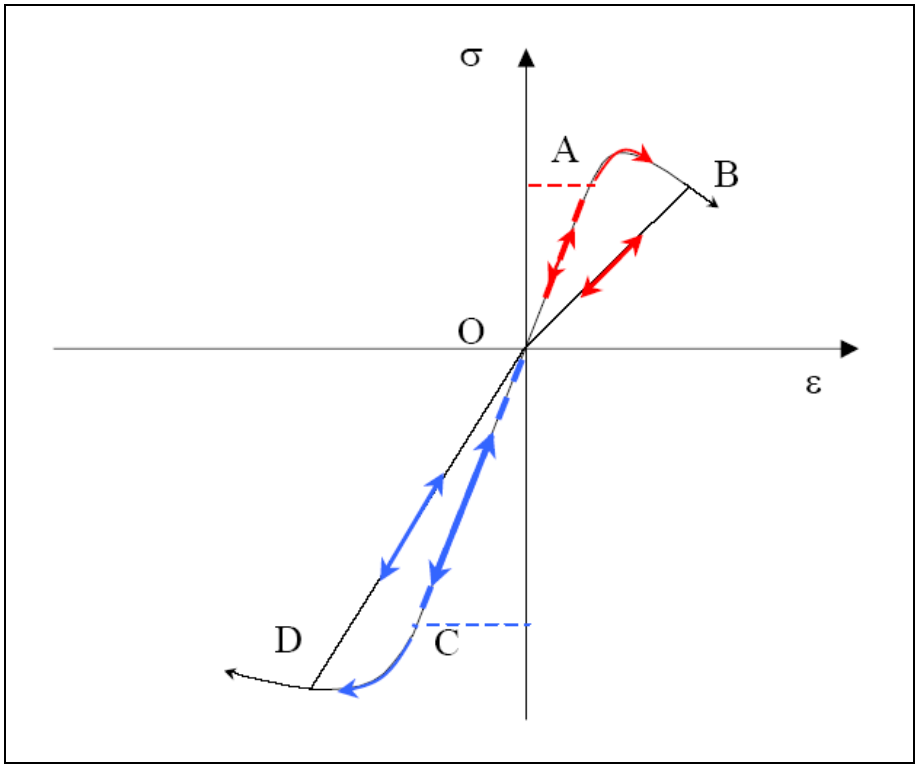

Figure 2.11 Unilateral effect under cyclical loading.

In particular, Figure 2.11 shows the following effects:

- The OA, OB, OC and OD branches correspond to elastic behaviour during loading or unloading.
- The stretches of the curve denoted by AB and CD correspond to damage growth under loading.
- The unloading paths after damage onset, i.e. BO and DO, are linear elastic according to a damaged stiffness.
- When the tensile damage process stops because of unloading, and then the material is subjected to compression, the stiffness is recovered. This situation represents the crack-closure phenomenon.

Several unilateral damage models are available in the literature (Mazars and Pijaudier-Cabot, 1989; Ju, 1989; Chaboche, 1995). In this section we will focus on the *Tension-Compression Damage Model* formulated by Faria and Oliver (1993) which has been extensively used (Faria *et al.* 1998, 2000, 2004; Cervera *et al.* 1995, 1996, 1999, 2003). This model is characterized by a split of the stress tensor into tensile and compressive components, in order to account for the unilateral effect. Moreover, two internal scalar variables are assumed to monitor the local damage under tension and compression, respectively. These choices provide a simple constitutive model which, nevertheless, is able to reproduce the overall nonlinear behaviour including strain-hardening/softening response, stiffness degradation and regradation under multiple stress reversal.

2.4.1 Tension-Compression Damage Model (Faria *et al.*, 1998)

This damage model is based on the assumption that a stress split is required to capture the unilateral behaviour exhibited by the material when passing from tension to compression. The split of the effective stress tensor $\overline{\boldsymbol{\sigma}}$ into tensile and compressive components, $\overline{\boldsymbol{\sigma}}^{+}$ and $\overline{\boldsymbol{\sigma}}^{-}$, is performed according to

$$\overline{\boldsymbol{\sigma}}^{+} = \sum_{j=1}^{3} \left\langle \overline{\sigma}_j \right\rangle \mathbf{p}_j \otimes \mathbf{p}_j \tag{2.47}$$

$$\overline{\boldsymbol{\sigma}}^{-} = \overline{\boldsymbol{\sigma}} - \overline{\boldsymbol{\sigma}}^{+} \tag{2.48}$$

where $\overline{\sigma}_j$ denotes the *j*-th principal stress value from tensor $\overline{\boldsymbol{\sigma}}$, $\mathbf{p}_j$ represents the unit vector associated with its respective principal direction and the symbols $\langle \cdot \rangle$ are the Macaulay brackets.

For a consistent derivation of a constitutive law, a Helmholtz free energy potential with the form

$$\psi\left(\boldsymbol{\varepsilon}, d^{+}, d^{-}\right) = \left(1 - d^{+}\right)\psi_0^{+}\left(\boldsymbol{\varepsilon}\right) + \left(1 - d^{-}\right)\psi_0^{-}\left(\boldsymbol{\varepsilon}\right) \geq 0 \tag{2.49}$$

is postulated, where $\psi_0^{+}\left(\boldsymbol{\varepsilon}\right)$ and $\psi_0^{-}\left(\boldsymbol{\varepsilon}\right)$ are elastic free energies, defined according to

$$\psi_0^{+}\left(\boldsymbol{\varepsilon}\right) = \frac{1}{2}\overline{\boldsymbol{\sigma}}^{+} : \mathbf{C}^{-1} : \overline{\boldsymbol{\sigma}} = \frac{1}{2}\overline{\boldsymbol{\sigma}}^{+} : \boldsymbol{\varepsilon} \geq 0 \tag{2.50}$$

$$\psi_0^{-}\left(\boldsymbol{\varepsilon}\right) = \frac{1}{2}\overline{\boldsymbol{\sigma}}^{-} : \mathbf{C}^{-1} : \overline{\boldsymbol{\sigma}} = \frac{1}{2}\overline{\boldsymbol{\sigma}}^{-} : \boldsymbol{\varepsilon} \geq 0 \tag{2.51}$$

The set of internal variables is therefore constituted by the d^{+} and d^{-} scalar damage variables. These damage variables are directly linked to tensile and compressive deteriorations, which are assumed as independent processes. Strain tensor $\boldsymbol{\varepsilon}$ is the only free variable admitted.

According to the Clausius-Duhem inequality, see Equation (2.22), the dissipation for an isothermic elasto-damageable process takes the form

$$D = -\dot{\psi} + \boldsymbol{\sigma} : \dot{\boldsymbol{\varepsilon}} = \left(-\frac{\partial \psi}{\partial \boldsymbol{\varepsilon}} + \boldsymbol{\sigma} \right) : \dot{\boldsymbol{\varepsilon}} + \psi_0^{+}\dot{d}^{+} + \psi_0^{-}\dot{d}^{-} \geq 0 \tag{2.52}$$

Applying the Coleman's method (Coleman and Gurtin, 1967) to guarantee the condition of positive dissipation in (2.52), the constitutive equation is obtained as

$$\boldsymbol{\sigma} = \frac{\partial \psi}{\partial \boldsymbol{\varepsilon}} = \left(1 - d^{+}\right) \frac{\partial \psi_0^{+}}{\partial \boldsymbol{\varepsilon}} + \left(1 - d^{-}\right) \frac{\partial \psi_0^{-}}{\partial \boldsymbol{\varepsilon}} \tag{2.53}$$

Owing to the non-negativeness of $\psi_0^{+}\left(\boldsymbol{\varepsilon}\right)$ and $\psi_0^{-}\left(\boldsymbol{\varepsilon}\right)$, from equation (2.52) it can be inferred that for the dissipation

$$D = \psi_0^{+} \dot{d}^{+} + \psi_0^{-} \dot{d}^{-} \geq 0 \tag{2.54}$$

Therefore, to satisfy the Clausius-Duhem inequality it suffices that

$$\dot{d}^{\pm} \geq 0 \tag{2.55}$$

Taking into consideration the equations (2.50) and (2.51), the linear dependency between $\overline{\boldsymbol{\sigma}}$ and $\boldsymbol{\varepsilon}$ expressed in (2.28), the stress split postulated in (2.47), and the fact that $\overline{\boldsymbol{\sigma}}^{+}$ and $\overline{\boldsymbol{\sigma}}^{-}$ are degree one homogeneous functions of $\boldsymbol{\varepsilon}$, owing to Euler's theorem we obtain

$$\frac{\partial \psi_0^{+}}{\partial \boldsymbol{\varepsilon}} = \overline{\boldsymbol{\sigma}}^{+} \tag{2.56}$$

$$\frac{\partial \psi_0^{-}}{\partial \boldsymbol{\varepsilon}} = \overline{\boldsymbol{\sigma}}^{-} \tag{2.57}$$

Substituting (2.56) and (2.57) in equation (2.53), the final form of the constitutive law is obtained:

$$\boldsymbol{\sigma} = \left(1 - d^{+}\right) \overline{\boldsymbol{\sigma}}^{+} + \left(1 - d^{-}\right) \overline{\boldsymbol{\sigma}}^{-} \tag{2.58}$$

Owing to the scalar form of the damage variables d^{+}, d^{-} and to the format of the presented constitutive law, equation (2.58) points out that a split of tensor $\boldsymbol{\sigma}$ into

tensile and compressive tensors $\overline{\boldsymbol{\sigma}}^{+}$ and $\overline{\boldsymbol{\sigma}}^{-}$ is implicit in the present formulation, that is,

$$\boldsymbol{\sigma}^{+} = \left(1 - d^{+}\right)\overline{\boldsymbol{\sigma}}^{+} \tag{2.59}$$

$$\boldsymbol{\sigma}^{-} = \left(1 - d^{-}\right)\overline{\boldsymbol{\sigma}}^{-} \tag{2.60}$$

This relevant property emphasises that the adopted split of the effective stress tensor leads in fact to a related dual split of the Cauchy stress tensor $\boldsymbol{\sigma}$.

Analogously to the equivalent strain (2.31) postulated by Simó and Ju (1987), Faria *et al.* (1987) define the dual concept of *equivalent stress*, which is again a strain-based scalar positive norm that allows identifying 'loading', 'unloading' or 'reloading' situations. Since a clear distinction between tension and compression is assumed, in view of the stress split defined in (2.47), a tensile equivalent stress τ^{+} and a compressive equivalent stress τ^{-} are postulated according to the forms

$$\overline{\tau}^{+} = \sqrt{\overline{\boldsymbol{\sigma}}^{+} : \boldsymbol{\Lambda}^{+} : \overline{\boldsymbol{\sigma}}^{+}} \tag{2.61}$$

$$\overline{\tau}^{-} = \sqrt{\overline{\boldsymbol{\sigma}}^{-} : \boldsymbol{\Lambda}^{-} : \overline{\boldsymbol{\sigma}}^{-}} \tag{2.62}$$

where $\boldsymbol{\Lambda}^{\pm}$ are non-dimensional fourth-order metric tensors that define the shape of the damage bounding surfaces.

Calling for the effective stress norms defined in (2.61) and (2.62), two damage criteria $g^{\pm}$ in terms of the effective stress tensors are introduced

$$g^{+}\left(\overline{\tau}^{+}, r^{+}\right) = \overline{\tau}^{+} - r^{+} \leq 0 \tag{2.63}$$

$$g^{-}\left(\overline{\tau}^{-}, r^{-}\right) = \overline{\tau}^{-} - r^{-} \leq 0 \tag{2.64}$$

The damage variables are computed in accordance to (Oliver *et al*., 1990)

$$d^{\pm}\left(r^{\pm}\right)=1-\frac{q\left(r^{\pm}\right)}{r^{\pm}} \tag{2.65}$$

where the positive hardening/softening functions $q\left(r^{\pm}\right)$ are related to internal variables $r^{\pm}$, which in turn obey the kinematics

$$\dot{r}^{\pm}=\dot{\mu}^{\pm} \tag{2.66}$$

with $\mu^{\pm}$ being damage multipliers which participate in the Kuhn Tucker conditions

$$\mu^{\pm}\geq 0 \quad g^{\pm}\leq 0 \quad \dot{\mu}^{\pm}g^{\pm}=0 \tag{2.67}$$

If $g^{\pm}<0$, the damage criterion is not satisfied and by condition $(2.67)_3$ $\dot{\mu}^{\pm}=0$, hence no further damage takes place. If, on the other hand, $\dot{\mu}^{\pm}>0$, that is, further damage ("loading") is taking place, condition $(2.67)_3$ now implies that $g^{\pm}=0$. In this event the value of $\dot{\mu}$ is determined by the damage consistency condition, i.e.

$$g^{\pm}=\dot{g}^{\pm}=0 \quad \rightarrow \quad \dot{\mu}^{\pm}=\dot{\bar{\tau}}^{\pm}=\dot{r}^{\pm} \tag{2.68}$$

Integrating for a generic instant *t*, in view of this equation the following conclusion arises

$$r_t^{\pm}=\max\left[r_0^{\pm},\max\left(\bar{\tau}_t^{\pm}\right)\right] \tag{2.69}$$

where $r_0^{\pm}$ are the thresholds that bound the initial linear elastic domains.

The consistent tangent constitutive tensor is derived by differentiating the constitutive law (2.58) with respect to time. After some calculations (see Faria *et al.*, 2000) we obtain

$$\mathbf{C}^{\tan} = \left\{ \left[\left(1-d^{+}\right)\mathbf{I} - \frac{h^{+}}{\overline{\tau}^{+}}\left(\overline{\boldsymbol{\sigma}}^{+} \otimes \overline{\boldsymbol{\sigma}}^{+}\right) : \boldsymbol{\Lambda}^{+} \right] : \mathbf{Q} + \right.$$
$$\left. + \left[\left(1-d^{-}\right)\mathbf{I} - \frac{h^{-}}{\overline{\tau}^{-}}\left(\overline{\boldsymbol{\sigma}}^{-} \otimes \overline{\boldsymbol{\sigma}}^{-}\right) : \boldsymbol{\Lambda}^{-} \right] : \left(\mathbf{I}-\mathbf{Q}\right) \right\} : \mathbf{C} \tag{2.70}$$

where $h^{\pm}$ are related to the evolution of the damage variables in the following way

$$\dot{d}^{\pm} = h^{\pm}\dot{r}^{\pm} \tag{2.71}$$

and $\mathbf{Q}$ is a projection operator defined as

$$\mathbf{Q} = \sum_{i=1}^{3} H\left(\overline{\sigma}_i\right)\mathbf{P}_{ii} \otimes \mathbf{P}_{ii} + 2\sum_{\substack{i,j=1 \\ j\neq i}}^{3} \frac{\left\langle \overline{\sigma}_i \right\rangle - \left\langle \overline{\sigma}_j \right\rangle}{\overline{\sigma}_i - \overline{\sigma}_j}\mathbf{P}_{ij} \otimes \mathbf{P}_{ij} \tag{2.72}$$

where $H\left(\overline{\sigma}_i\right)$ denotes the Heaviside function computed for the *i*-th principal stress $\overline{\sigma}_i$, $\langle\cdot\rangle$ are the Macaulay brackets and

$$\mathbf{P}_{ij} = \mathbf{P}_{ji} = \frac{1}{2}\left(\mathbf{p}_i \otimes \mathbf{p}_j + \mathbf{p}_j \otimes \mathbf{p}_i\right) = symm\left(\mathbf{p}_i \otimes \mathbf{p}_j\right) \tag{2.73}$$

This operator is non symmetric under general conditions, and it applies whilst loading conditions are observed. If unloading occurs in tension or in compression, the evolution of the corresponding damage variable is null, and consequently it suffices to take $h^{+}=0$ or $h^{-}=0$ in (2.70).

2.4.2 Numerical Implementation

Owing to the strain-driven formalism of the model proposed by Faria *et al.* (1998), and to the fact of $\boldsymbol{\varepsilon}$ being fully determined at the beginning of each step of a

displacement-based finite element algorithm, the code implementation is straightforward, as illustrated in Table 2.2.

Table 2.2 Algorithm for the implementation of the Tension Compression damage model of Faria *et al.* (1998).

1. Compute the displacement increment for step n from the equilibrium equation

   $\Delta \mathbf{u}_n$

2. Compute the strain increment and update the strain

   $\boldsymbol{\varepsilon}_n = \boldsymbol{\varepsilon}_{n-1} + \Delta \boldsymbol{\varepsilon}_n$

3. Impose

   $d_n^{\pm} = d_{n-1}^{\pm}$

   $r_n^{\pm} = r_{n-1}^{\pm}$

4. Calculate effective stress and split

   $\overline{\boldsymbol{\sigma}}_n = \mathbf{C} : \boldsymbol{\varepsilon}_n$

   $\overline{\boldsymbol{\sigma}}_n^{+} = \sum_{j=1}^{3} \left\langle \overline{\sigma}_j \right\rangle \mathbf{p}_j \otimes \mathbf{p}_j$

   $\overline{\boldsymbol{\sigma}}_n^{-} = \overline{\boldsymbol{\sigma}}_n - \overline{\boldsymbol{\sigma}}_n^{+}$

5. Compute the current equivalent strain

   $\overline{\tau}_n^{\pm} = \sqrt{\overline{\boldsymbol{\sigma}}_n^{\pm} : \boldsymbol{\Lambda}^{\pm} : \overline{\boldsymbol{\sigma}}_n^{\pm}}$

6. Check damage criterion

   $\overline{\tau}_n^{\pm} < r_n^{\pm}$

   Yes: elastic behaviour, no further damage. Go to 10.

   No: proceed to 7.

7. Compute the damage variable

$$d_n^{\pm} = 1 - \frac{q_n^{\pm}\left(r_n^{\pm}\right)}{r_n^{\pm}}$$

8. Update the damage threshold

$$r_n^{\pm} = \overline{\tau}_n^{\pm}$$

9. Compute the tangent constitutive tensor

$$\mathbf{C}_n^{\tan} = \left\{ \left[\left(1 - d_n^{+}\right)\mathbf{I} - \frac{h_n^{+}}{\overline{\tau}_n^{+}}\left(\overline{\boldsymbol{\sigma}}_n^{+} \otimes \overline{\boldsymbol{\sigma}}_n^{+}\right) : \boldsymbol{\Lambda}^{+} \right] : \mathbf{Q}_n + \right.$$
$$\left. + \left[\left(1 - d_n^{-}\right)\mathbf{I} - \frac{h_n^{-}}{\overline{\tau}_n^{-}}\left(\overline{\boldsymbol{\sigma}}_n^{-} \otimes \overline{\boldsymbol{\sigma}}_n^{-}\right) : \boldsymbol{\Lambda}^{-} \right] : \left(\mathbf{I} - \mathbf{Q}_n\right) \right\} : \mathbf{C}$$

10. Update the stress

$$\boldsymbol{\sigma}_n = \left(1 - d_n^{+}\right)\overline{\boldsymbol{\sigma}}_n^{+} + \left(1 - d_n^{-}\right)\overline{\boldsymbol{\sigma}}_n^{-}$$

11. End

As can be seen, the algorithm presents the same structure of the one proposed by Simó and Ju (1987) and described in Table 2.1. In particular, the strain-driven formalism, which is consistent with standard displacement-based finite element codes, provides high algorithmic efficiency.

The formulation presented is characterized by a particular versatility, which permits to include rate dependent effects (Cervera *et al.*, 1996, 1999) and also the plastic strains (Faria *et al.*, 2000). For further details on the corresponding numerical algorithms, the reader is referred to Faria *et al.* (1998) and Cervera (2003).

2.4.3 Comparison with Others Formulations

The Tension Compression Damage Model detailed in Section 2.4.2 is based on a split of the effective stress tensor $\bar{\boldsymbol{\sigma}}$ and on the definition of two scalar variables d^+, d^-. Such assumptions play an essential role in the definition of the free energy potential. Both the split and the structure of the free energy potential resemble the features of other models based on Continuum Damage Mechanics. For instance, Ortiz (1985), Mazars and Pijaudier-Cabot (1989) proposed a similar split, but over the strain tensor. This different approaches lead to different form of the free energy potential. For instance, the free energy potential presented in (2.49) can be compared to the one of Mazars and Pijaudier-Cabot (1989), whose form is:

$$\psi = \frac{1}{2\left(1-d^+\right)}\boldsymbol{\sigma}^+ : \mathbf{C}^{-1} : \boldsymbol{\sigma}^+ + \frac{1}{2\left(1-d^-\right)}\boldsymbol{\sigma}^- : \mathbf{C}^{-1} : \boldsymbol{\sigma}^- \tag{2.74}$$

An important difference is that in (2.74) the Cauchy stress tensor $\boldsymbol{\sigma}$ is considered, whilst in (2.49) the effective stress tensor $\bar{\boldsymbol{\sigma}}$ have been adopted. Since $\boldsymbol{\sigma}$ is the stress tensor to be evaluated, in (2.74) an implicit formulation is therefore involved, which obviously requires an iterative procedure to be implemented within the constitutive model. In (2.49) the constitutive model is written in terms of the effective stress tensor, which is an explicit entity because of its strain driven background. Anyway, and as emphasised in (2.59) and (2.60), a split of tensor $\boldsymbol{\sigma}$ is also implicit in the model of Faria *et al.* (1998), and equation (2.49) can be expressed as

$$\psi = \frac{1}{2}\boldsymbol{\sigma}^+ : \mathbf{C}^{-1} : \bar{\boldsymbol{\sigma}} + \frac{1}{2}\boldsymbol{\sigma}^- : \mathbf{C}^{-1} : \boldsymbol{\sigma} \tag{2.75}$$

The difference between the two models is evident comparing equations (2.74) and (2.75). This crucial modification does rather distinguish both models and leads to significant computational differences between the models.

La Borderie *et al.* (1990) carried out a split concerning the Cauchy stress tensor, but further complexities are included in the formulation due to the addition of a third damage variable $\tilde{d}$, linked to a coupling term describing the effects of micro-pores:

$$\psi = \frac{\boldsymbol{\sigma}^{+} : \boldsymbol{\sigma}^{+}}{2E\left(1-d^{+}\right)} + \frac{\boldsymbol{\sigma}^{-} : \boldsymbol{\sigma}^{-}}{2E\left(1-d^{-}\right)} + \frac{v\boldsymbol{\sigma} : \boldsymbol{\sigma}}{2E\left(1-\tilde{d}\right)} tr^{2}\left(\boldsymbol{\sigma}\right) \tag{2.76}$$

In (2.76), v is the Poisson's coefficient and $tr\left(\boldsymbol{\sigma}\right)$ is the trace of tensor $\boldsymbol{\sigma}$. Therefore an implicit formulation is also inherent to this model, leading to computational difficulties in what concerns the stress split and the uniqueness of tensor $\boldsymbol{\sigma}$ with respect to an arbitrary strain tensor.

Another important aspect involves the choice of the damage criteria. As seen in (2.61) and (2.62), the model of Faria *et al.* (1998) maps tensors $\overline{\boldsymbol{\sigma}}^{+}$ and $\overline{\boldsymbol{\sigma}}^{-}$ onto a 1D domain via the scalar norms $\overline{\tau}^{+}$ and $\overline{\tau}^{-}$, which are equivalent stresses that participate in the definition of the two damage criteria. They have been reported in equations (2.63) and (2.64) and they exhibit a format clearly inspired on the original one of Simó and Ju (1987), see Equation (2.31), but extended to account for the split of the effective stress tensor.

Many different norms have been proposed in the literature, associated to several damage criteria. A crucial distinction between them concerns the basic entity on which they are based, i.e. the strain or the stress tensor.

Mazars and Pijaudier-Cabot (1989) introduced a damage criterion in which crack propagation is assumed to be a consequence of the development of positive

straining, and accordingly an equivalent strain of the form (2.43) is adopted. The strain-based damage criterion is expressed in the form

$$g\left(\tau_{\varepsilon}, r\right) = \tau_{\varepsilon} - r \leq 0 \tag{2.77}$$

The damage variable *d* is defined as a weighted sum of the tensile damage d^{+} and the compressive damage d^{-}

$$d = \alpha^{+} d^{+} + \alpha^{-} d^{-} \tag{2.78}$$

where coefficients $\alpha^{\pm}$ depend on the tensile and compressive strain tensors $\boldsymbol{\varepsilon}^{\pm}$, these ones defined according to

$$\begin{aligned} \boldsymbol{\varepsilon}^{+} &= \left[\mathbf{C}\left(d\right)\right]^{-1} : \boldsymbol{\sigma}^{+} \\ \boldsymbol{\varepsilon}^{-} &= \left[\mathbf{C}\left(d\right)\right]^{-1} : \boldsymbol{\sigma}^{-} \end{aligned} \tag{2.79a, b}$$

Obviously an implicit formulation is involved here, since $\boldsymbol{\varepsilon}^{\pm}$ depend on the Cauchy stress tensor and on the rank-four secant matrix, which in turn depends on the weighted damage *d*. Such entities are not known a priori.

The previous strain-based damage model was improved by distinguishing the tensile damage from the compressive one, as postulated for the energy potential described in equation (2.74). This strategy allows accounting for the unilateral stiffness recovery effect. However, even with this modification, such version of the Mazars' model differs again from the model by Faria *et. al* (1998) in the damage criteria, which are defined in the following form

$$g^{\pm}\left(\tau_{\boldsymbol{\sigma}}^{\pm}, r^{\pm}\right) = \tau_{\boldsymbol{\sigma}}^{\pm} - r^{\pm} \leq 0 \tag{2.80}$$

with the norms $\tau_{\boldsymbol{\sigma}}^{\pm}$ coinciding with the damage energy release rates, that is,

$$\tau_{\boldsymbol{\sigma}}^{\pm} = -\frac{\partial \psi}{\partial d^{\pm}} = \frac{\boldsymbol{\sigma}^{\pm} : \mathbf{C}^{-1} : \boldsymbol{\sigma}^{\pm}}{2\sqrt{1-d^{\pm}}} \tag{2.81}$$

Formally, equations (2.80) are analogous to equations (2.63) and (2.64) but with an essential difference concerning the definitions of the norms: in equation (2.81) $\tau_{\boldsymbol{\sigma}}^{\pm}$ are clearly dependent on the Cauchy stress tensor and on the damage variables, whilst in the model of Faria *et. al* (1998) $\overline{\tau}^{\pm}$ are strain based entities. Therefore, the model of Faria *et al.* (1998) stands between the strain and the stress appraisals, since in norms $\overline{\tau}^{+}$ and $\overline{\tau}^{-}$ the effective stress tensors $\overline{\boldsymbol{\sigma}}^{+}$ and $\overline{\boldsymbol{\sigma}}^{-}$ are considered, see (2.61) and (2.62). Their strain-based nature permits to avoid iterative procedures inside the constitutive model. This strategy definitely improves the algorithmic efficiency and decreases the analysis computational cost.

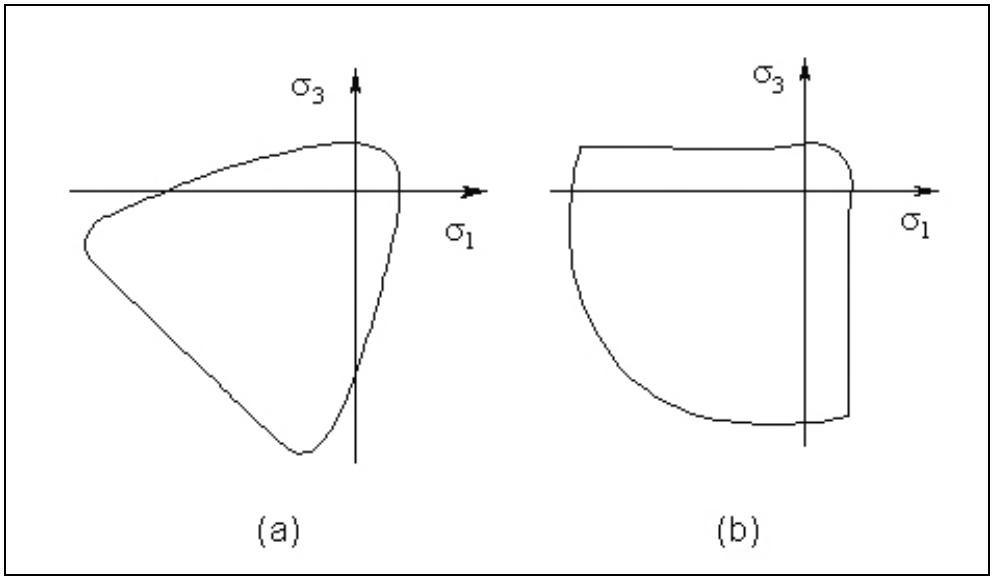

Figure 2.12 Damage threshold surfaces in the principal stress space, with $\sigma_3 = 0$, from Mazars and Pijaudier-Cabot (1989): model with one scalar damage variable (a) and with two scalar damage variables (b).

In addition, the purely strain-based norms are not able to account for strength increase in compression-compression states, which is a typical behaviour of geomaterials, such as concrete. Such undesirable result, pointed out in Figure 2.12, derives from the fact that the favourable effect due to the lateral confinement in samples axially compressed is compatible with some lateral expansion, a feature that can not be captured by a norm like (2.43), since it predicts τ_{ε} to increase with the lateral expansion.

2.5 Conclusions

In this Chapter we have presented a brief overview concerning the general framework of Continuum Damage Mechanics. For about 50 years since the pioneering work of Kachanov (1958), such theory has become theoretically popular in the constitutive modelling of materials. The research has considerably advanced and Continuum Damage Mechanics is nowadays a reliable engineering tool, with wide application to several fields. Among the reasons for such a large acceptance, we point out the theoretical simplicity for describing even complex physical phenomena, the versatility of the inherent Theory of Irreversible Processes, the thermodynamic consistency and the possibility to combine with other theories, such as Plasticity, Fracture Mechanics and Viscoelasticity.

The basic concepts of *damage variable*, *effective stress* and *strain-equivalence* have been discussed, together with the thermodynamical formulation of the theory. Among the different models available in the literature, we have turned our attention to the models based on the assumption of one or more scalar damage variables.

The formulation proposed by Simó and Ju (1987) has been considered. In this simple model, the stiffness degradation is described by a single scalar variable *d* which affects in the same measure all the components of the elastic constitutive tensor. The model presents a favourable strain-driven format, in compliance with

the fundamental hypothesis that damage in the material is directly linked to the history of total strain. The progressive degradation of mechanical properties due to damage is characterized by introducing the simple concept of *equivalent strain*, that is a scalar positive quantity which permits identify 'loading', 'unloading' or 'reloading' situations for a general 3D stress state. The damage criterion is therefore formulated in the strain space. The evolution law of the scalar damage variable can be described in terms of an internal thermodynamic variable, whose definition is consistent with the Kuhn-Tucker conditions. The formulation proposed by Simó and Ju (1987) provides a simple constitutive model which, nevertheless, can also account for rate dependent phenomena and plastic strains. The favourable strain-driven formalism, which is consistent with standard displacement-based finite element codes, provides high algorithmic efficiency. In fact, the numerical implementation concerns a closed-form algorithm which integrates the stress tensor in time and in an explicit way.

Then, we have discussed the model proposed by Faria *et al.* (1998), which introduces two scalar damage variables to account for the different behaviour of the material in tension and compression. Such model adopts a stress split to capture the unilateral behaviour of the material when passing from tension to compression. Similar assumptions have been pursued on many damage models, but with many differences being encountered on the strategies adopted for the implementation of such split, which sometimes is performed over the strain tensor. A comparative discussion on the implications of those splits has been conducted, as well as on the different choices for the norms that define the elastic domain in the stress space, providing a perspective on the advantages and disadvantages of the various approaches. The damage model proposed by Faria *et al.* (1998) adopts a strain-driven formalism, according to Simó and Ju (1987), but the stress split is performed on the effective elastic stress tensor, which is shown to correspond to a split of the Cauchy stress tensor. This strategy improves the algorithmic efficiency

and circumvents many of the drawbacks present in similar damage models, in which iterative procedures are necessary within the constitutive model. This is the most valuable feature for a model intended to be used in large scale computations, in which high algorithmic efficiency is required.

Owing to all the aforementioned considerations, the frameworks of the presented damage models will be considered in the following Chapters. The necessary enhancements and modifications will be integrated in order to provide a reliable and efficient computational tool for nonlinear analysis of masonry structures.

Chapter 3.
Scalar Damage Model for Orthotropic Materials

In general, a material is *anisotropic* when its properties at a point vary with direction or depend on the orientation of the reference axes. If the properties of the material along any direction are the same as those along a symmetric direction with respect to a plane, then that plane is defined as a *plane of material symmetry*. A material may have zero, one, two, three, or an infinite number of planes of material symmetry through a point. A material without any planes of symmetry is called *general anisotropic* (or *aeolotropic*). At the other extreme, an *isotropic* material has an infinite number of planes of symmetry.

Of special relevance to structural materials are the *orthotropic* materials, i.e., materials having at least three mutually perpendicular planes of symmetry. Very diffused orthotropic structural materials are, for instance, wood, fibre-reinforced composites and masonry.

The general concept of “material orthotropic behaviour” is related to several aspects and phenomena, hence it can be analyzed in depth. In detail, it is possible to distinguish three levels of orthotropy:

- *elastic* orthotropy;
- *strength* orthotropy (or *yield* orthotropy, in case of ductile materials);
- *brittleness* (or *softening*) *orthotropy*.

All the aforementioned features derive from the composite nature of the orthotropic materials. Heterogeneous materials have properties that vary from point to point. Consider a cross section of a tree, where each growth ring is different from the rest. The lighter rings (summer wood) are softer and the darker rings (winter wood) are stiffer. The same general idea can be extended to mortar and bricks of masonry, or to matrix and fibres of fibre-reinforced materials. Also the particular geometrical arrangement of constituents features prominently.

The elastic orthotropy of a material is due to the different elastic properties of the constituents. Also, the constituents can be arranged in such a way that the horizontal and vertical directions are not equivalent, e.g. in case of masonry.

The strength orthotropy is due to the different strengths of the constituents. For instance, in a fibre-reinforced composite the fibres provide strength in longitudinal direction, while the matrix in the transversal. Furthermore, the strength value in one direction is related to the particular failure mechanism activated by constituents along that direction of loading. For instance, a compression applied to a wood element causes in the longitudinal direction a complex failure mechanism due to buckling of grains, shearing or crushing of early-wood. It is obvious that in the transversal direction the mechanism is different.

Softening orthotropy is commonly attributed to the heterogeneity of the material, due to the presence of different phases or material defects, like flaws and voids. At the beginning of a displacement-controlled tensile loading, microcracks arise from

the discontinuities in the material. Then, they grow during load increasing until reaching a peak load value, from which an acceleration of cracks formation occurs and the formation of macrocracks starts. The macrocracks are unstable, which means that the load has to decrease to avoid an uncontrolled growth. The entity of such a phenomenon in an orthotropic material can depend on the direction of loading.

A sound model for orthotropic materials should account for the aforementioned features, in order to provide an appropriate representation of the real material behaviour. This Chapter deals with a generalized orthotropic model based on the classical isotropic damage models. The methodology is based on the concept of *mapped tensor* from the anisotropic real space to the isotropic fictitious one, firstly introduced by Betten (1981 and 1988). The proposed theory is a generalization of classical theories and allows one to use the models and algorithms developed for isotropic materials. It is based on establishing a one-to-one mapping relationship between the behaviour of an anisotropic real material and that of an isotropic fictitious one. Therefore, the problem is solved in the isotropic fictitious space and the results are transported to the real field. This theory is feasible and effective in the finite element analysis of orthotropic materials, such as masonry, fibre-reinforced composites and wood.

3.1 Orthotropic Elastic Behaviour

An anisotropic material is one which exhibits properties with different values when measured in different directions. Modelling the behaviour of an elastic anisotropic solid does not present big difficulties, since it is possible to use the general elasticity theory (e.g. Love, 1944; Lekhnitskii, 1963; Malvern, 1969).

This section is a brief overview of the fundamentals of anisotropic elasticity, with a particular attention paid to the special case of plane stress orthotropy. The basic

concepts exposed will be useful for formulating the model proposed in the present Chapter. First, a review of the stress-strain equations is presented. Then, the assumption of plane stress is introduced to obtain the constitutive equations for an in-plane loaded structural element, such as a masonry panel. Finally, a review of the coordinate transformations is developed.

3.1.1 Coordinate Systems

There are two coordinate systems that are used in the analyses of the orthotropic materials. The *material* coordinate system (denoted by axes 1 and 2, in the two-dimensional case) is a cartesian coordinate system coincident with the principal axes of orthotropy of the material (see Section 3.1.2). In case of masonry, for instance, axes 1 and 2 have directions aligned with the bed joints and the head joints, respectively. In case of composite materials, on the other hand, the 1-axis is aligned with the fibre direction while the 2-axis is on the surface of the composite shell and it is perpendicular to the 1-axis.

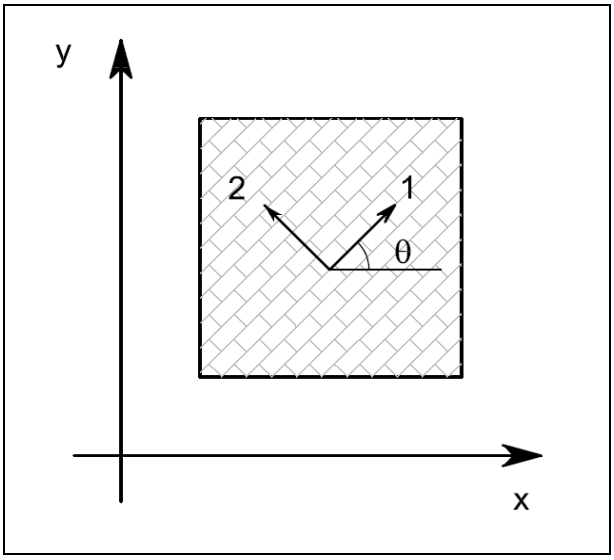

Figure 3.1 Orthotropic material with material axes of orthotropy 1 and 2.

The orientation of the *global* coordinate system (denoted by axes *x* and *y* in the two-dimensional case) is chosen for convenience during the structural analysis. Therefore, it may be aligned with the boundary of the structural element analyzed, or with the directions of the mayor loads, etc. As a rule we assume that the axes *x* and *y* have directions coincident with the horizontal and vertical ones, respectively. In Figure 3.1 the material coordinate system and the global coordinate system are shown, both with the angle θ between them.

3.1.2 Stress-Strain Equations

For a completely anisotropic material, 36 elastic constants are necessary to define the three-dimensional stress-strain relationship. The independent constants are 21 because of the symmetry of the constitutive tensor.

If certain symmetries exist in the material, the number of coefficients can be further reduced. When the elastic constants at a point have the same values for every pair of coordinate systems which are mirror images of each other in a certain plane, that plane is called a *plane of symmetry* (Malvern, 1969). If through each point of a body there pass three mutually perpendicular planes of elastic symmetry, the body is called *orthotropic*. The intersection of these planes are known as the *principal axes of orthotropy*. In the particular case of orthotropy, the number of elastic constants is reduced to 12, viz. 3 Young's moduli E_1, E_2, E_3, 6 Poisson's ratios $\nu_{12}, \nu_{13}, \nu_{21}, \nu_{23}, \nu_{31}, \nu_{32}$ and 3 shear moduli G_{12}, G_{13}, G_{23}:

$$\begin{Bmatrix} \varepsilon_1 \\ \varepsilon_2 \\ \varepsilon_3 \\ \gamma_{12} \\ \gamma_{13} \\ \gamma_{23} \end{Bmatrix} = \begin{bmatrix} \frac{1}{E_1} & \frac{-\nu_{21}}{E_2} & \frac{-\nu_{31}}{E_3} & 0 & 0 & 0 \\ \frac{-\nu_{12}}{E_1} & \frac{1}{E_2} & \frac{-\nu_{32}}{E_3} & 0 & 0 & 0 \\ \frac{-\nu_{13}}{E_1} & \frac{-\nu_{23}}{E_2} & \frac{1}{E_3} & 0 & 0 & 0 \\ 0 & 0 & 0 & \frac{1}{G_{12}} & 0 & 0 \\ 0 & 0 & 0 & 0 & \frac{1}{G_{13}} & 0 \\ 0 & 0 & 0 & 0 & 0 & \frac{1}{G_{23}} \end{bmatrix} \begin{Bmatrix} \sigma_1 \\ \sigma_2 \\ \sigma_3 \\ \tau_{12} \\ \tau_{13} \\ \tau_{23} \end{Bmatrix} \tag{3.1}$$

where $\nu_{21}/E_2 = \nu_{12}/E_1$, $\nu_{31}/E_3 = \nu_{13}/E_1$, $\nu_{32}/E_3 = \nu_{23}/E_2$. Therefore, the number of independent constants is reduced to 9. Note that, in orthotropic materials, there is no interaction between the normal stresses $\sigma_1, \sigma_2, \sigma_3$ and the shear strains $\varepsilon_{12}, \varepsilon_{13}, \varepsilon_{23}$.

Since the present work concerns the two-dimensional analysis of in-plane loaded masonry structural elements, the state of plane stress $(\sigma_3 = 0)$ is considered. Assuming the following Voigt forms for the in-plane stress and strain vectors, making reference to the material axes (Figure 3.1),

$$\{\sigma'\} = \{\sigma_1, \sigma_2, \tau_{12}\}^T \tag{3.2}$$

$$\{\varepsilon'\} = \{\varepsilon_1, \varepsilon_2, \gamma_{12}\}^T \tag{3.3}$$

for an orthotropic body with orthotropic material directions 1 and 2, the compliance equations are

$$\begin{Bmatrix} \varepsilon_1 \\ \varepsilon_2 \\ \gamma_{12} \end{Bmatrix} = \begin{bmatrix} \frac{1}{E_1} & \frac{-\nu_{21}}{E_2} & 0 \\ \frac{-\nu_{12}}{E_1} & \frac{1}{E_2} & 0 \\ 0 & 0 & \frac{1}{G_{12}} \end{bmatrix} \begin{Bmatrix} \sigma_1 \\ \sigma_2 \\ \tau_{12} \end{Bmatrix} \tag{3.4}$$

The compliance equations can be written in compact form as

$$\boldsymbol{\varepsilon}' = \mathbf{S}' : \boldsymbol{\sigma}' \tag{3.5}$$

The inversion of the compliance tensor $\mathbf{S}'$ leads to the constitutive equations

$$\begin{Bmatrix} \sigma_1 \\ \sigma_2 \\ \tau_{12} \end{Bmatrix} = \frac{1}{1-\nu_{12}\nu_{21}} \begin{bmatrix} E_1 & \nu_{21}E_1 & 0 \\ \nu_{12}E_2 & E_2 & 0 \\ 0 & 0 & (1-\nu_{12}\nu_{21})G_{12} \end{bmatrix} \begin{Bmatrix} \varepsilon_1 \\ \varepsilon_2 \\ \gamma_{12} \end{Bmatrix} \tag{3.6}$$

or, in compact form, to

$$\boldsymbol{\sigma}' = \mathbf{C}' : \boldsymbol{\varepsilon}' \tag{3.7}$$

where $\mathbf{C}'$ is the constitutive tensor defined in the material coordinates system. Therefore, 5 elastic constants are necessary to describe the elastic behaviour of an orthotropic material in two-dimensional problems: the two Young's moduli E_1, E_2, the two Poisson's ratios ν_{12}, ν_{21} and the shear modulus G_{12}. From the symmetry of the stiffness matrix it derives that

$$\nu_{12}E_2 = \nu_{21}E_1 \tag{3.8}$$

Although the shear modulus G_{12} is an independent constant and is in no way related to the other elastic constants, Lekhnitskii (1963) proposed an approximate formula for practical purposes, obtained from forty five rocks:

$$G_{12} \simeq \frac{E_1 E_2}{E_1\left(1+\nu_{21}\right)+E_2} \tag{3.9}$$

Finally, for sake of completeness we remark that in the state of plane stress, the only strains and stresses that have to be considered in finite element calculations are the three components in the 1-2 plane, according to (3.2) and (3.3). In fact, by definition, all other components of stress are zero and therefore give no contribution to internal work (Zienkiewicz and Taylor, 2000; Oñate, 1995).

3.1.3 Coordinate Transformations

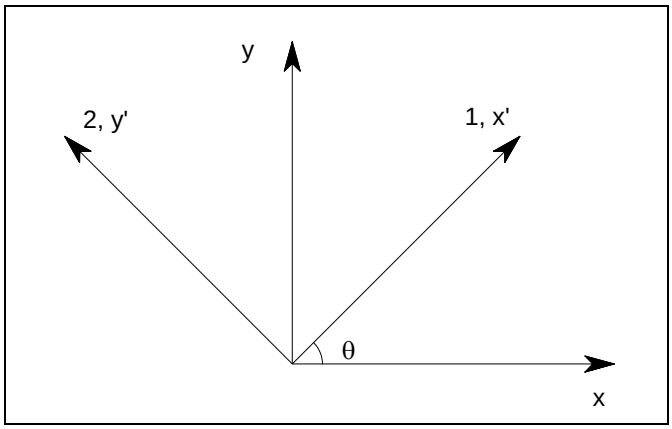

Figure 3.2 Coordinate transformations.

With reference to Figure 3.2, the position of a point with coordinates x, y in the global coordinates system can be described in the material coordinates system as

$$\begin{Bmatrix} x' \\ y' \end{Bmatrix} = \begin{bmatrix} \cos\theta & \sin\theta \\ -\sin\theta & \cos\theta \end{bmatrix} \begin{Bmatrix} x \\ y \end{Bmatrix} \tag{3.10}$$

The angle θ is measured counter clockwise from the x-axis to the 1-axis. The inverse relationship is

$$\begin{Bmatrix} x \\ y \end{Bmatrix} = \begin{bmatrix} \cos\theta & -\sin\theta \\ \sin\theta & \cos\theta \end{bmatrix} \begin{Bmatrix} x' \\ y' \end{Bmatrix} \tag{3.11}$$

In compact form, (3.10) and (3.11) take the form

$$\mathbf{x}' = \mathbf{R} \cdot \mathbf{x} \tag{3.12}$$

$$\mathbf{x} = \mathbf{R}^T \cdot \mathbf{x}' \tag{3.13}$$

since tensor **R** is orthogonal.

In two dimensions, the displacement of a point is described by two components *u* and *v*. The in-plane components of strain in global coordinates are given by

$$\begin{aligned} \varepsilon_x &= \frac{\partial u}{\partial x} \\ \varepsilon_y &= \frac{\partial v}{\partial y} \\ \gamma_{xy} &= \frac{\partial u}{\partial y} + \frac{\partial v}{\partial x} \end{aligned} \tag{3.14}$$

Whereas the components of strain in material coordinates are given by

$$\begin{aligned} \varepsilon_1 &= \frac{\partial u'}{\partial x'} \\ \varepsilon_2 &= \frac{\partial v'}{\partial y'} \\ \gamma_{12} &= \frac{\partial u'}{\partial y'} + \frac{\partial v'}{\partial x'} \end{aligned} \tag{3.15}$$

The relationship between global and material strains is easily obtainable from (3.10), (3.11), (3.14) and (3.15):

$$\begin{Bmatrix} \varepsilon_x \\ \varepsilon_y \\ \gamma_{xy}/2 \end{Bmatrix} = \begin{bmatrix} \cos^2\theta & \sin^2\theta & -2\cos\theta\sin\theta \\ \sin^2\theta & \cos^2\theta & 2\cos\theta\sin\theta \\ \cos\theta\sin\theta & -\cos\theta\sin\theta & \cos^2\theta-\sin^2\theta \end{bmatrix} \begin{Bmatrix} \varepsilon_1 \\ \varepsilon_2 \\ \gamma_{12}/2 \end{Bmatrix} \tag{3.16}$$

The inverse relationship is

$$\begin{Bmatrix} \varepsilon_1 \\ \varepsilon_2 \\ \gamma_{12}/2 \end{Bmatrix} = \begin{bmatrix} \cos^2\theta & \sin^2\theta & 2\cos\theta\sin\theta \\ \sin^2\theta & \cos^2\theta & -2\cos\theta\sin\theta \\ -\cos\theta\sin\theta & \cos\theta\sin\theta & \cos^2\theta-\sin^2\theta \end{bmatrix} \begin{Bmatrix} \varepsilon_x \\ \varepsilon_y \\ \gamma_{xy}/2 \end{Bmatrix} \tag{3.17}$$

Stresses are transformed in a similar way. The transformation from material to global axes is done using the following expression:

$$\begin{Bmatrix} \sigma_x \\ \sigma_y \\ \tau_{xy} \end{Bmatrix} = \begin{bmatrix} \cos^2\theta & \sin^2\theta & -2\cos\theta\sin\theta \\ \sin^2\theta & \cos^2\theta & 2\cos\theta\sin\theta \\ \cos\theta\sin\theta & -\cos\theta\sin\theta & \cos^2\theta-\sin^2\theta \end{bmatrix} \begin{Bmatrix} \sigma_1 \\ \sigma_2 \\ \tau_{12} \end{Bmatrix} \tag{3.18}$$

The inverse relationship is

$$\begin{Bmatrix} \sigma_1 \\ \sigma_2 \\ \tau_{12} \end{Bmatrix} = \begin{bmatrix} \cos^2\theta & \sin^2\theta & 2\cos\theta\sin\theta \\ \sin^2\theta & \cos^2\theta & -2\cos\theta\sin\theta \\ -\cos\theta\sin\theta & \cos\theta\sin\theta & \cos^2\theta-\sin^2\theta \end{bmatrix} \begin{Bmatrix} \sigma_x \\ \sigma_y \\ \tau_{xy} \end{Bmatrix} \tag{3.19}$$

The expressions (3.16), (3.17), (3.18) and (3.19) can be written in Voigt notation as

$$\boldsymbol{\varepsilon} = \mathbf{T}^T : \boldsymbol{\varepsilon}' \tag{3.20}$$

$$\boldsymbol{\varepsilon}' = \mathbf{T}^{-T} : \boldsymbol{\varepsilon} \tag{3.21}$$

$$\boldsymbol{\sigma} = \mathbf{T}^{-1} : \boldsymbol{\sigma}' \tag{3.22}$$

$$\boldsymbol{\sigma}' = \mathbf{T} : \boldsymbol{\sigma} \tag{3.23}$$

with

$$\mathbf{T}=\begin{bmatrix} \cos^2\theta & \sin^2\theta & 2\cos\theta\sin\theta \\ \sin^2\theta & \cos^2\theta & -2\cos\theta\sin\theta \\ -\cos\theta\sin\theta & \cos\theta\sin\theta & \cos^2\theta-\sin^2\theta \end{bmatrix} \tag{3.24}$$

$$\mathbf{T}^{-1}=\begin{bmatrix} \cos^2\theta & \sin^2\theta & -2\cos\theta\sin\theta \\ \sin^2\theta & \cos^2\theta & 2\cos\theta\sin\theta \\ \cos\theta\sin\theta & -\cos\theta\sin\theta & \cos^2\theta-\sin^2\theta \end{bmatrix} \tag{3.25}$$

$$\mathbf{T}^{-T}=\begin{bmatrix} \cos^2\theta & \sin^2\theta & \cos\theta\sin\theta \\ \sin^2\theta & \cos^2\theta & -\cos\theta\sin\theta \\ -2\cos\theta\sin\theta & 2\cos\theta\sin\theta & \cos^2\theta-\sin^2\theta \end{bmatrix} \tag{3.26}$$

Note that the use of 1/2 in front of the shear strains but not in front of the shear stresses. This is because the shear strain γ_{xy} is not a tensorial component, but $\varepsilon_{xy}=\gamma_{xy}/2$ is. Since only tensor components can be rotated with the rotation matrix **T**, the tensorial shear strain $\varepsilon_{xy}=\gamma_{xy}/2$ is used rather than the engineering shear strain γ_{xy} but only for coordinate transformations. The engineering shear strain will be used afterwards because of the convenience of writing the shear version of Hooke's law as $\tau=G\gamma$.

Finally, it is possible to obtain the transformations of the constitutive equations. The stress-strain equations (3.6) are limited to the case of having the stress and strains oriented along the material coordinates. To simplify the analysis as much as possible, it is convenient to relate stress and strains in global coordinates directly. This can be done by using the relationship

$$\boldsymbol{\sigma}=\mathbf{C}:\boldsymbol{\varepsilon} \tag{3.27}$$

In which **C** is the constitutive tensor defined in the global coordinate system in the form

$$\mathbf{C} = \mathbf{T}^{-1} \cdot \mathbf{C}' \cdot \mathbf{T}^{-T} \tag{3.28}$$

3.2 Formulation of the Model

The need to model the behaviour of a real orthotropic material requires the formulation of adequate constitutive laws, which can be based on such theories as elastoplasticity or damage. In particular, the choice of a suitable orthotropic criterion is a complex task. Several failure functions have been proposed but in many cases they do not describe the true behaviour of the material.

One of the more popular attempts to formulate orthotropic yield functions in the field of plasticity theory is due to Hill (1948, 1950), who succeeded in extending the von Mises (1928) isotropic model to the orthotropic case. The main limitation of this theory is the impossibility of modelling materials that present a behaviour which not only depends on the second invariant of the stress tensor, i.e. the case of geomaterials or composite materials. On the other hand, Hoffman (1967) and Tsai-Wu (1971) orthotropic yield criteria are useful tools for the failure prediction of composite materials.

For the description of incompressible plastic anisotropy, not only yield functions (Dutko *et al.*, 1993) and phenomenological plastic potentials (Życzkowski, 2001) have been proposed over the years. Other formulation strategies have been developed, related to general transformations based on *theory of tensor representation* (Wang, 1970 and Liu, 1982). A particular case of this general theory, which is based on linearly transformed stress components, has received more attention. This special case is of practical importance because convex formulations can be easily developed and, thus, stability in numerical simulations is ensured. Linear transformations on the stress tensor were first introduced by

Sobotka (1969) and Boehler and Sawczuck (1970). For plane stress and orthotropic material symmetry, Barlat and Lian (1989) combined the principal values of these transformed stress tensors with an isotropic yield function. Barlat et al. (1991) applied this method to a full stress state and Karafillis and Boyce (1993) generalized it as the so-called isotropic plasticity equivalent (IPE) theory with a more general yield function and a linear transformation that can accommodate other material symmetries.

The aforementioned approaches, principally addressed to plasticity constitutive laws, have not been applied yet to formulate orthotropic damage criteria. In fact, within the theoretical framework of Continuum Damage Mechanics, models related to isotropic criteria are usually preferred for practical purposes, especially in case of finite element analyses.

In this section, a model for the finite element analysis, based on Continuum Damage Mechanics, is presented. Orthotropic behaviour is simulated using the concept of *mapped stress tensor*, firstly introduced by Betten (1981 and 1988) and refined by Oller *et al.* (1995, 1996) afterwards. The idea to formulate the behaviour of an anisotropic material by means of an equivalent isotropic solid is achieved by means of an appropriate definition of a *transformation tensor*.

The method consists in studying the behaviour of a real solid by solving the problem in a fictitious isotropic space (mapped fictitious isotropic problem). It is based on assuming a *real* space, in which the orthotropic criterion is defined, and a corresponding *fictitious* space, in which the isotropic criterion is defined. The two stress spaces are related by means of a linear transformation, defined by a symmetric and rank-four transformation tensor, which allows a one-to-one mapping of an image of the stress (or strain) tensor defined in one space into the other and vice versa. This working strategy allows one to take advantage of the computational benefits of an isotropic model, while all the information concerning the real orthotropic properties of the material is included in the transformation

tensor. The parameters that define the transformation tensor can be calibrated from adequate experimental tests. The constitutive model in the fictitious isotropic space is defined by the same algorithms developed for standard isotropic materials. Therefore, the implementation of this theory into the framework of the standard finite element codes is straightforward.

The basic ingredients of the stress and strain spaces transformations are presented in the following, both with the description of the constitutive relationships adopted. The way the strength and softening orthotropies are modelled is also discussed. The aspects of implementation into a finite element code are detailed next.

3.2.1 Definition of the Space Transformation Tensors

The present methodology is based on assuming a real anisotropic space of stresses $\boldsymbol{\sigma}$ and a conjugate space of strains $\boldsymbol{\varepsilon}$, such that each of these spaces has its respective image in a fictitious isotropic space of stresses $\boldsymbol{\sigma}^*$ and strains $\boldsymbol{\varepsilon}^*$, respectively (see Figure 3.3). The relationship between these spaces is defined by

$$\boldsymbol{\sigma}^* = \mathbf{A}^{\sigma} : \boldsymbol{\sigma} \tag{3.29}$$

$$\boldsymbol{\varepsilon}^* = \mathbf{A}^{\varepsilon} : \boldsymbol{\varepsilon} \tag{3.30}$$

Where $\mathbf{A}^{\sigma}$ and $\mathbf{A}^{\varepsilon}$ are the transformation tensors, for stresses and strains, respectively, relating the fictitious and real spaces. These rank four-tensors embody the natural anisotropic properties of the material.

The assumption of a strain space transformation tensor (Oller *et al.* 1995, 1996), in addition to the definition of the conventional stress space transformation tensor, allows for no-proportionality between the strength and the elastic modulus for each material direction. For this reason, the adopted methodology has been also termed “isotropic mapped model for non-proportional materials” (Oller *et al.* 1995). This feature of the method avoids the basic assumption of elastic strains uniqueness for

both the real and fictitious spaces made in previous works (Oller *et al.* 1993). In fact, that situation would introduce a limitation in the anisotropic mapped theory, because it would result that $f_{11}/E_1 = f_{22}/E_{22} = f_{12}/G_{12}$. In the present work, the generalization of such basic theory is introduced, by providing the tensor transformations of both real stresses and strains.

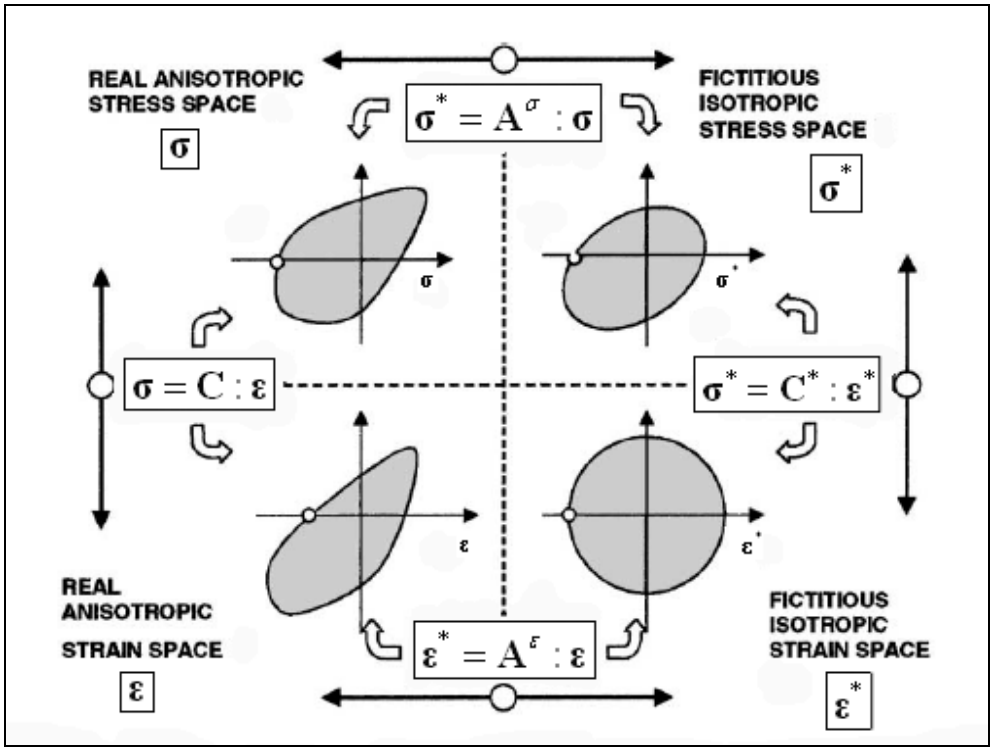

Figure 3.3 Relationship between the fictitious isotropic and the real anisotropic spaces (from Oller *et al.*, 2003).

For the definition of the shape and properties of the tensorial operator $\mathbf{A}^{\sigma}$ it is necessary to take into account the symmetry of the Cauchy stress tensor in the anisotropic and isotropic spaces, therefore the four-rank transformation tensor must satisfy the following symmetries:

$$A^{\sigma}_{ijkl} = A^{\sigma}_{jikl} = A^{\sigma}_{jilk} \tag{3.31}$$

The symmetry of the four-rank transformation tensor is also necessary:

$$A^{\sigma}_{ijkl} = A^{\sigma}_{klij} \tag{3.32}$$

In this work, the material is assumed initially orthotropic. There are different alternatives to define the tensor $\mathbf{A}^{\sigma}$ for this case. In this context, a diagonal fourth-order tensor is assumed, according to Betten (1981), Oller *et al.* (1995, 1996) and Car *et al.* (2000, 2001). The stress transformation tensor corresponds to a 6×6 matrix for the 3-dimensional case, according to equation (3.1). In the particular case of in-plane stress conditions, that will be considered in this work, the transformation tensor reduces to a 3×3 matrix. The components of the tensor are the ratios of the material strengths in the fictitious isotropic space (f^{*}_{ij}) and in the real orthotropic space (f_{ij}), all referred to the material axes directions (axes 1 and 2, see Figure 3.1). By assuming the Voigt forms (3.2) and (3.3) for the stress and strain vectors, the *stress space transformation tensor* in the material coordinate system takes the form

$$\left(\mathbf{A}^{\sigma}\right)' = \begin{bmatrix} \dfrac{f^{*}_{11}}{f_{11}} & 0 & 0 \\ 0 & \dfrac{f^{*}_{22}}{f_{22}} & 0 \\ 0 & 0 & \dfrac{f^{*}_{12}}{f_{12}} \end{bmatrix} \tag{3.33}$$

The orthotropic strengths f_{ij} can be obtained from simple experimental tests, shown in Figure 3.4. Since we assume an isotropic criterion in the isotropic space,

it results that $f_{11}^{*} = f_{22}^{*} = f^{*}$. The choice of f^{*} is arbitrary. The expression of f_{12}^{*} depends on the particular isotropic criterion adopted.

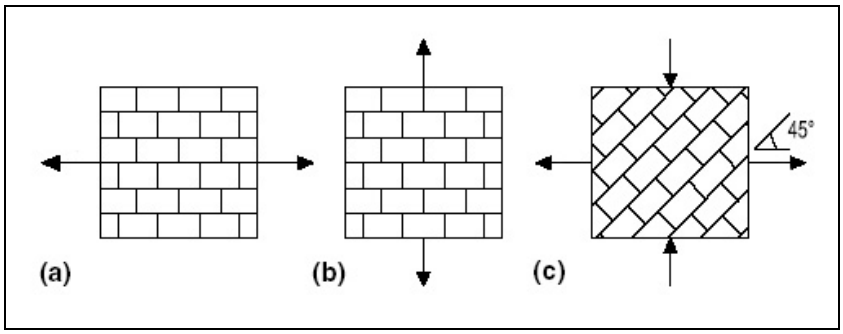

Figure 3.4 Experimental tests required for the definition of the stress transformation tensor components: uniaxial test in direction 1 (a) and direction 2 (b), pure shear test (c).

The stress tensor transformation is sufficient for approximating an explicit isotropic criterion to any implicit orthotropic desired. In fact, carrying out the transformation of stresses is equivalent to mapping the fictitious isotropic criterion desired. The space mapping allows one to represent appropriately even high anisotropic surfaces, such as in the case of fibre-reinforced composites (see Car *et al.* 2000 and 2001). The transformation leads to changes in the shape of the failure surface. This can be observed in Figure 3.5 for different criteria.

This procedure is advantageous since implicitly convex orthotropic functions are obtained from well-established isotropic ones, such as those of Tresca, von Mises, Mohr–Coulomb, Drucker–Prager, etc. (for more information, see Lubliner, 1990 and Maugin, 1992). Any known isotropic criterion can be mapped, as well as experimental set of data obtained from laboratory tests.

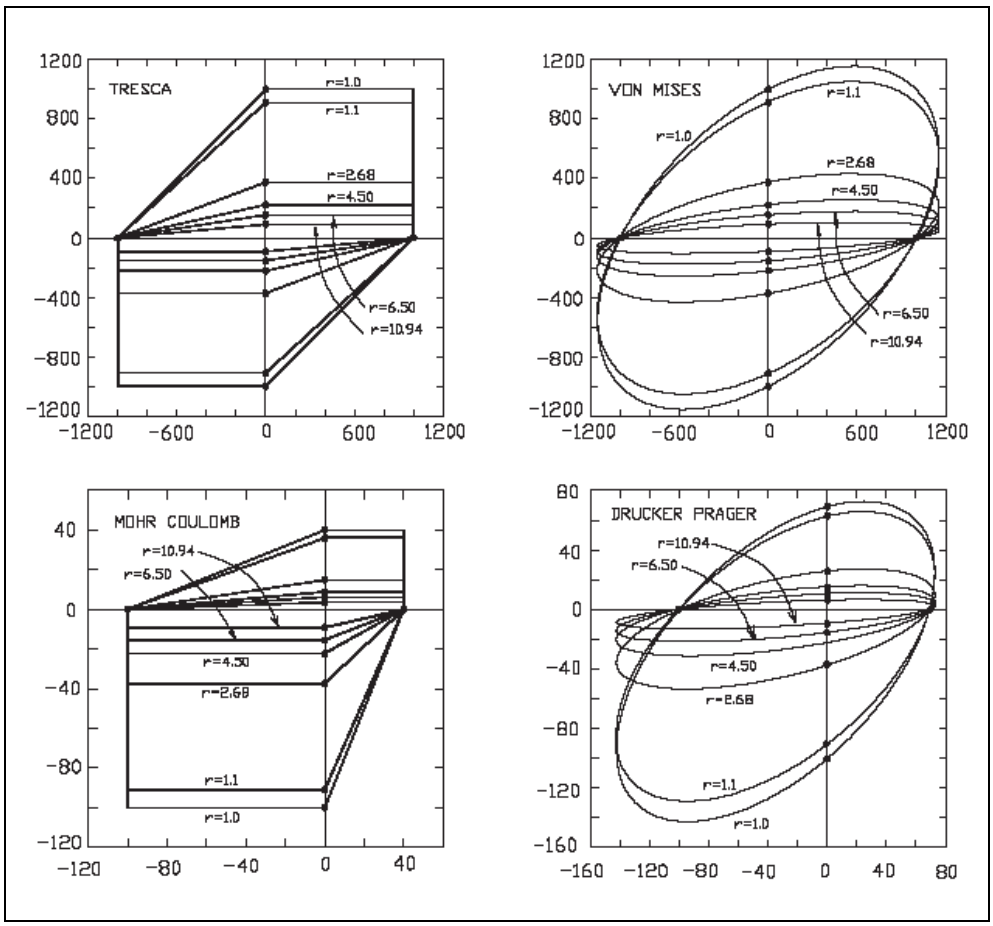

Figure 3.5 Changes in the shape of several isotropic criteria (from Oller *et al.*, 1995).

Although with definition (3.33) it is possible to find adequate orthotropic criteria, it could be difficult to adjust them ‘‘exactly’’ to represent the desired material behaviour. In order to circumvent this limitation, a more refined form of the stress transformation tensor was proposed by Oller *et al.* (2003). The authors provided an implicit general definition of an orthotropic yield criterion by using an isotropic formulation in a fictitious space and then transform it into an implicit orthotropic formulation in a real space. This means that the mathematical form of the orthotropic criterion need not be expressed explicitly; it is sufficient to express its

"isotropic form" explicitly and to assume the existence of a numerical transformation that allows a passage from an isotropic criterion to an implicit orthotropic one. Such numerical transformation, defined by the stress transformation tensor, must be properly defined in order to achieve the desired yield function adjustment. Oller *et al.* multiplied the transformation tensor defined in (3.33) by a "shape adjustment tensor", whose purpose is to adjust correctly the isotropic criterion to the desired orthotropic one. It is evident that the shape adjustment tensor must be derived by means of an iterative procedure. In practice, the non-linear solution of a quadratic system by the Newton-Rapson method is required. The governing equation is the equality of the fictitious isotropic criterion to the real implicit orthotropic one, in which transformation (3.29) has been introduced. The nonlinear solution of this quadratic system of equations is not an easy task and is quite wasteful, since $\mathbf{A}^{\sigma}$ depends on the stress state at the point at each instant of the mechanical process. Nevertheless, Oller *et al.* (2003) obtained with a considerable level of accuracy the Hill (1948, 1950) orthotropic criterion, by mapping appropriately the von Mises (1928) isotropic criterion. In the same way, the authors derived the Hoffman (1967) and Tsai-Wu (1971) orthotropic criteria from the adjustment of the Drucker-Prager (1952) one. The results obtained by Oller *et al.* are definitely very accurate, see Figure 3.6. However, the standard form of the stress transformation tensor will be considered in the present study, in order to disregard more complex assumptions and provide a low computational cost tool.

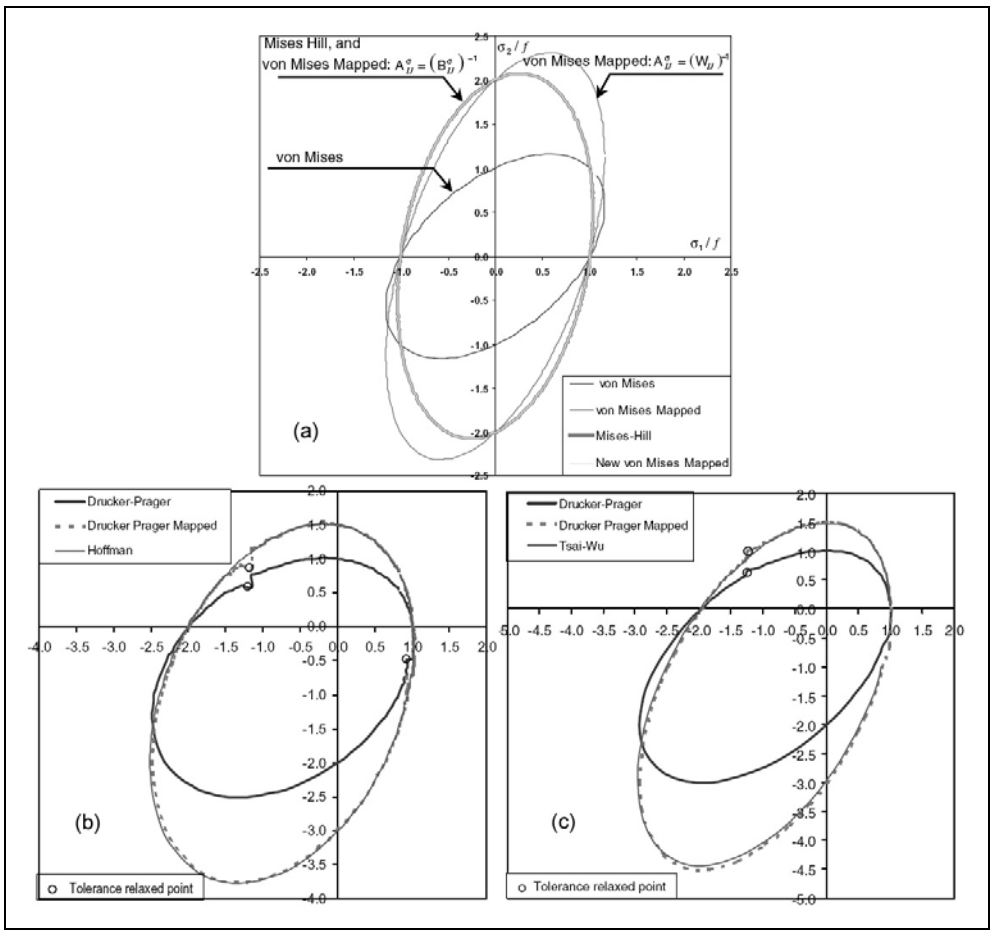

Figure 3.6 Representations of the adjustments of isotropic criteria to orthotropic ones: Mises to Hill (a), Drucker-Prager to Hoffman (b) and Tsai-Wu (c), from Oller *et al.*, 2003.

The stress space transformation tensor in the global coordinate system (axes *x* and *y*, see Figure 3.1) is readily obtainable from the definition (3.33) of the tensor components in the local principal axes of the orthotropic material. In fact, the stresses transformation with reference to the material local axes

$$\left(\boldsymbol{\sigma}^{*}\right)' = \left(\mathbf{A}^{\sigma}\right)' : \left(\boldsymbol{\sigma}'\right) \tag{3.34}$$

complemented with (3.23) as follows,

$$\begin{aligned} &\mathbf{T}:\boldsymbol{\sigma}^{*}=\left(\mathbf{A}^{\sigma}\right)'\cdot\mathbf{T}:\boldsymbol{\sigma} \\ &\boldsymbol{\sigma}^{*}=\mathbf{T}^{-1}\cdot\left(\mathbf{A}^{\sigma}\right)'\cdot\mathbf{T}:\boldsymbol{\sigma} \end{aligned} \qquad (3.35a, b)$$

permits to obtain

$$\mathbf{A}^{\sigma}=\mathbf{T}^{-1}\cdot\left(\mathbf{A}^{\sigma}\right)'\cdot\mathbf{T} \qquad (3.36)$$

The *strain space transformation tensor* $\mathbf{A}^{\varepsilon}$ defined in (3.30) can be derived from (3.29) and the constitutive equation as follows (Oller *et al.* 1995, 1996):

$$\begin{aligned} &\mathbf{A}^{\sigma}:\boldsymbol{\sigma}=\mathbf{C}^{*}\cdot\mathbf{A}^{\varepsilon}:\boldsymbol{\varepsilon} \\ &\boldsymbol{\sigma}=\left(\mathbf{A}^{\sigma}\right)^{-1}\cdot\mathbf{C}^{*}\cdot\mathbf{A}^{\varepsilon}:\boldsymbol{\varepsilon} \\ &\mathbf{C}=\left(\mathbf{A}^{\sigma}\right)^{-1}\cdot\mathbf{C}^{*}\cdot\mathbf{A}^{\varepsilon} \end{aligned} \qquad (3.37a, b, c)$$

and hence

$$\mathbf{A}^{\varepsilon}=\left(\mathbf{C}^{*}\right)^{-1}\cdot\mathbf{A}^{\sigma}\cdot\mathbf{C} \qquad (3.38)$$

where $\mathbf{C}$ and $\mathbf{C}^{*}$ are the constitutive tensors in the real and fictitious space, respectively. Equation (3.38) allows us to derive the relationship between the constitutive tensors in the real and fictitious spaces. This is:

$$\mathbf{I}=\mathbf{A}^{\varepsilon}\cdot\left(\mathbf{A}^{\varepsilon}\right)^{-1}=\left(\mathbf{C}^{*}\right)^{-1}\cdot\mathbf{A}^{\sigma}\cdot\mathbf{C}\cdot\left(\mathbf{A}^{\varepsilon}\right)^{-1} \qquad (3.39)$$

Or the inverse relation:

$$\mathbf{C}=\left(\mathbf{A}^{\sigma}\right)^{-1}\cdot\mathbf{C}^{*}\cdot\mathbf{A}^{\varepsilon} \qquad (3.40)$$

Note that in the expressions (3.38) and (3.40) the constitutive tensor **C** is expressed in the global reference system. This means that prior to the derivation of the space transformation tensors, the transformation (3.27) is required.

3.3 Underlying Fictitious Damage Model

In this section, a detailed description of the damage model adopted in the *fictitious space* is provided. The present work makes use of an *isotropic continuum* damage model with only one scalar internal variable to monitor the local damage (Simó and Ju, 1987; Cervera, 2003). This choice provides a simple constitutive model which, nevertheless, is able to reproduce the overall nonlinear behaviour including stiffness degradation and strain-hardening/softening response.

3.3.1 Constitutive Equations

The constitutive model considered in the fictitious space is based on the concept of *effective stress tensor*, introduced in connection with the *hypothesis of strain equivalence* (Lamaitre and Chaboche, 1978). The effective stresses $\overline{\boldsymbol{\sigma}}^*$ can be computed in terms of the total strain tensor, as

$$\overline{\boldsymbol{\sigma}}^* = \mathbf{C}^* : \boldsymbol{\varepsilon}^* \tag{3.41}$$

where **C*** is the usual (fourth-order) isotropic linear-elastic constitutive tensor. The constitutive equation for the isotropic damage model is defined as

$$\boldsymbol{\sigma}^* = \left(1-d\right)\overline{\boldsymbol{\sigma}}^* \tag{3.42}$$

where we have introduced one internal variable, *d*, the *damage index*, whose definition and evolution is given below.

In compliance with the formulation postulated by Simó and Ju (1987), a scalar positive quantity, termed as *equivalent stress* τ^*, is defined in order to identify

'loading', 'unloading' or 'reloading' situations for a general 3D stress state. The equivalent stress can assume several forms, depending on the damage threshold criterion assumed. A typical expression considered is (Cervera and Chiumenti, 2006)

$$\tau^* = \left[\overline{\boldsymbol{\sigma}}^* : \boldsymbol{\Lambda}^* : \overline{\boldsymbol{\sigma}}^* \right]^{1/2} \tag{3.43}$$

Note that the damage criterion is defined in the effective stress space. The shape of the corresponding damage threshold surface in this space depends on the particular fourth-order tensor $\boldsymbol{\Lambda}^*$ assumed.

With the definition (3.43) of the equivalent effective stress, the damage criterion, Φ^*, is introduced as

$$\Phi^* \left(\tau^*, r^* \right) = \tau^* - r^* \leq 0 \tag{3.44}$$

Variable r^* is an internal stress-like variable representing the current damage threshold, as its value controls the size of the (monotonically) expanding damage surface. The initial value of the damage threshold is $r_0^* = r_0^* \left(f^* \right)$, where f^* is the initial uniaxial damage stress.

The expansion of the damage bounding surface for loading, unloading and reloading conditions is controlled by the Kuhn–Tucker relations and the damage consistency condition, which are

$$\begin{aligned} &\dot{r}^* \geq 0 \quad \Phi^* \left(\tau^*, r^* \right) \leq 0 \quad \dot{r}^* \Phi^* \left(\tau^*, r^* \right) = 0, \\ &\textit{if} \quad \Phi^* \left(\tau^*, r^* \right) = 0 \quad \textit{then} \quad \dot{r}^* \dot{\Phi}^* \left(\tau^*, r^* \right) = 0 \end{aligned} \tag{3.45a, b}$$

leading, in view of (3.44), to the loading condition

$$\dot{\tau}^* = \dot{r}^* \tag{3.46}$$

This, in turn, leads to the explicit definition of the current values of the internal variable r^* in the form

$$r^* = \max\left[r_0^*, \max\left(\tau^* \right) \right] \tag{3.47}$$

Note that Eq. (3.47) allows one to compute the current values for r^* in terms of the current value of τ^*, which depends explicitly on the current total strains.

The constitutive equation for the real orthotropic material is obtained by writing the dissipation occurring in an isothermic elasto-damageable process in the real anisotropic space. The dissipation expression is obtained taking into account the first and second principles of thermodynamics.

We assume a free energy potential of the following form

$$\psi\left(\boldsymbol{\varepsilon}, r\right) = \left[1 - d\left(r\right)\right]\psi_0 = \left[1 - d\left(r\right)\right]\left[\frac{1}{2}\boldsymbol{\varepsilon} : \mathbf{C} : \boldsymbol{\varepsilon}\right] \geq 0 \tag{3.48}$$

where ψ_0 is the elastic free energy potential. All the variables in (3.48) are amenable to the classical thermodynamic representation (Lemaitre and Chaboche, 1985), i.e. the free variable $\boldsymbol{\varepsilon}$, the internal variable r and the dependent variable $d(r)$.

The second principle of thermodynamics requires the mechanical dissipation to be non-negative. Hence, according to the Clausius-Duhem inequality, the dissipation takes the form:

$$D = -\dot{\psi} + \boldsymbol{\sigma} : \dot{\boldsymbol{\varepsilon}} = \left(-\frac{\partial \psi}{\partial \boldsymbol{\varepsilon}} + \boldsymbol{\sigma} \right) : \dot{\boldsymbol{\varepsilon}} + \psi_0 \dot{d} \geq 0 \tag{3.49}$$

Applying the Coleman's method (Coleman and Gurtin, 1967) to guarantee the condition of positive dissipation in (3.49), the constitutive equation for the anisotropic material is obtained finally as

$$\boldsymbol{\sigma} = \frac{\partial \psi}{\partial \boldsymbol{\varepsilon}} = \left[1 - d\left(r\right)\right] \mathbf{C} : \boldsymbol{\varepsilon} \tag{3.50}$$

The expression (3.48) of the free energy potential can be rewritten by taking into account the relationship (3.40) between the constitutive tensors in the real and fictitious spaces. This gives

$$\psi\left(\boldsymbol{\varepsilon}, r\right) = \frac{1}{2}\left[1 - d\left(r\right)\right] \boldsymbol{\varepsilon} : \left[\left(\mathbf{A}^{\sigma}\right)^{-1} \cdot \mathbf{C}^{*} \cdot \mathbf{A}^{\varepsilon}\right] : \boldsymbol{\varepsilon} \tag{3.51}$$

The constitutive equation in the real anisotropic space, defined in terms of stress field in the fictitious isotropic space, is obtained by substituting (3.51) into (3.50), i.e.,

$$\begin{aligned} \boldsymbol{\sigma} &= \frac{\partial \psi}{\partial \boldsymbol{\varepsilon}} = \left[1 - d\left(r\right)\right]\left[\left(\mathbf{A}^{\sigma}\right)^{-1} \cdot \mathbf{C}^{*} \cdot \mathbf{A}^{\varepsilon}\right] : \boldsymbol{\varepsilon} = \\ &= \left[1 - d\left(r\right)\right]\left[\left(\mathbf{A}^{\sigma}\right)^{-1} \cdot \mathbf{C}^{*}\right] : \boldsymbol{\varepsilon}^{*} = \left[1 - d\left(r\right)\right]\left(\mathbf{A}^{\sigma}\right)^{-1} : \overline{\boldsymbol{\sigma}}^{*} = \\ &= \left(\mathbf{A}^{\sigma}\right)^{-1} : \boldsymbol{\sigma}^{*} \end{aligned} \tag{3.52}$$

Eq. (3.52) confirms the assumption of space transformations made in (3.29) and (3.30).

Finally, it is important to notice that (3.49) and (3.50) lead to

$$D = \psi_0 \dot{d} \geq 0 \tag{3.53}$$

i.e. the scalar damage variable increases monotonically.

3.3.2 Evolution of the Damage Variable. Inelastic Behaviour

The damage index $d = d\left(r^*\right)$ is explicitly defined in terms of the corresponding current value of the damage threshold, so that it is a monotonically increasing function such that $0 \le d\left(r^*\right) \le 1$.

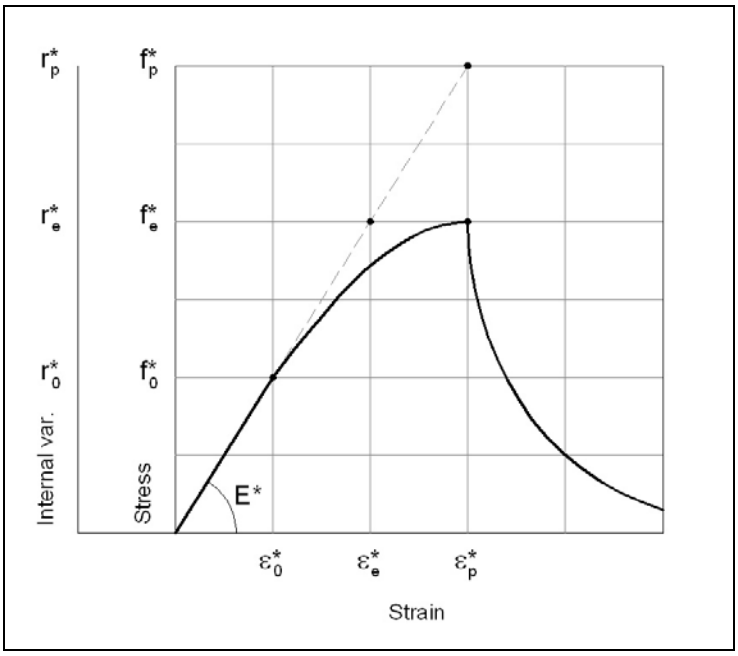

Figure 3.7 Uniaxial stress-strain curve. Parabolic hardening and exponential softening.

Let us consider the uniaxial stress-strain curve reported in Figure 3.7. Let us introduce the value r_0^*, establishing the size of the bounding damage surface for the onset of damage, according to (3.44). Then, we assume the value r_e^* corresponding to the peak value of the uniaxial strength f_e^* and the value $r_p^* \ge r_e^*$ corresponding to the size of the bounding damage surface at peak strength. These values define the hardening part of the uniaxial stress-strain curve for the material.

Note that $r_p^* \geq r_e^* \geq r_0^*$. For the limit case $r_p^* = r_e^* = r_0^*$, the material would exhibit softening immediately after the onset of damage, which is an option often used for tension strain softening.

In this work, we will use the following functions proposed by Cervera *et al.* (1999) and Cervera (2003). For parabolic hardening we assume

$$d\left(r^*\right) = A_d \frac{r_e^*}{r^*}\left(\frac{r^* - 1}{r_p^* - 1}\right)^2 \qquad r_0^* \leq r^* \leq r_p^* \tag{3.54}$$

while for exponential softening

$$d\left(r^*\right) = 1 - \frac{r_e^*}{r^*}\exp\left\{2H_d\left(\frac{r_p^* - r^*}{r_e^*}\right)\right\} \qquad r^* \geq r_p{}^* \tag{3.55}$$

where constants A_d, $H_d \geq 0$ are defined as

$$A_d = \frac{r_p^* - r_e^*}{r_e^*} \tag{3.56}$$

$$H_d = \frac{\bar{H}_d l_{ch}}{1 - \frac{r_p^*}{r_e^*}\bar{H}_d l_{ch} - 2\bar{A}_d \bar{H}_d l_{ch}} \tag{3.57}$$

where

$$\bar{A}_d = A_d\left[\left(r_p^*\right)^3 - 3r_p^* + 2\right] \Big/ \left[6r_e^*\left(r_p^* - 1\right)^2\right] \tag{3.58}$$

$$\bar{H}_d = \frac{\left(f^*\right)^2}{2E^* G_f^*} = \frac{1}{L} \tag{3.59}$$

The term $\bar{H}_d$ depends only on material properties in the fictitious space, i.e. the uniaxial damage threshold f^*, the Young's modulus E^* and the mode I fracture energy per unit area G_f^*. It measures the brittleness of the material and it can be also termed $1/L$, since the unit of the $\bar{H}_d$ parameter is the inverse of a length.

In Eq. (3.57), the characteristic length l_{ch} of the element has been introduced to ensure mesh-size objective results, according to Bazant and Oh (1983). The element characteristic length is the computational width of the fracture zone (Rots *et al.* 1985, Rots and Blaauwendraad 1989, Oliver 1989); it is computed depending on the geometric dimensions of the element. The specific dissipated energy D^* is then scaled for each element so that the equation

$$D^* l_{ch} = G_f^* \tag{3.60}$$

holds. This makes the softening modulus H_d, which defines the softening response, dependent on the element size. It also sets a maximum size for the elements that can be used in the analysis.

The expression (3.57) has been obtained by calculating the specific energy dissipated in an ideal uniaxial experiment in which the strain increases monotonically and quasi-statically from an initial unstressed state to another in which full degradation takes place. In fact, from Equations (3.49), (3.48), (3.41), (3.43), (3.47), (3.54) and (3.55) it derives that

$$
\begin{aligned}
D^* &= \int_{t=0}^{t=\infty} \dot{D}^* dt = \\
&= \int_{t=0}^{t=\infty} \psi_0^* \dot{d}\, dt \\
&= \frac{1}{2E^*} \int_{r^*=r_0^*}^{r^*=\infty} \left(r^*\right)^2 d'\, dr^* \\
&= \frac{1}{2E^*} \int_{r^*=r_0^*}^{r^*=r_p^*} \left(r^*\right)^2 d'\, dr^* + \frac{1}{2E^*} \int_{r^*=r_p^*}^{r^*=\infty} \left(r^*\right)^2 d'\, dr^*
\end{aligned}
\qquad \text{(3.61a, b, c, d)}
$$

where the rate of damage has been expressed as $\dot{d} = d'\dot{r}^*$. Using Equations (3.54) and (3.55), integrating and equating $D^* = G_f^* \big/ l_{ch}$, we finally obtain expression (3.57). For further details on calculations, the reader is referred to Cervera (2003). Note that for the limit case $r_p^* = r_e^* = r_0^*$ Equation (3.56) and (3.58) yield $A_d = \bar{A}_d = 0$ and then Equation (3.57) reduces to

$$H_d = \frac{\bar{H}_d l_{ch}}{1 - \bar{H}_d l_{ch}} \qquad (3.62)$$

a well known result for tension strain exponential softening (see Cervera and Chiumenti, 2006).

On the basis of the aforementioned considerations, it is evident that the *specific softening parameter* $\bar{H}_d$ measures the brittleness of the material, while the *elemental softening parameter* H_d measures the brittleness of the finite element.

3.3.3 Tangent and Secant Operators

Differentiating (3.41) and (3.42) with respect to time, we obtain in the fictitious space

$$\dot{\bar{\boldsymbol{\sigma}}}^* = \mathbf{C}^* : \dot{\boldsymbol{\varepsilon}}^* \tag{3.63}$$

$$\dot{\boldsymbol{\sigma}}^* = \left(1-d\right)\dot{\bar{\boldsymbol{\sigma}}}^* - \dot{d}\,\bar{\boldsymbol{\sigma}}^* \tag{3.64}$$

On the other hand, the rate of the damage index can be expressed as

$$\dot{d} = d'\dot{r}^* \tag{3.65}$$

where the first derivative term can be obtained from (3.54) or (3.55). On loading, consistency requires (3.46), and therefore, differentiating (3.43), we can write

$$\dot{r}^* = \dot{\tau}^* = \frac{1}{\tau^*}\left[\bar{\boldsymbol{\sigma}}^* : \boldsymbol{\Lambda}^* : \dot{\bar{\boldsymbol{\sigma}}}^*\right] \tag{3.66}$$

On unloading, it is $\dot{r}^* = 0$. Substituting (3.66) in (3.65), and the result in (3.64), we finally obtain the desired expression

$$\dot{\boldsymbol{\sigma}}^* = \mathbf{C}^{\tan *} : \dot{\boldsymbol{\varepsilon}}^* \tag{3.67}$$

With

$$\mathbf{C}^{\tan *} = \left[\left(1-d\right)\mathbf{I} - h^*\left(\bar{\boldsymbol{\sigma}}^* \otimes \bar{\boldsymbol{\sigma}}^*\right) : \boldsymbol{\Lambda}^*\right] : \mathbf{C}^* \tag{3.68}$$

where the coefficient h^* is

$$h^* = \begin{cases} \dfrac{d'}{\tau^*} & \textit{for loading} \\ 0 & \textit{for unloading} \end{cases} \tag{3.69}$$

Note that the tangent tensor is, in general, nonsymmetric. This is often inconvenient for practical finite element applications, as it results in a nonsymmetric tangent stiffness matrix. In those cases, and at the cost of the loss of rate of convergence, the tangent matrix can be replaced with the secant matrix, computed with the secant constitutive tensor

$$\mathbf{C}^{\sec *} = \left(1-d\right)\mathbf{C}^{*} \tag{3.70}$$

which is much simpler to compute and always symmetric.

Tangent and secant constitutive operators for the real orthotropic material are obtained in compliance with (3.40).

3.4 Orthotropic Softening Behaviour

It is important to note that in (3.42) and (3.54)-(3.59) there are terms without the apex (*) we have assigned to variables related to the fictitious isotropic space. In fact, such variables as d, H_d and $\bar{H}_d$ can be assumed equal in both the spaces, if we want to model an isotropic softening behaviour of the material. In fact, in this particular case it results that

$$\frac{\left(f_{11}\right)^2}{2E_1G_{f,1}} = \frac{\left(f_{22}\right)^2}{2E_2G_{f,2}} = \frac{\left(f^*\right)^2}{2E^*G_f^*} \quad \Rightarrow \quad \frac{1}{L_1} = \frac{1}{L_2} = \frac{1}{L^*} \tag{3.71}$$

This assumption leads to the same elemental softening parameters in the fictitious and real spaces.

As discussed before, the choices of f^*, E^*, G_f^* are arbitrary. In general, it is advisable to assume $f^* = f_{11}, E^* = E_1, G_f^* = G_{f,1}$. Such an assumption permits

also to obtain $\left(\mathbf{A}_{11}^{\sigma}\right)' = 1$ and deals to scale the isotropic damage threshold surface only along the 2-axis, see Figures 3.5 and 3.6. Moreover, from (3.71) it follows that

$$G_{f,2} = \frac{\left(f_{22}/f_{11}\right)^2}{E_2/E_1} G_{f,1} \tag{3.72}$$

i.e., a restriction on the fracture energy values, in order to ensure isotropic softening.

Nevertheless, the proposed model can also include the description of the material softening orthotropy. For this aim, it is necessary to assume two different elemental softening parameters along the material axes. This can be achieved by assuming an opportune specific softening parameter $\bar{H}_d^*$ (or $1/L^*$). In practice, in the present work the following properties are chosen in the fictitious space:

$$\begin{aligned} f^* &= f_{11} \\ E^* &= E_1 \\ G_f^* &= \frac{\left(f^*\right)^2}{2E^*} L^* \end{aligned} \tag{3.73a, b, c}$$

and the following expression is adopted for L^*:

$$L^* = L_1 \cos^2\left(\alpha - \theta\right) + L_2 \sin^2\left(\alpha - \theta\right) \tag{3.74}$$

in which $L_1 = 2E_1 G_{f,1} \big/ \left(f_{11}\right)^2$, $L_2 = 2E_2 G_{f,2} \big/ \left(f_{22}\right)^2$, θ is the angle of orthotropy and α is the angle denoting the direction of the main stress characterized by the maximum absolute value. Both the angles are measured counter clockwise from the global *x*-axis to the material 1-axis.

Such an assumption, permits to account for totally different fracture energies along the material axes, hence a full orthotropic softening behaviour. An alternative

would be to define another different mapping between the spaces of inelastic strains.

3.5 Numerical Implementation of the Proposed Model

The steps for implementing the scalar damage model for orthotropic materials into the framework of standard non-linear finite element programs (Simó and Hughes, 1998; Crisfield, 1991) are given in the following Table 3.1.

The model is implemented in a strain-driven form which leads to an almost closed-form algorithm to integrate the stress tensor in time. This is the most valuable feature for a model intended to be used in large scale computations.

Table 3.1 Algorithm used for the proposed model

START

- LOAD INCREMENTAL LOOP: n = 1, NINCR
  - EQUILIBRIUM ITERATION LOOP: i = 1, NITER

    IF ($n > 1 \quad or \quad i > 1$) GOTO 3

    1) Define strengths, constitutive tensors and rotation tensors

    f_{11} , f_{22} , f_{12} , f_{11}^{*} , f_{22}^{*} , f_{12}^{*}

    $\mathbf{C}'$, $\mathbf{C}^{*}$, $\mathbf{T}$

    $\mathbf{C} = \mathbf{T}^{-1} \cdot \mathbf{C}' \cdot \mathbf{T}^{-T}$

    2) Calculate the transformation tensors:

    $\left(\mathbf{A}^{\sigma}\right)'$

    $\mathbf{A}^{\sigma} = \mathbf{T}^{-1} \cdot \left(\mathbf{A}^{\sigma}\right)' \cdot \mathbf{T}$

$$\mathbf{A}^{\varepsilon} = \left(\mathbf{C}^{*}\right)^{-1} \cdot \mathbf{A}^{\sigma} \cdot \mathbf{C}$$

3) Compute tangent stiffness:

$$^{n}\left(\mathbf{C}^{\tan}\right)^{i-1} = \left(\mathbf{A}^{\sigma}\right)^{-1} \cdot {}^{n}\left(\mathbf{C}^{\tan *}\right)^{i-1} \cdot \mathbf{A}^{\varepsilon}$$

$$^{n}\left(\mathbf{K}^{(e)}\right)^{i-1} = \int_{V} \mathbf{B} : {}^{n}\left(\mathbf{C}^{\tan}\right)^{i-1} : \mathbf{B}\, dV$$

$$^{n}\left(\mathbf{K}\right)^{i-1} = \mathbf{A}_{e=1}^{ne} {}^{n}\left(\mathbf{K}^{(e)}\right)^{i-1}$$

4) Compute displacement and strains:

$$^{n}\left(\delta\mathbf{U}\right)^{i} = {}^{n}\left(\mathbf{K}^{-1}\right)^{i-1} \cdot {}^{n}\left(\mathbf{F}_{resid}\right)^{i-1}$$

$$^{n}\left(\Delta\mathbf{U}\right)^{i} = {}^{n}\left(\Delta\mathbf{U}\right)^{i-1} + {}^{n}\left(\delta\mathbf{U}\right)^{i}$$

$$^{n}\left(\boldsymbol{\varepsilon}\right)^{i} = \mathbf{B} : {}^{n}\left(\mathbf{U}\right)^{i}$$

5) Transform real strains to the fictitious isotropic space:

$$^{n}\left(\boldsymbol{\varepsilon}^{*}\right)^{i} = \mathbf{A}^{\varepsilon} : {}^{n}\left(\boldsymbol{\varepsilon}^{*}\right)^{i}$$

6) Calculate fictitious effective stresses:

$$\overline{\boldsymbol{\sigma}}^{*} = \mathbf{C}^{*} : \boldsymbol{\varepsilon}^{*}$$

7) Calculate damage index and total stresses in the fictitious space:

$$\boldsymbol{\sigma}^{*} = \left(1 - d\right)\overline{\boldsymbol{\sigma}}^{*}$$

8) Return to the real anisotropic stress space:

$$^{n}\left(\boldsymbol{\sigma}\right)^{i} = \left(\mathbf{A}^{\sigma}\right)^{-1} : {}^{n}\left(\boldsymbol{\sigma}^{*}\right)^{i}$$

9) Compute residual forces:

$$^{n}\left(\mathbf{F}_{resid}^{(e)}\right)^{i} = \int_{V} \mathbf{B}^{T} : {}^{n}\left(\boldsymbol{\sigma}\right)^{i}\, dV - \mathbf{f}_{ext}$$

$$ {}^{n}\left(\mathbf{F}_{resid}\right)^{i} = \mathbf{A}_{e=1}^{ne}\ {}^{n}\left(\mathbf{F}_{resid}^{(e)}\right)^{i} $$

IF $\dfrac{\left\| {}^{n}\left(\mathbf{F}_{resid}\right)^{i} \right\|}{\mathbf{f}_{ext}} > tol \quad \Rightarrow \quad i = i+1$ GO BACK TO 3

else:

- END EQUILIBRIUM ITERATION LOOP

  Converged solution for the n[th] increment.

  Compute new incremental solution: $n = n+1$

- END LOAD INCREMENTAL LOOP

3.6 Numerical Examples

This section delves into the numerical application of the proposed model to real experimental data of masonry strength. For this aim, we consider first a benchmark example consisting in a single element test, in order to better understand the behaviour of the model along the different material axes. Next, the ability of the proposed model to reproduce the directional strength of wood and the failure envelopes of composite laminates is assessed. Finally, the comparison between experimental data on masonry and numerical simulations is carried out.

Calculations are performed with an enhanced version of the finite element program COMET (Cervera *et al.* 2002), developed at the International Center for Numerical Methods in Engineering (CIMNE, Barcelona). The problem is solved incrementally in a (pseudo) time step-by-step manner. Within each step, a modified Newton–Raphson method (using the secant stiffness matrix), together with a line-search procedure, are used to solve the corresponding non-linear system of equations (Cook *et al.*, 2002; Zienkiewicz and Taylor, 2000; Simó and Hughes, 1998; Crisfield, 1991). Convergence of a time step is attained when the ratio

between the norm of the iterative residual forces and the norm of the total external forces is lower than 1%.

3.6.1 Behaviour of the Model. Elemental Test

The ability of the proposed model to represent tensile or compressive orthotropic behaviours is now discussed.

For this purpose, a single element test, subjected to pure uniaxial tension, is considered first. The material properties, referred to the material axes 1 and 2, are listed in Table 3.2. The material parameters of the 1-direction are selected for the fictitious isotropic space. The values chosen for the material parameters illustrate the fact that different behaviours along the two material axes can be reproduced. The case of isotropic softening is considered first. The fracture energies along the material axes are related by means of equation (3.64).

Table 3.2 Material properties for uniaxial tension test.

Material Properties			
$E_1=E^*$	3000 MPa	$f_{11}=f^*$	0.35 MPa
E_2	2000 MPa	f_{22}	0.15 MPa
$\nu_{12}=\nu^*$	0.1	f_{12}	0.20 MPa
ν_{21}	0.15	$G_{f,1}=G^*$	100 J/m^2
G_{12}	900 MPa	$G_{f,2}$	27.6 J/m^2

The single element is subjected to pure uniaxial tension in the *x*-global direction. Figure 3.8 shows the stress-strain responses for angles of orthotropy equal to 0°, 45° and 90°. As can be seen, the model is able to capture the stiffness, the strength and the inelastic dissipation in each direction. As previously mentioned in Section 3.3.2, the present model considers an exponential softening law. Once the fracture energy is exhausted, a no-tension material is recovered. The material strength in the

y-direction degrades at the same rate of the material strength in the *x*-direction, since material brittleness is the same in all directions.

The fracture energy of the material has been normalized by the characteristic length l_{ch} of the finite element, in order to ensure mesh-size objective results. Therefore, the area under each stress-strain curve is equal to the value $G_{f,i} \big/ l_{ch}$, in which $G_{f,i}$ is the fracture energy along the considered *i*-direction.

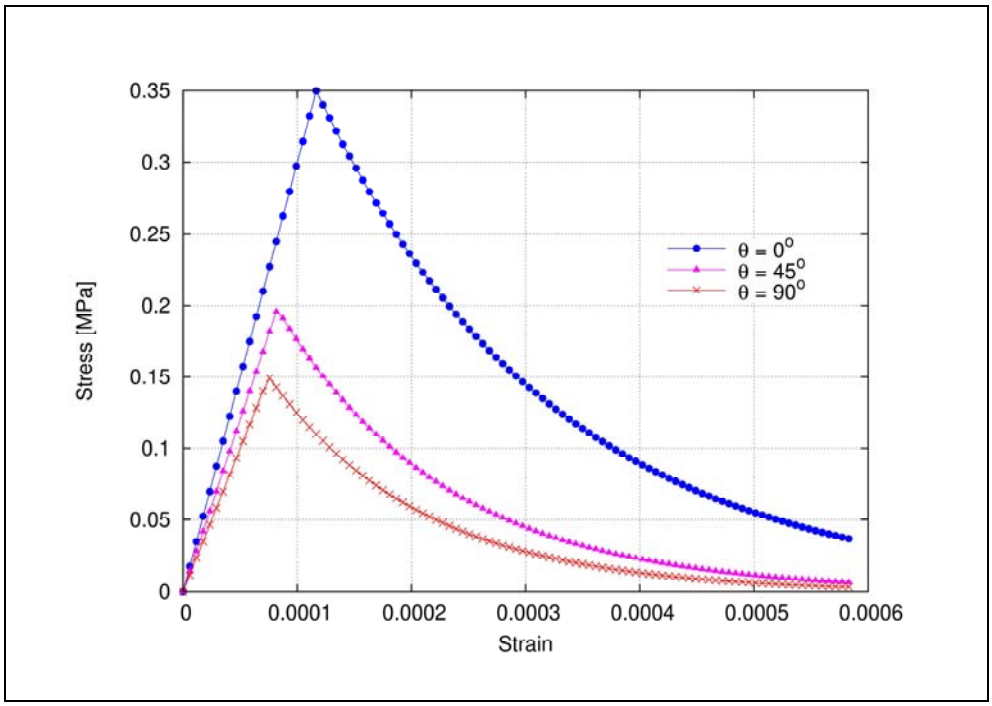

Figure 3.8 Stress-strain responses to uniaxial tension for different angles of orthotropy with isotropic softening.

In the second example, the compressive behaviour is investigated. For this aim, we consider again a single element test, under pure uniaxial compression. The material properties, referred to the material axes 1 and 2, are listed in Table 3.3. The

material parameters of the 1-direction are selected again for the fictitious isotropic space. The case of isotropic softening is considered once again.

Table 3.3 Material properties for uniaxial compression test.

Material Properties			
$E_1=E^*$	3000 MPa	$f_1=f^*$	7.00 MPa
E_2	2000 MPa	f_2	3.00 MPa
$v_{12}=v^*$	0.1	f_{12}	3.00 MPa
v_{21}	0.15	$G_{f,1}=G^*$	40000 J/m2
G_{12}	900 MPa	$G_{f,2}$	11020 J/m2

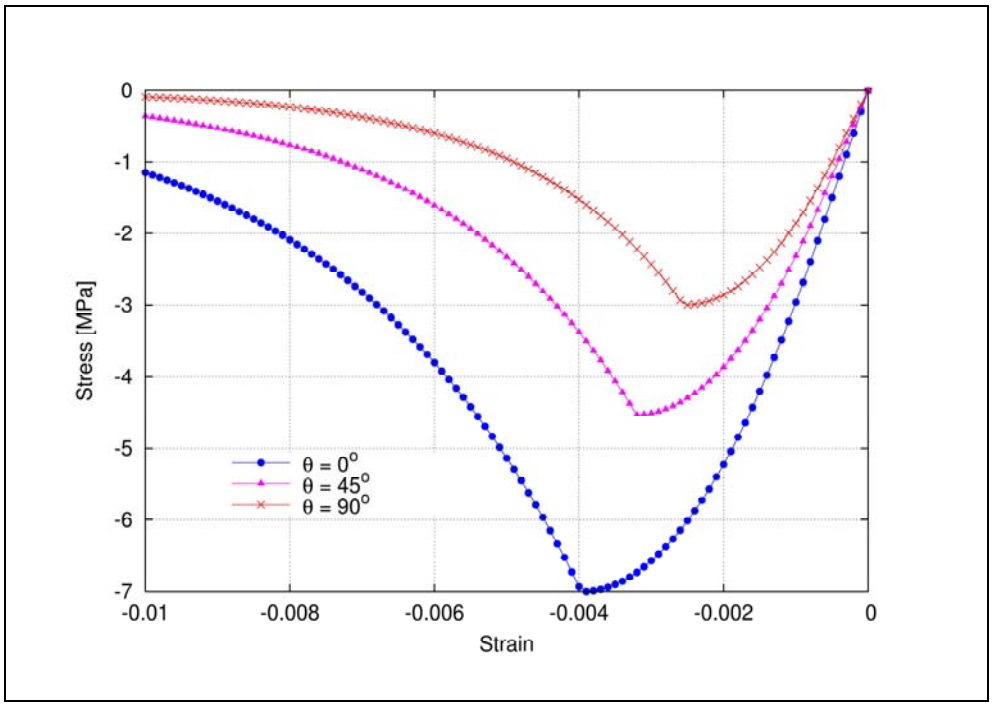

Figure 3.9 Stress-strain responses to uniaxial compression for different angles of orthotropy with isotropic softening.

The single element is subjected to pure uniaxial compression in the *x*-global direction. Figure 3.9 shows the stress-strain response for angles of orthotropy equal

to 0°, 45° and 90°. The same observations made for the tension test hold. Compared with the previous analysis, in compression we assumed hardening behaviour until the peak compressive strength. This could be the case of masonry, which exhibits limited ductility in compression. Once the ultimate strain is reached, the material begins to soften with behaviour dependent on the fracture energy of the material. The material strength in the *y*-direction degrades at the same rate of the material strength in the *x*-direction, since the softening is isotropic and hence the material brittleness is the same in all directions.

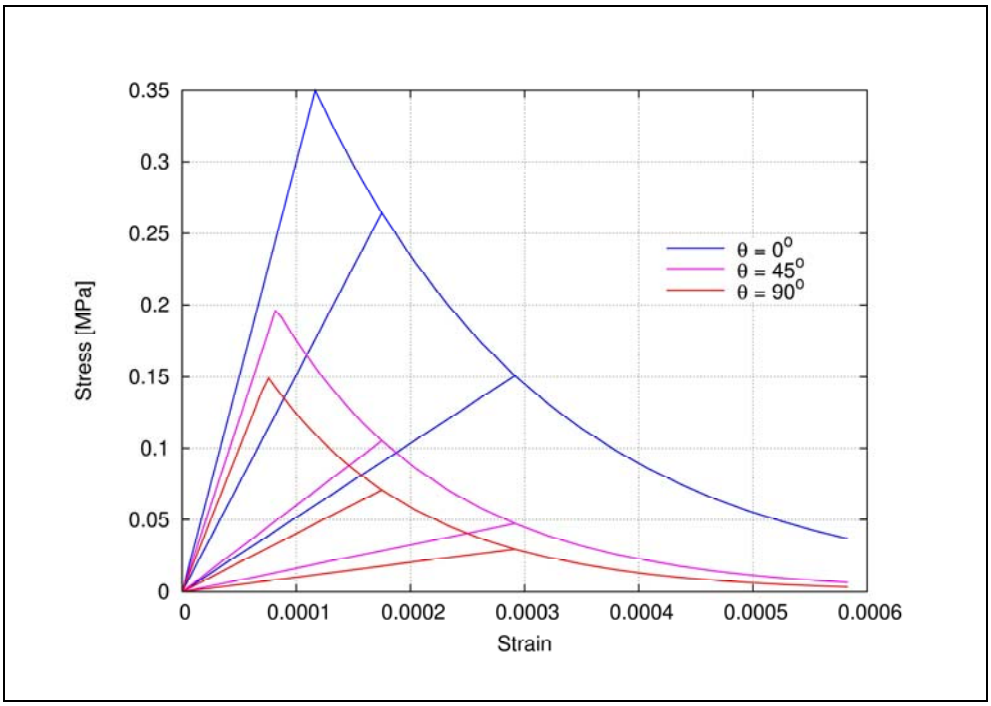

Figure 3.10 Uniaxial tension and unloading to origin.

An important feature of the proposed model is the particular behaviour during unloading/reloading conditions. In compliance with the Continuum Damage Mechanics (see Chapter 2), in case of unloading the damage does not rise and,

consequently, unloading occurs until the origin according to a damaged stiffness, see Equations (3.41) and (3.42). A successive reloading follows the same unloading branch, until the damage threshold is reached again. Figures 3.10 and 3.11 illustrate the aforementioned feature of the model, by showing the numerical response of a single element subjected to uniaxial tension cycles (Figure 3.10) or uniaxial compression cycles (Figure 3.11) in the *x*-global direction. Once again, we have assumed angles of orthotropy equal to 0°, 45° and 90°. As can be seen, the damage constitutive law differs from the plasticity constitutive law in that no plastic irreversible deformation occurs: all the deformation is recovered during the unloading, hence the unloading/reloading paths are not parallel.

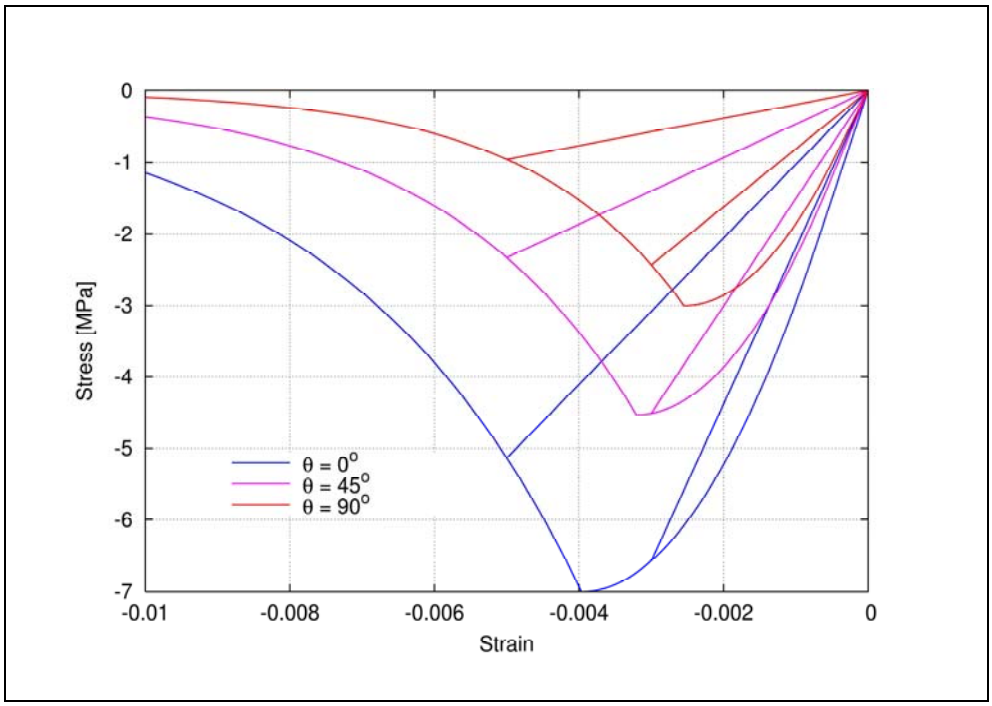

Figure 3.11 Uniaxial compression and unloading to origin.

Finally, the capability of the model to represent the softening orthotropy of a material is shown. For this aim, we consider a single finite element subjected to pure uniaxial tension in the *x*- and *y*-global directions. The same feature of the model could be demonstrated in the same manner by considering an uniaxial compression test. The material properties in the real space, referred to the material axes 1 and 2, are the same of Table 3.2. The material parameters for the fictitious isotropic space are selected according to (3.65a, b, c).

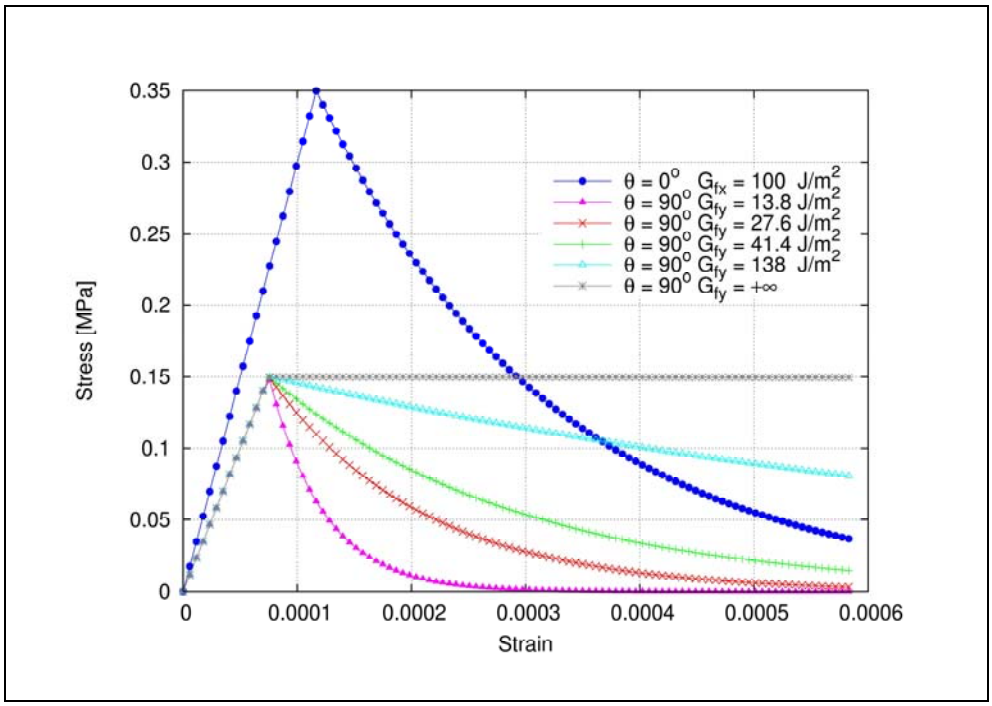

Figure 3.12 Stress-strain responses to uniaxial tension along the two material axes: influence of fracture energy $G_{f,y}$ on the orthotropic softening behaviour.

In addition to the value of fracture energy in the *y*-direction $G_{f,2} = 27.6\ J/m^2$, which has been obtained by (3.64) and corresponds to the case of isotropic softening, other values are considered: $13.8\ J/m^2$, $41.4\ J/m^2$, $138\ J/m^2$ and

$+\infty$. The assumption of these four values leads to two different softening parameters along the material axes *x* and *y*. In the first case, the material strength in the *y*-direction degrades at a faster rate than the material strength in the *x*-direction. In the second and third cases, the opposite occurs. The last case represents an hypothetic orthotropic material with a post-peak perfectly plastic behaviour in *y*-direction. Therefore, the proposed model permits to represent completely different inelastic behaviours along the two material axes, see Figure 3.12.

3.6.2 Directional Strength of Wood

Although the thesis principally deals with masonry structures, for the sake of completeness we discuss hereafter the capacity of the present model to simulate the behaviour of other orthotropic materials. First, we assess the uniaxial strength of wood elements for different orientations of the grain relative to the loading direction. The numerical results are compared with predictions obtained by the common strength criteria generally used for this material.

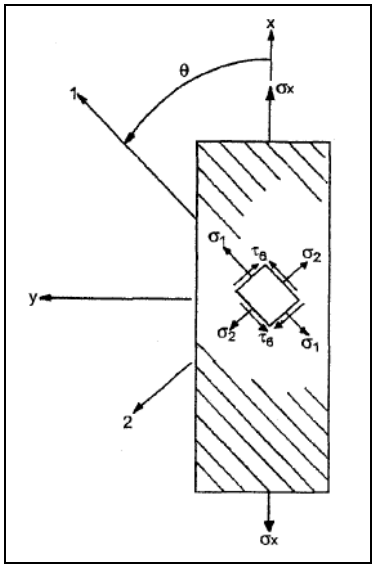

Figure 3.13 Material axes and global axes in a wood specimen.

Hankinson (1921) proposed an empirical formula for the determination of the strength of wood. The formula is expressed in terms of the strengths in the axes 1 and 2 (i.e. the grain direction and the perpendicular, Figure 3.13), the angle θ between the loading direction and the 1-axis, and a parameter n, which provides information about the shear strength f_{12}.

On the other hand, Norris (1955) developed a theory for the strength of orthotropic materials based on the von Mises (1928) theory for isotropic materials. He considered an orthotropic material to be made up of an isotropic material by introducing voids in the shape of equal rectangular prisms. The walls of isotropic material between these voids form the three principal planes of the orthotropic material. Using the energy of distortion expression, he obtained a formula for each of these planes, such as the plane 1-2.

Of all the macro-mechanical failure theories for anisotropic materials, the Tsai-Hill (1965) theory is the most widely used for wood.

The predictions obtained by the aforementioned criteria for a Sitka spruce (*Picea sitchensis*) element subjected to tension are compared with the numerical simulations. According to Green (2001), typical properties are assumed for this type of wood: f_1=78.3 MPa, f_2 =2.55 MPa and f_{12}=7.93 MPa. Figure 3.14 presents the tensile strength results obtained by assuming n=1.78 in the Hankinson formula and taking f_{12}=6.25 MPa for Norris and Tsai-Hill criteria. These results are compared with those derived by the numerical simulations, where we assume the von Mises criterion (1928) for the fictitious isotropic space. In this particular case, the $\mathbf{\Lambda}^*$ tensor in the expression (3.43) of the equivalent stress assumes the form

$$\mathbf{\Lambda}^* = \begin{bmatrix} 1 & 1/2 & 0 \\ -1/2 & 1 & 0 \\ 0 & 0 & 3 \end{bmatrix} \tag{3.75}$$

and $r_0^* = f^* = f_1$. In compliance with the examples discussed in Section 3.6.1, the material parameters of the 1-axis have been selected for the fictitious isotropic space. As can be seen, the different approaches lead to very similar results.

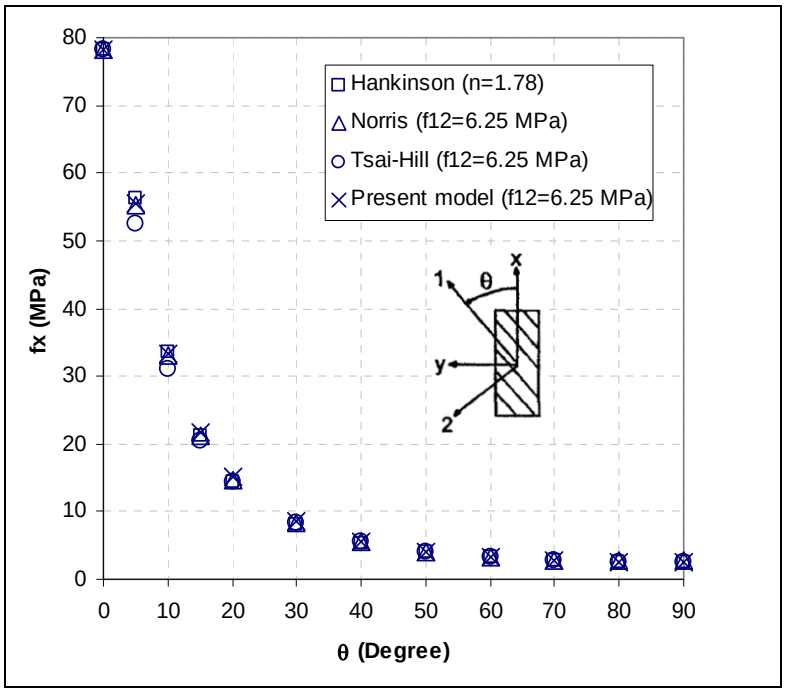

Figure 3.14 Comparison between numerical results and strength values obtained by Hankinson, Norris and Tsai-Hill theories (f_1=78.3 MPa, f_2 =2.55).

Figure 3.15 compares the numerical results with the different theories for the same data, except for n=1.97 in the Hankinson formula and f_{12}=7.93 MPa for Norris and Tsai-Hill criteria. Good agreement is discovered by comparing the numerical results and the analytical predictions.

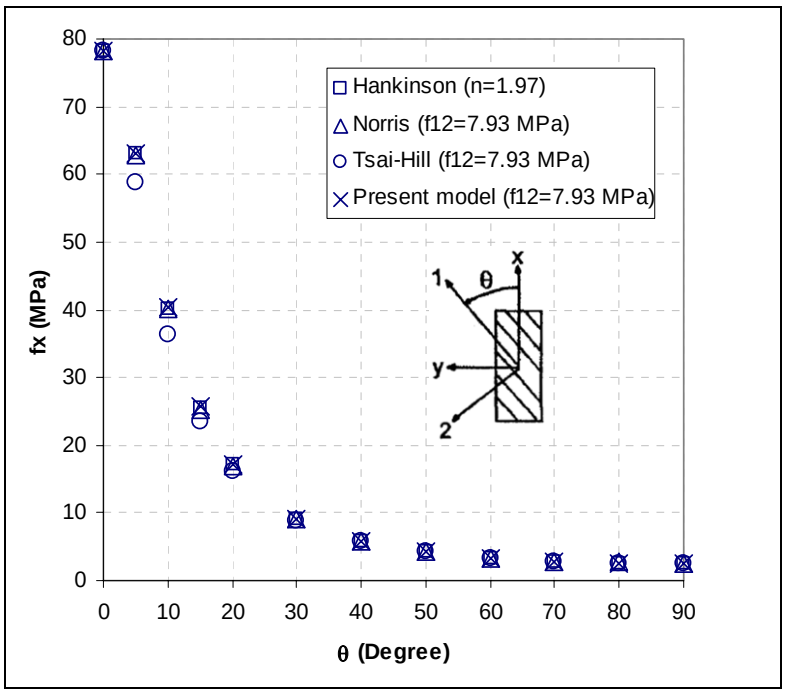

Figure 3.15 Comparison between numerical results and strength values obtained by Hankinson, Norris and Tsai-Hill theories (f_1=78.3 MPa, f_2 =2.55).

3.6.3 Biaxial Failure Envelopes for Unidirectional Fibre-Reinforced Composite Laminae

The biaxial failure envelopes of two unidirectional fibre-reinforced laminae are analyzed in this section. In recent years, considerable attention has been focused on the modelling of composite materials. Several approaches have been developed, but there is still a strong need of predicting models for stiffness and strength assessment. The problem is a hard task, since a reliable model should represent with a good level of approximation the overall behaviour of the laminate, taking into account the particular behaviour of the individual components (i.e. matrix, fibres and interface) and their spatial organization. Constitutive models for fibre reinforced composite laminates can be classified according to the scale in which

they are defined. Since the goal of the present work is not to propose an ad-hoc approach for this type of materials, a very simple macro-model is considered hereinafter. This type of approach generally results insufficient to describe the overall inelastic behaviour and failure of the laminate. However, this section would like to emphasize the potential applicability of the proposed tool to more refined models.

Figure 3.16 shows the comparison of the failure envelope obtained using the proposed model with experimental results (Soden *et al.* 2002) for an unidirectional glass fibre reinforced lamina (E-Glass/LY556/HT907/DY063), with a fibre volume fraction k_f =0.62, under shear stresses and normal stresses orthogonal to fibre direction. Experimental results correspond to tubes of 60 mm internal diameter and 2 mm thick. The average properties of the homogenized material are obtained by the information concerning the constituents provided by Soden *et al.* and the basic formulae of the mixing theory (Daniel and Ishai, 1994). The experimental data are compared with results derived by the numerical simulations, in which we have assumed the Drucker-Prager criterion (1952) for the fictitious isotropic space. In this case, the assumed fictitious damage criterion presents the following expression:

$$\Phi^*\left(\tau^*, r^*\right) = \tau^* - r_0^* = \left(\alpha I_1^* + \sqrt{J_2^*}\right) - k = 0 \tag{3.76}$$

Where I_1^* is the first invariant of the fictitious stress tensor, J_2^* is the second invariant of the deviatoric stress tensor, α and k are material constants defined as

$$\alpha = \frac{m-1}{\sqrt{3}\left(m+1\right)}, \quad k = \frac{2 f_c^*}{\sqrt{3}\left(m+1\right)} \tag{3.77}$$

where f_c^* and f_t^* are the fictitious isotropic compressive and tensile strengths, respectively, and $m = f_c^* / f_t^*$. In the numerical simulations, we have assumed $f_c^* = 140\text{MPa}$ and $f_t^* = 40\,\text{MPa}$, thus values equal to the strengths in the real space. Real shear strength has been assumed equal to 61.2 MPa in order to map properly the fictitious isotropic criterion to the orthotropic desired one.

It can be observed that the model reproduces with an acceptable approximation the experimental failure envelope.

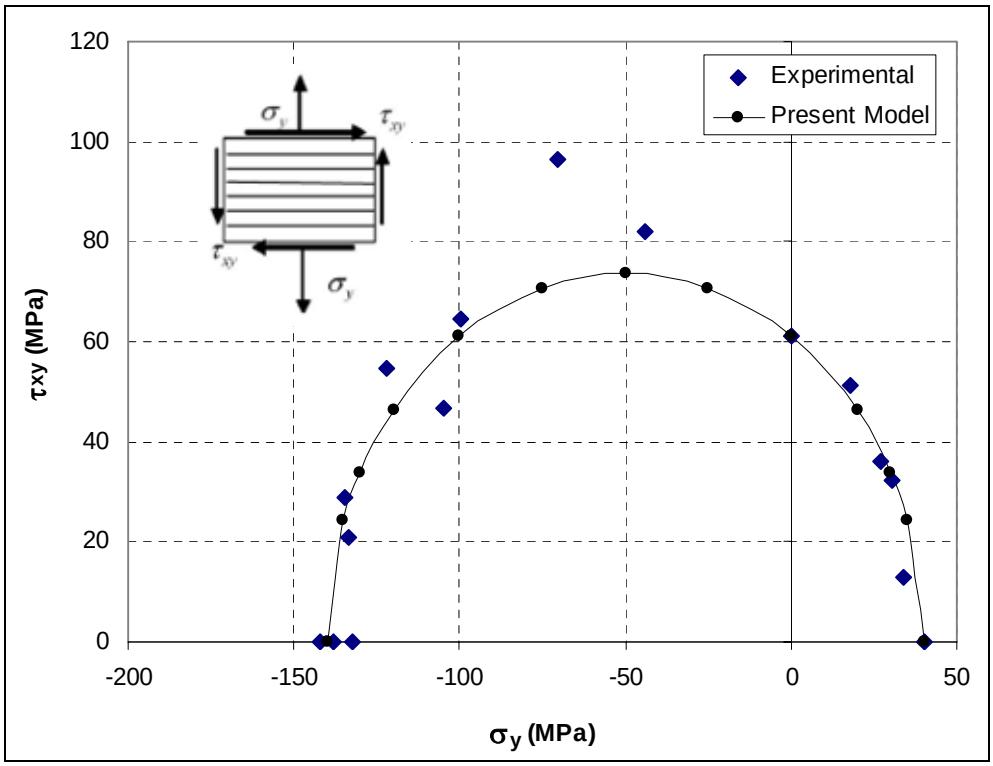

Figure 3.16 Failure envelope for unidirectional lamina (E-Glass/LY556/HT907/DY063).

Figure 3.17 shows the comparison of failures stresses obtained using the model proposed with experimental ones (Soden *et al.* 2002) for an unidirectional carbon

fiber reinforced lamina (T300/BSL914C epoxy), with a fibre volume fraction k_f=0.60, under shear stresses and normal stresses in the direction of the fibres. Experimental results were obtained from tubes tested under combined axial tension or compression and torsion. The tubes were 32 mm diameter and 1.9–2.3 mm thick.

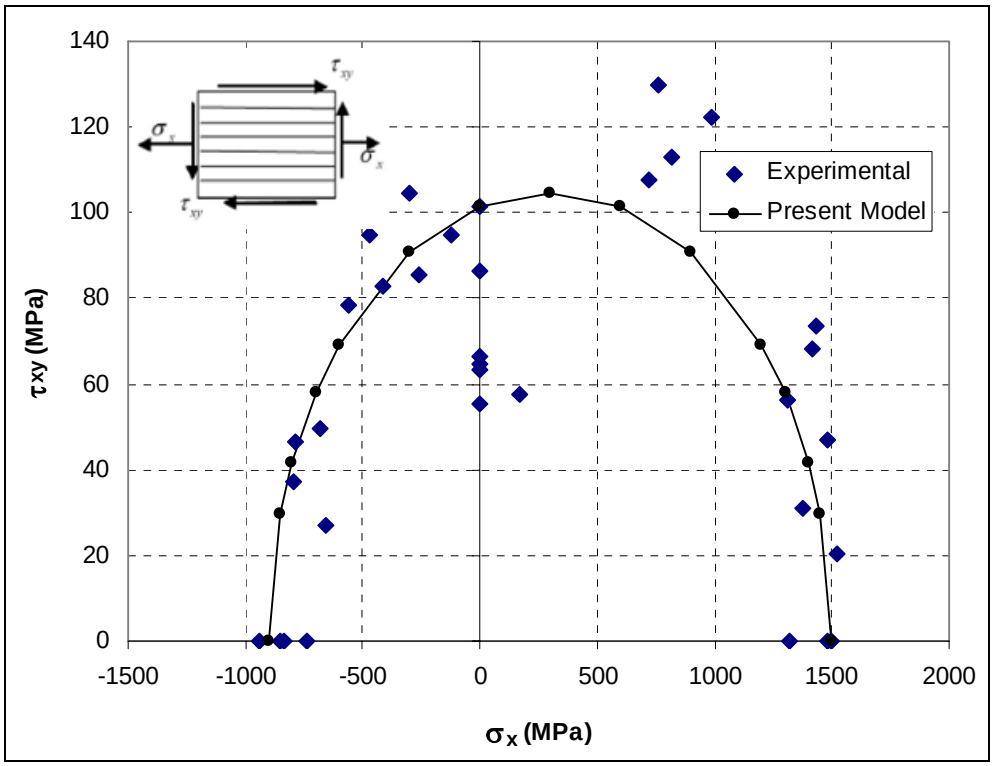

Figure 3.17 Failure envelope for unidirectional lamina (T300/BSL914C epoxy).

In the numerical simulations, we have assumed again the Drucker-Prager criterion for the fictitious isotropic space, with $f_c^* = 900\text{MPa}$ and $f_t^* = 1500\,\text{MPa}$. Real shear strength has been assumed equal to 101.3 MPa, in order to map properly the fictitious isotropic criterion to the orthotropic desired one.

It could be seen that the model approximately reproduces the lamina failure envelope. We do recognize that the presented results are coarse, since they do not provide any information about individual components, associated failures etc. Nevertheless, the presented methodology provides a basic tool that could be combined efficiently with more sophisticated models, in order to obtain more precise results. This could be the case, for example, of models based on an analysis at component materials level that allow obtaining the behaviour of the lamina and even the more complex laminate, composed of laminae with different fibre orientations.

3.6.4 Uniaxial and Biaxial Failure Envelopes for Masonry

The ability of the present model to reproduce the strength of masonry is assessed herein. A comparison with experimental data obtained by Page (1981, 1983) is carried out. Page published the results of a series of tests designed to assess the directional strength characteristics of masonry panels subjected to in-plane monotonic loading. For that purpose, he conducted a series of biaxial tension–compression and biaxial compression–compression tests, which are still the most comprehensive experimental program conducted on the in-plane behaviour of brick masonry.

First, we consider the results of numerical simulations carried out for different orientations of the bed joints relative to the loading direction. For each orientation, three different loading patterns were applied (Figure 3.18), namely uniaxial tension, uniaxial compression and biaxial tension–compression.

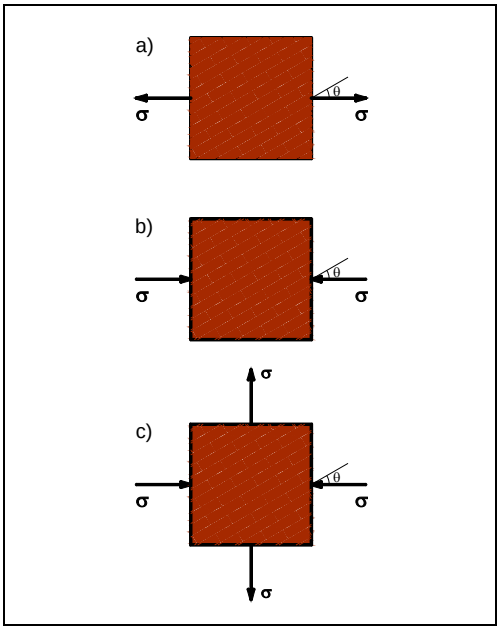

Figure 3.18 Load patterns for different orientations: uniaxial tension (a), uniaxial compression (b) and biaxial tension–compression (c).

For tensile stress states, the Rankine criterion is assumed in the fictitious isotropic space. In this particular case, calling $\mathbf{p}_1^*$ the unit vector associated with its respective principal direction, the tensor $\mathbf{\Lambda}^*$ in the expression (3.43) assumes the form

$$\mathbf{\Lambda}^* = \mathbf{p}_1^* \otimes \mathbf{p}_1^* \otimes \mathbf{p}_1^* \otimes \mathbf{p}_1^* \tag{3.78}$$

and, therefore, the equivalent stress is defined as

$$\tau^* = \left\langle \bar{\sigma}_1^* \right\rangle \tag{3.79}$$

Where $\bar{\sigma}_1^*$ is the largest principal effective stress and the symbols $\langle\cdot\rangle$ are the Macauley brackets $\left(\langle x\rangle = x, if\ x \geq 0, \langle x\rangle = 0, if\ x < 0\right)$. The initial value of the damage threshold is $r_0^* = f^*$, where f^* is the initial uniaxial damage stress.

For compressive stress states, the criterion proposed by Faria *et al.* (1998) is assumed. In this case, the equivalent stress is defined in the following form instead of (3.43):

$$\tau^* = \sqrt{3}\left(K\bar{\sigma}_{oct}^* + \bar{\tau}_{oct}^*\right) \tag{3.80}$$

In this format, directly inspired on the Drucker-Prager criterion, $\bar{\sigma}_{oct}^*$ and $\bar{\tau}_{oct}^*$ are the octahedral normal stress and the octahedral shear stress. Constant K controls the aperture of the inherent Drucker-Prager cone. According to (3.47) and (3.80), the initial value of the damage threshold is equal to

$$r_0^* = \frac{\sqrt{3}}{3}\left(K - \sqrt{2}\right) f^* \tag{3.81}$$

For all the tests, the material properties in the 1-axis have been selected for the fictitious isotropic space. We have assumed the following values for real strengths, extrapolated by the experimental data of Page (1983): f_1=0.4 MPa, f_2 =0.2 MPa, f_{12}=0.3 MPa for the tension criterion and f_1=3.5 MPa, f_2 =7.0 MPa and f_{12}=2.71 MPa for the compression criterion.

For uniaxial tension, masonry was subjected to the loading pattern shown in Figure 3.18 (a). The load was gradually increased until the ultimate conditions were reached. The simulations were performed for different orientations of the bed joints, namely 0°, 22.5°, 45°, 67.5° and 90°. The directional strength characteristics obtained from numerical simulations are presented in Figure 3.19 and are compared with the data of Page (1983). Also the results obtained by Shieh-Beygi

and Pietruszczak (2008) are reported for the sake of argument. Instead of the macro-model assumed in this work, they adopted a mesoscale approach, in which the structural behaviour is examined at the level of constituents, i.e. brick and mortar.

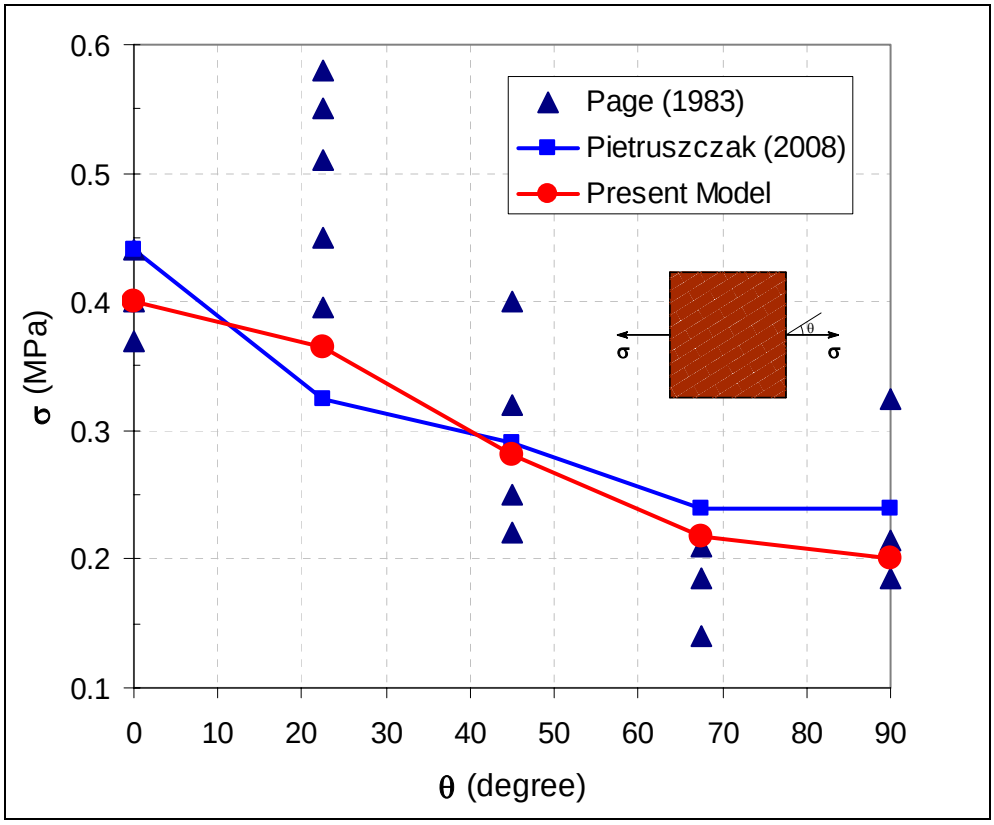

Figure 3.19 Failure envelope for uniaxial tension at different orientations of the bed joints.

It can be seen from this figure that the experimental data are quite scattered. For most orientations, however, the numerical predictions are in a reasonably good agreement with the mean values of the experimental data. The only exception is θ=22.5°, where the finite element simulation underestimates the ultimate strength of the panel by over 25%.

For uniaxial compression, masonry was subjected to the loading pattern shown in Figure 3.18 (b). The directional strength characteristics obtained from numerical simulations are presented in Figure 3.20. The assessed failure loads are quite consistent with Page's results on the average, except for θ=67.5°, where the finite element simulation overestimates the ultimate strength of the panel by over 15%.

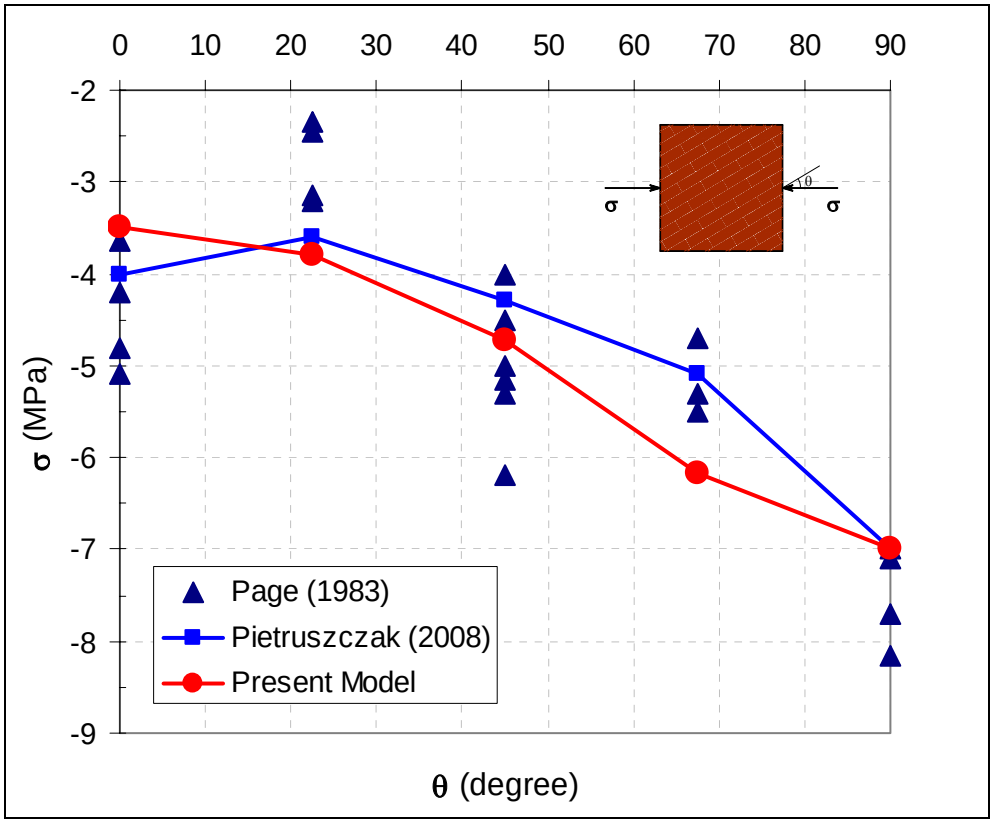

Figure 3.20 Failure envelope for uniaxial compression at different orientations of the bed joints.

For biaxial tension-compression, masonry was subjected to the loading pattern shown in Figure 3.18 (c), which is equivalent to pure shear of a specimen with bed joints at θ=45° with respect to the horizontal axis. The strength characteristic

obtained from numerical analysis are compared with the best fit to the experimental curves reported by Page (1983). The results are, in general, consistent with the experimental evidence, except for θ=67.5°, where the finite element simulation underestimates the ultimate strength of the panel by over 25% (Figure 3.21).

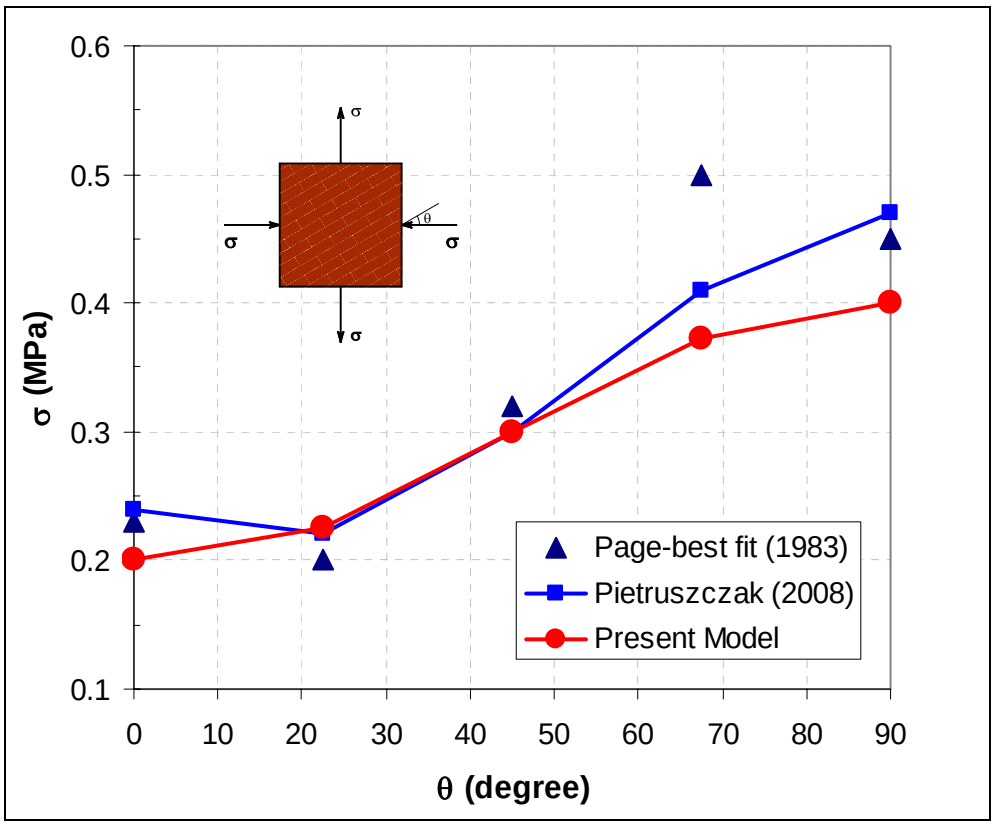

Figure 3.21 Failure envelope for biaxial tension-compression at different orientations of the bed joints.

Then, the comparison of numerical results with biaxial failure envelopes in compression is presented. The set of experimental strength data is again the one given by Page (1981). The panels were loaded proportionally in the principal stress directions σ_1 and σ_2 along different orientations θ with respect to the material axes.

The values assumed for real strengths are f_1=8.74 MPa, f_2 =8.03 MPa, f_{12}=2.71. For all the tests, the material properties in the 1-axis have been selected for the fictitious isotropic space. The criterion proposed by Faria *et al.* (1998) is considered again. The comparisons between the experimental values and the model are given in Figures 3.22-2.24, corresponding to orientations of the bed joints equal to 0°, 22.5° and 45°, respectively.

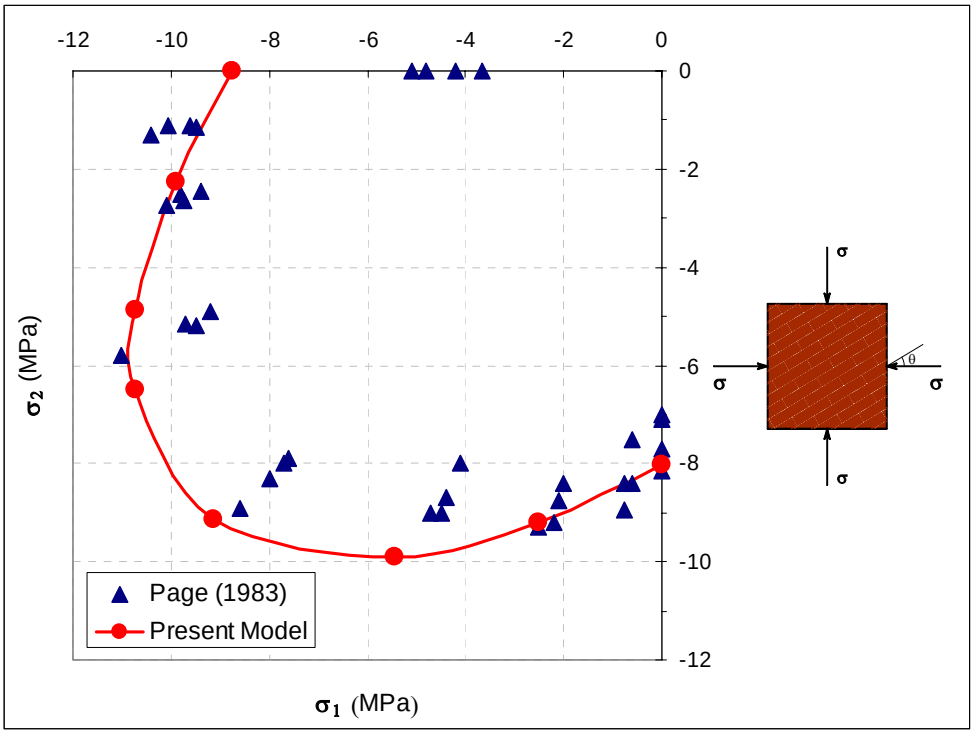

Figure 3.22 Failure envelope for biaxial compression–compression (θ = 0°).

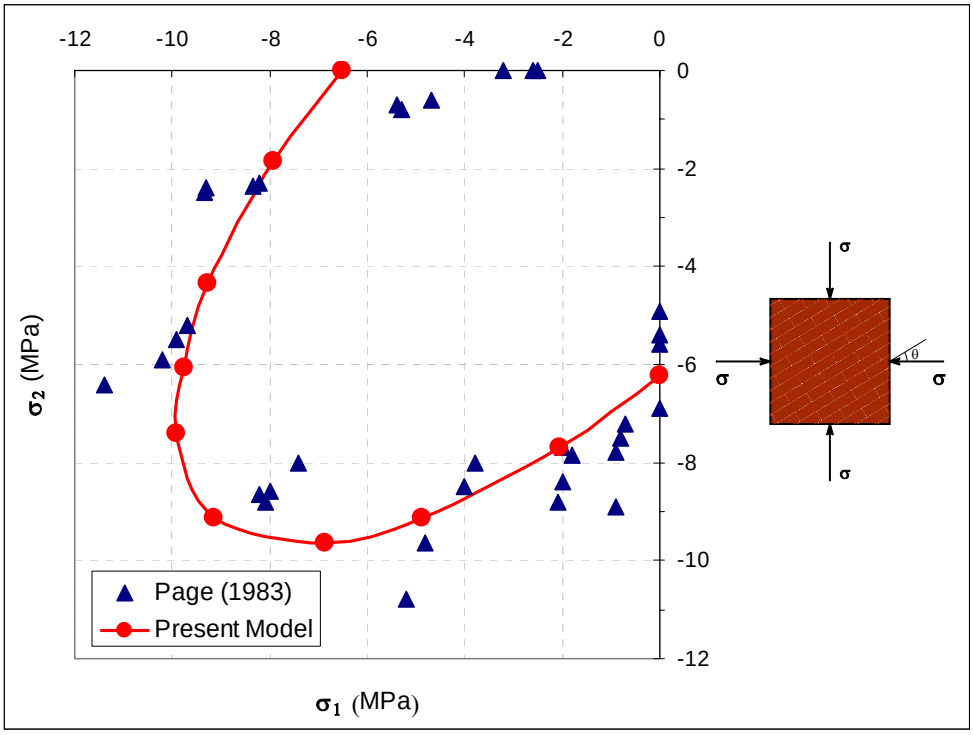

Figure 3.23 Failure envelope for biaxial compression–compression ($\theta = 22.5°$).

Globally, good agreement is found. The uniaxial compressive strength parallel to the bed joints seems to be overpredicted by the model, see Figure 3.22, which is due to a debatable definition of failure in the experiments for these loading conditions (early splitting of the bed joints in tension), see Dhanasekar *et al.* (1985). In fact, the individual "piers" of masonry formed after splitting of the bed joints can withstand a much higher load before collapse is obtained.

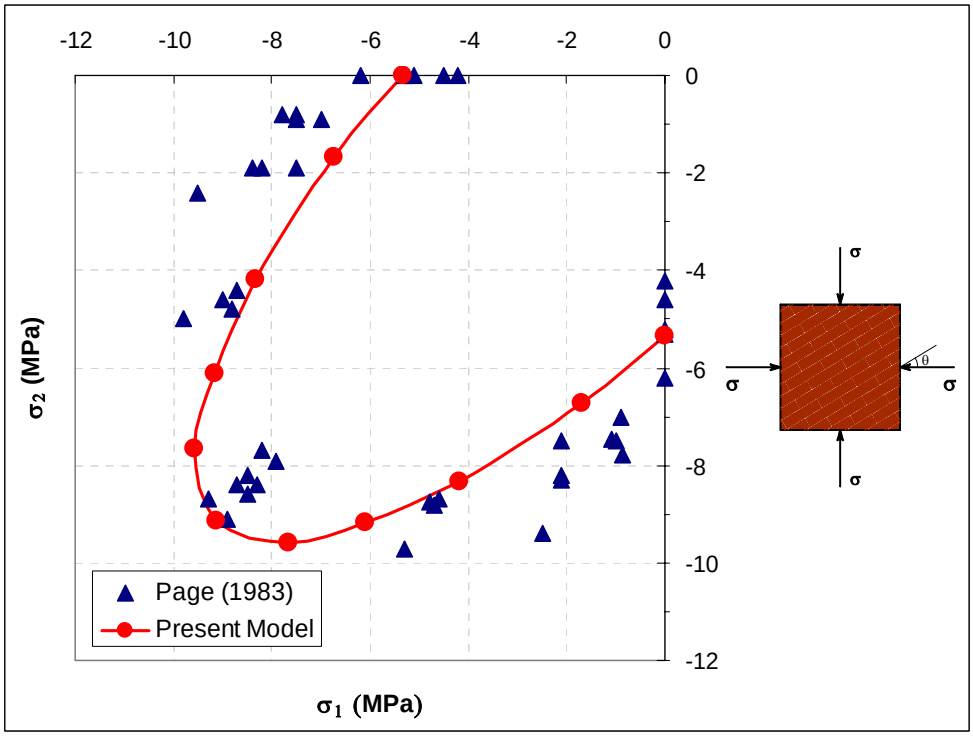

Figure 3.24 Failure envelope for biaxial compression –compression ($\theta = 45°$).

3.7 Conclusions

In this Chapter, an original methodology has been presented to model the mechanical behaviour of orthotropic materials. Such a theory, is based on non-linear damage constitutive laws and on the concept of *mapped tensor* from the anisotropic real space to the isotropic fictitious one. It allows the establishment of an implicit orthotropic damage criterion in the *real* anisotropic space by using the isotropic one formulated on the *fictitious* isotropic space. In this way, the different behaviours along the material axes can be reproduced by means of a very simple formulation, taking advantage of the well-known isotropic damage criteria. In fact, the principal advantage lies in the possibility of adjusting an arbitrary isotropic criterion to the particular behaviour of the orthotropic material.

The model has been fully formulated for the 2-dimensional case. However, it can be easily extended to the 3-dimensional case, as in Oller *et al.* (2003).

The implementation of this theory in finite element codes is straightforward. The model proposed is particularly suited for finite element computations of initially-orthotropic materials, such as wood, fibre reinforced composites and masonry. The brittleness orthotropy can also be modelled in a very easy and effective way.

Initial applications of the model to these types of materials have shown promising results. Nevertheless, some improvements are required in order to obtain a better description of the material behaviour. First of all, the methodology has to take into account the different behaviours in tension and compression. In case of masonry, for example, it is not possible to describe the material behaviour with a single criterion. Therefore, different inelastic criteria for tension and compression have to be properly mapped in order to achieve the correct description of ultimate conditions. This will be the main topic of the next Chapter.

Chapter 4.
Two-Parameters Damage Model for Orthotropic Materials: Application to Masonry

The present Chapter represents a step further in the formulation of damage models for orthotropic materials. The practical examples presented in Chapter 3 have shown the need for a more refined tool. In fact, a sound model should take into account the different behaviours in tension and compression, in order to describe correctly the real material behaviour.

An implicit composite damage criterion suitable for the modelling of orthotropic materials under plane stress conditions is presented herein. The presented methodology is based again on the concept of *mapped tensor* from the real space to the fictitious one, firstly introduced by Betten (1981 and 1988). Individual damage criteria are considered for tension and compression, according to different failure mechanisms. The former is associated with a localized fracture process, denoted by

cracking of the material, and the latter is associated with a more distributed fracture process, i.e. the crushing of the material. The aim of studying the behaviour of a real material by means of an equivalent fictitious solid can be achieved by means of the appropriate definitions of two stress *transformation tensors*. Each of them is related to tensile or compressive stress states, respectively.

The proposed model, based on Continuum Damage Mechanics, is principally devoted to the finite element analysis of masonry structures. Thus, the modelling of the orthotropic behaviour of such a material is discussed. Then, the formulation of the model is presented, together with the description of the constitutive relationships adopted. The aspects related to the implementation in a finite elements code are detailed next. Finally, the capability of the model to represent correctly the orthotropic strength behaviour of different masonry types is demonstrated through a comparison with available experimental data.

4.1 Modelling the Orthotropic Behaviour of Masonry

From a phenomenological point of view, masonry is a composite material with an overall orthotropic behaviour. The effective constitutive behaviour of masonry features anisotropy arising from the geometrical arrangements of units and mortar, even if the properties of these constituents are isotropic. A complete description of the material mechanical behaviour is not pursued in this study and the reader is referred to Drysdale *et al.* (1994) and Hendry (1990) for this purpose.

The *elastic orthotropy* of masonry is due to the different elastic properties of mortar and units. Moreover, the constituents are arranged in such a way that the horizontal and vertical directions are obviously not equivalent. This may be even emphasized when the units themselves are elastically anisotropic due to the presence of horizontal or vertical holes. Existing approaches for the determination of overall elastic properties of masonry are based on the homogenization theory.

Such a methodology consists in identifying an elementary cell, which generates an entire panel by regular repetition. In this way, a field problem can be written on the unit cell in order to achieve average values for the homogenized masonry material, starting from the knowledge of the mechanical properties of the constituents and the geometry of the elementary cell. Homogenization techniques have been extensively developed for periodic media and have been widely employed for modelling masonry structures in the elastic and also inelastic field. Fore a more exhaustive information about the topic, the author is referred to the vast available scientific literature (e.g. Anthoine 1995, Cecchi and Sab 2002, Massart *et al.* 2004, Milani 2004).

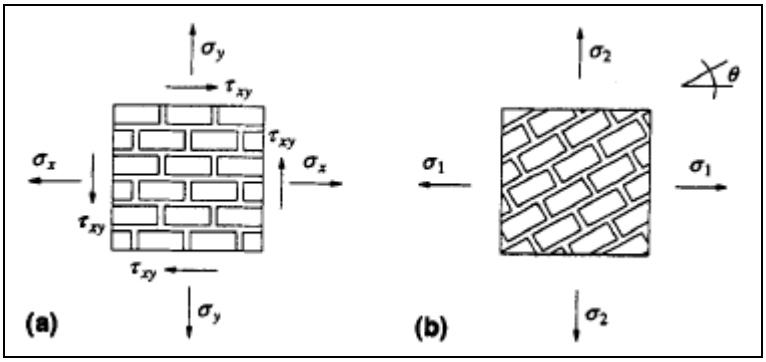

Figure 4.1 Representation of masonry stresses in plane stress: full stress vector components (a), principal stresses and angle θ between principal and material axes (b).

Concerning the *strength orthotropy* of masonry, the representation of an orthotropic failure surface in terms of principal stresses or stress invariants only is not possible. For plane stress situations, which is the case of the present study, a graphical representation in terms of the full stress vector (σ_x, σ_y and τ_{xy}) is necessary. The material axes are assumed to be defined by the bed joints direction (x direction) and the head joints direction (y direction), see Figure 4.1. Another possible representation can be obtained in terms of principal stresses and an angle

θ. The angle θ measures the rotation between the principal stress axes and the material axes. Clearly, different principal stress diagrams are found according to different values of θ.

There have been few attempts to obtain a general failure criterion for masonry because of the difficulties in developing a representative biaxial test and the large number of tests involved. The problem was discussed by Yokel and Fatal (1976) with reference to the failure of shear walls. Dhanasekar *et al.* (1985) interpolated the test data of Page (1981, 1983) by means of three elliptic cones, see Figure 4.2. However, as the authors mentioned, the cones do not correspond with the observed distinct modes of failure. The elliptic cones have been expressed by a second-order tensor polynomial. A wide review of the subject can be found in Hendry (1990), Anthoine (1992) and Molins Borrell (1996).

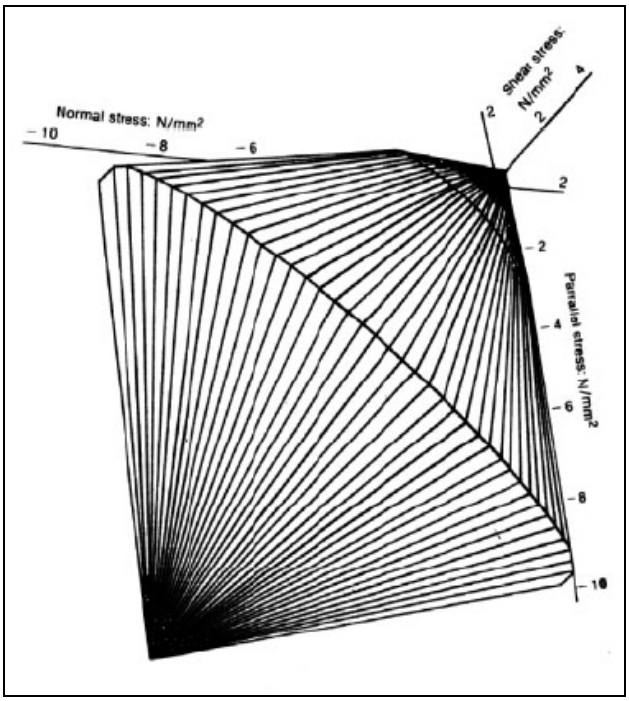

Figure 4.2 Failure surface idealized by Dhanasekar *et al.* (2002).

Several authors proposed polynomials already available for composite materials for the expression of analytical failure models of masonry. Syrmakesis and Asteris (2001), for instance, used a Tsai-Wu (1971) cubic tensor polynomial. The ability to ensure the closed shape of the failure surface and the unique mathematical form for all possible combinations of plane stress are not returned by a satisfactory approximation of Page's experimental data (1981), as can be easily noticed in Figure 4.3.

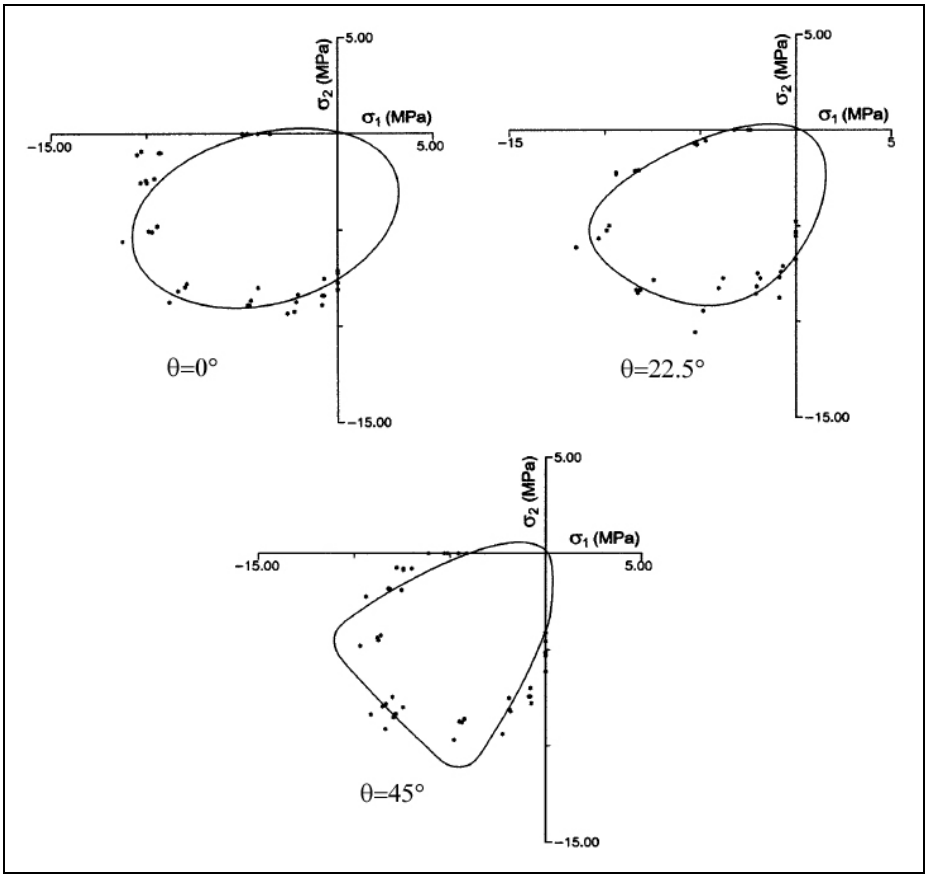

Figure 4.3 Comparison between experimental results from Page (1981) and the failure curves proposed by Syrmakesis and Asteris (2001).

Berto *et al.* (2002) assumed a double pyramid with rectangular base for the shape of the admissible field, for which the slopes of the faces correspond to the internal friction angles of the material, see Figure 4.4. The damage threshold surface, defined in the effective stress space, is simple, regular and convex. Nevertheless, this formulation is incapable of reproducing the increase of strength in biaxial compression, occurring in most materials known. Also, this surface leads to conservative values of shear strength, and this drawback will be discussed in the validation examples presented in Section 4.5.3.

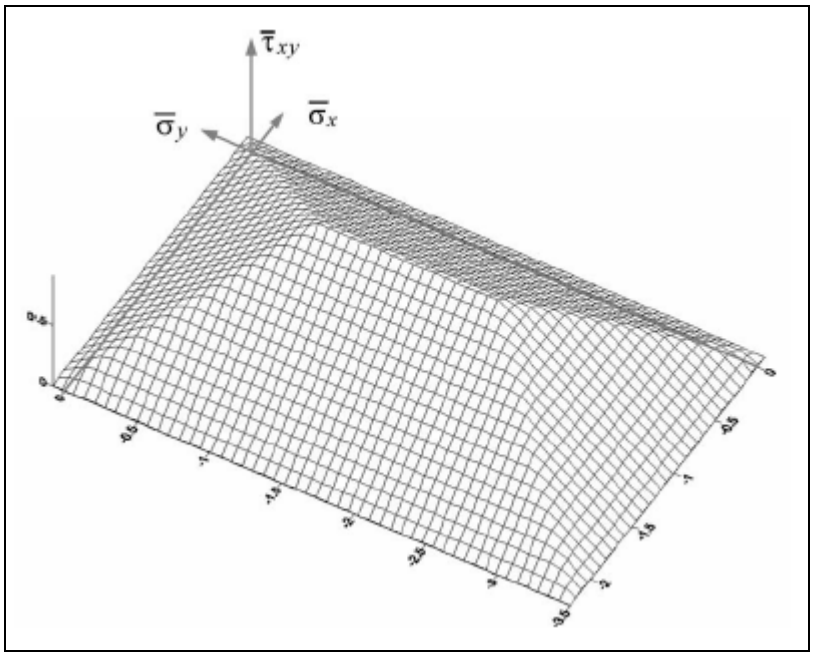

Figure 4.4 Damage threshold surface proposed by Berto *et al.* (2002).

Lourenço (1996) emphasized the inadequacy of describing the material behaviour with a single failure criterion. Figure 4.5, for instance, shows the non-acceptable fit of masonry experimental values which results by the Hoffman criterion. A least squares fit of the experimental results from Page (1981,1983) with a Hoffman

criterion turns out to show no tensile strength in the uniaxial behaviour. A manual fit through the different uniaxial strengths and the compressive failure obtained upon loading with $\sigma_1 = \sigma_2$ also gives a very poor representation of the set of experimental data.

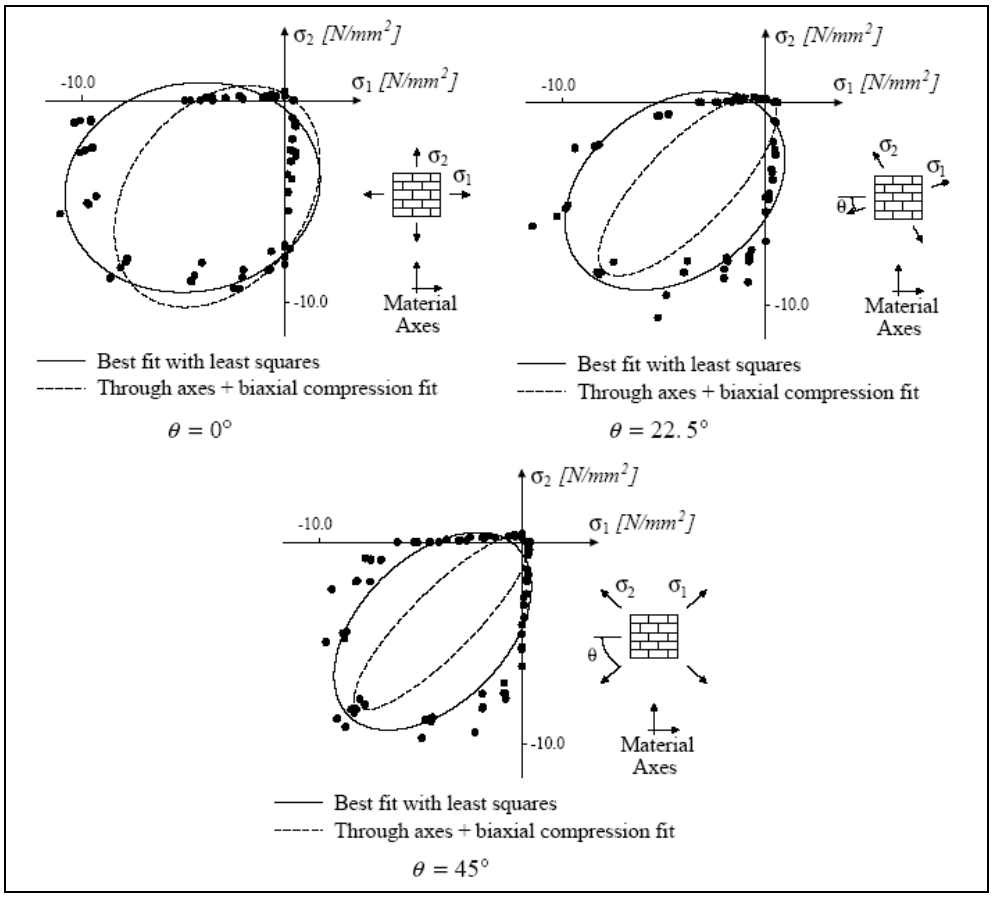

Figure 4.5 Comparison between experimental results from Page (1981,1983) and a Hoffman type yield surface (from Lourenço, 1996).

Furthermore, a single surface fit of the experimental values would lead to an extremely complex yield surface with a mixed hardening/softening rule in order to describe properly the inelastic behaviour. It is believed that this approach is

practically non-feasible. Thus, an alternative approach consists in expanding the conventional formulations for isotropic quasi-brittle materials to describe orthotropic behaviour. Formulations of isotropic quasi-brittle materials behaviour consider, generally, different inelastic criteria for tension and compression. Lourenço *et al.* (1997) proposed an extension of the work of Feenstra and De Borst (1996), who utilized this approach for concrete with Rankine and Drucker-Prager criteria. In particular, Lourenço formulated a non-linear constitutive model for in-plane loaded walls based on the plasticity theory, for which the material admissible field is bounded by a Hill-type yield criterion for compression and a Rankine-type yield criterion for tension, see Figure 4.6. This model considers the influence of the tangential stress (i.e. of the inclination of the principal stress with respect to the natural axes of the material) on the material strength and allows a good fitting with available experimental results.

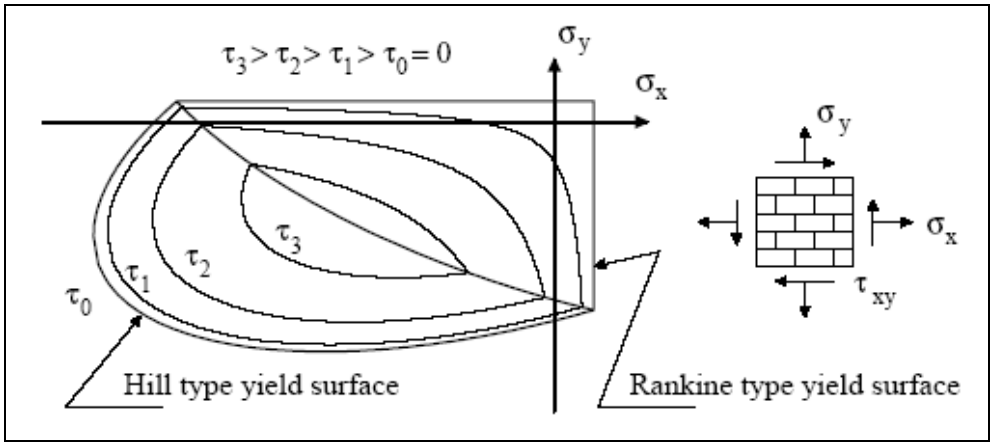

Figure 4.6 Composite yield surface formulated by Lourenço (1997).

Few numerical macro-models specifically devoted to masonry have been implemented in recent years, because of the intrinsic complexity of introducing orthotropic behaviour in the non-linear range. A sound procedure should represent

with an acceptable level of approximation the *brittleness* (or *softening*) *orthotropy* of masonry.

Softening behaviour is commonly attributed to the heterogeneity of the material, due to the presence of different phases and material defects, like flaws and voids. Even prior to loading, mortar contains microcracks due to the shrinkage during curing and the presence of the aggregates. The clay brick contains inclusions and microcracks due to the shrinkage during the burning process. The initial stresses and cracks, as well as variations of internal stiffness and strength, cause progressive crack growth when the material is subjected to progressive deformation. Initially, the microcracks are stable which means that they grow only when the load is increased. Around peak load an acceleration of crack formation takes place and the formation of macrocracks starts. The macrocracks are unstable, which means that the load has to decrease to avoid an uncontrolled growth. In a deformation-controlled test, the macrocrack growth results in softening and the localization of cracking occurs in a small zone, while the rest of the specimen unloads. Figure 4.7 shows characteristic stress-displacement diagrams for quasi-brittle materials in uniaxial tension and compression. As can be seen, the inelastic behaviours are totally different. Therefore, regarding a numerical model, it is crucial to represent separately the correct softening behaviours in tension or compression.

In several studies, including the present one, it is assumed that the inelastic behaviour both in tension and compression are related to the integral of the $\sigma-\delta$ diagram. These quantities, denoted respectively as tensile fracture energy G_f and compressive fracture energy G_c, are assumed to be material properties. With this energy-based approach, tensile and compressive softening can be described within the same context, since the underlying failure mechanisms are similar, namely continuous crack growth at micro-level. It is noted that masonry presents another type of failure mechanism, generally identified as mode II, that consists of slip of

the unit-mortar interface under shear loading. Again, the inelastic behaviour in shear can be described by the mode II fracture energy $G_{f,II}$, defined by the integral of the $\tau-\delta$ diagram in the absence of normal confining load. Shear failure is a salient feature of masonry behaviour, which must be incorporated in a micro-modelling strategy. However, for continuum models, this failure cannot be directly included because the unit and mortar geometries are not discretized. Failure is then associated with tension and compression modes in a principal stress space.

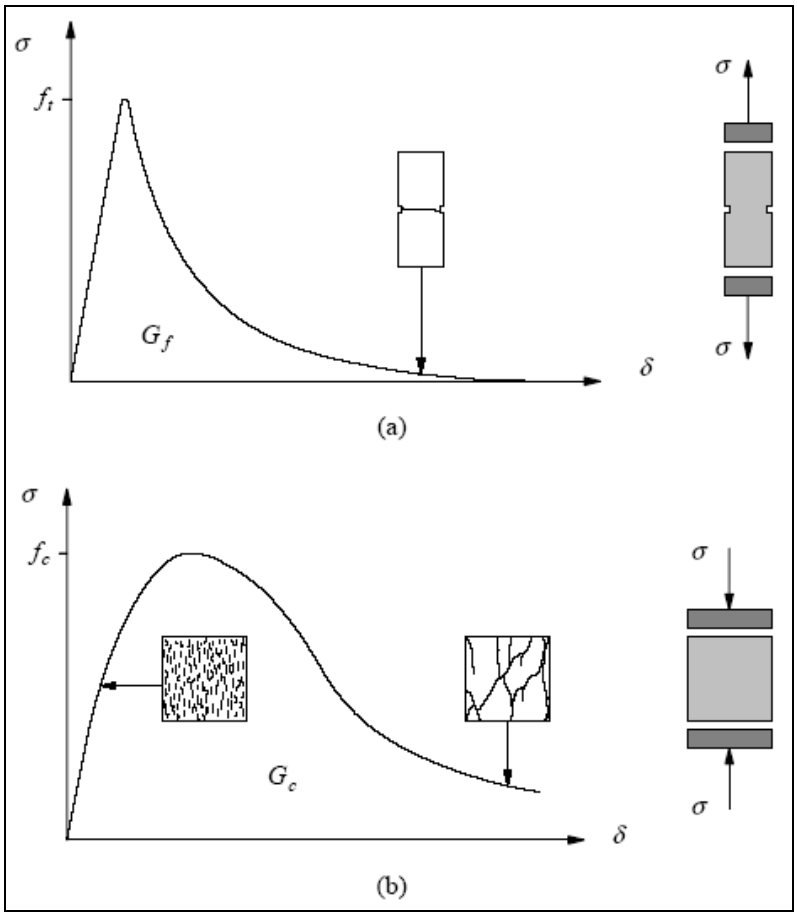

Figure 4.7 Typical behaviour of quasi-brittle materials under uniaxial loading and definition of fracture energy: tensile loading (a); compressive loading (b).

Several procedures have been proposed to model the aforementioned softening behaviour of masonry. In the field of Continuum Damage macro-models, Berto *et al.* (2002) developed a specific model for orthotropic brittle materials, starting from the observation that in masonry the development of damage can modify the intensity of the anisotropy but does not alter the initial symmetries of the material. The basic assumption of the model is the acceptance of the natural axes of the masonry (i.e. the bed joints and the head joints directions) also as principal axes of the damage. In each direction, two independent damage parameters are assumed, one for compression and one for traction. Their evolution are described by functions similar to that used for isotropic damage of concrete, different for tension and compression. The fourth-rank damage tensor, which reduces to a 3×3 matrix for in-plane stress conditions, is written in terms of the four scalar damage parameters and of the strain tensor.

Lourenço *et al.* (1997), on the other hand, proposed a plane-stress softening plasticity model for masonry. As commented before, they adopted a composite yield criterion, by combining the Rankine-type and the Hill-type criteria. In tension they adopted an exponential softening law for the stress-strain diagrams, with different fracture energies along each material axes. Hence, the principal directions of damage are indeed fixed and aligned with the initial orthotropy axes. Although the model incorporates two different fracture energies, a single scalar internal parameter is used in the plasticity algorithm in order to measure simultaneously the amount of softening in two material axes. In compression, the authors adopted an isotropic parabolic hardening law, followed by a parabolic/exponential softening law with different compressive fracture energies along the material axes.

The dissimilar behaviour exhibited by masonry under tension or under compression is an essential feature when dealing with cyclic actions. This peculiarity of masonry behaviour, also exhibited by other geomaterials, is a consequence of the rather different strengths exhibited under tension or under compression, the first

one associated to significant fragility, responsible for visible cracking. Under cyclic loading tensile cracking is usually the first evidence of nonlinearity, and consequently important changes in stiffness are observed when passing from tension to compression. The constitutive model must be able to distinguish tension from compression, in order to allows for this unilateral effect, clearly visible when reversing the sign of the external loading (as in the earthquake motion). The plasticity models, by definition, are not able to model either the damaged stiffness during unloading/reloading or the stiffness recovery at crack closure under alternate loading. These effects, shown in Figure 4.8, can only be represented by means of Continuum Damage Mechanics models which account for different behaviours in tension and compression (Papa, 1996).

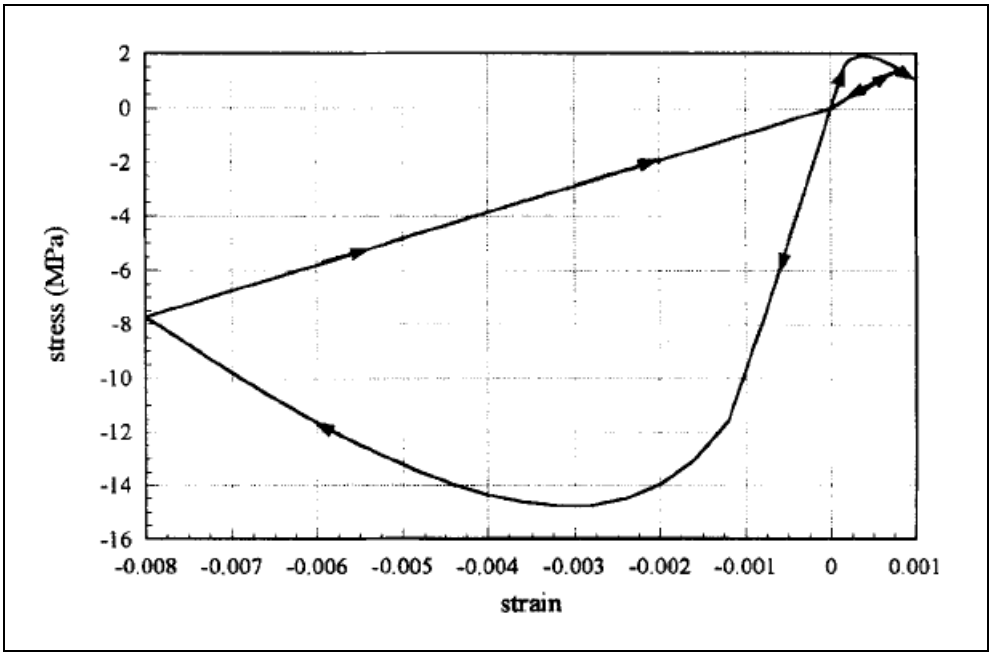

Figure 4.8 Numerical response of a masonry specimen subjected to a tensile-compressive cycle, making use of the unilateral continuum damage model proposed by Papa (1996).

4.2 Formulation of the Model

In this section, a model for the finite element analysis, based on Continuum Damage Mechanics, is presented. Orthotropic behaviour is simulated using the concept of *mapped stress tensor*, firstly introduced by Betten (1981 and 1988) and refined by Oller *et al.* (1995, 1996) afterwards. A one-to-one mapping relationship is established between the behaviour of the real material and that of a fictitious one. The problem is solved in a fictitious space and the results are transported to the real field. Compared to the formulation proposed in Chapter 3, the model proposed herein presents several enhancements, in order to account for different behaviours in tension and compression of masonry.

4.2.1 Definition of the Space Transformation Tensors

In compliance with the procedure exposed in Section 3.2.1, the proposed methodology is based on assuming a real anisotropic space of stresses $\boldsymbol{\sigma}$ and a conjugate space of strains $\boldsymbol{\varepsilon}$, such that each of these spaces has its respective image in a fictitious isotropic space of stresses $\boldsymbol{\sigma}^*$ and strains $\boldsymbol{\varepsilon}^*$, respectively. The relationship between the spaces is defined again by

$$\boldsymbol{\sigma}^* = \mathbf{A}^{\sigma} : \boldsymbol{\sigma} \tag{4.1}$$

$$\boldsymbol{\varepsilon}^* = \mathbf{A}^{\varepsilon} : \boldsymbol{\varepsilon} \tag{4.2}$$

Where $\mathbf{A}^{\sigma}$ and $\mathbf{A}^{\varepsilon}$ are the transformation tensors, for stresses and strains, respectively, relating the fictitious and real spaces. These rank-four tensors embody the natural anisotropic properties of the material (Oller *et al.* 2003).

As discussed before, masonry presents different strengths as well as failure mechanisms and inelastic behaviours in tension and compression. For these reasons, two distinct damage criteria must be introduced both with a constitutive

model able to distinguish tension stress states from compression stress states. An essential feature of the proposed model is that a split into tensile and compressive contributions is introduced. Such a split is carried out on the stress tensor, according to Faria and Oliver (1993), Faria *et al.* (1998, 2000, 2004) and Cervera *et al.* (1995, 1996, 1999, 2003):

$$\boldsymbol{\sigma}^{+} = \sum_{i=1}^{3} \langle \sigma_i \rangle \, \mathbf{p}_i \otimes \mathbf{p}_i \tag{4.3}$$

$$\boldsymbol{\sigma}^{-} = \boldsymbol{\sigma} - \boldsymbol{\sigma}^{+} \tag{4.4}$$

where σ_i denotes the *i*-th principal stress value from tensor $\boldsymbol{\sigma}$ and $\mathbf{p}_i$ represents the unit vector associated with its respective principal direction. The ramp function indicated by the Macaulay brackets $\langle \cdot \rangle$ returns the value of the enclosed expression if positive, but sets a zero value if negative. As in equations (4.3) and (4.4), in the ensuing lines tensile and compressive entities will be pointed out through the using of indices (+) and (-), respectively.

The split shown by equations (4.3) and (4.4) can be expressed in an alternative compact form as follows

$$\boldsymbol{\sigma}^{+} = \mathbf{P} : \boldsymbol{\sigma} \tag{4.5}$$

$$\boldsymbol{\sigma}^{-} = (\mathbf{I} - \mathbf{P}) : \boldsymbol{\sigma} \tag{4.6}$$

where **I** is the rank-four identity tensor and **P** is a projection tensor such that

$$\mathbf{P} = \sum_{i=1}^{3} H(\sigma_i) \mathbf{p}_i \otimes \mathbf{p}_i \tag{4.7}$$

where $H(\sigma_i)$ denotes the Heaviside function computed for the *i*-th principal stress σ_i.

The present model proposes the following transformations of the tensile and compressive stress components from the real to the fictitious space:

$$\boldsymbol{\sigma}^{+*} = \mathbf{A}^{\sigma+} : \boldsymbol{\sigma}^{+} \tag{4.8}$$

$$\boldsymbol{\sigma}^{-*} = \mathbf{A}^{\sigma-} : \boldsymbol{\sigma}^{-} \tag{4.9}$$

Where $\mathbf{A}^{\sigma+}$ and $\mathbf{A}^{\sigma-}$ are the stress transformation tensors, for positive and negative components $\boldsymbol{\sigma}^{+}$ and $\boldsymbol{\sigma}^{-}$, respectively, relating the fictitious and real spaces. Since we assume two distinct stress transformation tensors, it is possible to map the real stresses into the fictitious space and solve the problem there, by adopting two different isotropic damage criteria for tension and compression.

In this work, a diagonal fourth-order tensor is assumed for each transformation tensor, according to Betten (1981), Oller *et al.* (1995, 1996) and Car *et al.* (2000, 2001). The transformation tensors correspond to 6×6 matrices for the 3-dimensional case, according to equation (3.1). In the particular case of in-plane stress conditions, that will be considered in this work, the transformation tensors reduce to 3x3 matrices. The components of each tensor are the ratios of the strengths in the fictitious isotropic space ($f_{ij}^{\pm *}$) and in the real orthotropic space ($f_{ij}^{\pm}$), all referred to the material axes directions. By assuming the Voigt forms (3.2) and (3.3) for the stress and strain vectors, the stress space transformation tensors in the material coordinate system take the forms

$$\left(\mathbf{A}^{\sigma+}\right)' = \begin{bmatrix} \dfrac{f_{11}^{+*}}{f_{11}^{+}} & 0 & 0 \\ 0 & \dfrac{f_{22}^{+*}}{f_{22}^{+}} & 0 \\ 0 & 0 & \dfrac{f_{12}^{+*}}{f_{12}^{+}} \end{bmatrix} \tag{4.10}$$

$$\left(\mathbf{A}^{\sigma-}\right)' = \begin{bmatrix} \dfrac{f_{11}^{-*}}{f_{11}^{-}} & 0 & 0 \\ 0 & \dfrac{f_{22}^{-*}}{f_{22}^{-}} & 0 \\ 0 & 0 & \dfrac{f_{12}^{-*}}{f_{12}^{-}} \end{bmatrix} \tag{4.11}$$

The parameters $f_{ij}^{\pm *}$ represent the intersections of the fictitious damage threshold surfaces with axes 1, 2 and 3. Since we assume two distinct isotropic criteria in the fictitious space, it results that $f_{11}^{+*} = f_{22}^{+*} = f^{+*}$ and $f_{11}^{-*} = f_{22}^{-*} = f^{-*}$. The choices of f^{+*} and f^{-*} are arbitrary. The expressions of the fictitious pure-shear strengths f_{12}^{+*} and f_{12}^{-*} derive from the particular isotropic criteria adopted for tension and compression.

The parameters $f_{ij}^{\pm}$ represent the intersections with axes 1, 2 and 3 of the damage threshold surfaces mapped into the real orthotropic space. This concept will be detailed in Section 4.3.2. The orthotropic real strengths can be obtained from simple experimental tests, which will be also discussed in Section 4.3.2.

The need for two stress transformation tensors to account for different behaviours of the material in tension and compression is evident from definitions (4.10) and (4.11). Most of all, it always results that $\left(\mathbf{A}_{33}^{\sigma+}\right)' \neq \left(\mathbf{A}_{33}^{\sigma-}\right)'$, i.e. $f_{12}^{+*} / f_{12}^{+} \neq f_{12}^{-*} / f_{12}^{-}$. In fact, we generally observe that $f_{12}^{+*} \neq f_{12}^{-*}$, since we assume distinct isotropic damage criteria in tension and compression. Also, the two isotropic fictitious criteria have to be mapped in two distinct ways into the real space, so $f_{12}^{+} \neq f_{12}^{-}$ (see Section 4.3.2). Therefore, a single stress transformation tensor would not lead to the correct masonry shear strength. Moreover, such a

choice would force the ratio between the tensile and compressive strength to be equal along each axis (Pelà *et al.* 2008), whilst in masonry typically $f_x^- / f_x^+ \neq f_y^- / f_y^+$.

The stress space transformation tensors in global coordinates are readily obtainable from the definitions (4.10) and (4.11) of the tensor components in the local principal axes of the orthotropic material. In fact, according to (3.36),

$$\mathbf{A}^{\sigma+} = \mathbf{T}^{-1} \cdot \left(\mathbf{A}^{\sigma+} \right)' \cdot \mathbf{T} \tag{4.12}$$

$$\mathbf{A}^{\sigma-} = \mathbf{T}^{-1} \cdot \left(\mathbf{A}^{\sigma-} \right)' \cdot \mathbf{T} \tag{4.13}$$

where tensor **T** has been defined in (3.24) and is related to the angle θ between the material and global axes. It permits the transformation of stress/strain components from one axes reference system to the other.

It is possible to relate the positive and negative stress transformation tensors to the global stress transformation tensor. In fact, after the definitions (4.1), (4.2), (4.8), and (4.9), the condition

$$\boldsymbol{\sigma}^* = \boldsymbol{\sigma}^{+*} + \boldsymbol{\sigma}^{-*} \tag{4.14}$$

must still apply. Therefore, the previous expression yields

$$\begin{aligned} &\mathbf{A}^{\sigma} : \boldsymbol{\sigma} = \mathbf{A}^{\sigma+} : \boldsymbol{\sigma}^{+} + \mathbf{A}^{\sigma-} : \boldsymbol{\sigma}^{-} \\ &\mathbf{A}^{\sigma} : \boldsymbol{\sigma} = \mathbf{A}^{\sigma+} \cdot \mathbf{P} : \boldsymbol{\sigma} + \mathbf{A}^{\sigma-} \cdot (\mathbf{I} - \mathbf{P}) : \boldsymbol{\sigma} \end{aligned} \tag{4.15a, b}$$

and hence

$$\mathbf{A}^{\sigma} = \mathbf{A}^{\sigma+} \cdot \mathbf{P} + \mathbf{A}^{\sigma-} \cdot (\mathbf{I} - \mathbf{P}) \tag{4.16}$$

The strain space transformation tensor $\mathbf{A}^{\varepsilon}$ defined in (4.2) can be derived analogously to (3.37a, b, c) and results:

$$\mathbf{A}^{\varepsilon} = \left(\mathbf{C}^{*}\right)^{-1} \cdot \mathbf{A}^{\sigma} \cdot \mathbf{C} \tag{4.17}$$

where $\mathbf{C}$ and $\mathbf{C}^{*}$ are the constitutive tensors in the real and fictitious space, respectively. Equation (4.17) also allows us to derive the relationship between the constitutive tensors in the real and fictitious spaces. This is:

$$\mathbf{C} = \left(\mathbf{A}^{\sigma}\right)^{-1} \cdot \mathbf{C}^{*} \cdot \mathbf{A}^{\varepsilon} \tag{4.18}$$

Notice that in the expressions (4.17) and (4.18) the real orthotropic constitutive tensor $\mathbf{C}$ is expressed in the global reference system. This means that prior to the derivation of the space transformation tensors, the transformation (3.28) is required.

4.3 Underlying Fictitious Damage Model

In this section, a detailed description of the continuum damage model adopted in the *fictitious space* is provided. The present work makes use of the *Tension-Compression Damage Model* formulated by Faria and Oliver (1993) which has been extensively used (Faria *et al.* 1998, 2000, 2004; Cervera *et al.* 1995, 1996, 1999, 2003). This model is characterized by two internal scalar variables, which monitor the local damage under tension and compression, respectively. This choice provides a simple constitutive model which, nevertheless, is able to reproduce the overall nonlinear behaviour including unilateral effects, strain-hardening/softening response, stiffness degradation and regradation under multiple stress reversal.

4.3.1 Constitutive Equations

The *Tension-Compression Damage Model* adopted in the fictitious space is based on the concept of the concept of effective stress tensor $\bar{\boldsymbol{\sigma}}$, introduced in connection

with the *hypothesis of strain equivalence* (Lamaitre and Chaboche, 1978). Thus, the following relation is defined in the fictitious space:

$$\bar{\boldsymbol{\sigma}}^{*} = \mathbf{C}^{*} : \boldsymbol{\varepsilon}^{*} \tag{4.19}$$

where **C*** is the usual (fourth-order) isotropic linear-elastic constitutive tensor. In order to account for different behaviours of masonry in tension and compression, the split of the effective stress tensor (Faria *et al.*, 2000) into tensile and compressive components, $\bar{\boldsymbol{\sigma}}^{+*}$ and $\bar{\boldsymbol{\sigma}}^{-*}$, is introduced according to (4.3) and (4.4):

$$\bar{\boldsymbol{\sigma}}^{+*} = \sum_{j=1}^{3} \left\langle \bar{\sigma}_j^{*} \right\rangle \mathbf{p}_j^{*} \otimes \mathbf{p}_j^{*} \tag{4.20}$$

$$\bar{\boldsymbol{\sigma}}^{-*} = \bar{\boldsymbol{\sigma}}^{*} - \bar{\boldsymbol{\sigma}}^{+*} \tag{4.21}$$

where $\bar{\sigma}_j^{*}$ denotes the *j*-th principal stress value from tensor $\bar{\boldsymbol{\sigma}}^{*}$, $\mathbf{p}_j^{*}$ represents the unit vector associated with its respective principal direction and the symbols $\langle \cdot \rangle$ are the Macaulay brackets.

The split shown by equations (4.20) and (4.21) can also be expressed, in compliance with (4.5) and (4.6), in the forms

$$\bar{\boldsymbol{\sigma}}^{+*} = \mathbf{P}^{*} : \bar{\boldsymbol{\sigma}}^{*} \tag{4.22}$$

$$\bar{\boldsymbol{\sigma}}^{-*} = \left(\mathbf{I} - \mathbf{P}^{*} \right) : \bar{\boldsymbol{\sigma}}^{*} \tag{4.23}$$

where **I** is the rank-four identity tensor and $\mathbf{P}^{*}$ is a projection tensor such that

$$\mathbf{P}^{*} = \sum_{j=1}^{3} H\left(\bar{\sigma}_j^{*} \right) \mathbf{p}_j^{*} \otimes \mathbf{p}_j^{*} \tag{4.24}$$

where $H\left(\overline{\sigma}_j^*\right)$ denotes the Heaviside function computed for the *j*-th principal stress $\overline{\sigma}_j^*$.

The constitutive equation for the damage model is defined as

$$\boldsymbol{\sigma}^* = \left(1-d^+\right)\overline{\boldsymbol{\sigma}}^{+*} + \left(1-d^-\right)\overline{\boldsymbol{\sigma}}^{-*} \tag{4.25}$$

where we have introduced two internal variables, d^+ and d^-, the *damage indexes*, each related with the sign of the stress and thus with tension and compression. The internal damage variables are equal to zero when the material is undamaged and equal to one when it is completely damaged. Their definition and evolution are detailed afterwards.

Owing to the scalar form of the damage variables d^+, d^- and to the format of the presented constitutive law, equation (4.25) points out that a split of tensor $\boldsymbol{\sigma}^*$ into tensile and compressive tensors $\boldsymbol{\sigma}^{+*}$ and $\boldsymbol{\sigma}^{-*}$ is implicit in the present formulation, that is,

$$\boldsymbol{\sigma}^{+*} = \left(1-d^+\right)\overline{\boldsymbol{\sigma}}^{+*} \tag{4.26}$$

$$\boldsymbol{\sigma}^{-*} = \left(1-d^-\right)\overline{\boldsymbol{\sigma}}^{-*} \tag{4.27}$$

This relevant property emphasises that the adopted split of the effective stress tensor leads in fact to a related dual split of the Cauchy stress tensor $\boldsymbol{\sigma}^*$.

Although the Tension-Compression Damage Model has been usually termed "isotropic" (Faria and Oliver, 1993; Cervera *et. al.*, 1996; Faria *et al.*, 2000; Cervera, 2003; Wu and Li, 2008), it is possible to demonstrate that the model is definitely *orthotropic*. In fact, by recalling (4.22) and (4.23), (4.25) can be rewritten as follows:

$$\boldsymbol{\sigma}^* = \left(1-d^+\right)\mathbf{P}^* : \overline{\boldsymbol{\sigma}}^* + \left(1-d^-\right)\left(\mathbf{I}-\mathbf{P}^*\right) : \overline{\boldsymbol{\sigma}}^*$$
$$\boldsymbol{\sigma}^* = \left[\left(1-d^+\right)\mathbf{P}^* + \left(1-d^-\right)\left(\mathbf{I}-\mathbf{P}^*\right)\right] : \overline{\boldsymbol{\sigma}}^* \qquad (4.28a, b, c)$$
$$\boldsymbol{\sigma}^* = \left[\mathbf{I} - d^+\mathbf{P}^* - d^-\left(\mathbf{I}-\mathbf{P}^*\right)\right] : \overline{\boldsymbol{\sigma}}^*$$

and therefore the constitutive relationship can assume the form

$$\boldsymbol{\sigma}^* = \left(\mathbf{I}-\mathbf{D}\right) : \overline{\boldsymbol{\sigma}}^* \qquad (4.29)$$

where

$$\mathbf{D} = d^+\mathbf{P}^* + d^-\left(\mathbf{I}-\mathbf{P}^*\right) \qquad (4.30)$$

is the fourth-order tensor which characterizes the state of damage. As can be easily seen, such a tensor is not isotropic and entails directional orthotropic damage. The dependence on principal directions of stress, expressed by tensor $\mathbf{P}^*$, is relevant since we have assumed the microcracks and microvoids to growth in different manners under tensile or compressive stress states. If $\mathbf{P}^* = \mathbf{I}$, a tensile isotropic damage model is recovered, while if $\mathbf{P}^*$ is a zero tensor, we recover a compressive isotropic damage model.

Equation (4.30) has a structure similar to (4.16), used to define the global stress transformation tensor, thus a crucial relationship is emphasized. In fact, the stress transformation in the form (4.16) has been hypothesized in order to be consistent with the constitutive law to be adopted in the fictitious space.

An important remark concerns the distinctive characteristic of the fictitious space adopted in the proposed Two-Parameters Damage Model for Orthotropic Materials. The concept of mapping a real *anisotropic* space into a fictitious *isotropic* one, exhaustively discussed in Chapter 3, is not feasible in the presented new framework. In fact, in this particular case the fictitious space cannot be termed “isotropic”, since we assume an orthotropic damage constitutive law and also a

composite damage criterion. Therefore, the present methodology turns the original concept of "mapping the real space into an *isotropic* fictitious one" into the innovative and more general one of "mapping the real space into a *favourable* (or *convenient*) fictitious one".

4.3.2 Damage Threshold Surfaces in the Fictitious Space

Analogously to the concept of *equivalent strain* postulated by Simó and Ju (1987), the dual concept of *equivalent stress* is introduced, according to Faria and Oliver (1993), Faria *et al.* (1998, 2000, 2004) and Cervera *et al.* (1995, 1996, 1999, 2003). Such a scalar positive norm allows identifying loading, unloading or reloading situations. Since a clear distinction between tension and compression is assumed by means of the stress split defined in (4.20) and (4.21), a tensile equivalent stress τ^{+*} and a compressive equivalent stress τ^{-*} are postulated.

Individual criteria for tension and compression have to be considered in the fictitious space, in order to describe different failure mechanisms for masonry. The first criterion is associated with a localised fracture process, namely cracking of the material, and the second criterion is associated with a more distributed fracture process, viz. crushing of the material. The two damage criteria Φ^{+*} and Φ^{-*} are defined as follows

$$\Phi^{+*}\left(\tau^{+*}, r^{+*}\right) = \tau^{+*} - r^{+*} \leq 0 \tag{4.31}$$

$$\Phi^{-*}\left(\tau^{-*}, r^{-*}\right) = \tau^{-*} - r^{-*} \leq 0 \tag{4.32}$$

Variables r^{+*} and r^{-*} are the internal stress-like variables representing the current damage thresholds in tension and compression. Their values control the size of each (monotonically) expanding damage surface. Notice that the damage criteria are defined in terms of effective stresses. This strategy preserves the advantages of

a strain-driven formulation, since the effective stress tensor is itself a strain-based entity, and circumvents the drawbacks inherent to those formulations based on the final Cauchy stress tensor, which require an iterative procedure inside the constitutive model (for more details, see Faria *et al.* 2000).

The expansion of the damage bounding surfaces for loading, unloading and reloading conditions is controlled by the Kuhn–Tucker relations and the damage consistency conditions, which are

$$\begin{aligned} &\dot{r}^{\pm *} \geq 0 \quad \Phi^{\pm *}\left(\tau^{\pm *}, r^{\pm *}\right) \leq 0 \quad \dot{r}^{\pm *} \cdot \Phi^{\pm *}\left(\tau^{\pm *}, r^{\pm *}\right) = 0, \\ &\textit{if} \quad \Phi^{\pm *}\left(\tau^{\pm *}, r^{\pm *}\right) = 0 \quad \textit{then} \quad \dot{r}^{\pm *} \cdot \dot{\Phi}^{\pm *}\left(\tau^{\pm *}, r^{\pm *}\right) = 0 \end{aligned} \tag{4.33a, b}$$

leading, in view of (4.31) and (4.32), to the loading conditions

$$\dot{\tau}^{\pm *} = \dot{r}^{\pm *} \tag{4.34}$$

These, in turn, lead to the explicit definition of the current values of the internal variables $r^{\pm *}$ in the form

$$r^{\pm *} = \max\left[r_0^{\pm *}, \max\left(\tau^{\pm *}\right)\right] \tag{4.35}$$

where $r_0^{\pm *} = r_0^{\pm *}\left(f^{\pm *}\right)$ are the initial values of the damage thresholds and $f^{\pm *}$ are the initial uniaxial damage stresses.

Notice that Eq. (4.35) allows one to compute the current values for r^{+*} and r^{-*} in terms of the current values of τ^{+*} and τ^{-*}, respectively, which depend explicitly on the current total strains.

In the present work, the Rankine criterion is assumed in the fictitious isotropic space for tensile stress states. Therefore, the tensile equivalent stress is defined as

$$\tau^{+*} = \left\langle \bar{\sigma}_1^* \right\rangle \tag{4.36}$$

Where $\overline{\sigma}_1^*$ is the largest principal effective stress and the symbols $\langle\cdot\rangle$ are the Macaulay brackets. The initial value of the damage threshold is

$$r_0^{+*} = f^{+*} \tag{4.37}$$

where f^{+*} is the initial uniaxial damage stress.

Expression (4.36) represents the equation of a three-dimensional surface defined in the coordinates system denoted by axes σ_x^*, σ_y^*, τ_{xy}^*, see Figure 4.9.

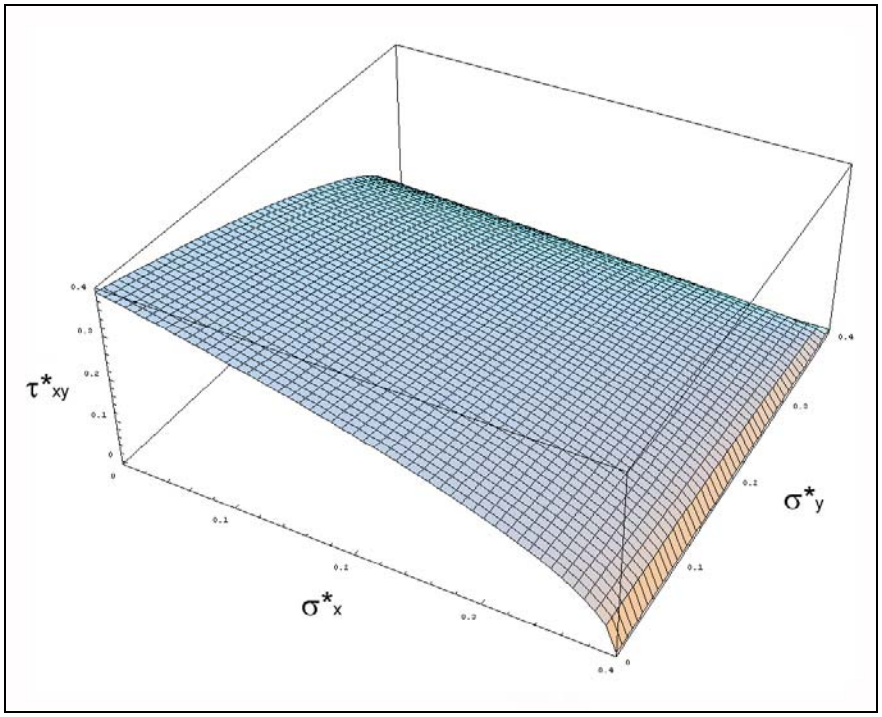

Figure 4.9 Rankine damage threshold in the fictitious space.

For compressive stress states, the criterion proposed by Faria *et al.* (1998, 2000) is assumed. In this case, the equivalent stress is defined in the following form:

$$\tau^{-*} = \sqrt{3}\left(K\bar{\sigma}_{oct}^{-*} + \bar{\tau}_{oct}^{-*}\right) \tag{4.38}$$

In this format, directly inspired on the Drucker-Prager criterion, $\bar{\sigma}_{oct}^{-*}$ and $\bar{\tau}_{oct}^{-*}$ are the octahedral normal stress and the octahedral shear stress obtained from $\bar{\sigma}^{-*}$. Constant *K* controls the aperture of the inherent Drucker-Prager cone. According to (4.35) and (4.38), the initial value of the damage threshold is equal to

$$r_0^{-*} = \frac{\sqrt{3}}{3}\left(K - \sqrt{2}\right) f^{-*} \tag{4.39}$$

Expression (4.38) represents the equation of a three-dimensional surface defined in the coordinates system denoted by axes σ_x^*, σ_y^*, τ_{xy}^*, see Figure 4.10.

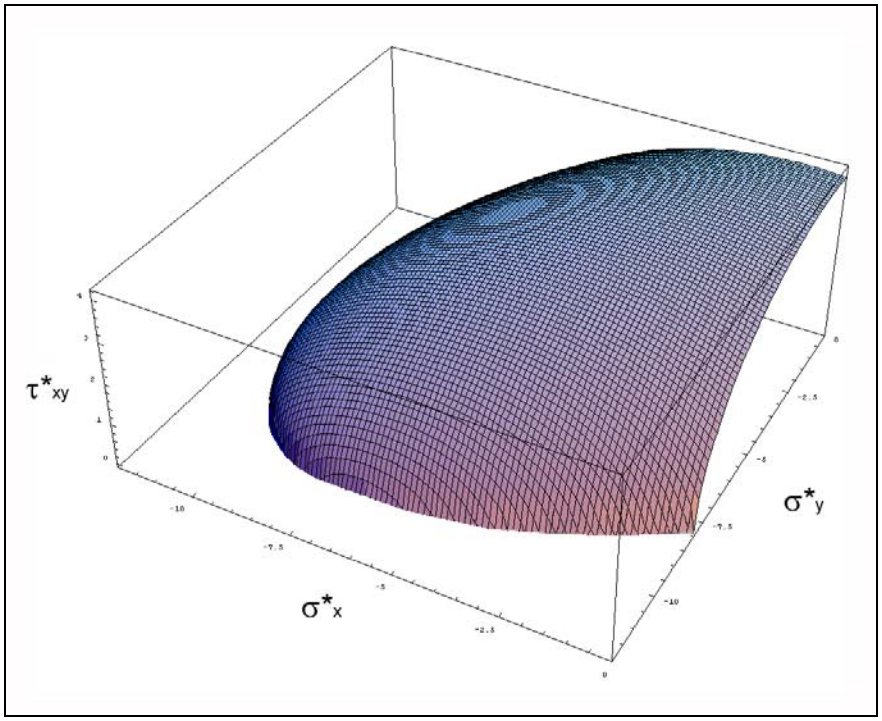

Figure 4.10 Faria damage threshold in the fictitious space.

4.3.3 Evolution of the Damage Variables. Inelastic Behaviour

The damage indexes $d^+ = d^+\left(r^{+*}\right)$ and $d^- = d^-\left(r^{-*}\right)$ are explicitly defined in terms of the corresponding current values of the damage thresholds, so that they are monotonically increasing functions such that $0 \le d^{\pm} \le 1$. In the present work, the damage variables are computed according to the laws proposed by Cervera *et al.* (1999) and Cervera (2003). In tension, the softening law takes the exponential form

$$d^+\left(r^{+*}\right) = 1 - \frac{r_0^{+*}}{r^{+*}} \exp\left\{2H_d^+\left(\frac{r_0^{+*} - r^{+*}}{r_0^{+*}}\right)\right\} \tag{4.40}$$

where constant $H_d^+ \ge 0$ is defined as

$$H_d^+ = \frac{\bar{H}_d^+ \, l_{ch}}{1 - \bar{H}_d^+ \, l_{ch}} \tag{4.41}$$

where

$$\bar{H}_d^+ = \frac{\left(f^{+*}\right)^2}{2E^* G_f^{+*}} = \frac{1}{L^+} \tag{4.42}$$

The term $\bar{H}_d^+$ depends only on material properties in the fictitious space, i.e. the uniaxial tensile damage threshold f^{+*}, the Young's modulus E^* and the tensile mode I fracture energy per unit area G_f^{+*}. It measures the brittleness of the material in tension and it can be also termed $1/L^+$, since the unit of the $\bar{H}_d^+$ parameter is the inverse of a length.

In Eq. (4.41), the characteristic length l_{ch} of the element has been introduced to ensure mesh-size objective results, according to Bazant and Oh (1983). The

element characteristic length is the computational width of the fracture zone (Rots *et al.* 1985, Rots and Blaauwendraad 1989, Oliver 1989); it is computed depending on the geometric dimensions of the element. The specific dissipated energy D^{+*} is then scaled for each element so that the equation

$$D^{+*} l_{ch} = G_f^{+*} \tag{4.43}$$

holds. This makes the tensile softening modulus H_d^+, which defines the softening response, dependent on the element size. It also sets a maximum size for the elements that can be used in the analysis.

The expression (4.41) has been obtained by calculating the specific energy dissipated in an ideal uniaxial experiment in which the tensile strain increases monotonically and quasi-statically from an initial unstressed state to another in which full degradation takes place. In fact, from Equations (4.19), (4.20), (4.35) and (4.36) it derives that

$$\begin{aligned} D^{+*} &= \int_{t=0}^{t=\infty} \dot{D}^{+*} dt \\ &= \int_{t=0}^{t=\infty} \psi_0^{+*} \dot{d}^{+} \, dt \\ &= \frac{1}{2E^*} \int_{r^{+*}=r_0^{+*}}^{r^{+*}=\infty} \left(r^{+*}\right)^2 \left(d^{+}\right)' \, dr^{+*} \end{aligned} \tag{4.44a, b, c}$$

where $\psi_0^{+*} = 1/2\, \overline{\boldsymbol{\sigma}}^{+*} : \boldsymbol{\varepsilon}^* \geq 0$ is the positive part of the elastic free energy potential (see Chapter 2), and the rate of damage has been expressed as $\dot{d}^{+} = \left(d^{+}\right)' \dot{r}^{+*}$. Using Equation (4.40), integrating and equating $D^{+*} = G_f^{+*} \big/ l_{ch}$, we finally obtain

expression (4.41). For further details on calculations, the reader is referred to Cervera (2003).

On the basis of the aforementioned considerations, it is evident that the *specific softening parameter* $\bar{H}_d^+$ measures the brittleness of the material in tension, while the *elemental softening parameter* H_d^+ measures the brittleness of the finite element in tension.

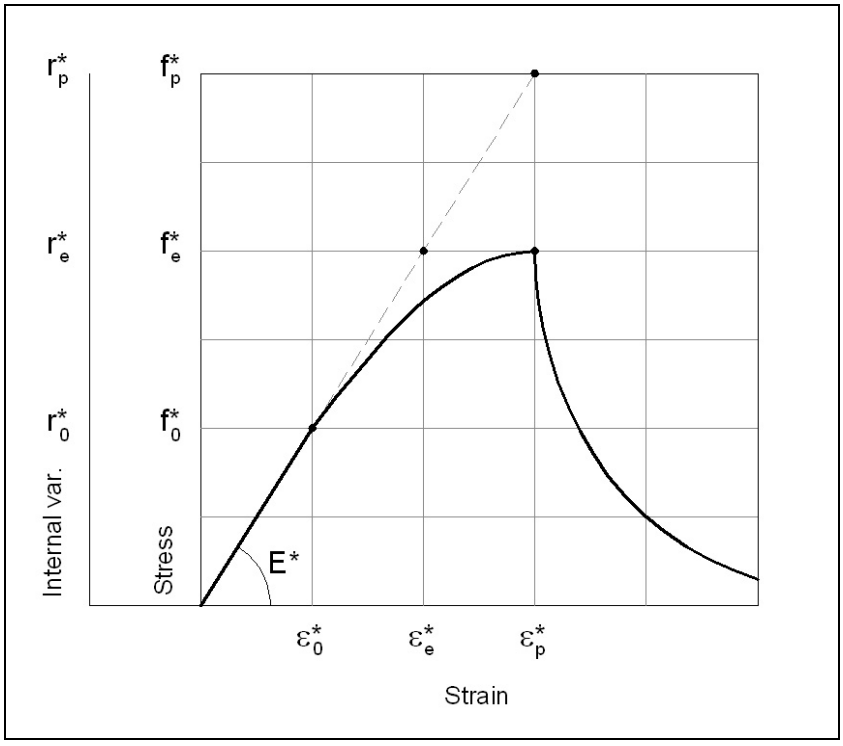

Figure 4.11 Uniaxial stress-strain curve. Parabolic hardening and exponential softening.

A different law is considered for damage variable d^-, in order to represent the peculiar compressive inelastic behaviour of masonry. Let us consider the uniaxial stress-strain curve reported in Figure 4.11. Let us introduce the value r_0^{-*}, establishing the size of the bounding damage surface for the onset of damage,

according to (4.35) and (4.39). Then, we assume the value r_e^{-*} corresponding to the peak value of the uniaxial strength f_e^{-*} and the value $r_p^{-*} \geq r_e^{-*}$ corresponding to the size of the bounding damage surface at peak strength. These values define the hardening part of the compressive uniaxial stress-strain curve for masonry. Notice that $r_p^{-*} \geq r_e^{-*} \geq r_0^{-*}$. For parabolic hardening we assume

$$d^- \left(r^{-*} \right) = A_d \frac{r_e^{-*}}{r^{-*}} \left(\frac{r^{-*} - 1}{r_p^{-*} - 1} \right)^2 \qquad r_0^{-*} \leq r^{-*} \leq r_p^{-*} \tag{4.45}$$

while for the consequent exponential softening

$$d^- \left(r^{-*} \right) = 1 - \frac{r_e^{-*}}{r^{-*}} \exp\left\{ 2H_d^- \left(\frac{r_p^{-*} - r^{-*}}{r_e^{-*}} \right) \right\} \qquad r^{-*} \geq r_p^{-*} \tag{4.46}$$

where constants A_d, $H_d^- \geq 0$ are defined as

$$A_d = \frac{r_p^{-*} - r_e^{-*}}{r_e^{-*}} \tag{4.47}$$

$$H_d^- = \frac{\bar{H}_d^- l_{ch}}{1 - \dfrac{r_p^{-*}}{r_e^{-*}} \bar{H}_d^- l_{ch} - 2\bar{A}_d \bar{H}_d^- l_{ch}} \tag{4.48}$$

where

$$\bar{A}_d = A_d \left[\left(r_p^{-*} \right)^3 - 3r_p^{-*} + 2 \right] \Big/ \left[6r_e^{-*} \left(r_p^{-*} - 1 \right)^2 \right] \tag{4.49}$$

$$\bar{H}_d^- = \frac{\left(f^{-*} \right)^2}{2E^* G_f^{-*}} = \frac{1}{L^-} \tag{4.50}$$

As can be seen, also in compression the softening modulus is regularized according to the material fracture energy and the element size, in order to ensure mesh-size objective results. Therefore, the specific dissipated energy D^{-*} is scaled for each element so that the equation

$$D^{-*} l_{ch} = G_f^{-*} \tag{4.51}$$

holds.

The expression (4.48) has been obtained by calculating the specific energy dissipated in an ideal uniaxial experiment in which the compressive strain increases monotonically and quasi-statically from an initial unstressed state to another in which full degradation takes place. In fact, from Equations (4.19), (4.20), (4.35), (4.36), (4.38), (4.45) and (4.46) it derives that

$$\begin{aligned} D^{-*} &= \int_{t=0}^{t=\infty} \dot{D}^{-*} dt \\ &= \int_{t=0}^{t=\infty} \psi_0^{-*} \dot{d}^{-} dt \\ &= \frac{1}{2E^*} \int_{r^{-*}=r_0^{-*}}^{r^{-*}=\infty} \left(r^{-*}\right)^2 \left(d^{-}\right)' dr^{-*} \\ &= \frac{1}{2E^*} \int_{r^{-*}=r_0^{-*}}^{r^{-*}=r_p^{-*}} \left(r^{-*}\right)^2 \left(d^{-}\right)' dr^{-*} + \frac{1}{2E^*} \int_{r^{-*}=r_p^{-*}}^{r^{-*}=\infty} \left(r^{-*}\right)^2 \left(d^{-}\right)' dr^{-*} \end{aligned} \tag{4.52a, b, c, d}$$

where $\psi_0^{-*} = 1/2\, \bar{\boldsymbol{\sigma}}^{-*} : \boldsymbol{\varepsilon}^* \geq 0$ is the negative part of the elastic free energy potential (see Chapter 2) and the rate of damage has been expressed as $\dot{d}^{-} = \left(d^{-}\right)' \dot{r}^{-*}$. Using Equations (4.45) and (4.46), integrating and equating $D^{-*} = G_f^{-*} / l_{ch}$, we

finally obtain expression (4.48). For further details on calculations, the reader is referred to Cervera (2003).

On the basis of the aforementioned considerations, it is evident that the *specific softening parameter* $\bar{H}_d^-$ measures the brittleness of the material in compression, while the *elemental softening parameter* H_d^- measures the brittleness of the finite element in compression.

4.3.4 Tangent and Secant Operators

Differentiating the constitutive law (4.25) with respect to time, we obtain in the fictitious space

$$\dot{\boldsymbol{\sigma}}^* = \left(1-d^+\right)\dot{\bar{\boldsymbol{\sigma}}}^{+*} + \left(1-d^-\right)\dot{\bar{\boldsymbol{\sigma}}}^{-*} - \dot{d}^+\bar{\boldsymbol{\sigma}}^{+*} - \dot{d}^-\bar{\boldsymbol{\sigma}}^{-*} \tag{4.53}$$

Despite the simplicity of the stress split postulated in (4.20), which expresses $\bar{\boldsymbol{\sigma}}^{\pm *}$ as functions of the eigenvalues and eigenvectors of $\bar{\boldsymbol{\sigma}}^*$, quite more complex operations are required to express $\dot{\bar{\boldsymbol{\sigma}}}^{+*}$ as a function of $\dot{\bar{\boldsymbol{\sigma}}}^*$. It can be shown that the appropriate expressions are (Faria *et al.* 2000)

$$\dot{\bar{\boldsymbol{\sigma}}}^{+*} = \mathbf{Q}^* : \dot{\bar{\boldsymbol{\sigma}}}^* = \mathbf{Q}^* : \mathbf{C}^* : \dot{\boldsymbol{\varepsilon}}^* \tag{4.54}$$

$$\dot{\bar{\boldsymbol{\sigma}}}^{-*} = \left(\mathbf{I}-\mathbf{Q}^*\right) : \dot{\bar{\boldsymbol{\sigma}}}^* = \left(\mathbf{I}-\mathbf{Q}^*\right) : \mathbf{C}^* : \dot{\boldsymbol{\varepsilon}}^* \tag{4.55}$$

where the projection operator is

$$\mathbf{Q}^* = \sum_{i=1}^{3} H\left(\bar{\sigma}_i^*\right)\mathbf{P}_{ii}^* \otimes \mathbf{P}_{ii}^* + 2\sum_{\substack{i,j=1 \\ j\neq i}}^{3} \frac{\left\langle \bar{\sigma}_i^* \right\rangle - \left\langle \bar{\sigma}_j^* \right\rangle}{\bar{\sigma}_i^* - \bar{\sigma}_j^*} \mathbf{P}_{ij}^* \otimes \mathbf{P}_{ij}^* \tag{4.56}$$

where $H\left(\bar{\sigma}_i^*\right)$ denotes the Heaviside function computed for the *i*-th principal stress $\bar{\sigma}_i^*$, $\langle\cdot\rangle$ are the Macaulay brackets and

$$\mathbf{P}_{ij}^* = \mathbf{P}_{ji}^* = \frac{1}{2}\left(\mathbf{p}_i^* \otimes \mathbf{p}_j^* + \mathbf{p}_j^* \otimes \mathbf{p}_i^*\right) = symm\left(\mathbf{p}_i^* \otimes \mathbf{p}_j^*\right) \tag{4.57}$$

On the other hand, the rate of the damage index can be expressed as

$$\dot{d}^{\pm} = \left(d^{\pm}\right)' \dot{r}^{\pm *} \tag{4.58}$$

where the first derivative term can be obtained from (4.40), (4.45) or (4.46). On loading, consistency requires (4.34), and therefore, it is necessary to differentiate (4.36) or (4.38) to derive the second term. On unloading, it is $\dot{r}^{\pm *} = 0$. Substituting (4.58) in (4.53), we finally obtain the desired expression

$$\dot{\boldsymbol{\sigma}}^* = \mathbf{C}^{\tan *} : \dot{\boldsymbol{\varepsilon}}^* \tag{4.59}$$

At the cost of the loss of rate of convergence, the tangent matrix can be replaced with the secant matrix, computed with the secant constitutive tensor

$$\mathbf{C}^{\sec *} = \left[\left(1-d^+\right)\mathbf{Q}^* + \left(1-d^-\right)\left(\mathbf{I}-\mathbf{Q}^*\right)\right] : \mathbf{C}^* \tag{4.60}$$

which is much simpler to compute.

Tangent and secant constitutive operators for the real orthotropic material are obtained in compliance with (4.18).

4.4 Damage in the Real Orthotropic Space

4.4.1 Damage Threshold Surfaces in the Real Orthotropic Space

In Section 4.3.2 we have presented the two isotropic damage criteria to be assumed in the fictitious space. The expressions (4.36) and (4.38) represent the equations of

two three-dimensional surfaces defined in the coordinates system denoted by axes $\sigma_x^*,\ \sigma_y^*,\ \tau_{xy}^*$.

Transformations of stresses (4.8) and (4.9) allow one to scale in distinct manners the two isotropic damage threshold surfaces assumed in the fictitious space. By means of such a mapping operation, shown in Figures 4.12 and 4.13, the desired real orthotropic criteria are reproduced in the coordinate system denoted by axes $\sigma_x,\ \sigma_y,\ \tau_{xy}$. The corresponding orthotropic composite damage threshold surface is reported in Figure 4.14.

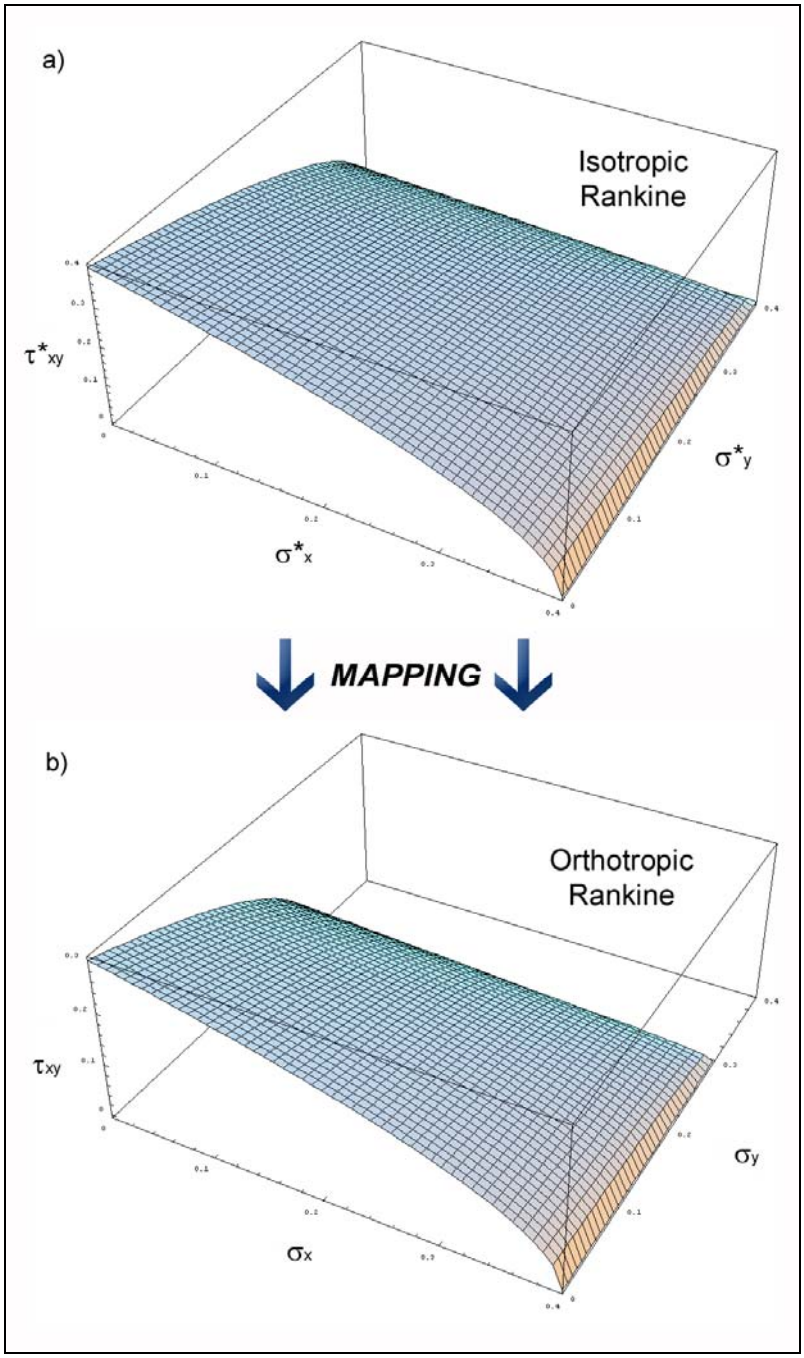

Figure 4.12 Rankine criterion in the fictitious space (a) and in the real space (b).

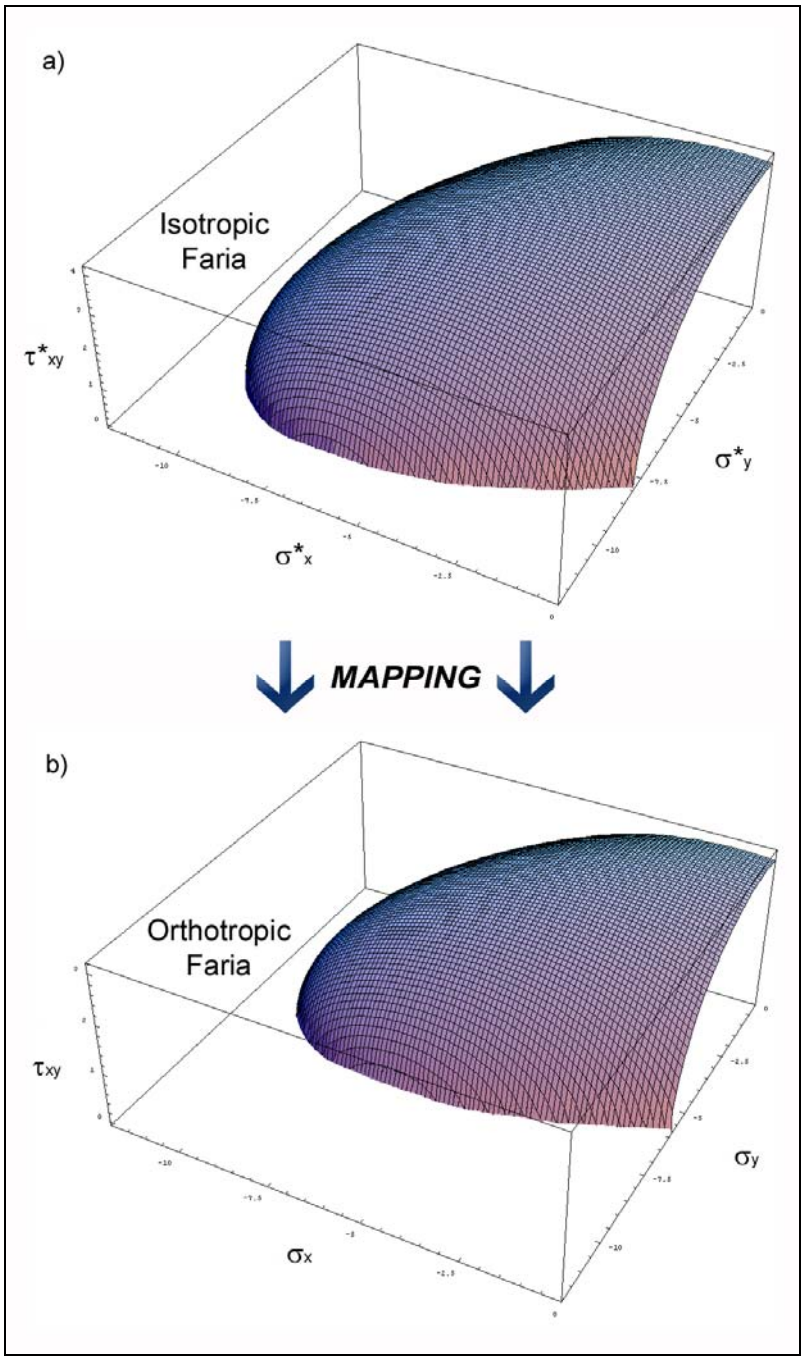

Figure 4.13 Faria criterion in the fictitious space (a) and in the real space (b).

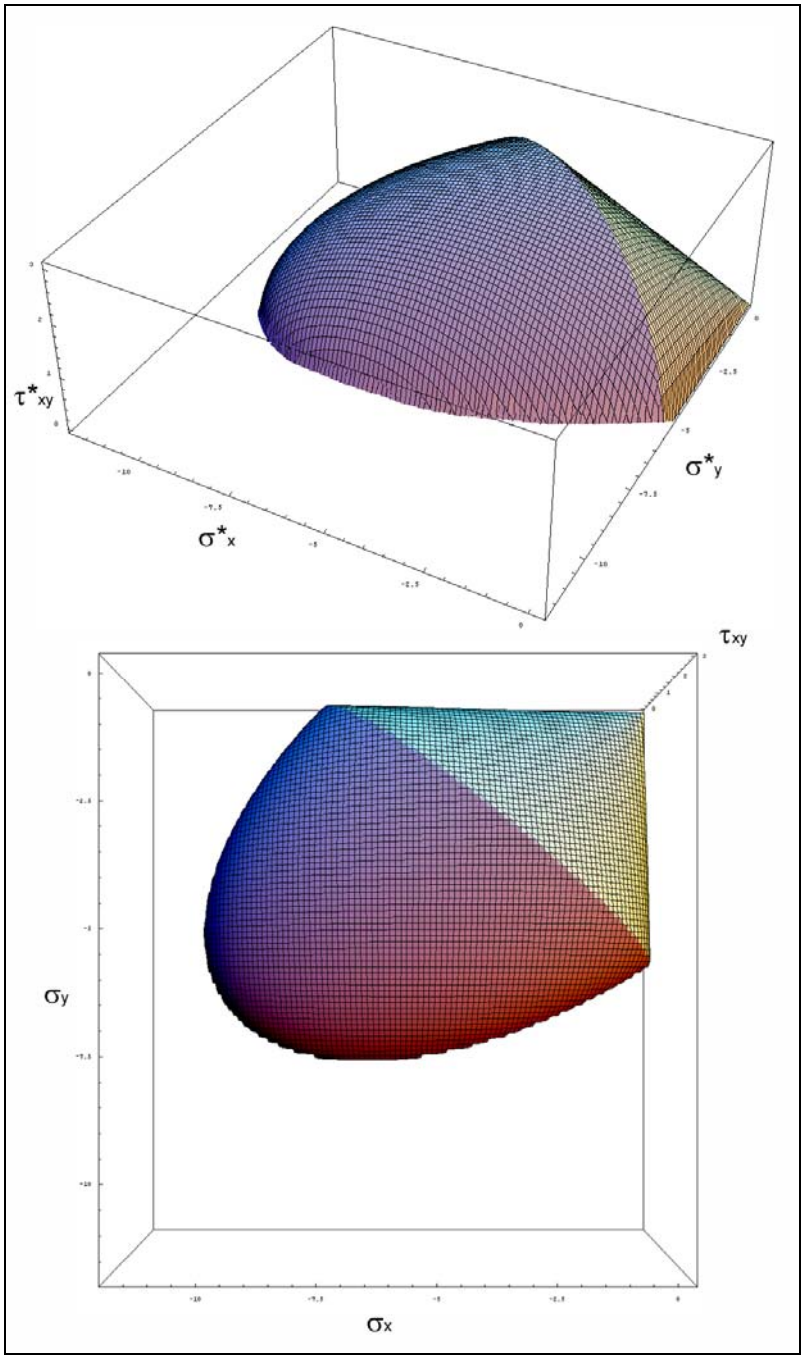

Figure 4.14 Orthotropic composite damage threshold surface.

Owing to the choices of the Rankine and Faria criteria in the fictitious isotropic space, the stress transformation tensors, which have been defined in (4.10) and (4.11), take the specific forms

$$\left(\mathbf{A}^{\sigma+}\right)' = \begin{bmatrix} \dfrac{f^{+*}}{f_{11}^{+}} & 0 & 0 \\ 0 & \dfrac{f^{+*}}{f_{22}^{+}} & 0 \\ 0 & 0 & \dfrac{f^{+*}}{f_{12}^{+}} \end{bmatrix} \tag{4.61}$$

$$\left(\mathbf{A}^{\sigma-}\right)' = \begin{bmatrix} \dfrac{f^{-*}}{f_{11}^{-}} & 0 & 0 \\ 0 & \dfrac{f^{-*}}{f_{22}^{-}} & 0 \\ 0 & 0 & \dfrac{f^{-*}\left(\sqrt{2}-K\right)\Big/\sqrt{6}}{f_{12}^{-}} \end{bmatrix} \tag{4.62}$$

The choices of f^{+*} and f^{-*} are arbitrary. It is advisable to assume $f^{+*} = f_{11}^{+}$ and $f^{-*} = f_{11}^{-}$, in order to obtain $\left(\mathbf{A}_{11}^{\sigma+}\right)' = \left(\mathbf{A}_{11}^{\sigma-}\right)' = 1$. Such an assumption leads to scale the isotropic criteria only along the 2- and 3-axes, see Figures 4.9 and 4.10. It is evident that the transformation of space is feasible only if we know all the six parameters $f_{11}^{+}, f_{11}^{-}, f_{22}^{+}, f_{22}^{-}, f_{12}^{+}, f_{12}^{-}$, i.e. the strengths of the real orthotropic material. Such parameters also represent the intersections of the real damage threshold surfaces with axes 1, 2 and 3, see Figure 4.15.

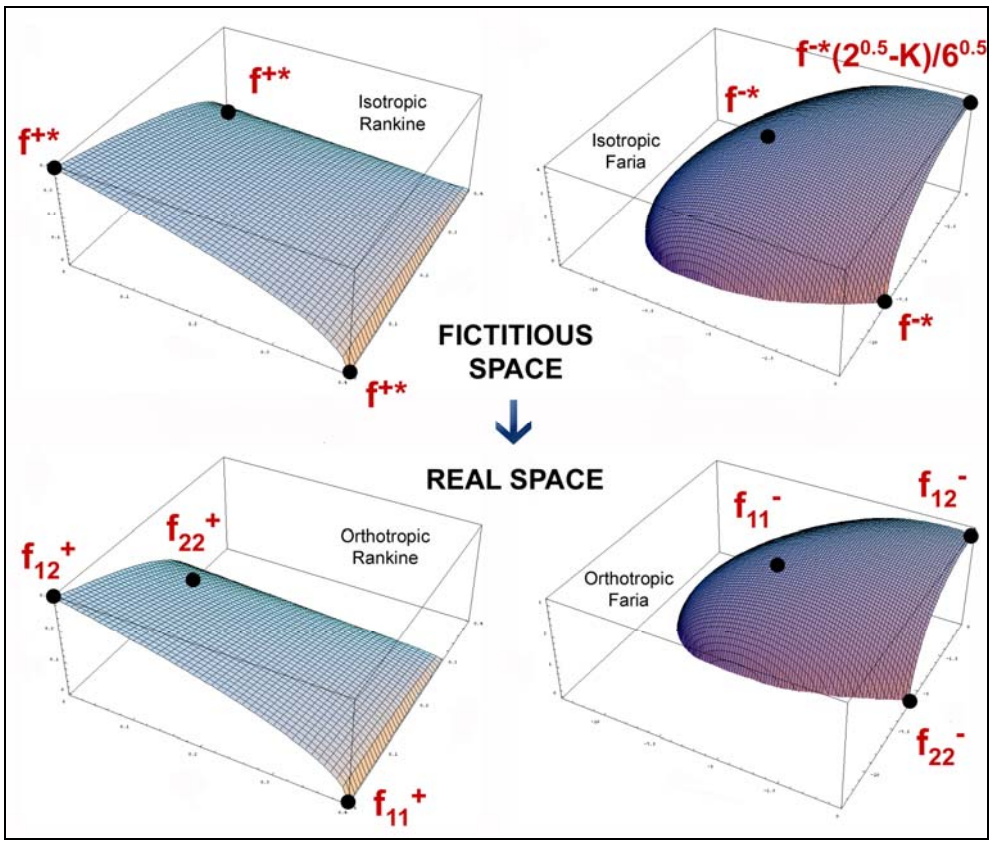

Figure 4.15 Damage surfaces intersections with the axes, in the fictitious isotropic space (a) and in the real orthotropic space (b).

The first group of four strength parameters (f_{11}^{+}, f_{11}^{-}, f_{22}^{+}, f_{22}^{-}) are the uniaxial tensile and compressive strengths along the material axes, which are natural in view of the orthotropic behaviour of masonry. They can be estimated by means of the experimental tests shown in Figure 4.16. It suffices that these tests are performed under displacement control conditions to obtain also the inelastic parameters that define the model, viz. the four independent fracture energies (tension and compression) and the peak strain in compression.

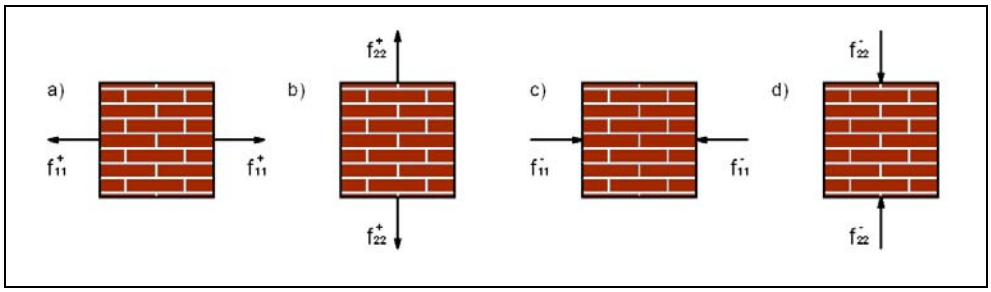

Figure 4.16 Natural tests used to define the transformation of space. Uniaxial tension: parallel to bed joints (a) and normal to bed joints (b). Uniaxial compression: parallel to bed joints (c) and normal to bed joints (d).

Three additional tests are necessary to fully define the space transformation. They are nonstandard and were proposed by Lourenco *et al.* (1998). The first one (Figure 4.17a) controls the coupling between normal stress values in the case of compressive failure and permits to estimate the parameter *K* termed in (4.38). The second test (Figure 4.17b) weights the shear stress contribution to compressive failure and permits to evaluate the f_{12}^{-} parameter. The third test (Figure 4.17c) weights the shear stress contribution to tensile failure and permits to evaluate the f_{12}^{+} parameter.

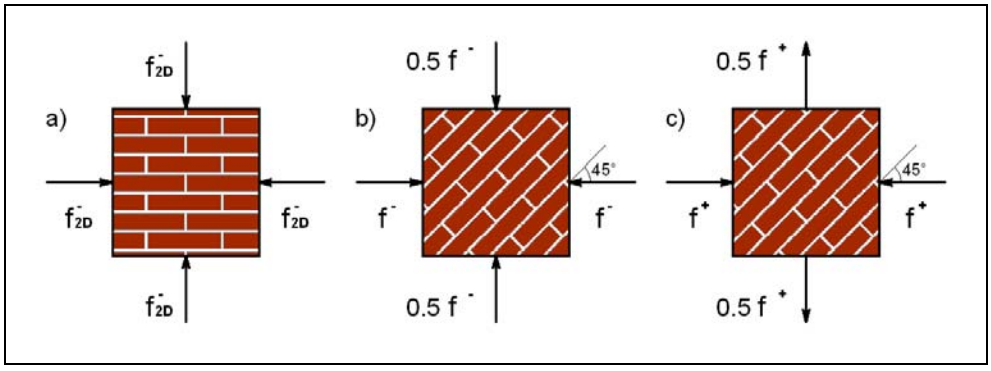

Figure 4.17 Nonstandard tests used to calibrate the parameters: *K* (a), f_{12}^{-} (b) and f_{12}^{+} (c).

4.4.2 Orthotropic Softening Behaviour

It is important to note that in (4.40)-(4.42) and (4.45)-(4.50) there are terms without the apex (*) we have assigned to variables related to the fictitious isotropic space. In fact, such variables as $d^{\pm}$, $H_d^{\pm}$ and $\bar{H}_d^{\pm}$ can be assumed equal in both the spaces, if we want the material brittleness to be the same, in tension or compression, in all directions. In this particular case it results that

$$\frac{\left(f_{11}^{\pm}\right)^2}{2E_1G_{f,1}^{\pm}}=\frac{\left(f_{22}^{\pm}\right)^2}{2E_2G_{f,2}^{\pm}}=\frac{\left(f^{\pm *}\right)^2}{2E^*G_f^{\pm *}} \quad \Rightarrow \quad \frac{1}{L_1^{\pm}}=\frac{1}{L_2^{\pm}}=\frac{1}{L^{\pm *}} \tag{4.63}$$

This assumption leads to the same elemental softening parameters, for tension and compression, in the fictitious and real spaces. Since conventionally we assume $f^{\pm *}=f_{11}^{\pm}, E^*=E_1, G_f^{\pm *}=G_{f,1}^{\pm}$, as discussed in Section 3.2.3, it follows that

$$G_{f,2}^{\pm}=\frac{\left(f_{22}^{\pm}/f_{11}^{\pm}\right)^2}{E_2/E_1}G_{f,1}^{\pm} \tag{4.64}$$

i.e., a restriction on the fracture energy values, in order to ensure isotropic brittleness in tension or compression.

In Chapter 3, the possibility of including the material softening orthotropy has been discussed. The same concept is generalized herein for the Tension-Compression Damage Model. In the same way, we assume two different elemental softening parameters along the material axes, for tension and for compression. Consequently, two opportune specific softening parameters $\bar{H}_d^{\pm *}$ (or $1/L^{\pm *}$) are chosen in the fictitious space. In practice, in the present work the following properties are chosen in the fictitious space:

$$f^{\pm *} = f_{11}^{\pm}$$
$$E^{*} = E_1 \qquad (4.65a, b, c)$$
$$G_f^{\pm *} = \frac{\left(f^{\pm *}\right)^2}{2E^{\pm *}} L^{\pm *}$$

and the following expressions are adopted for L^{+*} and L^{-*}:

$$L^{+*} = L_1^{+} \cos^2\left(\alpha - \theta\right) + L_2^{+} \sin^2\left(\alpha - \theta\right) \qquad (4.66)$$

$$L^{-*} = L_1^{-} \sin^2\left(\alpha - \theta\right) + L_2^{-} \cos^2\left(\alpha - \theta\right) \qquad (4.67)$$

in which $L_1^{+} = 2E_1 G_{f,1}^{+} \Big/ \left(f_{11}^{+}\right)^2$, $L_2^{+} = 2E_2 G_{f,2}^{+} \Big/ \left(f_{22}^{+}\right)^2$, α is the angle denoting the direction of the maximum main stress and θ is the angle of orthotropy. Both the angles are measured counter clockwise from the global *x*-axis to the material 1-axis.

Such an assumption permits to account for totally different fracture energies along the material axes, hence a full orthotropic softening behaviour.

4.5 Numerical Implementation of the Proposed Model

The steps for implementing the Two-Parameters Damage Model for orthotropic materials into the framework of standard non-linear finite element programs (Simó and Hughes, 1998; Crisfield, 1991) are given in the following Table 4.1.

The proposed model adopts a strain-driven formalism consistent with standard displacement-based finite element codes. This feature provides high algorithmic efficiency, which is of primary importance when analyses of even large scale masonry structures are carried out.

Table 4.1 Algorithm used for the proposed model

START

- LOAD INCREMENTAL LOOP: n = 1, NINCR
  - EQUILIBRIUM ITERATION LOOP: i = 1, NITER

    IF ($n>1 \quad or \quad i>1$) GOTO 2

    1) Define strengths, constitutive tensors and rotation tensors

    f_{11}^{+} , f_{22}^{+} , f_{12}^{+} , f_{11}^{+*} , f_{22}^{+*} , f_{12}^{+*}

    f_{11}^{-} , f_{22}^{-} , f_{12}^{-} , f_{11}^{-*} , f_{22}^{-*} , f_{12}^{-*}

    $\mathbf{C}'$, $\mathbf{C}^{*}$, $\mathbf{T}$

    $\mathbf{C}=\mathbf{T}^{-1}\cdot\mathbf{C}'\cdot\mathbf{T}^{-T}$

    2) Calculate the transformation tensors:

    $\left(\mathbf{A}^{\sigma+}\right)',\left(\mathbf{A}^{\sigma-}\right)'$

    $\mathbf{A}^{\sigma\pm}=\mathbf{T}^{-1}\cdot\left(\mathbf{A}^{\sigma\pm}\right)'\cdot\mathbf{T}$

    $\left(\mathbf{A}^{\sigma}\right)^{i-1}=\mathbf{A}^{\sigma+}\cdot\mathbf{P}^{i-1}+\mathbf{A}^{\sigma-}\cdot(\mathbf{I}-\mathbf{P}^{i-1})$

    $\left(\mathbf{A}^{\varepsilon}\right)^{i-1}=\left(\mathbf{C}^{*}\right)^{-1}\cdot\left(\mathbf{A}^{\sigma}\right)^{i-1}\cdot\mathbf{C}$

    3) Compute tangent stiffness:

    ${}^{n}\left(\mathbf{C}^{\tan}\right)^{i-1}=\left[\left(\mathbf{A}^{\sigma}\right)^{i-1}\right]^{-1}\cdot{}^{n}\left(\mathbf{C}^{\tan *}\right)^{i-1}\cdot\left(\mathbf{A}^{\varepsilon}\right)^{i-1}$

    ${}^{n}\left(\mathbf{K}^{(e)}\right)^{i-1}=\int_{V}\mathbf{B}:{}^{n}\left(\mathbf{C}^{\tan}\right)^{i-1}:\mathbf{B}\,dV$

    ${}^{n}\left(\mathbf{K}\right)^{i-1}=\mathbf{A}_{e=1}^{ne}\,{}^{n}\left(\mathbf{K}^{(e)}\right)^{i-1}$

    4) Compute displacement and strains:

$$ {}^{n}\left(\delta\mathbf{U}\right)^{i} = {}^{n}\left(\mathbf{K}^{-1}\right)^{i-1} \cdot {}^{n}\left(\mathbf{F}_{resid}\right)^{i-1} $$

$$ {}^{n}\left(\Delta\mathbf{U}\right)^{i} = {}^{n}\left(\Delta\mathbf{U}\right)^{i-1} + {}^{n}\left(\delta\mathbf{U}\right)^{i} $$

$$ {}^{n}\left(\boldsymbol{\varepsilon}\right)^{i} = \mathbf{B} : {}^{n}\left(\mathbf{U}\right)^{i} $$

5) Calculate real effective stresses and split:

$$ {}^{n}\left(\bar{\boldsymbol{\sigma}}\right)^{i} = \mathbf{C} : {}^{n}\left(\boldsymbol{\varepsilon}\right)^{i} $$

$$ \left(\mathbf{P}\right)^{i} = \sum_{j=1}^{3} H\left(\bar{\sigma}_{j}\right)\mathbf{p}_{j} \otimes \mathbf{p}_{j} $$

$$ {}^{n}\left(\bar{\boldsymbol{\sigma}}^{+}\right)^{i} = \left(\mathbf{P}\right)^{i} : {}^{n}\left(\bar{\boldsymbol{\sigma}}\right)^{i} $$

$$ {}^{n}\left(\bar{\boldsymbol{\sigma}}^{-}\right)^{i} = {}^{n}\left(\bar{\boldsymbol{\sigma}}\right)^{i} - {}^{n}\left(\bar{\boldsymbol{\sigma}}^{+}\right)^{i} = \left[\mathbf{I} - \left(\mathbf{P}\right)^{i}\right] : {}^{n}\left(\bar{\boldsymbol{\sigma}}\right)^{i} $$

6) Update the transformation tensors:

$$ \left(\mathbf{A}^{\sigma}\right)^{i} = \mathbf{A}^{\sigma+} \cdot \mathbf{P}^{i} + \mathbf{A}^{\sigma-} \cdot \left(\mathbf{I} - \mathbf{P}^{i}\right) $$

$$ \left(\mathbf{A}^{\varepsilon}\right)^{i} = \left(\mathbf{C}^{*}\right)^{-1} \cdot \left(\mathbf{A}^{\sigma}\right)^{i} \cdot \mathbf{C} $$

7) Transform real strains to the fictitious isotropic space:

$$ {}^{n}\left(\boldsymbol{\varepsilon}^{*}\right)^{i} = \mathbf{A}^{\varepsilon} : {}^{n}\left(\boldsymbol{\varepsilon}^{*}\right)^{i} $$

8) Calculate fictitious effective stresses and split:

$$ {}^{n}\left(\bar{\boldsymbol{\sigma}}^{*}\right)^{i} = \mathbf{C}^{*} : {}^{n}\left(\boldsymbol{\varepsilon}^{*}\right)^{i} $$

$$ \left(\mathbf{P}^{*}\right)^{i} = \sum_{j=1}^{3} H\left(\bar{\sigma}_{j}^{*}\right)\mathbf{p}_{j}^{*} \otimes \mathbf{p}_{j}^{*} $$

$$ {}^{n}\left(\bar{\boldsymbol{\sigma}}^{+*}\right)^{i} = \left(\mathbf{P}^{*}\right)^{i} : {}^{n}\left(\bar{\boldsymbol{\sigma}}^{*}\right)^{i} $$

$$ {}^{n}\left(\bar{\boldsymbol{\sigma}}^{-*}\right)^{i} = {}^{n}\left(\bar{\boldsymbol{\sigma}}^{*}\right)^{i} - {}^{n}\left(\bar{\boldsymbol{\sigma}}^{+*}\right)^{i} = \left[\mathbf{I} - \left(\mathbf{P}^{*}\right)^{i}\right] : {}^{n}\left(\bar{\boldsymbol{\sigma}}^{*}\right)^{i} $$

9) Compute damage indexes and total stresses in the fictitious space:

$$^{n}\left(\boldsymbol{\sigma}^{+*}\right)^{i} = \left(1-d^{+}\right)\,^{n}\left(\overline{\boldsymbol{\sigma}}^{+*}\right)^{i}$$

$$^{n}\left(\boldsymbol{\sigma}^{-*}\right)^{i} = \left(1-d^{-}\right)\,^{n}\left(\overline{\boldsymbol{\sigma}}^{-*}\right)^{i}$$

10) Return to the real orthotropic stress space:

$$^{n}\left(\boldsymbol{\sigma}^{+}\right)^{i} = \left(\mathbf{A}^{\sigma+}\right)^{-1} : {}^{n}\left(\boldsymbol{\sigma}^{+*}\right)^{i}$$

$$^{n}\left(\boldsymbol{\sigma}^{-}\right)^{i} = \left(\mathbf{A}^{\sigma-}\right)^{-1} : {}^{n}\left(\boldsymbol{\sigma}^{-*}\right)^{i}$$

$$^{n}\left(\boldsymbol{\sigma}\right)^{i} = {}^{n}\left(\boldsymbol{\sigma}^{+}\right)^{i} + {}^{n}\left(\boldsymbol{\sigma}^{-}\right)^{i}$$

11) Compute residual forces:

$$^{n}\left(\mathbf{F}_{resid}^{(e)}\right)^{i} = \int_{V} \mathbf{B}^{T} : {}^{n}\left(\boldsymbol{\sigma}\right)^{i}\, dV - \mathbf{f}_{ext}$$

$$^{n}\left(\mathbf{F}_{resid}\right)^{i} = \mathbf{A}_{e=1}^{ne}\,{}^{n}\left(\mathbf{F}_{resid}^{(e)}\right)^{i}$$

IF $\dfrac{\left\| {}^{n}\left(\mathbf{F}_{resid}\right)^{i} \right\|}{\mathbf{f}_{ext}} > tol \quad \Rightarrow \quad i = i+1$ GO BACK TO 3

else:

- END EQUILIBRIUM ITERATION LOOP

  Converged solution for the nth increment.

  Compute new incremental solution: $n = n+1$

- END LOAD INCREMENTAL LOOP

4.6 Numerical Examples

This section delves into the numerical application of the proposed model to real cases study. The capability of the proposed model to reproduce the strength of

different masonry types is demonstrated through a comparison with available experimental data in masonry panels subjected to in-plane loading conditions. The nonlinear behaviour of the model is also discussed.

Calculations are performed with an enhanced version of the finite element program COMET (Cervera *et al.* 2002), developed at the International Center for Numerical Methods in Engineering (CIMNE, Barcelona). The problem is solved incrementally in a (pseudo) time step-by-step manner. Within each step, a modified Newton–Raphson method (using the secant stiffness matrix), together with a line search procedure, are used to solve the corresponding non-linear system of equations (Cook *et al.*, 2002; Zienkiewicz and Taylor, 2000; Simó and Hughes, 1998; Crisfield, 1991). Convergence of a time step is attained when the ratio between the norm of the iterative residual forces and the norm of the total external forces is lower than 1%.

4.6.1 Simulation of Experimental Tests Conducted by Page

In the early 1980s, Page published the results of a series of tests designed to assess the directional strength characteristics of masonry panels subjected to in-plane monotonic loading. For that purpose, he conducted a series of biaxial tension-compression (Page, 1983) and biaxial compression–compression (Page, 1981) tests, which still are the most comprehensive experimental program conducted on the in-plane behaviour of brick masonry. The test specimen consisted of a 360 x 360 x 54 mm^3 panel of running bond brick masonry constructed by adhering the bricks in their designated place to a temporary plate, and then pouring in mortar. A total number of 102 panels were tested. Half-scale bricks were used, where the actual bricks were cut in half in all three dimensions, in order to obtain 115 x 40 x 54 mm^3 elements. In the corners, each individual brick was sawn to the appropriate shape required to fit the designated angle. The specimens were subjected to a biaxial load-controlled test in the load rig shown in Figure 4.18. In order to

alleviate the restraining effect of the loading caps, a series of brush platens were used to transfer the load to the panel. The tests were conducted for five different orientations, 0°, 22.5°, 45°, 67.5° and 90°. The results from all orientations were then gathered to obtain a fairly comprehensive picture of the directional strength characteristics of brick masonry.

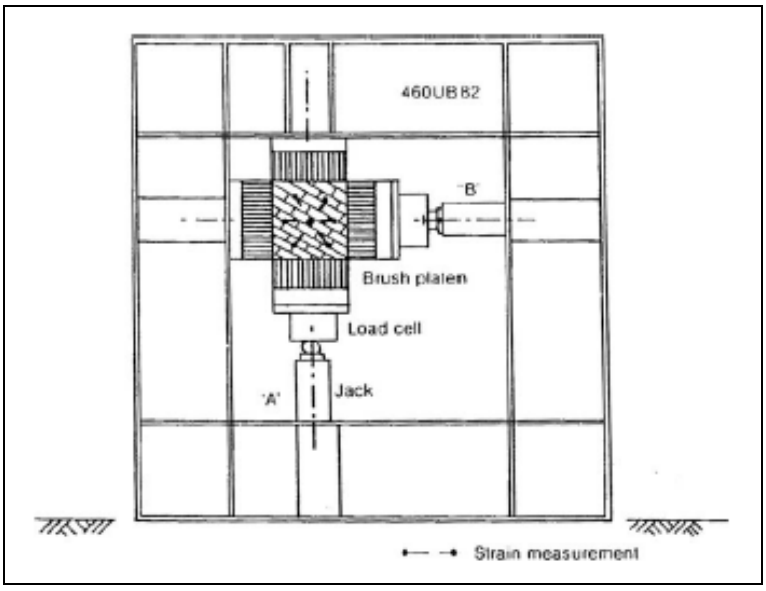

Figure 4.18 Page test setup.

The panels were loaded proportionally in the principal stress directions σ_1 and σ_2 along different orientations θ with respect to the material axes.

The values assumed for real strengths are $f_{11}^{+} = 0.43\,MPa$, $f_{22}^{+} = 0.32\,MPa$ and $f_{12}^{+} = 0.33\,MPa$ for tension and $f_{11}^{-} = 8.74\,MPa$, $f_{22}^{-} = 8.03\,MPa$ and $f_{12}^{-} = 2.71\,MPa$ for compression. The parameter *K* of (4.38) has been considered equal to 0.118. All the aforementioned values have been selected according to data given by Page (1983) and parameters calibrated by *Lourenço et al.* (1998). The

composite damage criterion features a low degree of anisotropy ($f_x^+ / f_y^+ = 1.34$ and $f_x^- / f_y^- = 1.09$). For all the tests, the material properties in the 1-axis have been selected for the fictitious space. The comparisons between the experimental values and the model are given in Figures 4.19-4.21, corresponding to orientations of the bed joints equal to 0°, 22.5° and 45°, respectively. For sake of comparison, the figures also report the results of the simulations obtained by the plasticity model of Lourenco *et al.* (1997).

Globally, good agreement is found. The uniaxial compressive strength parallel to the bed joints seems to be overpredicted by the model, see Figure 4.19, which is due to a debatable definition of failure in the experiments for these loading conditions (early splitting of the bed joints in tension), see Dhanasekar *et al.* (1985). In fact, the individual "piers" of masonry formed after splitting of the bed joints can withstand a much higher load before collapse is obtained.

The results obtained by the proposed model are consistent with the ones obtained by Lourenço *et al.*. Nevertheless, the Two-Parameters Damage Model that has been presented is much more advantageous, because of its intrinsic simplicity. The favourable strain-driven format provides robustness and high algorithmic efficiency, whereas the stress-driven format of an orthotropic plasticity model can sometimes lead to ill-conditioning of the return-mapping algorithm (Lourenço *et al.* 1995).

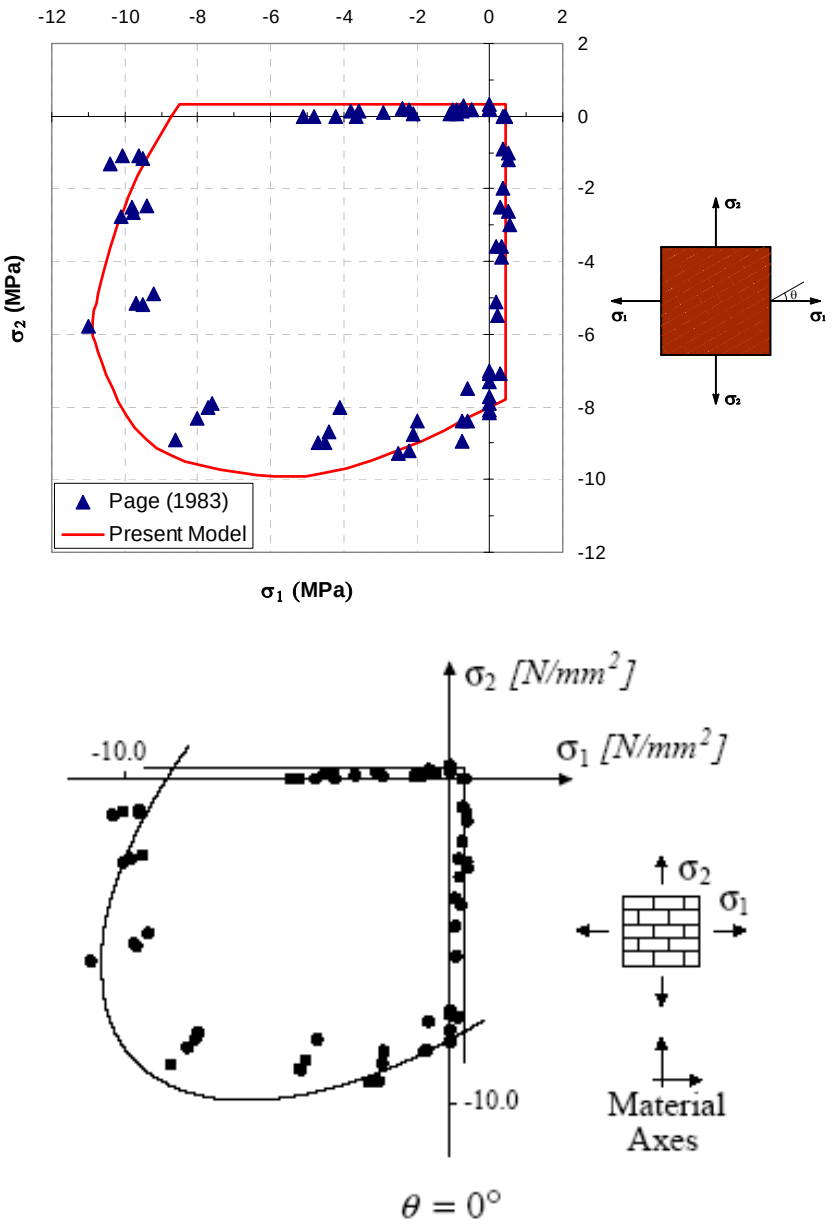

Figure 4.19 Comparison between the proposed model, the plasticity model of Lourenço *et al.* (1997) and the experimental results from Page (1983): θ=0°.

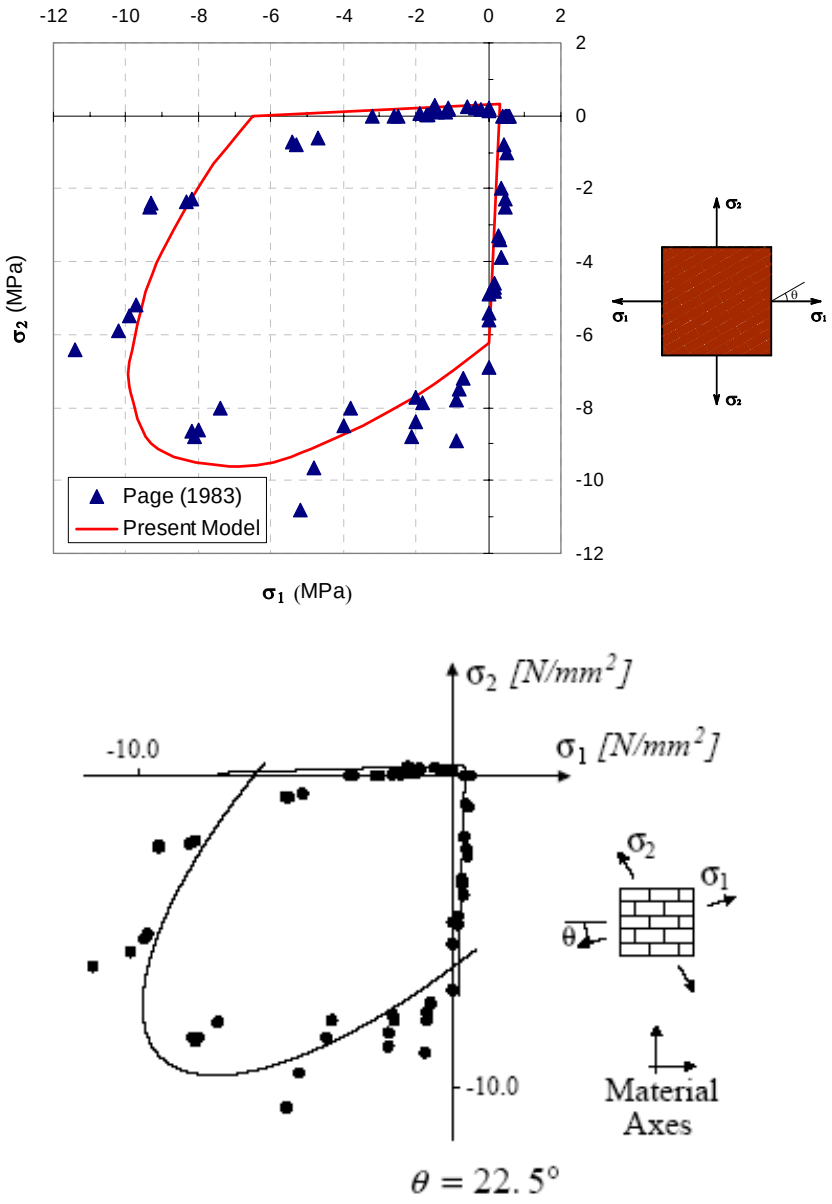

Figure 4.20 Comparison between the proposed model, the plasticity model of Lourenço *et al.* (1997) and the experimental results from Page (1983)): θ=22.5°.

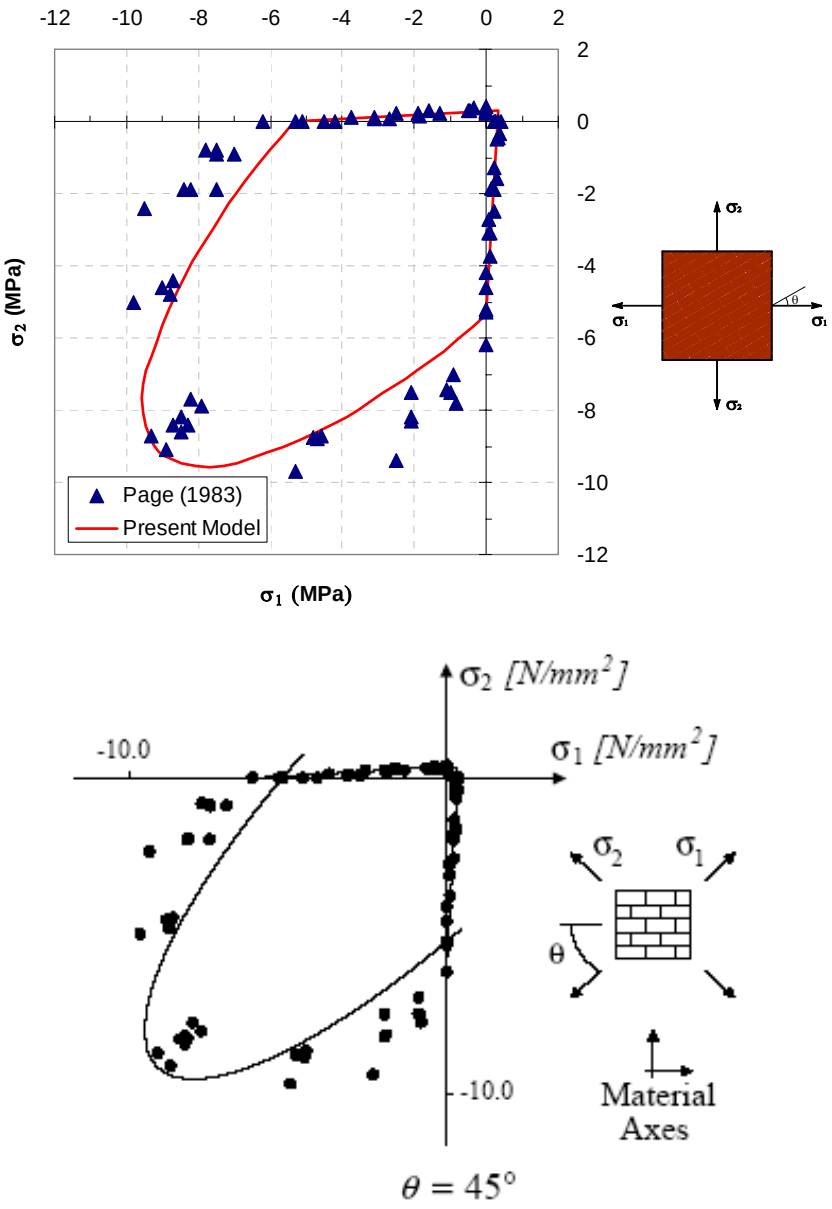

Figure 4.21 Comparison between the proposed model, the plasticity model of Lourenço *et al.* (1997) and the experimental results from Page (1983)): θ=45°.

4.6.2 Simulation of Experimental Tests Conducted by Ganz and Thürlimann

A smaller testing program of biaxially loaded masonry panels was carried out at ETH Zurich. The panels, with dimensions 1200 × 1200 × 150 mm^3, were loaded proportionally in the principal stress directions σ_1 and σ_2 along different orientations θ with respect to the material axes as defined previously. The twelve panels of hollow clay brick masonry, denoted by panels K1 to K12 and reported by Ganz and Thürlimann (1982), are considered.

The values assumed for real strengths are $f_{11}^{+} = 0.28\,MPa$, $f_{22}^{+} = 0.01\,MPa$ and $f_{12}^{+} = 0.04\,MPa$ for tension and $f_{11}^{-} = 1.83\,MPa$, $f_{22}^{-} = 7.63MPa$ and $f_{12}^{-} = 3.41\,MPa$ for compression. The parameter *K* of (4.38) has been considered equal to 0.072. All the aforementioned values have been selected according to data given by Ganz and Thürlimann (1982) and parameters calibrated by *Lourenço et al.* (1998). The composite damage criterion features a high degree of anisotropy ($f_x^{+} \big/ f_y^{+} = 28$ and $f_y^{-} \big/ f_x^{-} = 4.17$) These high ratios are due to the high perforation of the clay bricks. For all the tests, the material properties in the 1-axis have been selected for the fictitious space. Figure 4.22 shows the shape of the adopted composite damage criterion both with the points representing the set of strength experimental data.

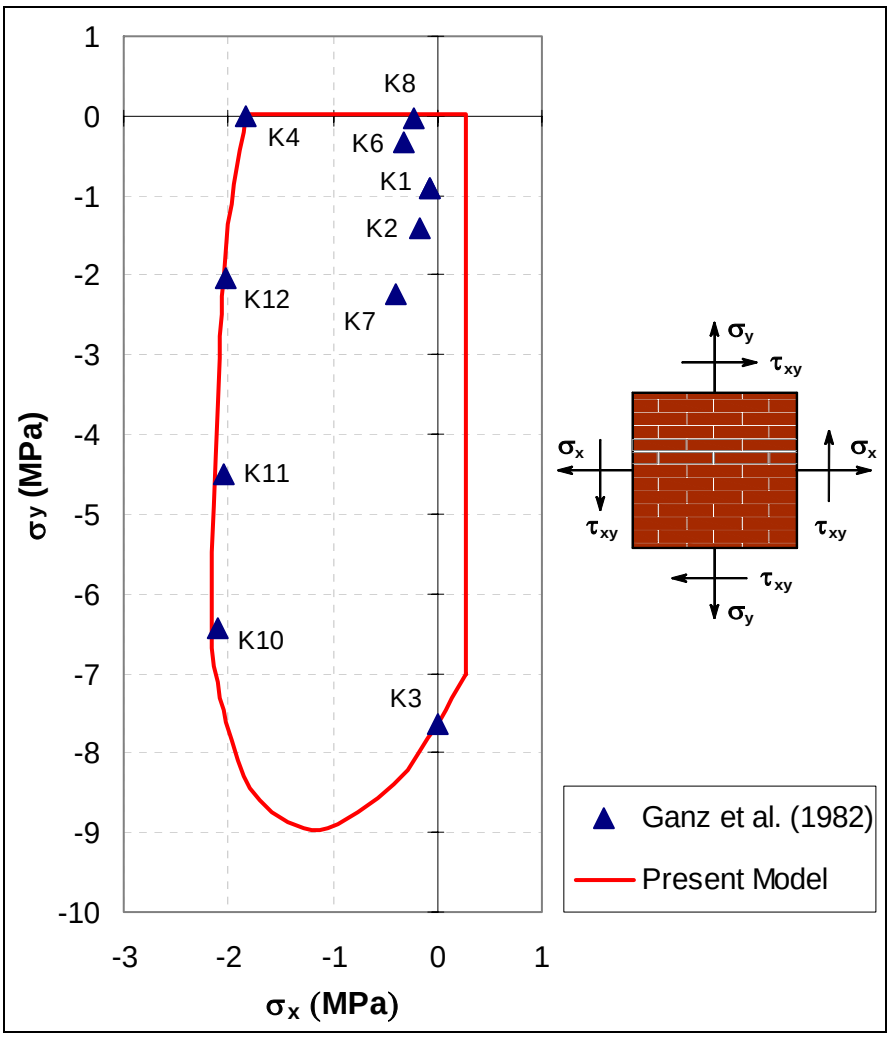

Figure 4.22 Composite damage criterion and experimental results from Ganz and Thürlimann (1982).

A single finite element was considered in the numerical simulation. Two stresses were applied to the element, namely σ_x and σ_y, and then the tangential stress τ_{xy} was increased until failure.

The test results, the proposed model results and the ratio between experimental and predicted failure are given in Table 4.2. Notice that this ratio is a measure of the

norm of the stress vector in the (σ_x, σ_y, τ_{xy})-space which equals $\left(\sigma_x^2+\sigma_y^2+\tau_{xy}^2\right)^{1/2}$. Panels K5 and K9 are not included because the boundary conditions affected the failure mode of panel K5 and panel K9 included reinforcement.

The model seems to be able to reproduce the strength behaviour of this type of anisotropic masonry with good accuracy. The error is bounded by a maximum value of 5%, corresponding to test K8. The mean of the ratios results equal to 0.995.

Table 4.2 Comparison between the proposed model and the experimental results obtained by Ganz and Thürlimann (1982).

Panel	Experimental results			Present model			Ratio
	σ_x (MPa)	σ_y (MPa)	τ_{xy} (MPa)	σ_x (MPa)	σ_y (MPa)	τ_{xy} (MPa)	
K1	-0.08	-0.92	0.42	-0.08	-0.92	0.44	0.99
K2	-0.17	-1.42	0.62	-0.17	-1.42	0.61	1.00
K3	0.00	-7.63	0.00	0.00	-7.63	0.00	1.00
K4	-1.83	0.00	0.00	-1.83	0.00	0.00	1.00
K6	-0.32	-0.32	0.32	-0.32	-0.32	0.34	0.98
K7	-0.39	-2.25	0.93	-0.39	-2.25	0.94	1.00
K8	-0.22	-0.04	0.09	-0.22	-0.04	0.12	0.95
K10	-2.11	-6.44	0.00	-2.15	-6.44	0.00	1.00
K11	-2.04	-4.49	1.23	-2.04	-4.49	1.39	0.99
K12	-2.03	-2.03	1.08	-2.03	-2.03	0.69	1.04

For sake of completeness, Figures 4.23-4.29 report, for each test, the comparison between the point of coordinates $\sigma_{x,u}$, $\sigma_{y,u}$, $\tau_{xy,u}$, which denote the experimental failure conditions, with the section of the composite damage threshold surface at a constant value of $\sigma_{y,u}$. These figures help to understand better how the proposed methodology models the shear strength behaviour of this type of masonry. It appears that the tension regime represents the majority of the composite damage surface domain.

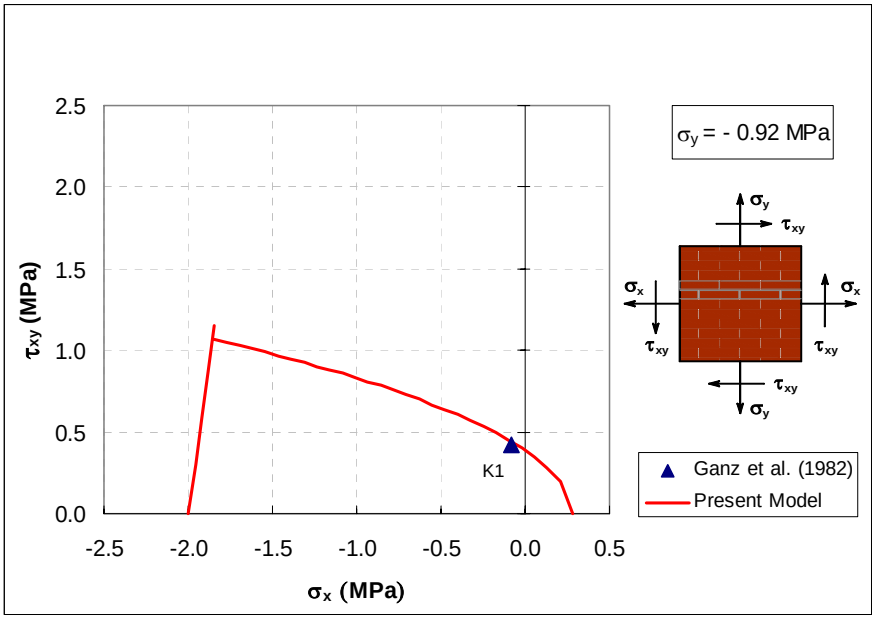

Figure 4.23 Comparison between K1 test and the composite damage threshold surface.

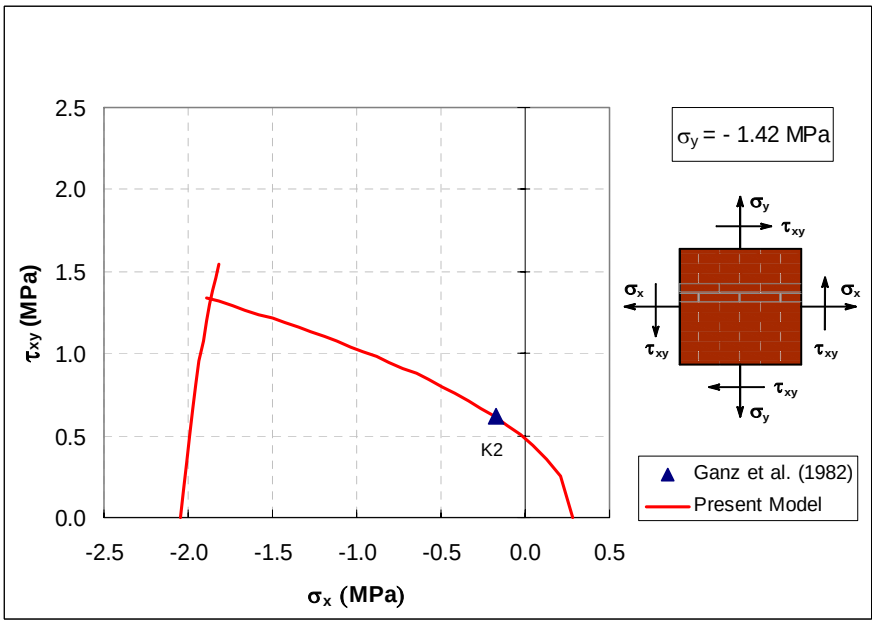

Figure 4.24 Comparison between K2 test and the composite damage threshold surface.

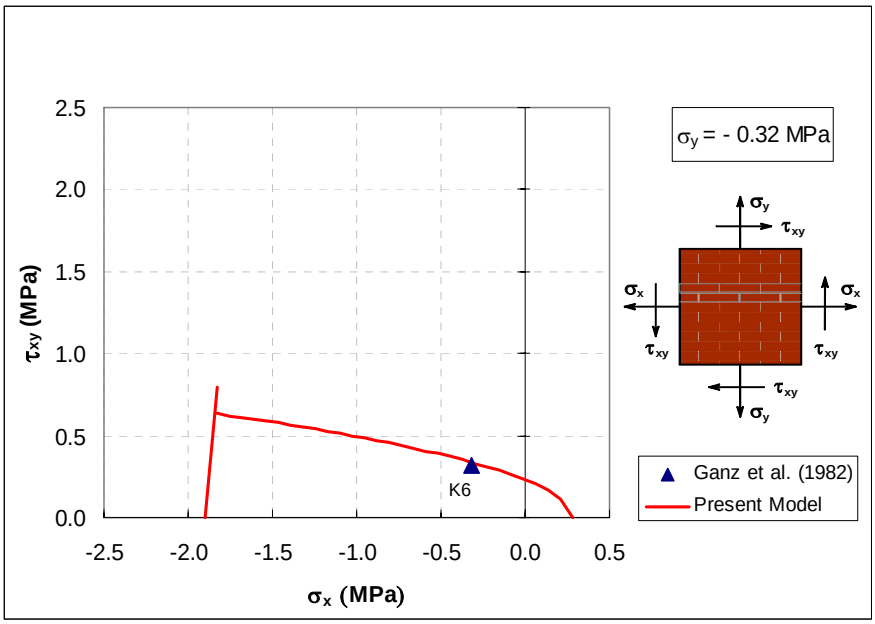

Figure 4.25 Comparison between K6 test and the composite damage threshold surface.

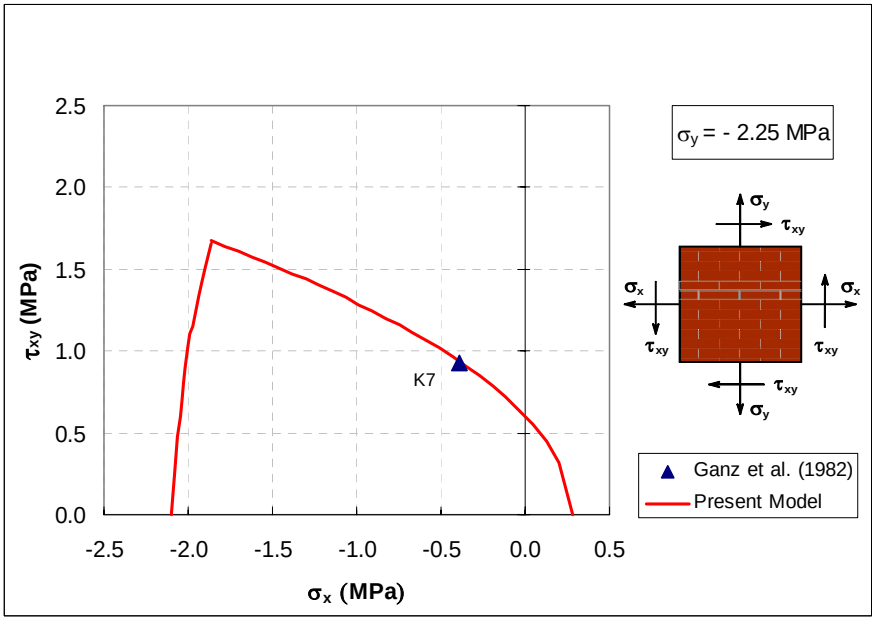

Figure 4.26 Comparison between K7 test and the composite damage threshold surface.

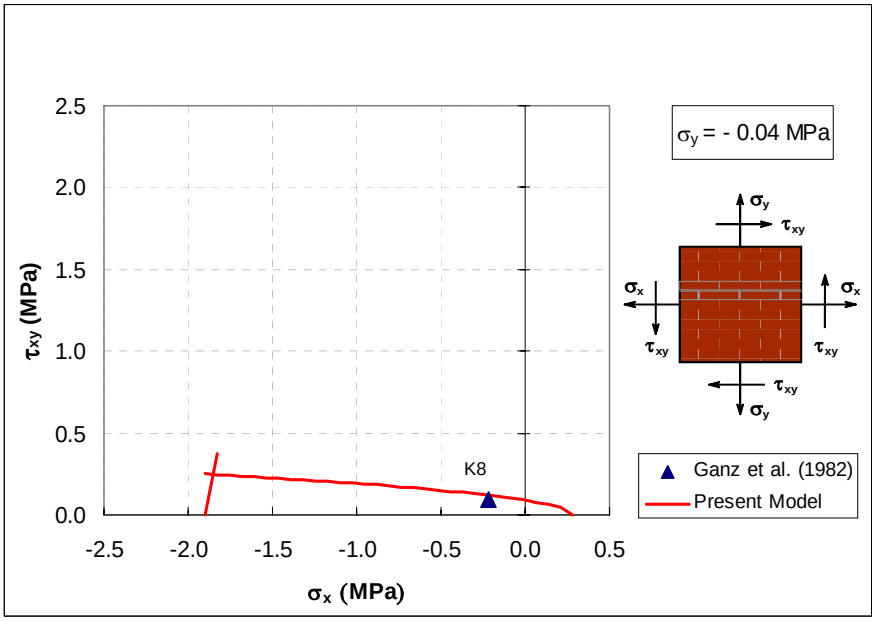

Figure 4.27 Comparison between K8 test and the composite damage threshold surface.

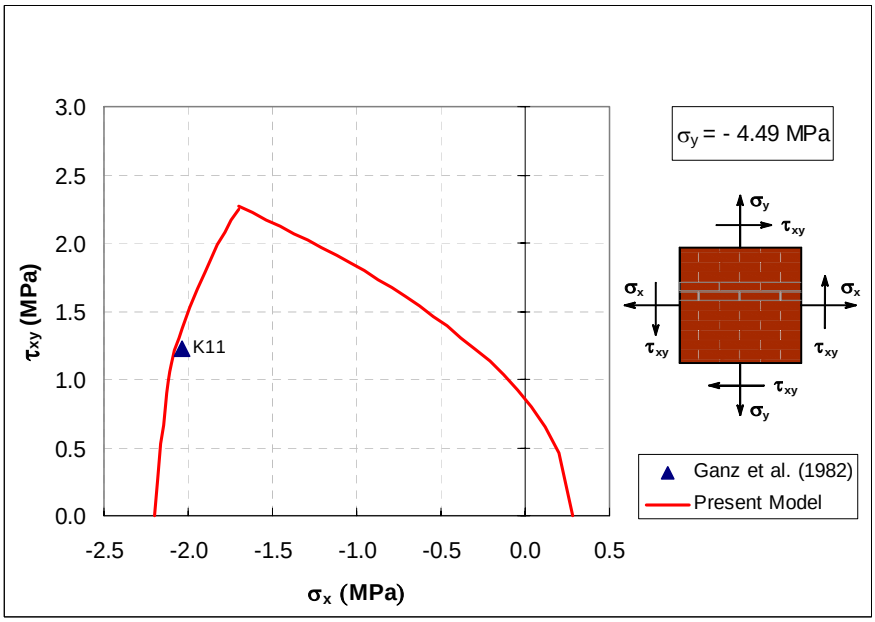

Figure 4.28 Comparison between K11 test and the composite damage threshold surface.

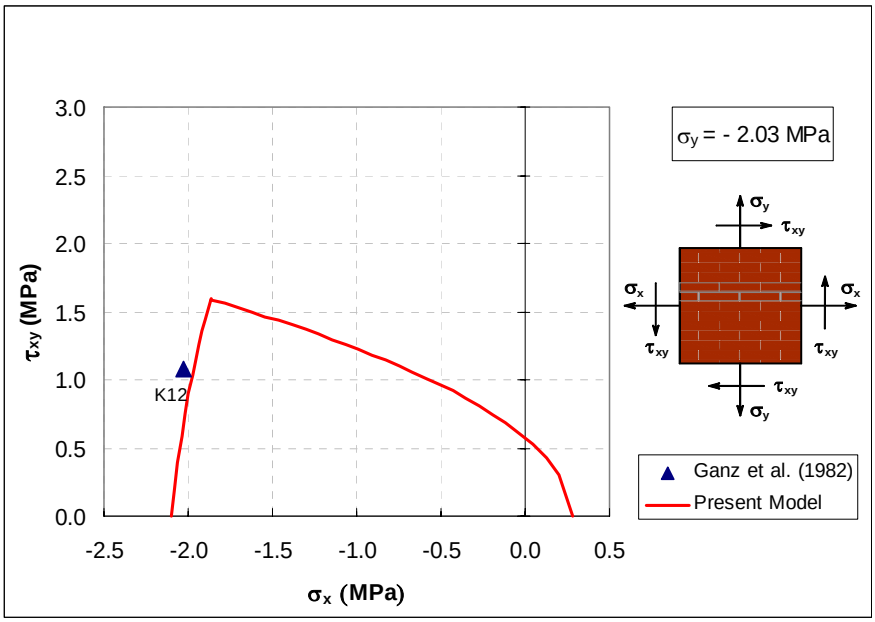

Figure 4.29 Comparison between K12 test and the composite damage threshold surface.

4.6.3 Simulation of Experimental Tests Conducted by Lurati *et al.*

The nine panels of hollow concrete block masonry, denoted by panels ZSW1 to ZSW9 and tested by Lurati *et al.* (1990) as a part of the ETH Zurich program, are considered next. Panel ZSW3 is not considered because the head joints were not filled.

The values assumed for real strengths are $f_{11}^{+} = 0.01 MPa$, $f_{22}^{+} = 0.01 MPa$ and $f_{12}^{+} = 0.01 MPa$ for tension and $f_{11}^{-} = 5.78 MPa$, $f_{22}^{-} = 9.12 MPa$ and $f_{12}^{-} = 3.98 MPa$ for compression. This type of masonry is practically a no-tension material. The parameter K of (4.38) has been considered equal to 0.0. All the aforementioned values have been selected according to data given by Lurati *et al.* (1990) and parameters calibrated by *Lourenço et al.* (1998). The composite damage criterion features a reasonable degree of anisotropy in compression, with

$f_y^- / f_x^- = 1.58$. For all the tests, the material properties in the 1-axis have been selected for the fictitious space. Figure 4.30 shows the shape of the adopted composite damage criterion both with the points representing the set of strength experimental data. For sake of comparison, the damage domain formulated by Berto *et al.* (2002) is also reported.

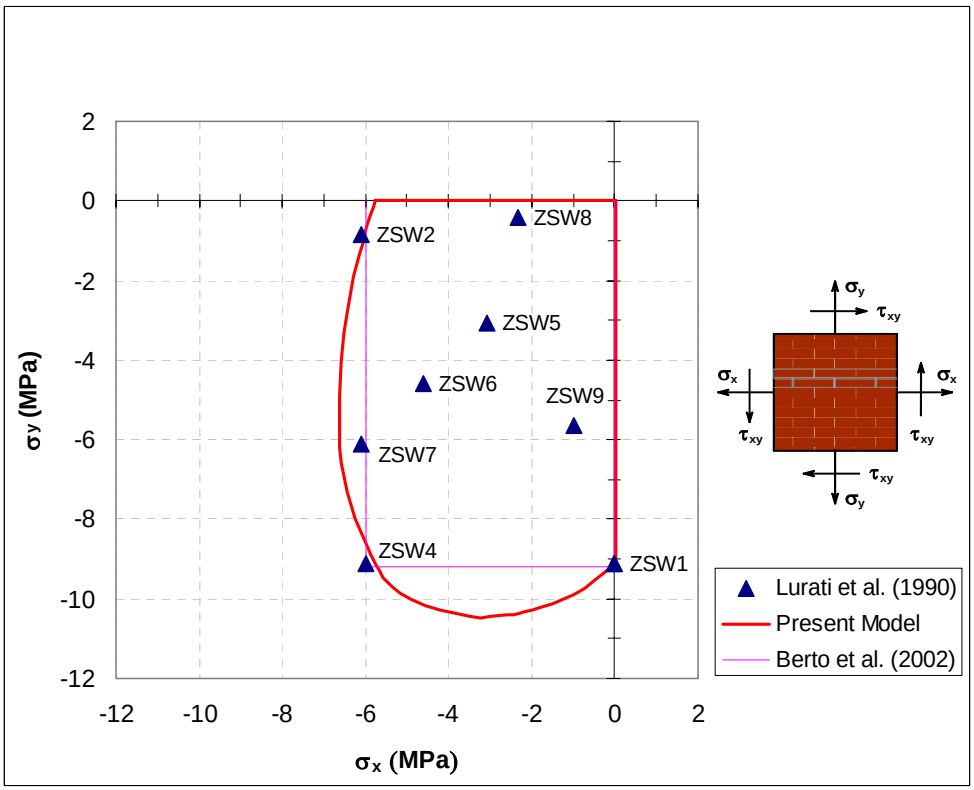

Figure 4.30 Composite damage criterion, damage domain formulated by Berto *et al.* (2002) and experimental results from Lurati *et al.* (1990).

A single finite element was considered in the numerical simulation. Two stresses were applied to the element, namely σ_x and σ_y, and then the tangential stress τ_{xy} was increased until failure.

The test results, the proposed model results and the ratio between experimental and predicted failure are given in Table 4.3. This ratio is again a measure of the norm of the stress vector in the (σ_x, σ_y, τ_{xy})-space which equals $\left(\sigma_x^2+\sigma_y^2+\tau_{xy}^2\right)^{1/2}$.

The model seems to be able to reproduce the strength behaviour of this type of anisotropic masonry with good accuracy. The error is bounded by a maximum value of 7%, corresponding to test ZSW7. The mean of the ratios results equal to 0.993.

Table 4.3 Comparison between the proposed model and the experimental results obtained by Lurati *et al.* (1990).

Panel	Experimental results			Present model			Ratio
	σ_x (MPa)	σ_y (MPa)	τ_{xy} (MPa)	σ_x (MPa)	σ_y (MPa)	τ_{xy} (MPa)	
ZSW1	0.00	-9.12	0.00	0.00	-9.12	0.00	1.00
ZSW2	-6.12	-0.83	0.00	-6.01	-0.83	0.00	1.02
ZSW4	-5.98	-9.13	0.00	-5.76	-9.12	0.00	1.01
ZSW5	-3.06	-3.06	3.06	-3.06	-3.06	3.07	1.00
ZSW6	-4.60	-4.60	2.93	-4.60	-4.60	3.06	0.99
ZSW7	-6.12	-6.12	0.00	-6.60	-6.60	0.00	0.93
ZSW8	-2.34	-0.40	0.97	-2.34	-0.40	0.98	1.00
ZSW9	-0.97	-5.66	2.35	-0.97	-5.66	2.36	1.00

For sake of completeness, Figures 4.31-4.34 report, for each test, the comparison between the point of coordinates $\sigma_{x,u}$, $\sigma_{y,u}$, $\tau_{xy,u}$, which denote the experimental failure conditions, with the section of the composite damage threshold surface at a constant value of $\sigma_{y,u}$. As can be seen, the proposed model is able to capture the correct shear strength of this orthotropic masonry. On the contrary, the damage domain formulated by Berto *et al.* leads to conservative ultimate values, see Figures 4.32-4.34.

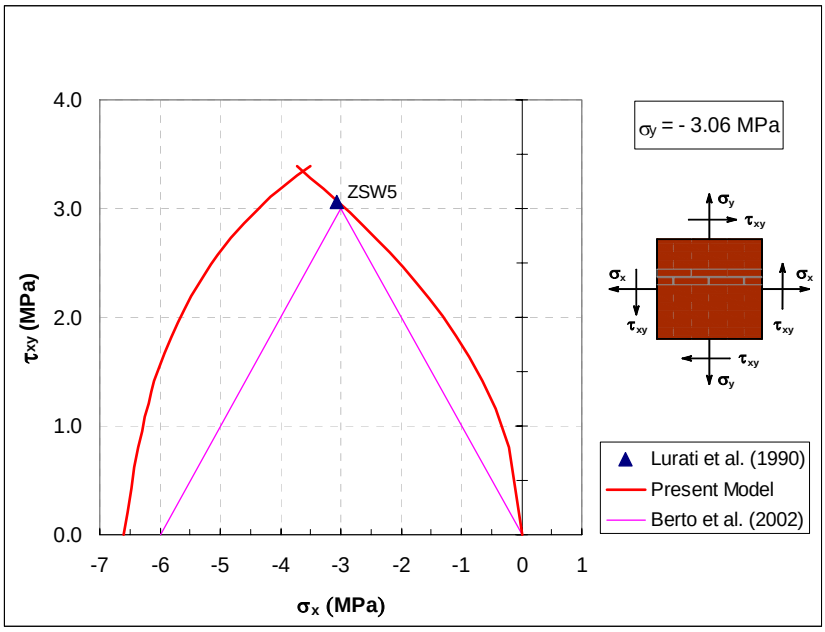

Figure 4.31 ZSW5 test, domain by Berto *et al.* (2002) and proposed model.

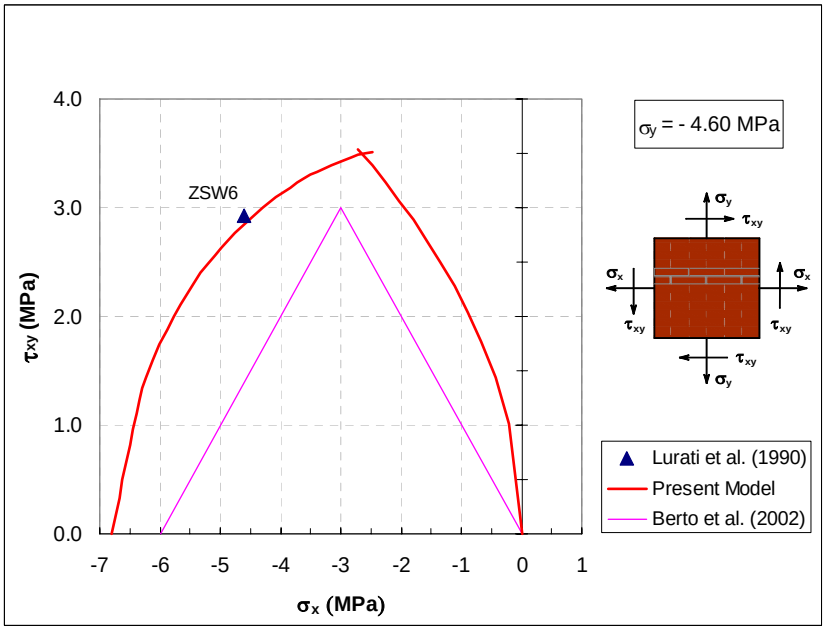

Figure 4.32 ZSW6 test, domain by Berto *et al.* (2002) and proposed model.

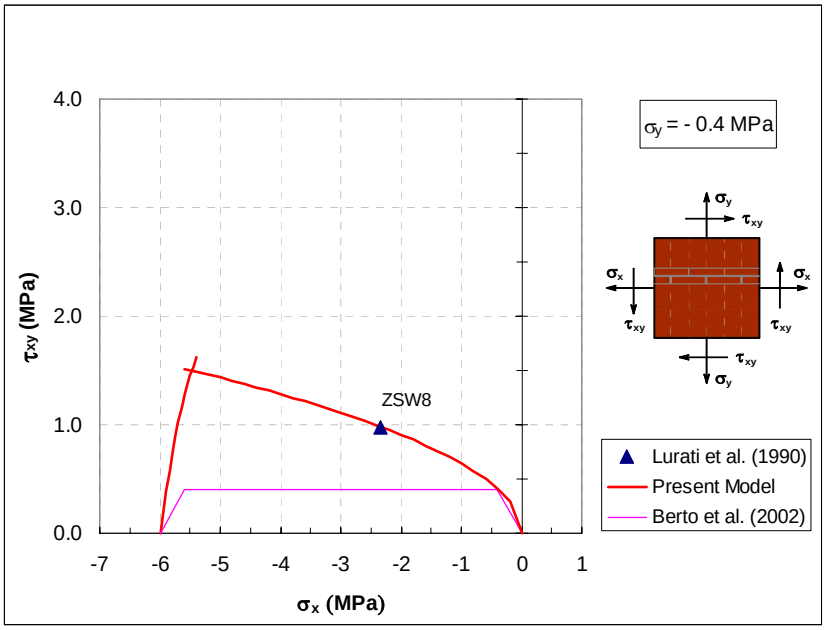

Figure 4.33 ZSW8 test, domain by Berto *et al.* (2002) and proposed model.

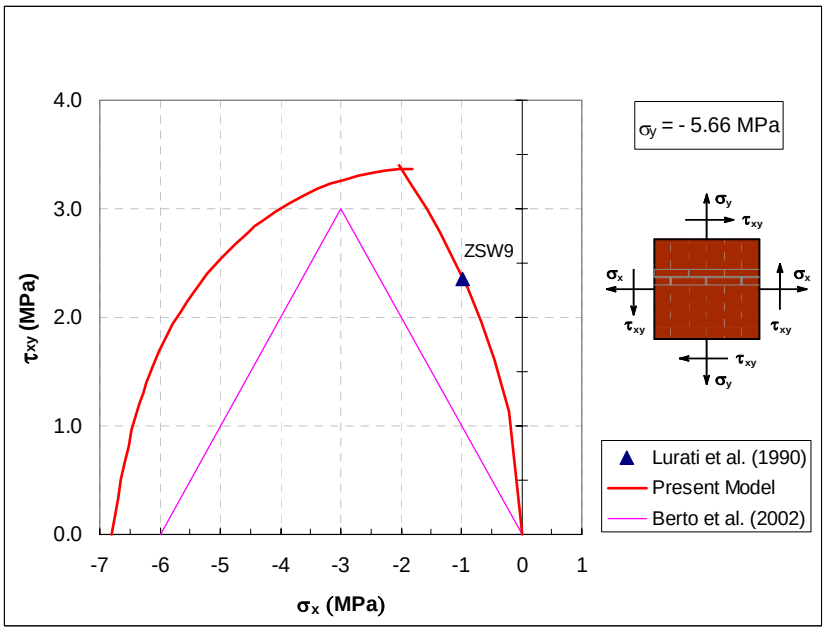

Figure 4.34 ZSW9 test, domain by Berto *et al.* (2002) and proposed model.

4.6.4 Inelastic tensile and compressive orthotropic behaviour

This example delves into the proposed model in order to understand how it models the inelastic orthotropic behaviour of masonry.

For this aim, we consider a masonry subjected to uniaxial tension. The material properties, referred to the material axes 1 and 2, are listed in Table 4.4. The values chosen for the material parameters illustrate the fact that completely different behaviours along the two material axes can be reproduced. In particular, it results that the restriction (4.64) between fracture energies is not valid. Therefore, the brittleness of the material is not the same in all the directions. This softening orthotropy can be adequately described by the proposed model. In fact, two different softening parameters along the material axes *x* and *y* can be considered, by choosing the material properties for the mapped fictitious solid according to (4.65a, b, c).

Table 4.4 Material properties for uniaxial tension test.

Material Properties					
$E_1=E^*$	3000 MPa	$f_{11}^{+}=f^{+}*$	0.35 MPa	$f_1^{-}=f^{-}*$	7.00 MPa
E_2	2000 MPa	f_{22}^{+}	0.15 MPa	f_2^{-}	3.00 MPa
$\nu_{12}=\nu^*$	0.1	f_{12}^{+}	0.20 MPa	f_{12}^{-}	3.00 MPa
ν_{21}	0.15	$G_{f,1}^{+}=G^{+}*$	100 J/m^2	$G_{f,1}^{-}=G^{-}*$	40000 J/m2
G_{12}	900 MPa	$G_{f,2}^{+}$	13.8 J/m^2	$G_{f,2}^{-}$	5510 J/m2

Figure 4.35 shows the stress-strain responses for angles of orthotropy equal to 0°, 45° and 90°. The present model considers an exponential softening law, which is sound for a quasi-brittle material such as masonry. Once the fracture energy is exhausted, a no-tension material is recovered. The material strength in the *y*-direction degrades at a faster rate than the material strength in the *x*-direction, according to the selected material data.

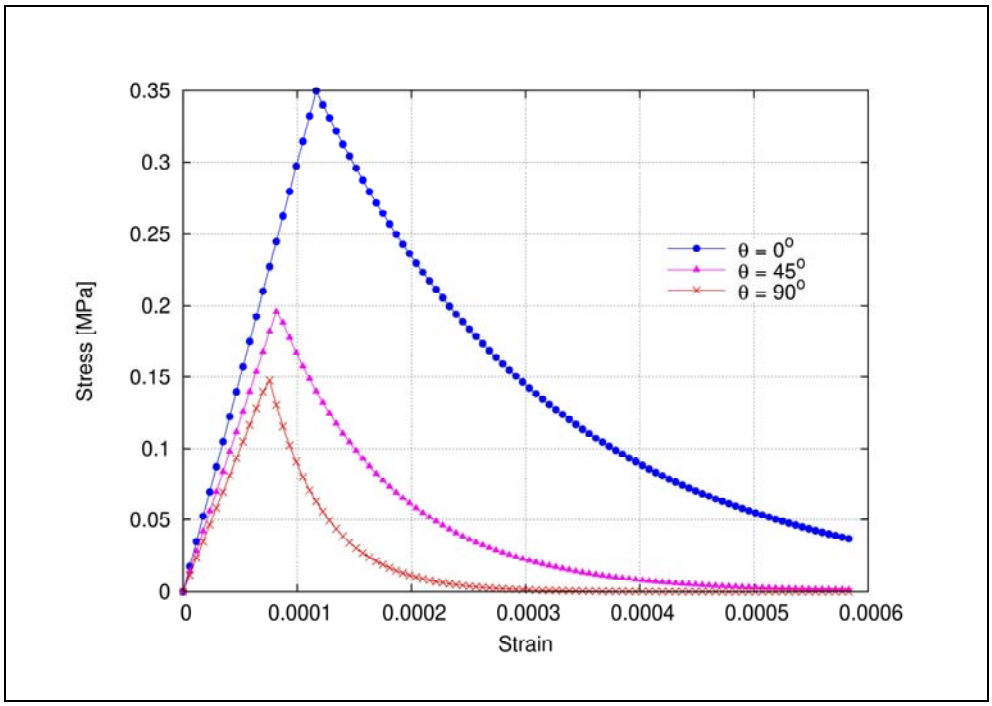

Figure 4.35 Stress-strain responses to uniaxial tension for different angles of orthotropy with orthotropic brittleness.

Then, we consider a masonry subjected to uniaxial compression. The same observations made for the tension test hold. The only exception concerns the compressive nonlinear behaviour. A parabolic hardening followed by exponential softening is considered for the stress-strain diagrams, with completely different compressive fracture energies along the material axes, see Figure 4.36. The peak strength value is assumed to be reached simultaneously on both materials axes, i.e. isotropic hardening, followed by orthotropic softening as determined by the different fracture energies. The model allows one to set an ultimate value of the strain, from which the material begins to soften.

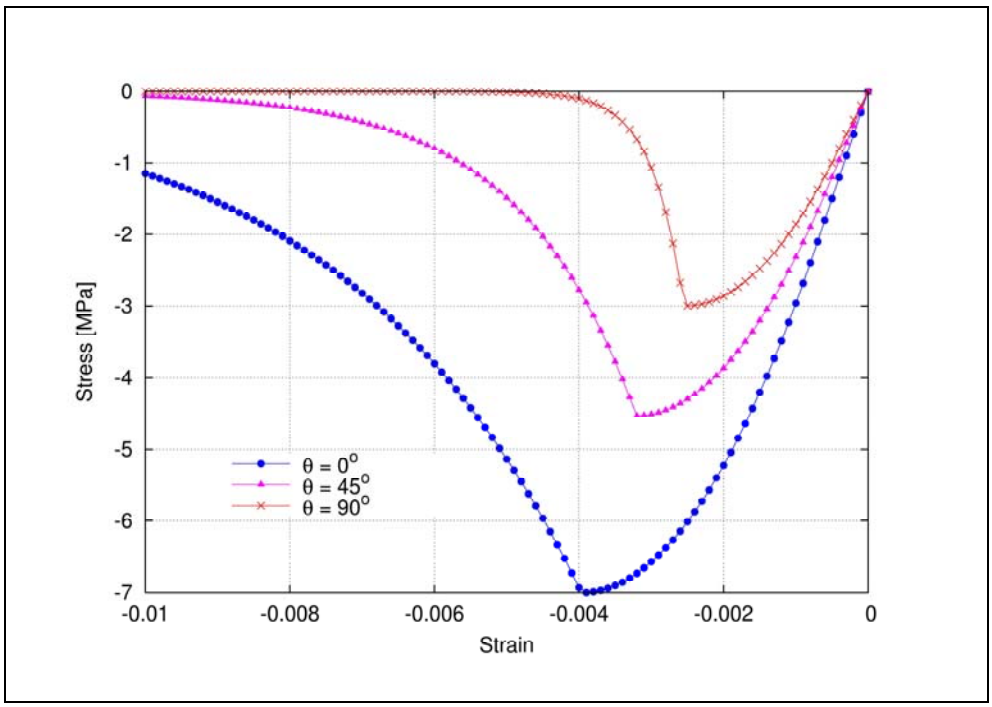

Figure 4.36 Stress-strain responses to uniaxial compression for different angles of orthotropy with orthotropic brittleness.

An important feature of the proposed model is the particular behaviour during unloading/reloading conditions. In compliance with the Continuum Damage Mechanics (see Chapter 2), in case of unloading the damage does not rise and, consequently, unloading occurs until the origin according to a damaged Young modulus, see Equations (4.26) and (4.27). As discussed in Chapter 3, the damage constitutive law differs from the plasticity constitutive law in that no plastic irreversible deformation occurs: all the deformation is recovered during the unloading, hence the unloading paths are not parallel.

In addition, the two-parameters damage model is able to capture the unilateral behaviour exhibited by masonry when passing from tension to compression. This is due to the assumption of the stress split described by Equations (4.20) and (4.21)

and to the definition of two different variables to describe tensile and compressive damage, see Equations (4.25), (4.26) and (4.27).

This peculiarity of the model is emphasized in Figure 4.37, which shows the numerical response of a masonry specimen subjected to tensile-compressive cycles. A cyclical displacement history is applied to the specimen with horizontal bed joints. As can be seen, the unloading occurs until the origin of the stress-strain diagram, according to a damaged stiffness. A successive reloading follows the same unloading branch, until the damage threshold is reached again.

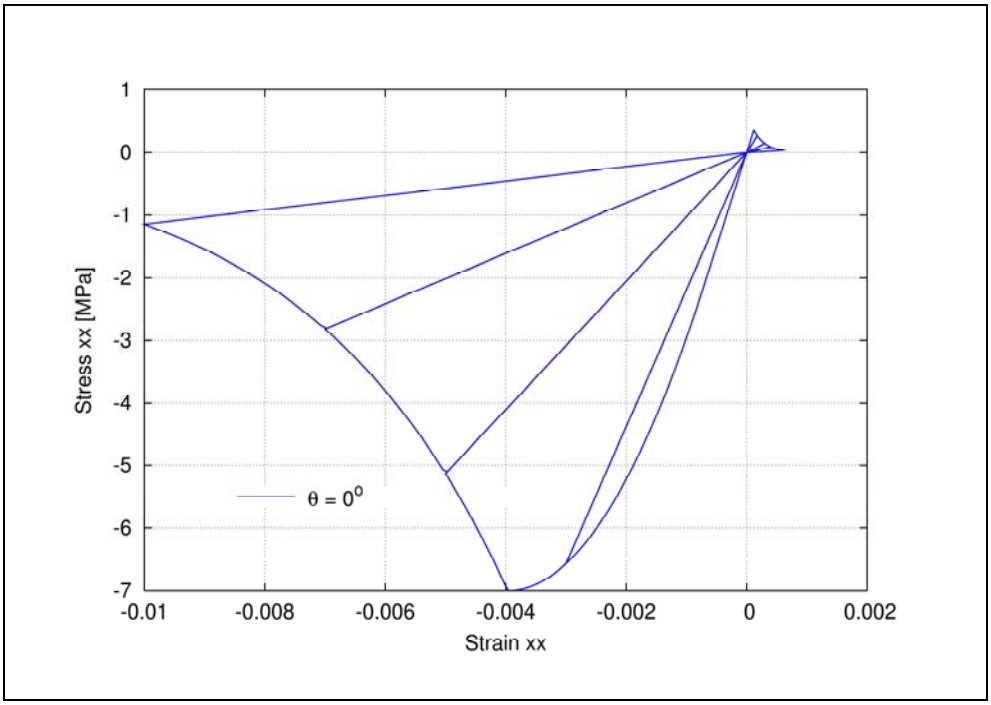

Figure 4.37 Uniaxial response under cyclical displacement history: global behaviour.

Figure 4.38 shows a zoom to the origin of the strain-stress diagram of Figure 4.37. As can be seen, when reversing the sign of the external loading, the constitutive model is able to distinguish tension from compression. In particular, the stiffness recovery upon loading reversal is correctly represented. For instance, when passing

from tension to compression, the model accounts for the crack closure phenomenon in masonry.

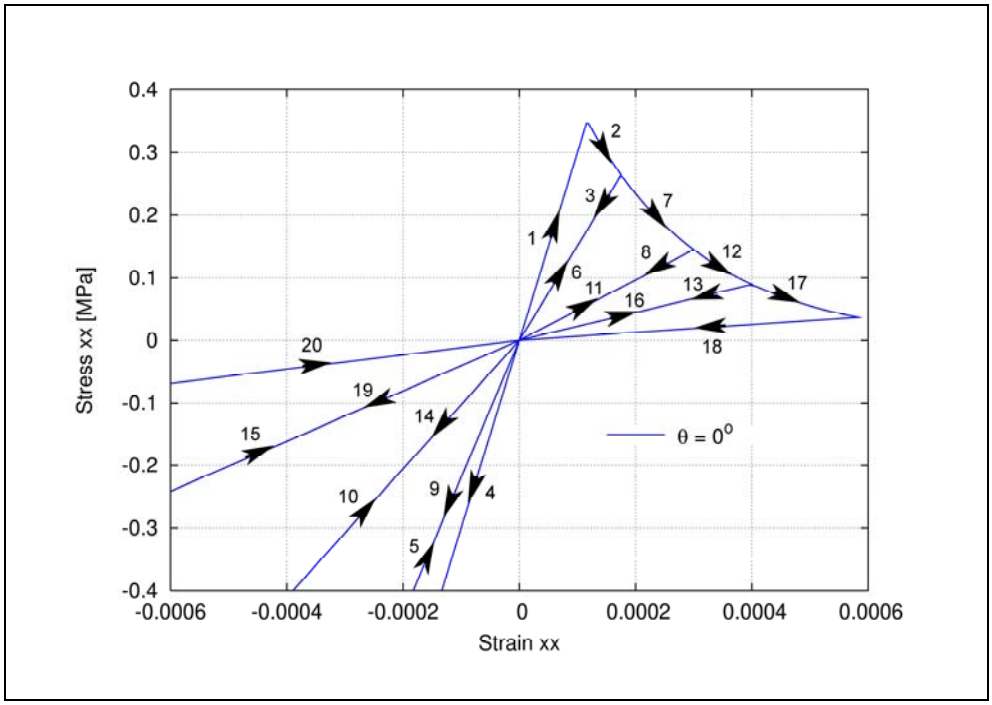

Figure 4.38 Uniaxial response under cyclical displacement history: detail of the stiffness recovery upon loading reversal.

4.7 Conclusions

In this Chapter, a plane-stress macro model for finite element analysis of orthotropic materials has been presented. The study focuses on application to masonry, but the model can also be suitable for other orthotropic materials, such as wood and fibre reinforced composites.

The proposed model is capable of modelling the following features of masonry:

- the elastic orthotropy of the intact material;

- the orthotropy along the two natural directions of masonry, parallel and orthogonal to the mortar joints;
- the different strengths and inelastic behaviours along these two directions;
- the dependence of the response on the inclination of the natural axes of the material;
- the unloading (and reloading) depending on the damaged stiffness;
- the stiffness recovery at crack closure under alternate loading.

The Two-Parameters Damage Model is based on the concept of *mapped tensor* (Betten, 1983) from the orthotropic real space to the fictitious one. A one-to-one mapping relationship is established between the behaviour of the real material and that of a fictitious one. The problem is solved in a fictitious space and the results are transported to the real field.

In order to account for different behaviours in tension and compression, the relationship between the two spaces is defined by means of two *transformation tensors*, which are related to tensile stress states and compressive stress states, respectively. Such an enhancement of the model proposed in Chapter 2, permits to reproduce different ultimate behaviours in tension and compression by considering two distinct isotropic criteria in the fictitious space. Each of them describes different failure mechanisms. The first criterion is associated with a localised fracture process, namely cracking of the material, and the second criterion is associated with a more distributed fracture process, i.e. the crushing of the material. In this study, a Rankine criterion for tension and a Faria criterion in compression have been selected for the fictitious space.

It is possible to adjust the two assumed isotropic criteria to the particular behaviour of the orthotropic material. In fact, the two distinct transformations allow one to scale in distinct manners the two isotropic damage threshold surfaces assumed in

the fictitious space. The result is an implicit composite damage threshold surface defined in the real space.

The constitutive model assumed in the fictitious space is the Tension-Compression Damage model proposed by Faria and Oliver (1993) which has been extensively used (Faria *et al.* 1998, 2000, 2004; Cervera *et al.* 1995, 1996, 1999, 2003). An essential feature of the proposed model is that a split into tensile and compressive contributions is introduced. The model includes different hardening/softening behaviour for tension and compression. The softening behaviour has been modelled with a smeared approach in which the damaged material is still considered as a continuum. The damage variables are related by an equivalent length to the released energy per unit cracked area. With the assumption that the fracture energy is uniformly dissipated in a representative area, the finite element calculations lead to objective results with regard to mesh refinement.

The orthotropic nature of the Tension-Compression Damage Model adopted in the fictitious space has been demonstrated. This feature, both with the assumption of two distinct damage criteria for tension and compression, does not permit to term the fictitious space as “isotropic”. Therefore, the present methodology turns the original concept of “mapping the real space into an *isotropic* fictitious one” into the innovative and more general one of “mapping the real space into a *favourable* (or *convenient*) fictitious one”.

The model has been fully formulated for the 2-dimensional case. However, it can be easily extended to the 3-dimensional case, see Oller *et al.* (2003).

The proposed model provides high algorithmic efficiency, a feature of primary importance when analyses of even large scale masonry structures are carried out. To account for this requisite it adopts a strain-driven formalism consistent with standard displacement-based finite element codes. The implementation of the model in finite element programs is straightforward.

Chapter 5.
Localized Damage Model for Orthotropic Materials

Local continuum damage models are generally combined with the traditional smeared damage approach in the finite elements analyses of masonry structures, as previously discussed in Chapter 1. In this case, only a general information is provided about the level of damage expected on the structure. In fact, the damage is simulated in an unrealistic way, involving significant volumes and spreading over large regions of the structure. This is not accurate, since localized cracks can be normally observed in structures with brittle behaviour, such as masonry constructions, both in service and at the ultimate condition.

In addition, it has been observed that the smeared crack approach suffers from spurious mesh-bias dependence in the discrete problem. This drawback leads to loss of results objectivity when different spatial discretizations are considered in the finite elements problem.

In order to overcome all these drawbacks, in this work the traditional smeared crack approach has been modified in such a way that it can reproduce localized individual (discrete) cracks. This is achieved by means of the implementation of a *crack tracking algorithm*.

Compared with the smeared cracking approach, the tracking method shows a better capacity to predict realistic collapsing mechanisms. The resulting damage in the ultimate condition appears localized in individual cracks. Moreover, the results do not suffer from spurious mesh-size or mesh-bias dependence.

In this Chapter, the crack tracking technique formulated by Clemente *et al.* (2006), is adopted to study the structural behaviour of in-plane loaded shear walls. The original formulation is enhanced, by combining it with the continuum damage model for orthotropic materials that has been detailed in Chapter 4. The result is an efficient numerical tool which is able to account for material orthotropy and crack localization.

After a brief overview of the cracking approaches and the description of the crack tracking technique, we will consider an in-plane loaded shear wall with an opening. The validity of the model will be demonstrated, by comparing the numerical results with the experimental evidence. The analysis will be carried out by utilizing a finite elements macro-model, in which no distinction is made between bricks and mortar. Therefore, the computational strategy proposed herein is firstly aimed at the analysis of large and complex masonry structures.

5.1 Cracking Approaches

The numerical modelling of cracks growth and propagation is a difficult task. The question of predicting correctly the direction of crack propagation is deemed as the main difficulty to be overcome in the discrete problem.

With the advent of digital computers and computational mechanics, two different formats have evolved to model the phenomenon of tensile cracking in the context of finite element analysis: the discrete and the smeared crack approaches.

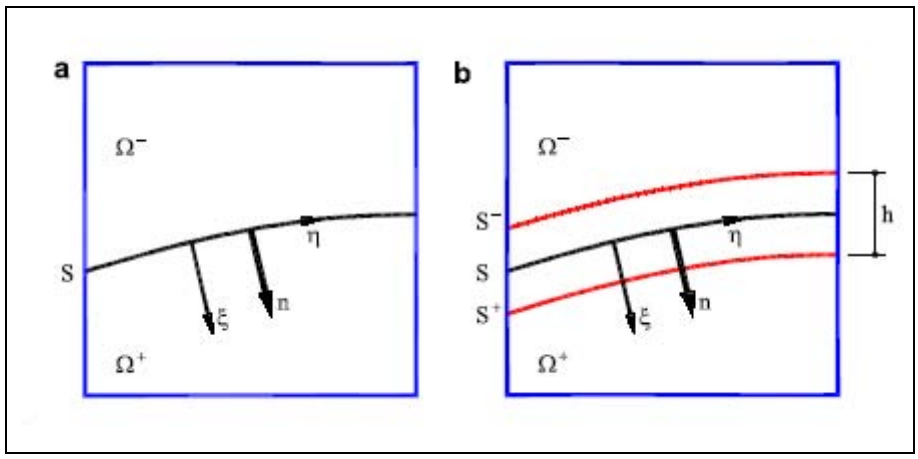

Figure 5.1 Crack modelling at continuum level: discrete approach (a) and smeared approach (b).

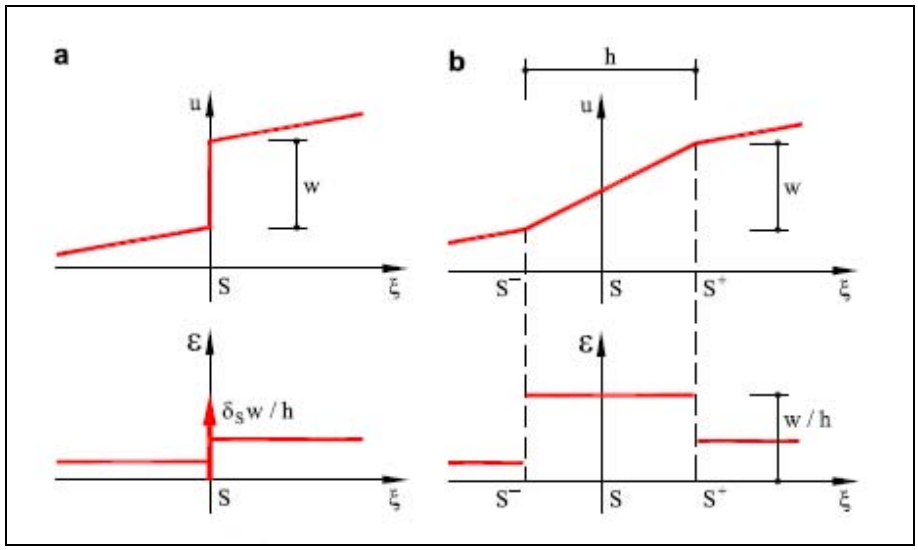

Figure 5.2 Continuum and discrete approaches to crack modelling: discontinuous displacement (a) and continuous (smeared) displacement (b).

In the *discrete crack models*, displacements jumps across the crack are explicitly considered. Consider the body Ω, as shown in Figure 5.1a, crossed by a discontinuity S, which represents a crack. Regions Ω^+ and Ω^- are the parts of the body located "in front" and "behind" the crack. In Figure 5.2a, the top graph shows the normal displacement along a line normal to the crack, with a discontinuous jump *w*, which represents the normal opening of the crack, occurring at *S*. The corresponding normal strain component is shown in the bottom graph, with a singularity occurring at *S*. The behaviour of the crack must be established through a softening traction-jump law.

In the *smeared crack models*, displacements jumps across the crack are smeared over the affected elements. In Figure 5.1b, S^+ and S^- are two lines that run parallel to *S*, at a relative distance *h*. In this model, the normal jump *w* occurring at *S* is smeared over the distance *h*. The top graph in Fig. 5.2b shows the normal displacement along a line normal to the crack, with the normal jump *w* smeared continuously between S^+ and S^-. The corresponding normal strain is shown in the bottom graph, with no discontinuity occurring at *S*. The behaviour of the crack can be established through a softening stress–(total) strain law.

5.1.1 Discrete Crack Approach

The discrete crack approach is usually based on the Fracture Mechanics theory. The criteria for crack propagation and, eventually, the prediction of the direction of propagation come directly from this theory, which is, mostly, based on energy criteria. Discrete cracks models represent the individual cracks as actual discontinuities in the topology of the FE mesh.

One of the first records of such an approach is due to Ngo and Scordelis (1967), who modelled cracks by separation of nodal points initially occupying the same spatial position. Obviously, the response was strongly mesh-dependent, as cracks

could only form along the element boundaries, see Figure 5.3a. Furthermore, when a crack propagates, the topology of the mesh is changed, and the updating procedures are time consuming. The approach was later refined so that new elements could be introduced whose boundaries were along the spreading crack, see Figure 5.3b. This reduces the mesh dependency of the approach, but remeshing techniques are required and the computing time increases. Also, it was recognized almost from the beginning that standard FE were not appropriate to capture the singular stress and strain fields that develop at the tip of the crack (Tong and Pian, 1973). Consequently, special FE were developed, see Owen and Fawkes (1983).

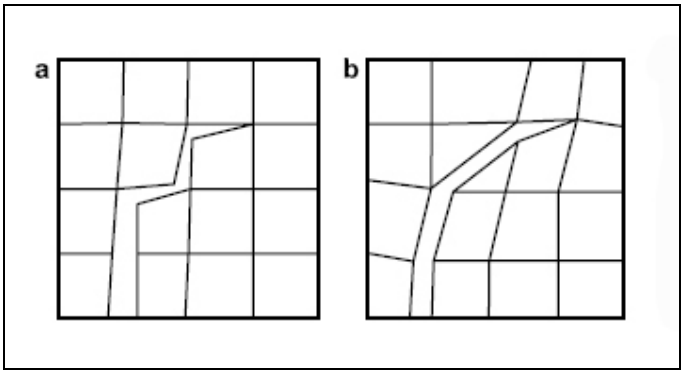

Figure 5.3 Discrete crack models: without (a) and with (b) remeshing.

5.1.2 Smeared Crack Approach

The smeared crack approach is based on the Continuum Mechanics theory. The criteria for crack propagation and the prediction of the direction of propagation come directly from this theory, which is, mostly, based on failure criteria expressed in terms of stresses or strains. The cracked material is assumed to remain a continuum and the mechanical properties (stiffness and strength) are modified to account for the effect of cracking, according to the evolving states of strain and/or stress. Therefore, remeshing is, in principle, unnecessary, see Figure 5.4a.

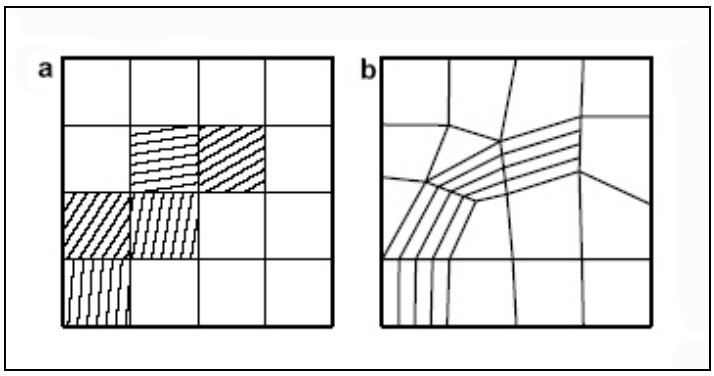

Figure 5.4 Smeared crack approach (a) and mesh bias dependence (b).

The simplicity of the approach, proposed by Rashid (1968), has caught the attention of the engineering community and many of today commercial FE codes use this approach, with little refinement over the original concept. Smeared crack models can be readily implemented in any nonlinear FE code, by simply writing a routine for a new material constitutive model.

The first drawback of the approach was discovered in the 1970s. It was realized that if a smeared crack is only one element across, the total energy dissipated in the cracking process is proportional to the size (the volume) of the element. Thus, upon mesh refinement, for infinitesimally small elements, the dissipated energy vanishes. This is unacceptable from the physical point of view.

Bazant and Oh (1983) showed that, in the context of FE models, the always controversial concept of *strain softening* should not be considered as a characteristic of the material, as it is related to the fracture energy of the material and the *size of the FE* crossed by the smeared crack. Today, most of the commercial FE codes implement smeared models with strain softening related to the fracture energy of the material and the element size.

But once the problem of mesh-size dependence was quite satisfactorily overcome, a more difficult one was identified. In the early 1990s it was widely recognized that FE solutions based on Continuum Mechanics suffered from mesh-bias dependence

in a strong manner. Also, it was noted that if the spatial discretization was designed in such way that an “appropriate” path for the advancing crack was available, the solutions obtained were satisfactory, see Figure 5.4b. Again, adaptive remeshing was suggested as a partial solution to this problem. In the last 15 years, a significant part of the research effort in Computational Solid Mechanics has been devoted to this problem.

5.1.3 Some Recent Trends

Nowadays, most structural engineers and FE codes for computational solid mechanics opt for the smeared crack approach. On the other hand, the observed mesh-bias dependence exhibited by these models makes the academic world very suspicious about this format. Therefore, a lot of effort has been spent in the last 30 years to investigate and remedy the observed drawbacks of the smeared approach. However, the most promising of the newly proposed methods resign from the smeared approach and turn back to the discontinuous format.

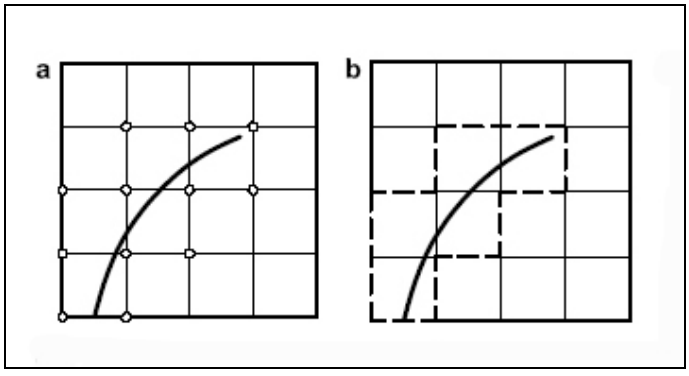

Figure 5.5 Finite elements with nodal enrichment (X-FEM) (a) and elemental enrichment (b).

Belytschko and Black (1999), Möes *et al.* (1999) Sukumar *et al.* (2000) have recently introduced the concept of the *extended finite element method* (X-FEM).

This approach allows for crack propagation without remeshing, at the expense of tracking the advance of the crack through the FE mesh and progressively enriching the nodal degrees of freedom with new ones that represent both the displacement jumps across the crack and the developed singular field at the tip of the advancing crack (Figure 5.5a, where the “enriched” nodes are marked). The main disadvantage of this approach is that it requires special integration rules inside the affected finite elements to take into account what happens at and outside the discontinuity.

On the other hand, the *strong discontinuity approach* (Simó *et al.*, 1993; Oliver, 1995; Oliver *et al.*, 1999; Oliver *et al*., 2004; Oliver and Huespe, 2004) leads to enhanced formulations for finite elements with *embedded displacement discontinuities*. Such concept does not really depart from the usual continuum framework. The application invariably needs the use of discontinuity *tracking algorithms* (Oliver *et al*., 2004; Oliver and Huespe, 2004; Mosler and Meschke, 2004), in order to establish which elements lie in the crack and need to be enriched (Figure 5.5b, where the elements with embedded discontinuities are marked). The displacement field inside the affected elements is assumed to be discontinuous and the strain field is decomposed into a regular part, outside the crack, and a singular part at the crack, see Figure 5.6a. This, as the explicit control on the energy dissipated in the formation of the crack, represents another link with the established tradition of fracture mechanics.

Another option has been recently investigated: the adoption of a smeared model that incorporates the effect of the displacement jumps in the strain field of the elements, rather than the actual jumps themselves. This approach has been termed *smeared-embedded continuum crack model* (Cervera, 2008a and Cervera, 2008b) and it is a refinement of the basic smeared continuum model. The displacement field is assumed continuous inside the localization band but, as in the discontinuous embedded models, the strain field is decomposed into its elastic and inelastic parts,

the latter due to the crack, see Figure 5.6b. All computations are made at constitutive level and this allows the use of standard elements with continuous displacement fields, making the implementation of these models straight-forward in nonlinear FE codes. Necessary corrections are introduced in the model to avoid mesh-size and mesh-bias dependency. The solution for the latter drawback is found in the form of a *mesh corrected crack model* where the structure of the inelastic strain tensor is linked to the geometry of the cracked element (Cervera, 2008a and Cervera, 2008b). The situation described is similar to what happens when using incompressible von Mises type softening models, either in a plasticity or damage format. In those cases, the discrete problem has to be modified appropriately, or "mesh corrected", to obtain mesh independent results, see Cervera *et al.* (2003).

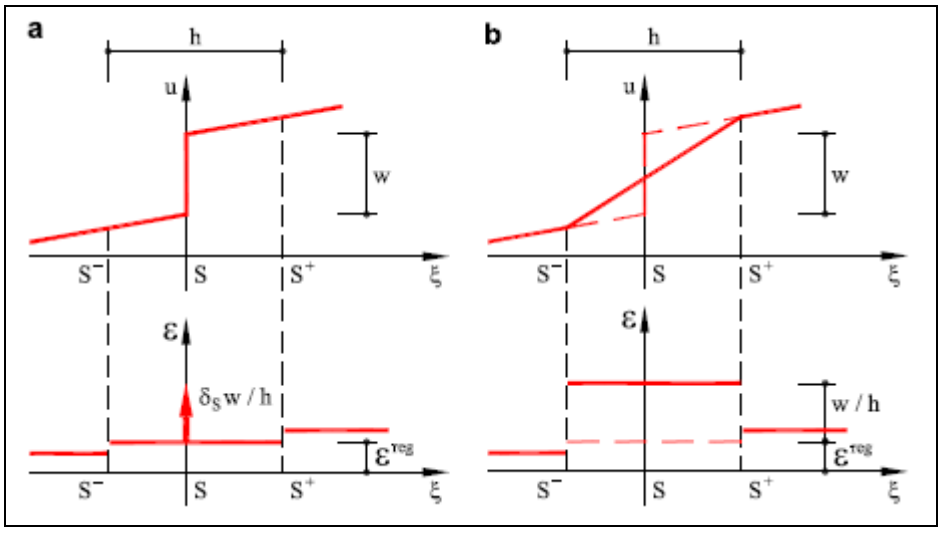

Figure 5.6 Embedded discrete approaches to crack modelling: discontinuous displacement (a) and continuous (smeared) displacement (b).

This can be considered a particular case of the smeared damage approach, implemented at constitutive level. On the other hand, similarities between the X-FEM and the smeared damage approach are evident.

5.2 Problem of Crack Propagation in Smeared Damage Approaches

As pointed out in the previous Section, the main drawbacks concerning the smeared crack approaches are the observed mesh-size and mesh-bias spurious dependences. The former problem has been properly solved by relating the softening behaviour to the size of the FE crossed by the smeared crack (Bazant and Oh, 1983), in addition to the material fracture energy. Nevertheless, a great effort has been devoted to the latter problem, which is definitely more complicated.

To propose, implement and use a computational failure model, set up within the Continuum Mechanics framework, three items are necessary (Cervera and Chiumenti, 2006):

- a *continuum model* that defines the variables and equations of the continuum BVP to be solved;
- a *constitutive model* for the cracked and non-cracked parts of the domain;
- a *spatial discretization procedure* to turn the continuum differential equations into discrete algebraic equations.

If the resulting computational discrete model has a flaw, its origin must be sought in one of the links of the chain.

The disagreeable effects of mesh dependence have been attributed to the fact that, when strain softening occurs and the slope of the local stress–strain curve becomes negative, the governing equations of the continuum problem lose their “natural” elliptic character. Therefore, many solutions have been sought by modifying either the continuum or the constitutive models. Many so-called *non-local* constitutive models have been proposed in different versions, see Jirásek (1998). All these strategies introduce a “localization limiter” (a length parameter) into the problem that effectively precludes the occurrence of sharp displacement gradients (strains). On the other hand, even if these strategies have proved effective to some extent,

they pose theoretical and computational difficulties. Just to mention a serious one, non-local models do not predict maximum stress values and, therefore, crack initiation, at the tip of a sharp crack, but rather at a finite distance ahead of the tip.
In this work, we will deal with the problem from a different point of view. The established fact that "well-aligned" meshes produce good results strongly suggests that the main flaw lies in the spatial discretization procedure.

5.2.1 Local Approximation Error

In a Continuum Mechanics framework, the problem of crack propagation involves a procedure amenable to two steps. For a given damage distribution, we need to (i) solve the mechanical problem in order to compute the stress field and, consequently, (ii) update the damage distribution. This second stage entails two different operations: (ii.a) to update the damage index in those elements previously damaged and (ii.b) to decide which elements are newly damaged. Stage (ii.a) is trivial, as damage is an explicit function of the strain history. Stage (ii.b), deciding which elements are newly damaged, requires some more deliberation.
In the smeared crack approach it has always been implicitly assumed that the criterion for the onset of cracking, which is always established in terms of stresses/strains, also must automatically define the direction of propagation. This may be a natural assumption in the *continuum problem*, with proper evaluation of stress and strain values and directions. However, in the *discrete problem* the stress and strain fields evaluated in the vicinity of the crack tip differ greatly from being exact. Therefore, the computed damage distribution is "incorrect", as it depends spuriously on the alignment of the finite element mesh. As a consequence, the automatic application of the cracking criterion for the evaluation of the direction of crack growth leads to an unacceptable dependence on the mesh bias at the crack tip. In fact, that point in the continuum problem is a singular, hence the L_∞ - norm

of the error on the displacement gradients (strains) in the computed discrete solution is unbounded.

We may conclude that the main difficulty in solving the problem of tensile crack propagation using standard elements, with continuous displacement fields and local constitutive models, with properly size-adjusted strain-softening, is the approximation error due to the spatial discretization (Cervera and Chiumenti, 2006). This error must be overcome if reasonable solutions are to be obtained with the smeared crack approach.

5.2.2 Evaluation of the propagation direction

In the last decade, the so-called strong discontinuity approach has been developed as a Continuum Mechanics alternative to the Fracture Mechanics formulation. Successful applications of this approach use tracking algorithms to determine the direction of crack propagation (Oliver *et al*., 2004; Oliver and Huespe, 2004; Mosler and Meschke, 2004). This evidence points to the potential advantages of using a crack tracking algorithm in the discrete format of the crack propagation problem, also if continuous displacement fields are used in the interpolation basis.

The *crack tracking algorithm* to be used in crack propagation problems must be consistently linked to the cracking criterion, as this is the established cracking mechanism at continuum level. For a Rankine criterion based on the value of the maximum tensile principal stress, it is consistent to assume that the crack propagates in the plane orthogonal to the corresponding first stress eigenvector.

A *global* crack tracking technique has been proposed by (Oliver *et al*., 2004) and used by Cervera and Chiumenti (2006). Such a methodology considers the evaluation of the propagation direction as a separate problem, independent from the local values of the discrete stress/strain fields, as these may be substantially off-track. The direction of propagation is evaluated by solving a conduction-like

problem which, by definition, is sufficiently well-behaved and does not present any singular point in the vicinity of the advancing crack.

Also *local crack tracking algorithms* have been formulated (Manzoli, 2005; Clemente *et al.*, 2006 and 2008), in which the propagation direction is evaluated locally. This approach will be adopted in this work and improved in order to include some peculiar features of masonry material.

5.3 Local Crack Tracking Technique

The local crack tracking technique detects the point where a crack is originated and then it lets the crack develop as a function of the direction of the main tensile stress (Clemente, 2006). The algorithm marks a track of finite elements pertaining to the crack path which can experience potential damage. The crack is forced to develop along a single row of finite elements. The fracture energy normalization respect to the characteristic length ensures that dissipation will be element-size independent.

The proposed method is applied at every time step during the analysis, just before the stress evaluation. The method works with a flags system, where finite elements are labelled to delimit the zones where cracks will appear or develop. The criteria used to define these zones depend on the magnitude and direction of the principal stresses at each element. The algorithm has been implemented for 2D problems using three-noded elements (constant strain-triangles, see Cook *et al.*, 2002).

The procedure is divided into two steps. First, new cracks are detected by checking the stress values at every finite element located on the boundary of the structure. Then, the track of finite elements pertaining to the crack path is marked by the algorithm, in order to compute the crack propagation direction.

5.3.1 New Cracks Detection

The input data of this first stage of the procedure are (i) the main tensile stress values of the elements located on the boundary of the mesh and (ii) the list of the elements labelled as *crack root*, all referred to the previous time step.

Then, the following operations are carried out:

1. New elements are labelled as potential crack roots. For this aim, we consider some criteria:
   - The crack starts once the main tensile stress value reaches the material strength, according to the Rankine tensile criterion. This check is performed only on finite elements located on the boundary of the mesh. Therefore, cracks are assumed to start only from the border of the structure.
   - When several neighbour elements reach the tensile strength at the same time step, the *exclusion radius* criterion is applied. This radius (defined by the user) is the minimum distance imposed between two crack root elements, and it is used to guarantee the creation of separated discrete cracks. In case of masonry, for instance, it could be the size of the elements (bricks or blocks). Among all the elements which have reached the tensile strength at the same time step, and which are contained into the exclusion radius, the one with the greatest main tensile stress is labelled as crack root.
2. The spatial coordinates of the crack origin are computed. The midpoint of the element side located at the mesh boundary is considered. In case of corner elements, the centroid is assumed, see Figure 5.7.

The output data of the new cracks detection procedure is the list of the potential crack root elements, together with their spatial coordinates.

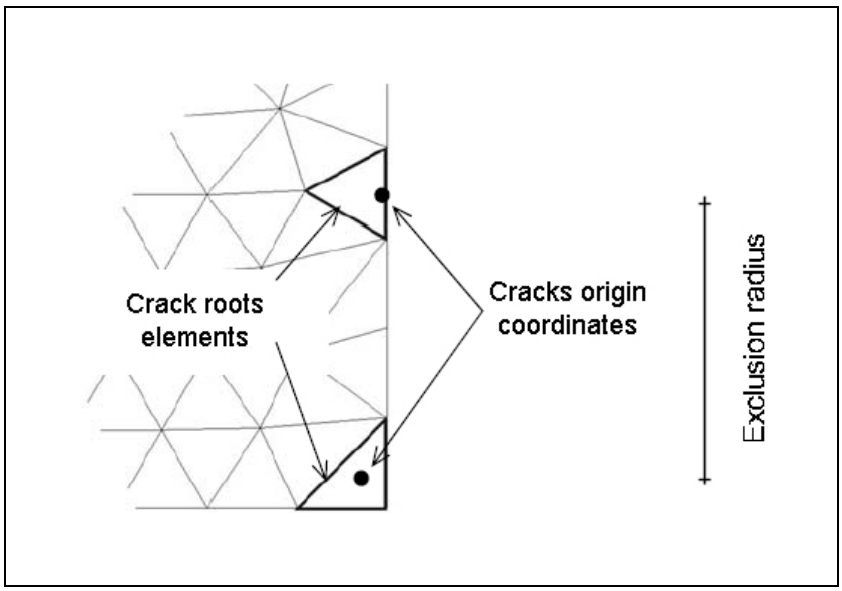

Figure 5.7 Location of cracks origin coordinates.

5.3.2 Cracks Propagation

The input data of this second stage of the procedure are (i) the list of the potential crack root elements, together with their spatial coordinates, (ii) the main tensile stress values and directions of all the mesh elements and (iii) the list of the elements belonging to consolidated cracks referred to the previous time step.

Then, the following operations are carried out:

1. Determine the *tip of the crack element* for each existing consolidated crack. This is defined as the damaged element with only *one* neighbour damaged element.
2. For each tip of the crack element, as well as for the new crack root elements, we act as follows:
   - Determine the *exit point* coordinates. A vector is drawn from the entry point coordinates (defined below), using the direction perpendicular to the principal tensile direction of the element. The exit point is defined

as the intersection of that vector with the corresponding face of the element, see Figure 5.8a.

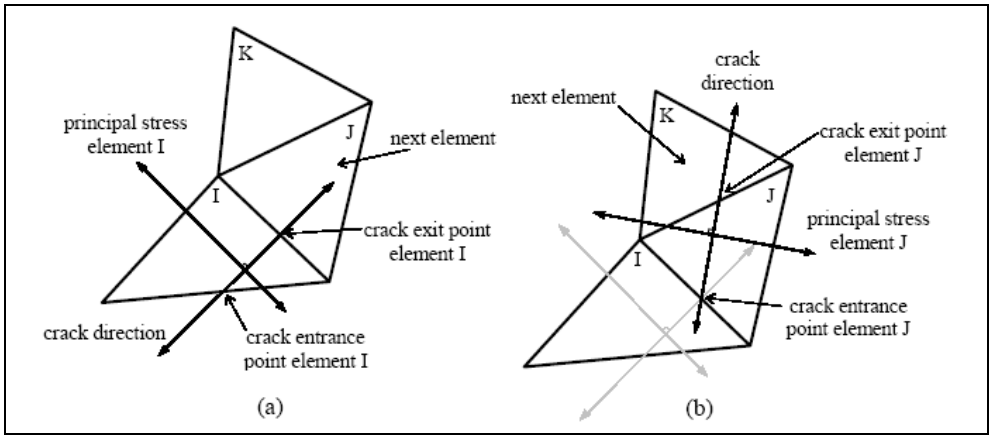

Figure 5.8 Exit point of element I (a); new potential element J and its entry point (b).

- Determine the next *potential element* on the crack for the current time step. This is the neighbouring element whose face in common with the current element corresponds with the face where its exit point is located. The element is marked as a potential element belonging to this crack.
- Determine the *entry point* coordinates. The entry point of the new element on the crack is located at the same coordinates of the exit point of the previous element, see Figure 5.8b.
- Repeat the three previous steps, taking the new potential element as the crack tip element.

For each crack, the previous procedure is repeated until one of the following criteria is satisfied:

a. *Stress threshold criterion*. Element tracking and labelling is stopped when the principal tensile stress is lower than a threshold defined by

the user. The experience has demonstrated that 75% of tensile strength usually works well.

b. *Crack meeting criterion*. The procedure stops when a previously damaged element, or an element marked as a potentially cracking one, is found along the current crack. This means that two cracks have met, and from then on they will be considered as a single one.

c. *Boundary criterion*. When the exit point of an element is on the boundary of the structure, the cracking process finishes.

3. Once any of the previous criteria is reached, the current crack is considered totally developed and the next one is studied, by restarting the cycle. Finally, after applying this procedure to all the cracks, each element will have one of the three following labels:

- *Intact element, not able to damage* (out of potential crack track; it will keep elastic behaviour during the current time step)
- *Intact element, able to damage* (in a potential crack track; it will initiate inelastic behaviour if the material strength is reached)
- *Damaged element* (belonging to a crack consolidated in previous time steps; it will develop inelastic behaviour during the rest of the calculations)

The analysis procedure recognizes these labels and activates the corresponding constitutive law (elastic or damage) in each element for the current time step. Also, once the stresses have been updated and the damaged indexes are known, the elements with potential cracking that really suffer damage are relabelled as included in a consolidated crack for the rest of calculations. Finally, elements potentially cracking that do not suffer damage are restored to their original status, i.e. unlabelled.

5.3.3 Maximum Curvature Criterion

The implementation of the crack tracking algorithm in the form described in Sections 5.3.1 and 5.3.2 leads to some problems in case of bending stress states. Figure 5.9 shows the finite elements simulation of an advancing flexural crack in the middle of a 3-point loaded concrete beam. The contour of tensile damage is zoomed in the proximity of the neutral axes, as well as the tensile main directions. As can be seen, since the algorithm assumes the direction of the crack to be perpendicular to the main tensile stress, the track should propagate from the crack tip (element A) to element B and then to element C. This is obviously erroneous, because the vertical crack should go up to the element D. Therefore, the local crack tracking technique needs a specific device to overcome such a drawback.

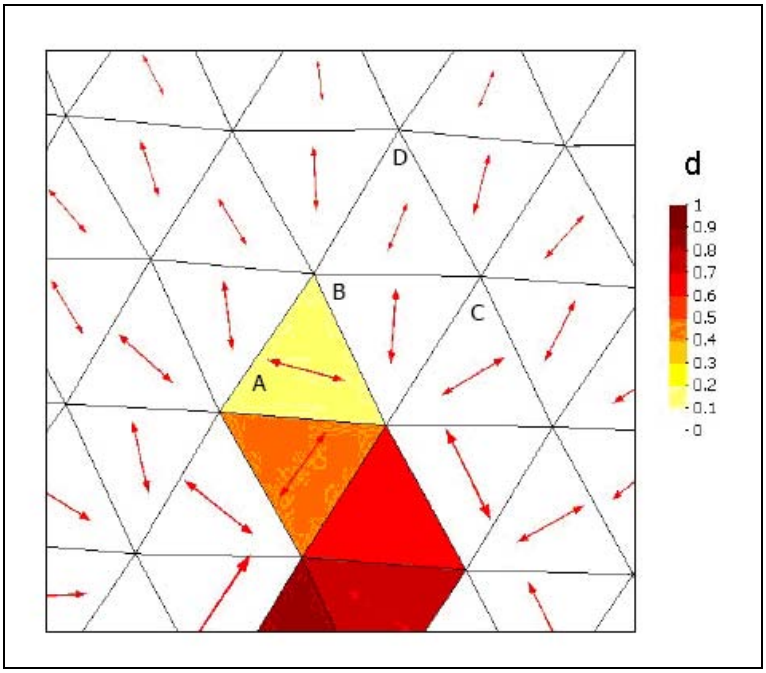

Figure 5.9 Crack “about-turn” in the proximity of the neutral axes, under bending conditions.

Clemente *et al.* (2008) introduced the *maximum curvature criterion* in order to correct such spurious changes of propagation direction. The procedure consists in identifying and correcting the sudden change of curvature in the crack track, before marking each potential element. Making reference to Figure 5.10, the following parameters are considered:

- Crack direction vector for the current element V_e.
- Crack average direction vector V_f. It is equal to the vectorial sum of all the elemental cracking vectors $V_{e,i}$. All the elements belonging to the crack are considered in the calculations, both the potential at the current time step and the consolidated at the previous time steps.
- Angle α between V_f and V_e.
- Maximum curvature angle $\bar{\alpha}$, defined by the user at the beginning of the calculations.
- Vector $\bar{V}_f$ which forms an angle $\bar{\alpha}$ with vector V_f.

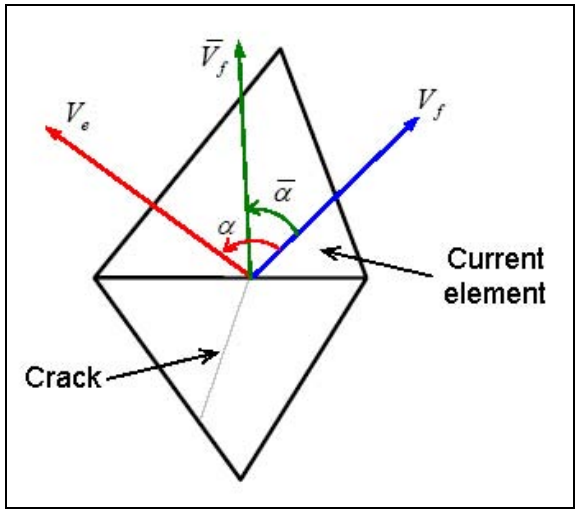

Figure 5.10 Maximum curvature criterion.

If it results that $\alpha \leq \bar{\alpha}$, the considered element is marked as potential for the current time step with a corresponding direction V_e. Then, the following element of the crack is considered.

If it results that $\alpha > \bar{\alpha}$, the crack direction is deflecting sharply and a correction is needed. Two possibilities are available:

- Use V_f instead of V_e. In this case, we impose the crack to maintain the average direction exhibited until the step considered. This is feasible for problems characterized by straight or low curvature cracks.
- Use $\bar{V}_f$ instead of V_e. This case permits to allow for curved cracks, but it is necessary to calculate vector V_f making reference to a limited number of elements. This number is another parameter defined by the user.

Once the most convenient possibility is chosen, the standard procedure is followed, i.e. the element is marked as potential and the new one is considered.

5.3.4 Validation Example

The numerical analysis of a holed strip subjected to uniaxial stretching is now considered, in order to point out the difference between a traditional smeared damage model and its enhanced version improved by a local crack tracking algorithm.

The example is solved using the continuum isotropic damage model presented in Chapter 2 with exponential softening, adjusted according to the element size. The following material properties are assumed: Young's modulus E = 30 MPa, Poisson's ratio ν = 0.2, tensile strength f = 2 kPa and mode I fracture energy G_f = 100 J/m^2.

The discrete problem is solved incrementally, in a (pseudo) time step-by-step manner. In all cases 200 equal time steps are performed to complete the analyses.

Within each step, a modified Newton–Raphson method (using the secant stiffness matrix), together with a line search procedure, is used to solve the corresponding non-linear system of equations. Convergence of a time step is attained when the ratio between the norm of the iterative and the incremental norm of the computed displacements is lower than 1%. Calculations are performed with an enhanced version of the finite element program COMET (Cervera *et al.* 2002), developed by at the International Center for Numerical Methods in Engineering (CIMNE). Pre- and post-processing is done with GiD (2002), also developed at CIMNE.

The holed strip is subjected to axial vertical straining imposed at both ends. A two-dimensional plane strain condition is assumed. Because of the symmetry of the domain and boundary conditions, only one half of the domain (the right half) is considered. Dimensions of the specimen are 200 x 400 mm^2 and the radius of the perforation is r = 10 mm. This example is selected because the initial geometry does not present any singular point; tensile stresses are larger in the vicinity of the perforation and damage starts there. Also, it represents an example of pure mode I fracture. The computational domain is discretized in two different unstructured meshes with average mesh sizes of h_e = 5 mm (2023 nodes) and h_e = 2.5 mm (7648 nodes).

Two separate analyses are performed using both meshes. First, a traditional smeared damage model is used for finite elements calculations. The computed deformed shapes of the strip in the vicinity of the perforation are shown in Figure 5.11 for the two different meshes ((half)-imposed vertical displacement d = 0.1 mm, with a displacement amplification factor of 100; the other half-imposed displacement is applied at the opposite end of the strip). The different element sizes in both meshes can be appreciated in this figure. As shown, the crack initiates horizontally in both meshes, but it soon departs from this course to spuriously follow a line of elements along the mesh bias (30° in this case).

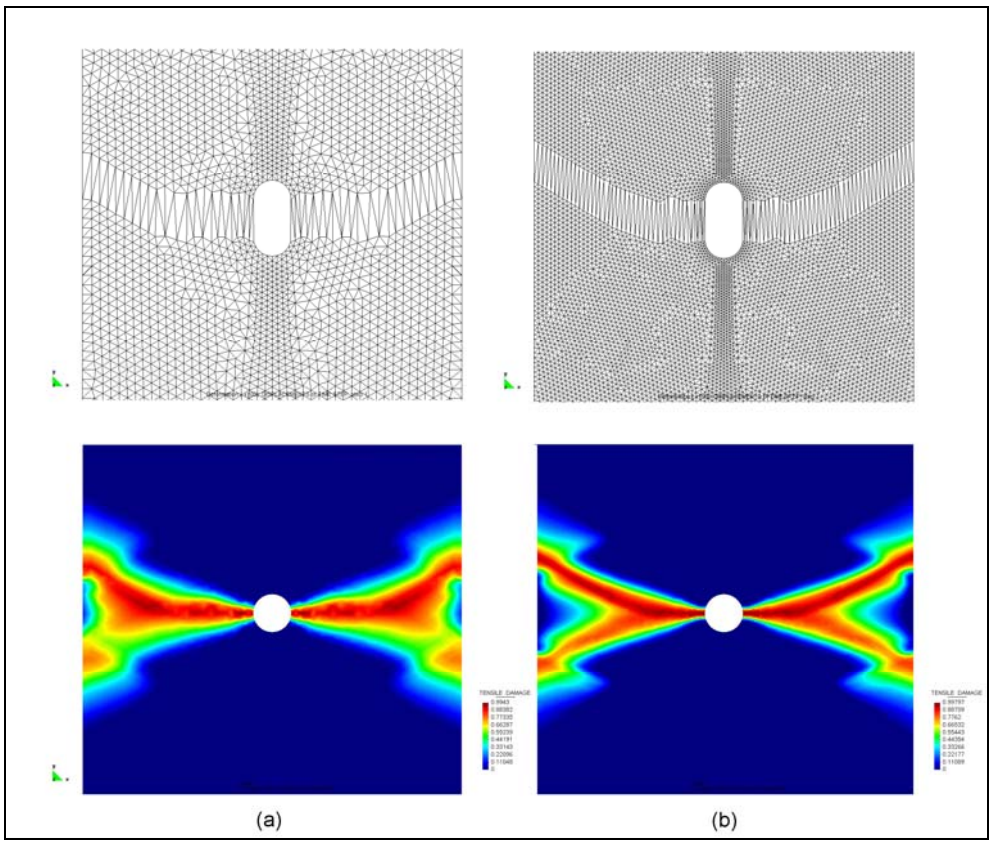

Figure 5.11 Deformed mesh (x100) and tensile damage contour with a smeared damage model: mesh with average size h_e = 5 mm (a) and mesh with average size h_e = 2.5 mm (b).

Then, a smeared damage model with crack tracking technique is adopted in the analyses. Figure 5.12 shows the computed cracks in both the meshes, which follow exactly the horizontal axis of symmetry of the perforation, even if the elements in neither of the two meshes are aligned along this line.

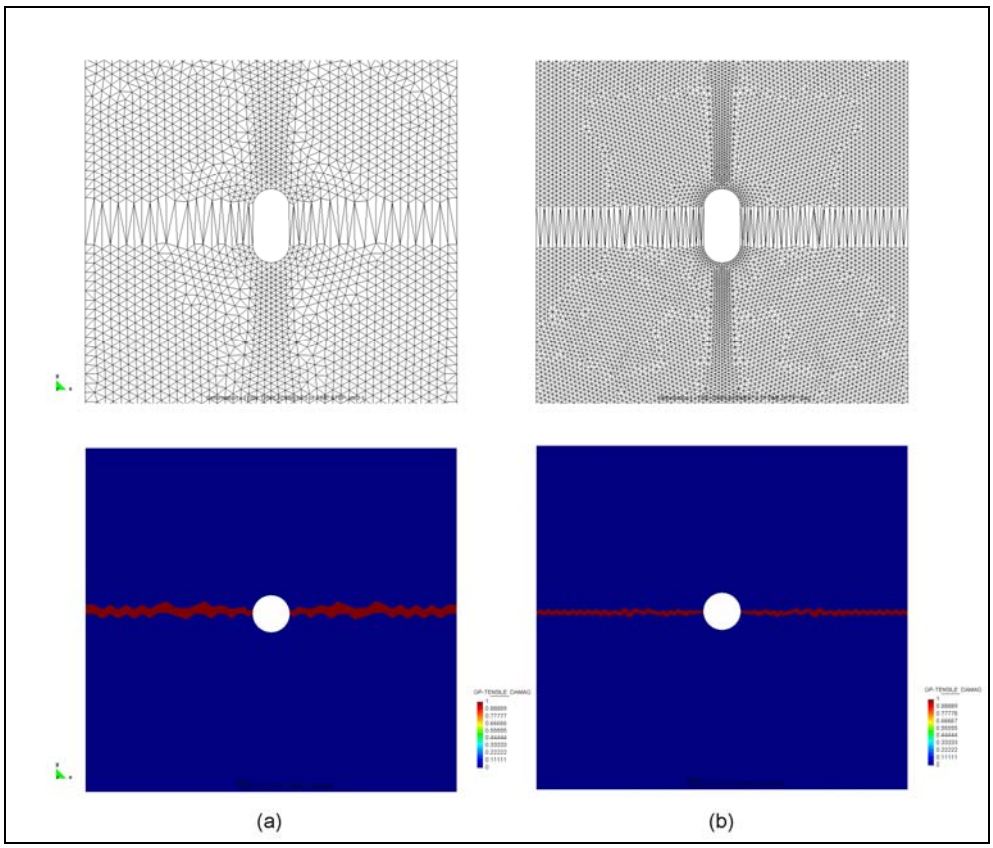

Figure 5.12 Deformed mesh (x100) and tensile damage contour with the localized damage model: mesh with average size h_e = 5 mm (a) and mesh with average size h_e = 2.5 mm (b).

Figure 5.13 shows the (half)-load vs. (half)-imposed vertical displacement curves obtained in the two analyses with crack tracking technique. Because in this example the strain field is almost uniform prior to the inception of the cracks, the response curve is almost linear until the cracks form suddenly, with a nearly exponential softening branch after the limit load is attained.

Note that the overall global response is satisfactorily similar upon mesh refinement, with the total area under the load–displacement curve converging to the correct amount of energy dissipated to create the cracks. This should be equal, for half of

the domain, to $D_{tot} = G_f \cdot l_{cr} \cdot t = 100 \cdot 0.09 \cdot 1 = 9\,J$, where l_{cr} is the length of the crack (0.09 m) and t is the thickness (1 m). The area under the curves is almost exactly, half of this value. No spurious brittleness is observed when the size of the elements is reduced.

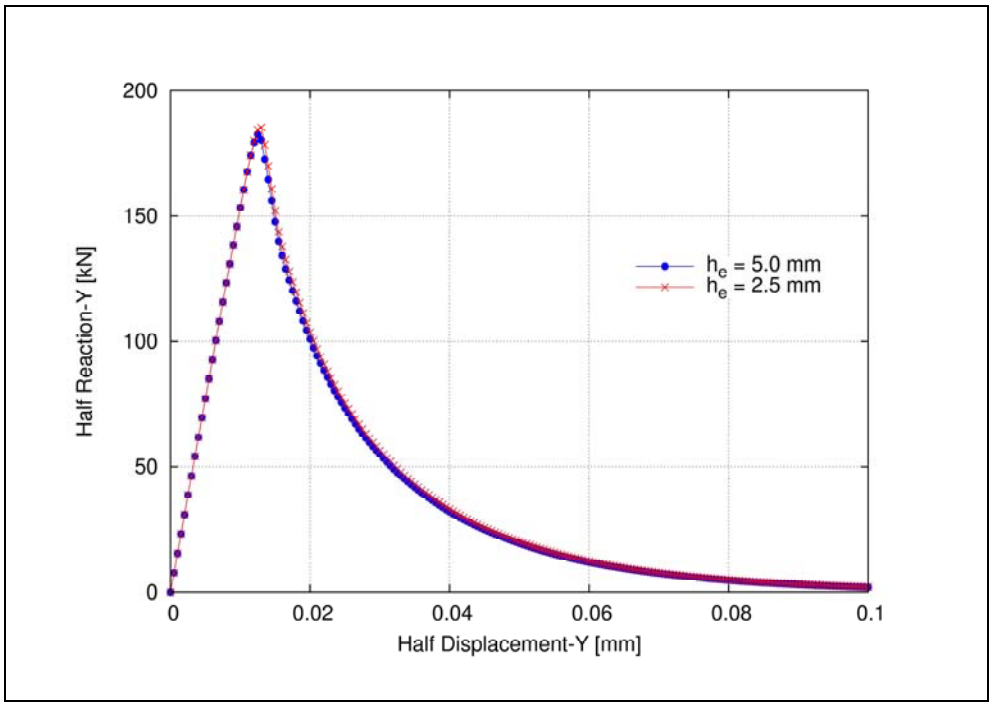

Figure 5.13 Load versus displacement for holed strip with the localized damage model. Comparison between different mesh sizes.

5.4 Localized Damage Model for Orthotropic Materials

The local crack tracking technique which has been detailed in the previous Section has been used by Clemente *et al.* (2006) to analyze the response of the Mallorca Cathedral under gravity and seismic forces. Compared with the traditional smeared cracking approach, the tracking method has shown a better capacity to predict

realistic collapsing mechanisms; the resulting damage in the ultimate condition appears localized in individual cracks, thus is more realistic; the computed ultimate loads become less sensitive to the variation of the tensile strength and other material parameters. Owing to the huge dimension of the structure and being the first application of such a model to a complex building, the authors have modelled masonry as an isotropic material in order to simplify the analysis.

The present work has been providing a simple model with an original formulation which permits to account for the orthotropy of the material in an effective way. The versatility of the model allows us to cover a wide range of applications. Therefore, the damage model detailed in Chapter 4 can also be combined with a localized cracking approach, making use of the crack tracking technique. In this way, an efficient tool is obtained, without increasing considerably the computational cost.

Nevertheless, it is necessary to combine carefully the crack tracking and the mapped tensor-based algorithms, in order to implement a fully operative localized damage model for orthotropic materials.

The tracking algorithm is once again executed at every time step during the analysis, just before the stress evaluation. The same operations described in Chapter 5.3 are followed, but several adjustments are necessary. In simplistic terms, it is necessary to map all the stress based parameters in the *fictitious space*. Therefore, the crack tracking process is fully carried out in that space.

The algorithm is divided into two steps, i.e. the new cracks detection and the cracks propagation evaluation. Such procedures are schematized in Tables 5.1 and 5.2, respectively.

Table 5.1 New cracks detection procedure.

START

Input data:

- list of *fictitious main tensile stresses* $\left(\sigma_I^*\right)_{i_b}$ in boundary elements at time step *n*-1

- list of crack root elements at time step *n*-1

- LOOP ON BOUNDARY ELEMENTS i_b= 1, NBOUEL
  1. Check the isotropic Rankine criterion defined in the *fictitious space:*

     IF $\Phi_{i_b}^{+*} = \left(\left\langle \bar{\sigma}_1^* \right\rangle\right)_{i_b} - f^* < 0 \quad \Rightarrow$ *GO TO* 4

     ELSE $\Rightarrow$ Label new potential crack root element at time step *n*.
  2. Check the exclusion radius criterion.
  3. Compute the crack root coordinates.
  4. Next boundary element: $i_b = i_b + 1 \Rightarrow$ *GO BACK TO* 1
- END LOOP ON BOUNDARY ELEMENTS

Output data:

- list of potential crack root elements at time step *n*

- list of crack root coordinates at time step *n*

END

Table 5.2 Cracks propagation evaluation.

START

Input data:

- list of potential crack root elements at time step *n*

- list of crack root coordinates at time step *n*

- list of *fictitious main tensile stresses* $\left(\sigma_1^*\right)_i$ and *fictitious main tensile directions* $\mathbf{p}_j^*$ for all the elements at time step *n*-1

- list of elements belonging to consolidated cracks at time step *n*-1

- LOOP ON CRACKS k = 1, NCRACKS
  1. Define the tip of the crack (element next to only one damaged element or potential crack root elements at time step *n*)
  2. Determine the exit point coordinates of the tip of the crack (using the direction perpendicular to the *fictitious principal tensile direction* $\mathbf{p}_j^*$ of the element)
  3. *IF* $\alpha > \bar{\alpha} \Rightarrow$ Maximum curvature criterion (vectors V_f and V_e are computed in the *fictitious space*)
  4. Determine the next potential element on the crack for time step *n*
  5. Determine the entry point coordinates of next potential element for time step *n* (equal to exit point coordinates of the tip of the crack element).
  6. The potential element on the crack becomes tip of the crack
  7. *IF* current element is a boundary element $\Rightarrow$ *GO TO* 10
  8. *IF* current element stays between two marked elements (two cracks join) $\Rightarrow$ *GO TO* 10
  9. *IF* for the current element $\left(\sigma_I^*\right)_i \geq 0.75\ f^*$ (criterion in the *fictitious space*) $\Rightarrow$ *GO TO* 1

     ELSE $\Rightarrow$ *GO TO* 10
  10. Next crack: $k = k + 1 \Rightarrow$ *GO BACK TO* 1
- END LOOP ON CRACKS

Output data:

- List of intact elements, not able to damage (out of potential crack track) at step *n*
- List of intact elements, able to damage (in a potential crack track) at step *n*
- Damaged element (belonging to a crack consolidated at time step *n*-1)

END

The tracking algorithm output data, i.e. the elements flags (intact element able to damage, intact element no able to damage, damaged element), are then recalled inside the constitutive model subroutine after the mapping into the fictitious space has been performed. Once the stresses and the damaged indexes have been computed in the fictitious space, the elements with potential cracking that really suffer damage are included in a consolidated crack. Elements potentially cracking that do not suffer damage are unlabelled instead.

5.4.1 Validation Example

The benchmark example of Section 5.3.4 is considered. The geometry is once again the same, but the material is assumed orthotropic. This could be the case, for instance, of a metal strip in which the rolling direction does not coincide with the axes of the specimen. When it is pulled in tension, the neck does not form directly across the strip, but at an oblique angle which depends on the state of anisotropy (Hill, 1950).

The following material properties are assumed: Young's moduli E_x = 20 MPa, E_y = 30 MPa, Poisson's ratio v_{xy} = 0.2, real tensile strengths f_{11} = 1 kPa, f_{22} = 2 kPa, f_{12} = 1 kPa, mode I fracture energy $G_{f,1}$ = 37.5 J/m^2 and $G_{f,2}$ = 100 J/m^2. The orthotropy angle is θ = 30°. The parameters in the fictitious space are E^* = 20MPa, v^* = 0.2, f^* = 1 kPa, G^* = 37.5 J/m^2.

The holed strip is subjected to axial vertical straining imposed at both ends. A two-dimensional plane stress condition is assumed. The computational domain is discretized in an unstructured mesh with average mesh sizes of h_e = 5 mm (2023 nodes). Because of the symmetry of the domain and boundary conditions, only one half of the domain (the right half) is considered.

First, a traditional smeared crack approach is adopted in combination with the damage model for orthotropic materials, which has been proposed in Chapter 4.

The computed deformed shape of the strip in the vicinity of the hole is shown in Figure 5.14a, for an half-imposed vertical displacement d = 0.1 mm. As shown, the crack follows a favourable path given by the spatial discretization. The situation is evident by analyzing the corresponding contour of the tensile damage variable computed in the Gauss points. The solution is not reliable, since the crack track spuriously follows a line of elements along the mesh bias.

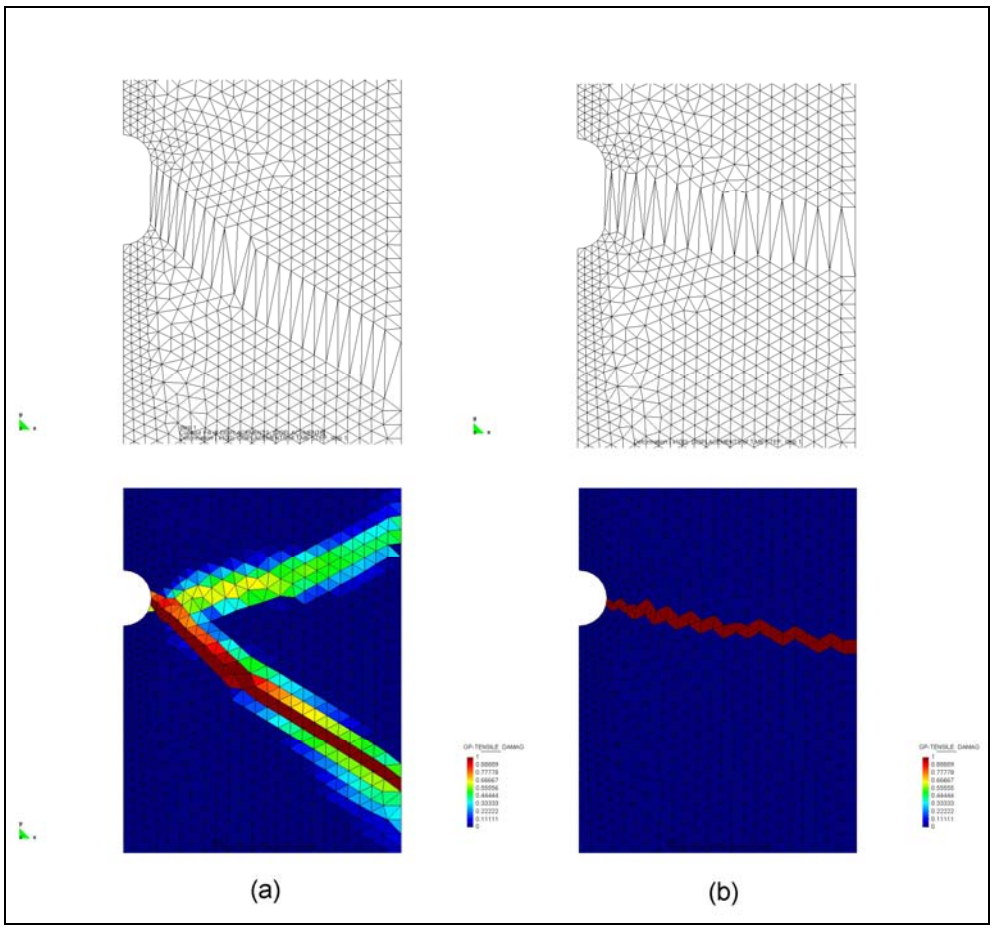

Figure 5.14 Half-deformed mesh (x100) and tensile damage contour: smeared damage model (a) and localized damage model (b).

Then, we adopt the localized damage model for orthotropic materials in finite elements calculations. As shown in Figure 5.14b, the crack-tracking algorithm leads to a solution which is definitely mesh-unbiased. The direction of propagation of the crack is determined in an objective manner, since it does not depend on the spatial discretization assumed.

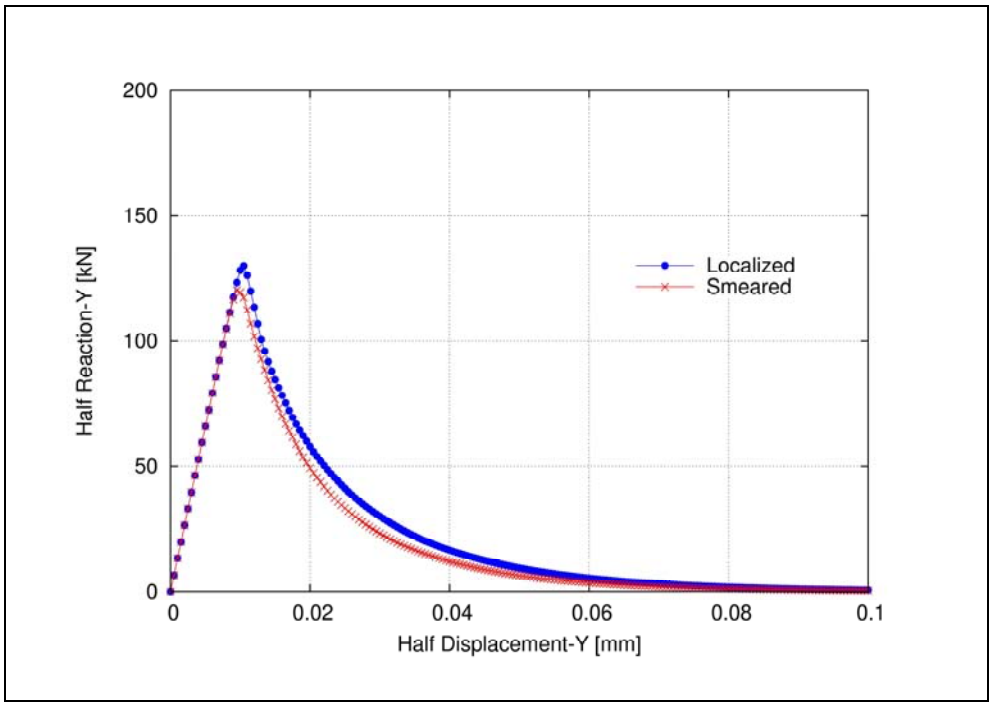

Figure 5.15 Load versus displacement for holed strip. Comparison between localized and smeared damage models.

Figure 5.15 shows the (half)-load vs. (half)-imposed vertical displacement curves obtained by the two analyses. After preliminary uniform extension, which corresponds to the elastic branch of the curve, necking begins from the hole, which is a geometrical non-uniformity. The phenomenon of cracking leads to a nearly exponential softening branch after the limit load is attained. Comparing the curves

obtained by the two approaches, the smeared damage approach provides a lower estimate of the ultimate load.

5.5 Finite Elements Analysis of a Masonry Shear Wall

The localized damage model for orthotropic materials is validated next via a comparison with experimental results available in the literature. In particular, we consider the shear wall tests carried out by Raijmakers and Vermeltfoort (1992).

In this study, we will analyze the walls with a central opening, here denoted J2G and J3G. They have dimensions 990 × 1000 mm^2 and are constituted by 18 courses, from which 16 courses are active and 2 courses are clamped in steel beams, see Figure 5.16a.

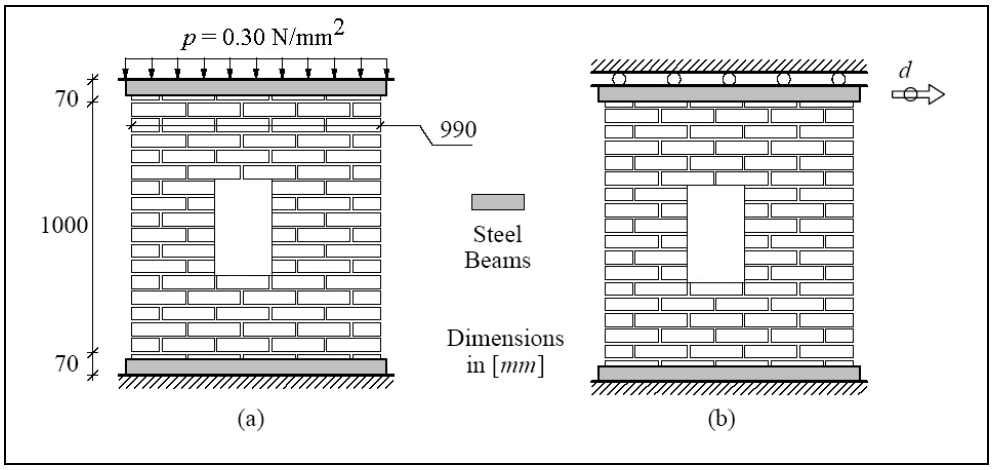

Figure 5.16 Geometry and loading phases for Raijmakers and Vermeltfoort (1992) shear walls: vertical loading (a); horizontal loading under displacement control (b).

The walls are made of wire-cut solid clay bricks with dimensions 210 × 52 × 100 mm^3 and 10 mm thick mortar, prepared with a volumetric cement:lime:sand ratio of 1: 2: 9. Vertical precompression uniformly distributed forces p = 0.30 N/mm^2

are applied to the walls, before a horizontal load is monotonically increased under top displacement control *d* in a confined way, i.e. keeping the bottom and top boundaries horizontal and precluding any vertical movement, see Figure 5.16b.
The experimental crack patterns for the two tested walls are shown in Figure 5.17. Diagonal cracks arise from the opening and propagate up to the top and the bottom of the wall. In addition, tensile cracks arise from the vertical external sides of the wall. They involve the two piers next to the opening. Such cracks occur at the top of the left pier and at the bottom of the right one.

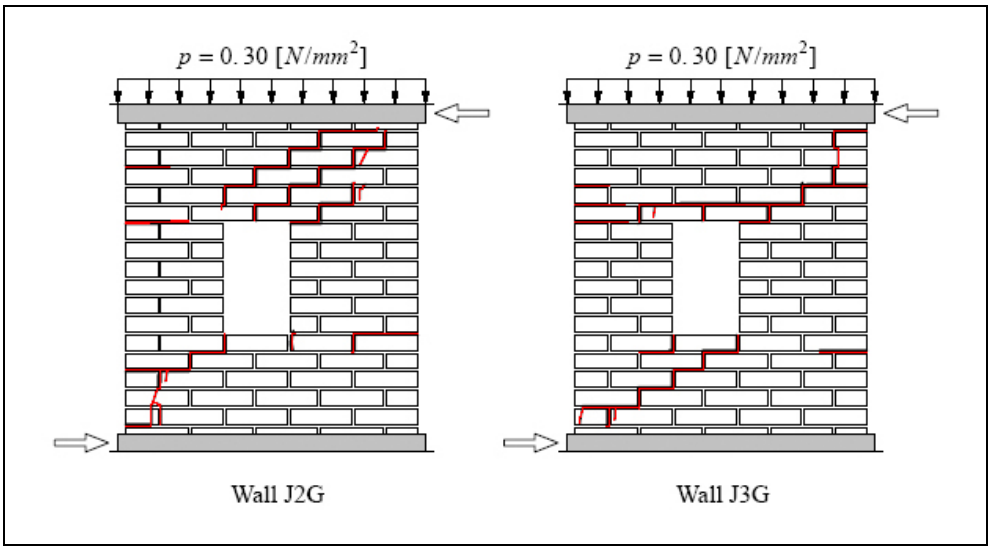

Figure 5.17 Experimental crack patterns of the walls tested by Raijmakers and Vermeltfoort (1992).

The resulting collapse mechanism is schematized in Figure 5.18. As can be seen, the kinematism is amenable to four hinged rigid blocks, and it is activated when compressive failure occurs in the highlighted zones.

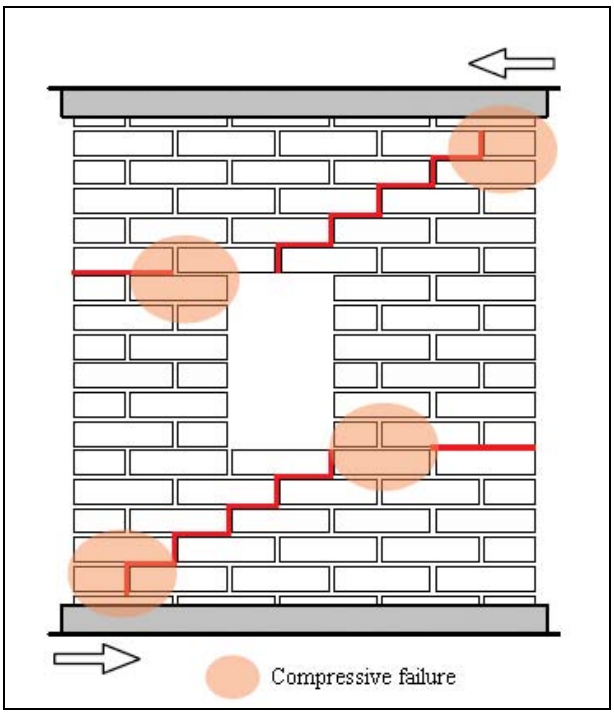

Figure 5.18 Collapse mechanism of the tested shear walls.

For the numerical analysis, the wall is represented by 5982 bi-dimensional plane-stress 3-noded linear triangular elements. The computational domain is discretized with an unstructured mesh with average mesh size of h_e = 20 mm (3128 nodes). Calculations are performed again with an enhanced version of the finite element program COMET (Cervera *et al.* 2002). Pre- and post-processing is done with GiD (2002).

The discrete problem is solved incrementally, in a (pseudo) time step-by-step manner. The analysis is completed by means of 500 equal time steps. Within each step, a modified Newton–Raphson method (using the secant stiffness matrix), together with a line search procedure, is used to solve the corresponding non-linear system of equations. Convergence of a time step is attained when the ratio between

the norm of the iterative residual forces and the norm of the total external forces is lower than 1%.

The values of the mechanical parameters used in the numerical analysis to describe the masonry behaviour are summarized in Table 5.3. Some of them are the mechanical characteristics of masonry provided by Raijmakers and Vermeltfoort (1992), others are data obtained via a homogenization procedure (Lourenço, 1996), and finally a few parameters have been chosen by fitting the experimental data.

Table 5.3 Parameters adopted in the numerical analysis.

Material Properties					
$E_1=E^*$	7520 MPa	$f_{11}^{+}=f^{+}*$	0.35 MPa	$f_1^{-}=f^{-}*$	6.30 MPa
E_2	3960 MPa	f_{22}^{+}	0.25 MPa	f_2^{-}	4.50 MPa
$v_{12}=v^*$	0.09	f_{12}^{+}	0.30 MPa	f_{12}^{-}	3.00 MPa
v_{21}	0.05	$G_{f,1}^{+}=G^{+}*$	50 J/m^2	$G_{f,1}^{-}=G^{-}*$	20000 J/m2
G_{12}	1460 MPa	$G_{f,2}^{+}$	48 J/m^2	$G_{f,2}^{-}$	19400 J/m2

The crack tracking technique has been set by imposing a minimum distance of 350 mm between the cracks (exclusion radius criterion) and a maximum value for angle $\bar{\alpha} = 32°$ (maximum curvature criterion).

The comparison between the calculated and experimental load-displacement diagrams is shown in Figure 5.19. The results agree reasonably well, both in the elastic field and in the inelastic one. This indicates that the deformability of the wall as well as the failure mechanism are properly represented.

The experimental behaviour of the walls is well captured by the numerical model as illustrated in Figure 5.20, which shows the computed deformed shape (imposed horizontal displacement d = 20 mm, with a displacement amplification factor of 30). Note the cracks opening that causes the global failure kinematism.

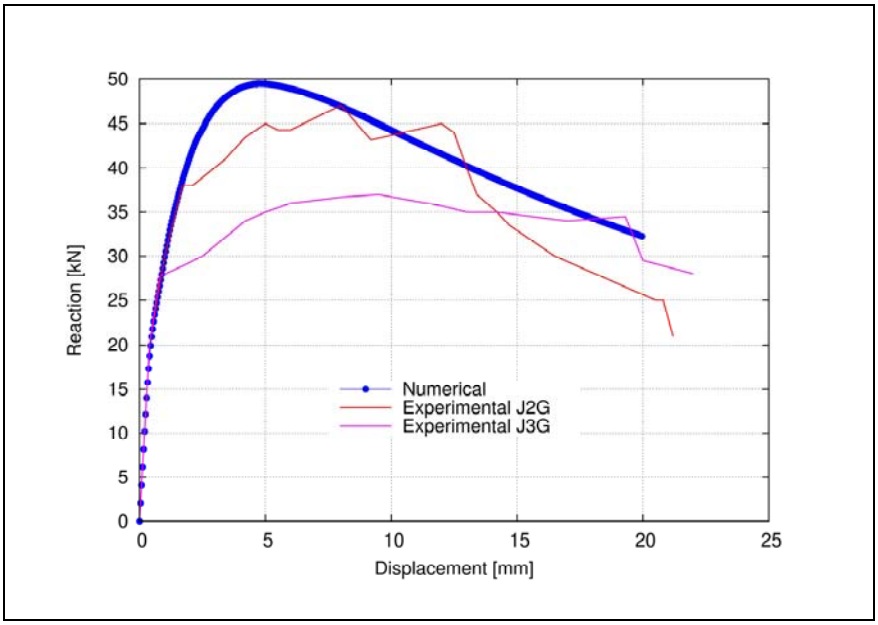

Figure 5.19 Walls J2G and J3G. Load vs. displacement diagrams.

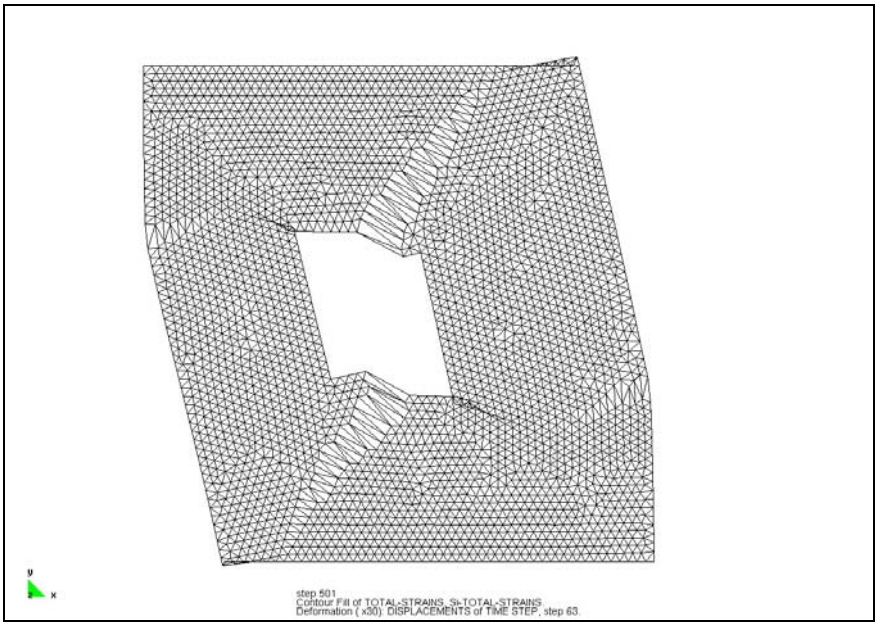

Figure 5.20 Computed deformed mesh (x30).

Figure 5.21 illustrates the tensile damage contour. As shown, the damage in the ultimate conditions is represented in the form of discrete cracks, thanks to the tracking technique which permits to describe the tensile cracks localization phenomenon. Obviously, the model cannot closely reproduce the experimental evidence depicted in Figure 5.17, since it entails a macroscopic approach to the structure, as discussed in Chapter 1. However, the numerical model shows his capability to capture the real behaviour observed in the experiments. In fact, the tensile cracks related to the failure mechanism illustrated in Figure 5.18 are properly represented.

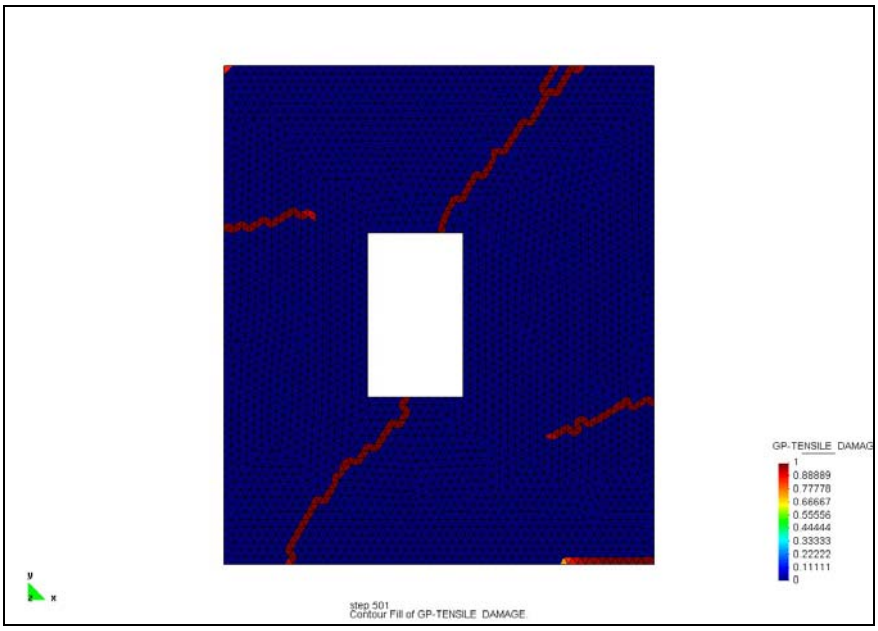

Figure 5.21 Tensile localized damage contour.

Figure 5.22 shows the maximum principal strain vectors. The concentration of the displacement gradients (strains) in the elements lying along the computed crack is evident. Therefore, the resolution of the cracks is optimal for the mesh used. The correct failure mechanism has been predicted although the directions of the

computed maximum principal strain vectors (as the related vectors of maximum principal effective stress) are clearly dependent on the mesh bias (Cervera, 2008a).

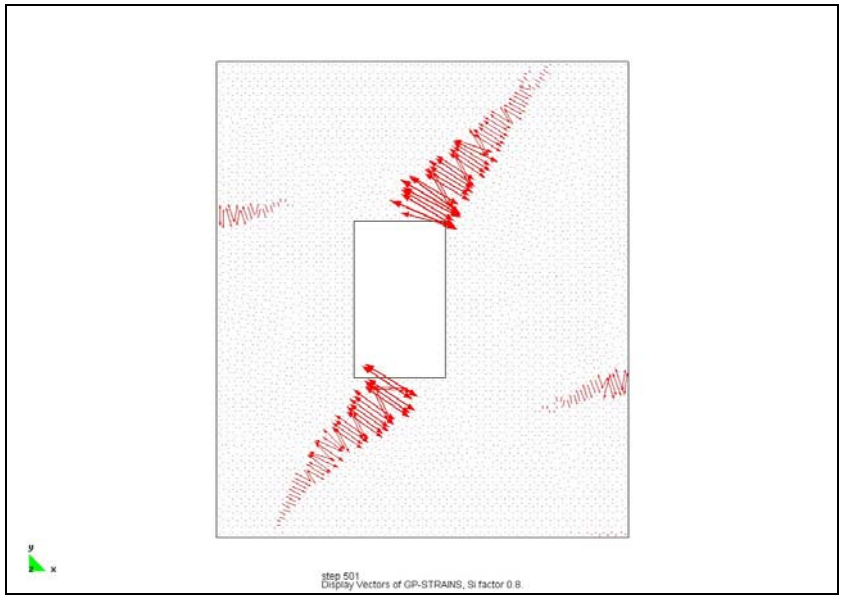

Figure 5.22 Vectors of maximum principal strain.

Figure 5.23 shows the compressive smeared damage contour. As can be seen, the model predicts correctly the location of the areas interested by material compressive failure. The failure mechanism is properly represented. We notice the compressed struts located next to the opening which fail at both of their ends.

Finally, Figure 5.24 reports the tensile damage contour obtained by a finite element analysis with a traditional smeared damage approach. It is evident as the damage spreads unrealistically. The comparison with Figure 5.21 points out a very important issue. Although it seems that almost the same result has been obtained, the smeared model is considerably mesh-bias dependent: the crack follows a favourable path given by the spatial discretization. This would imply lost of solution objectivity when different inclination of the mesh would be considered in the discrete problem.

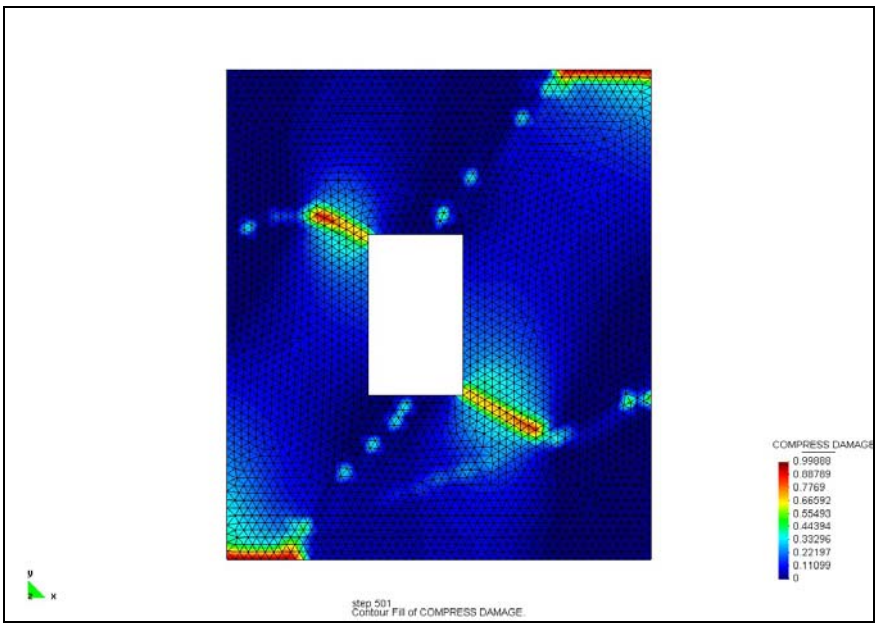

Figure 5.23 Compressive damage contour.

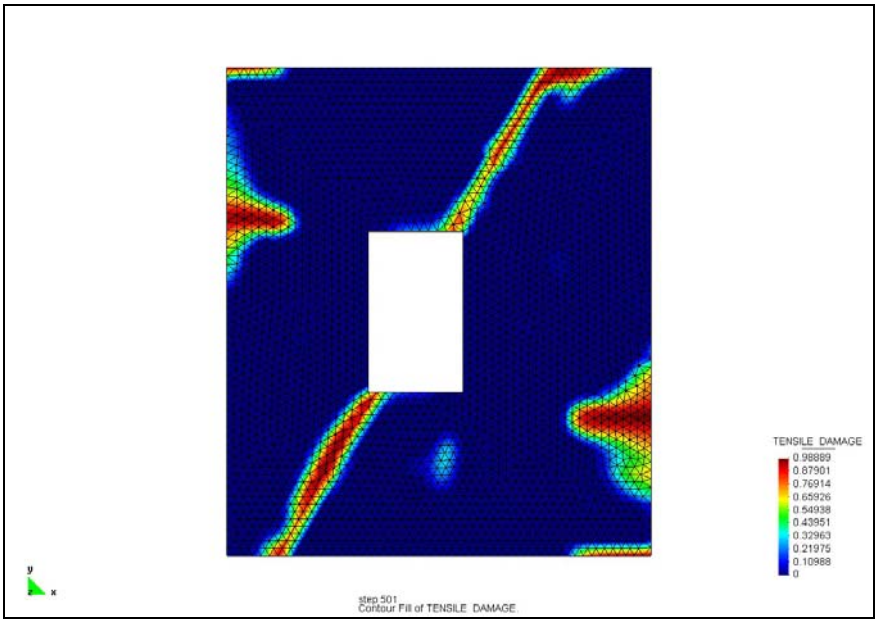

Figure 5.24 Tensile damage contour for a smeared damage model: mesh-bias dependence.

5.6 Conclusions

In this Chapter, we have presented the formulation of a Localized Damage Model for Orthotropic Materials. The model is based on the traditional smeared cracking approach, modified in such a way that it can reproduce localized individual (discrete) cracks. This is achieved by means of a *local crack tracking technique*. The corresponding algorithm detects the point in the discrete problem where a crack is originated and then it lets the crack develop as a function of the direction of the main tensile stress. Then, it marks a track of finite elements pertaining to the crack path which can experience potential damage. The crack is forced to develop along a single row of finite elements. The method works with a flags system, where finite elements are labelled to distinguish which elements are going to damage during the current time step. The fracture energy normalization respect to the characteristic length ensures that dissipation will be element-size independent.

The crack tracking model enables the simulation of more realistic damage distributions than the original smeared-crack model. The localized cracks predicted by the tracking model reproduce consistently the ones usually observed on masonry structures, which develop gradually and lead to the full collapsing mechanism. In turn, the smeared-crack model describes damage in a widely distributed, unrealistic way. The tracking model represents a more suitable method to predict the structural behaviour of masonry structures, without requiring significant additional computation cost. The algorithm has been implemented for 2D plain-stress problems using three-noded elements (constant strain triangles).

The crack tracking technique which has been presented is inspired to the format proposed by Clemente *et al.* (2006) but an important additional improvement has been supplied. The model which has been presented in Chapter 4 has been included in the algorithm, in order to account for the orthotropic behaviour of the material. The mapped tensor and crack tracking algorithms have been carefully combined in

order to obtain an efficient and reliable tool. It has been validated via a comparison with experimental results available in the literature. In particular, the finite element analysis of a shear wall has been carried out, showing good agreement with the experimental evidence. Compared with the result obtained by means of a smeared crack approach, the localized damage model for orthotropic materials has shown a better capacity of predict realistic collapse mechanisms and a better description of damage distribution on the structure in the ultimate condition. Moreover, the use of a crack tracking algorithm considerably helps to avoid the dependence of the predicted failure mechanisms on the mesh directional bias. This leads to solution objectivity when different inclinations of the mesh are considered in the discrete problem.

Chapter 6.

Summary and Conclusions

The growing concern about the preservation of ancient constructions, particularly of the architectural heritage, has led to great innovation in the development of specific techniques for studying structures made with traditional materials. This research represents an original contribution to numerical strategies aimed to the structural analysis of masonry constructions. Reliable and accurate numerical methods reveal to be fundamental in the engineering calculations and in supporting the definition of rational design rules. Therefore, a great effort has been devoted to this field.

The Chapter 1 of the thesis reports a brief review of the most recent trends in computational modelling of masonry structures. The formulation of an appropriate numerical method for analysing masonry structures must start from the knowledge of the peculiarity of such a composite material, which is characterized by a very particular mechanical behaviour. Different approaches to the problem are possible. Micro-modelling is probably the best tool available to analyse and understand the

real behaviour of masonry, particularly concerning its local response. It leads to very accurate results, but requires an intensive computational effort. Since the main objective of the thesis is to provide an efficient numerical tool for the nonlinear analysis of large and complex structures, we have aimed the research at the *macro-modelling* approach. In this case, the material is represented by a fictitious homogeneous continuum whose behaviour is described by constitutive laws based on Continuum Mechanics Theory.

We have focused on the constitutive laws based on *Continuum Damage Mechanics*, which provides a powerful and general framework for the derivation of consistent material models suitable for many engineering fields. Such a theory is characterized by simplicity in the formulation, versatility, compatibility with other theories (Plasticity, Fracture Mechanics, Viscoelasticity) and consistency, since it is based on the thermodynamics of irreversible processes, the internal state variable theory and relevant physical considerations. In Chapter 2 we have discussed all this features, together with the basic concepts. Among the different models available in the literature, we have turned our attention to the ones based on the assumption of one or more scalar damage variables. Such models provide a simple constitutive model characterized by a favourable strain-driven format consistent with standard displacement-based finite element codes. This leads to high algorithmic efficiency, which is the most valuable feature for a model intended to be used in large scale computations, in which high algorithmic efficiency is required.

In the case of Continuum Damage finite element models, isotropic criteria are usually preferred in the analysis of complex masonry structures, because of their simplicity, hence the need for only few material parameters. Moreover, smeared damage models are generally adopted even if they only provide general information about the level of damage expected on the structure. This work constitutes a step further from such a situation. At first, attention has been paid to aspects related to the modelling of the material orthotropic behaviour.

Chapter 3 has presented an original methodology related to the aforementioned topic. It is based on the concept of *mapped tensor* from the anisotropic real space to the isotropic fictitious one. The proposed theory, which in literature has been mainly used in the framework of Plasticity, is a generalization of classical theories and allows one to use the models and algorithms developed for isotropic materials. It is based on establishing a one-to-one mapping relationship between the behaviour of an anisotropic real material and that of an isotropic fictitious one. Therefore, the problem is solved in the isotropic fictitious space and the results are transported to the real field. The relationship between the two spaces is expressed in terms of a *transformation tensor* which contains all the information concerning the real orthotropy of the material. A first preliminary model adopts an isotropic scalar damage model in the fictitious space. The final result is an implicit damage model for orthotropic materials able to reproduce the overall nonlinear behaviour, including stiffness degradation and strain-hardening/softening response. This general formulation permits to adjust an arbitrary isotropic criterion to the particular behaviour of the orthotropic material. The orthotropic elastic and inelastic behaviours can be modelled in such a way that totally different mechanical responses can be predicted along the material axes. The model has been fully formulated for the 2-dimensional case but it can be easily extended to the 3-dimensional one, by providing additional material parameters. Initial applications of the model have shown promising results.

In Chapter 4 the model has been improved further, by accounting for the different material behaviour in tension and compression. The aim of studying a real material via an equivalent fictitious solid has been achieved by means of the appropriate definitions of two transformation tensors related to tensile or compressive states, respectively. Although the model shows potential applicability to many orthotropic materials, such as wood and fibre reinforced composites, it has been specifically formulated for masonry. The constitutive model adopted in the fictitious space

makes use of two scalar variables to monitor the local damage under tension and compression. Such a model, which is based on a stress tensor split into tensile and compressive contributions, permits to account for masonry unilateral effects, as well as for different damage criteria. The tensile Rankine and the compressive (Drucker Prager inspired) Faria isotropic damage criteria are mapped in the fictitious space, in order to provide in the real orthotropic space a composite damage threshold surface. This permits to account for different failure mechanisms, i.e. cracking in tension and crushing in compression. The internal damage parameters associated with each failure mechanism are related to the finite elements size and to the tensile or compressive fracture energies. This leads to objective results with respect to the finite element mesh size. The model is capable of predicting independent, in the sense of completely different, behaviour along the material axes. The brittleness orthotropy can also be modelled in a very easy and effective way. The strength parameters involved appear to be enough to reproduce the biaxial behaviour of all masonry types, ranging from isotropic behaviour to extreme anisotropic behaviour. This validation has been carried out by means of comparisons with experimental results on different types of orthotropic masonry.

The orthotropic nature of the Tension-Compression Damage Model adopted in the fictitious space has been demonstrated. This feature, both with the assumption of two distinct damage criteria for tension and compression, does not permit to term the fictitious space as “isotropic”. Therefore, the proposed formulation turns the original concept of “mapping the real space into an *isotropic* fictitious one” into the innovative and more general one of “mapping the real space into a *favourable* (or *convenient*) fictitious one”.

Finally, attention has been given to the role of the developed model in engineering practice. With the aim of performing reliable non linear numerical analyses of masonry structures, a *localized damage model for orthotropic materials* has been formulated in Chapter 5. The model proposed in Chapter 4 has been successfully

combined with a *local crack tracking technique*, which modifies the traditional smeared cracking approach in order to reproduce localized individual (discrete) cracks. The crack tracking process is fully carried out in the fictitious space. The implemented algorithm detects the point in the discrete problem where a crack is originated and then it lets the crack develop as a function of the direction of the main tensile stress. Then, it marks a track of finite elements pertaining to the crack path which can experience potential damage. The crack is forced to develop along a single row of finite elements. The method works with a flags system, where finite elements are labelled to distinguish which elements are going to damage during the considered time step. The crack tracking model enables the simulation of more realistic tensile damage distributions than the original smeared-crack model. The computed discrete cracks reproduce consistently the ones usually observed on masonry structures, which develop gradually and lead to the full collapsing mechanism. Moreover, the results do not suffer from mesh-bias dependence in the discrete problem. The tracking model represents a more suitable method to predict the structural behaviour of masonry structures, without requiring significant additional computation cost. The algorithm has been easily implemented in a finite element code making reference to 2D plain-stress problems and using three-noded elements (constant strain triangles). The finite element analysis of a shear masonry wall has pointed out that a stable and accurate algorithm has been achieved. The entire pre- and post-failure regimes have been properly represented. Converged solutions have been obtained even in the presence of softening behaviour. A comparison with experimental observations has shown good agreement.

In retrospect, the present study has successfully achieved the objectives defined in Chapter 1. In particular, a robust and accurate numerical tool has been developed for masonry structures analysis, both in case of new buildings design and vulnerability assessment of existing constructions. However, it is necessary to apply the formulations and techniques described in this work to a variety of

elements and structures in order to gain more experience and confidence on its usage. In addition, the following investigations can be suggested as further work:

- The extension of the damage model to the three-dimensional case. This should be relatively simple, but at the cost of providing additional material parameters. On the other hand, the local crack tracking algorithm is impossible to apply in 3D.
- The study and the comparison of different formats for the transformation tensor from the real to the fictitious space. The definition of the mathematical relationship between the two spaces could be enhanced in order to achieve an optimal mapping of the behaviour of the real solid.
- Improve the orthotropic softening model, possibly with another mapping for inelastic strains.
- The combination with homogenization procedures. At its current state, the model needs the evaluation of parameters which are obtainable from expensive experimental tests, such as the ones related to post peak behaviour and the ones performed on masonry small assemblages. The use of homogenization techniques, aimed to the determination of the elastic constants and the inelastic parameters (strengths and fracture energies), would reduce the costs and would permit to account for material properties variability.
- The inclusion in the model of the damage-induced anisotropy description. The development of damage necessarily modifies the intensity of the material anisotropy. The inclusion of such an effect is a hard task and the problem is twofold. On one hand, it is very difficult to compare the experimental evidence with the induced anisotropic damage predicted by the computational models, with the aim of choosing the most proper form of the damage tensor. On the other hand, it is well known that several

numerical problems, such as stress locking, arise when orthotropic models are used in the discrete problem. The fact that acceptable results can be obtained by assuming opportune spatial discretizations, aims the future research at working on it.

- The improvement of the localized crack approach. The smeared crack approach combined with a crack tracking technique has shown some limitations. For example, at the actual state the algorithm detects the crack origin only from the boundary of the mesh. This is unacceptable, for instance, in case of horizontally in-plane loaded shear walls without openings, in which the cracks could start from the interior of the mesh. In addition, the need for external control parameters, related for instance to the concept of maximum curvature criterion, represents a drawback since it requires analyst experience and practice. In this sense, a more robust approach which includes in its formulation such check devices would lead to a more user-friendly numerical tool.

References

Anthoine A. (1992). In-plane behaviour of masonry: a literature review. Commission of the European Communities, Industrial Processes, Luxemburg.

Anthoine A. (1995). Derivation of the in-plane elastic characteristics of masonry through homogenization theory. *International Journal of Solids and Structures*; 32: 137–163.

Atkinson R.H., Amadei B.P., Saeb S., Sture S. (1989). Response of masonry bed joints in direct shear. *Journal of Structural Engineering*; 115(9): 2276-2296.

Azzi, V. D., Tsai S. W. (1965). Anisotropic Strength of Composites. *Exp. Mech*.; 5 (9): 283-288.

Backes H.P. (1985). On the behaviour of masonry under tension in the direction of the bed joints (in German). Ph.D. thesis, Aachen University of Technology, Aachen, Germany.

Barlat F., Lian J. (1989). Plastic Behaviour and Stretchability of Sheet Metals. Part I: a Yield Function for Orthotropic Sheets Under Plane Stress Conditions. *International Journal of Plasticity*; 5: 51–66.

Barlat F., Lege D.J., Brem J.C. (1991). A Six-Component Yield Function for anisotropic materials. *International Journal of Plasticity*; 7: 693–712.

Bazant Z.P., Oh B.H. (1983). Crack band theory for fracture of concrete. *Materials and Structures*; 16: 155–177.

Belytschko T., Black T. (1999). Elastic crack growth in finite elements with minimal remeshing. *Computer Methods in Applied Mechanics and Engineering*; 45(5): 601–620.

Benedetti A., Pelà L., Aprile A. (2008). Masonry properties determination via splitting tests on cores with a rotated mortar layer. In: Sinha B. and Tanaçan L., editors, *Proceedings of 8th International Seminar on Structural Masonry*, Istanbul, Turkey.

Betten J. (1981). Creep Theory of Anisotropic Solids. *Journal of Rheology*; 25 (6): 565–581.

Betten J. (1988). Applications of tensor functions to the formulation of yield criteria for anisotropic materials. *International Journal of Plasticity*; 4: 29–46.

Boehler J.P., Sawczuk A. (1970). Equilibre limite des sols anisotropes. *J. Mécanique*; 9: 5–33.

Brencich A., Lagomarsino S. (1998). A macro-element dynamic model for masonry shear walls. In: Pande G.N. and Middleton J., editors, Computer methods in structural masonry – 4, Proc. of the Int. Symp., E&FN Spon, London.

Car E., Oller S., Oñate E. (2001). A large strain plasticity model for anisotropic material – composite material application. *International Journal of Plasticity*; 17: 1437–1463.

Car E., Oller S., Oñate E. (2000). An anisotropic elastoplastic constitutive model for large strain analysis of fiber reinforced composite materials. *Computer Methods in Applied Mechanics and Engineering*; 185: 245–277.

Carol I., Rizzi E., Willam K. (2001). On the formulation of anisotropic elastic degradation , part I: theory based on a pseudo-logarithmic damage tensor rate. *International Journal of Solids and Structures*; 38 (4): 491-518.

Carol I., Rizzi E., Willam K. (2001). On the formulation of anisotropic elastic degradation , part II: Generalized Pseudo Rankine Model for Tensile Damage. *International Journal of Solids and Structures*; 38 (4): 491-518.

Cecchi, A. Sab K. (2002). A multi-parameter homogenization study for modeling elastic masonry. *European Journal of Mechanics A/Solids*; 21: 249–268.

Cecchi A., Milani G., Tralli A. (2007). A Reissner–Mindlin limit analysis model for out-of-plane loaded running bond masonry walls. *International Journal of Solids and Structures*; 44: 1438–1460.

Cervera M., Oliver J., Faria R. (1995). Seismic evaluation of concrete dams via continuum damage models. *Earthquake Engineering and Structural Dynamics*; 24(9): 1225–1245.

Cervera M., Oliver J., Manzoli O. (1996). A Rate-Dependent Isotropic Damage Model for the Seismic Analysis of Concrete Dams. *Earthquake Engineering and Structural Dynamics*; 25: 987-1010.

Cervera M., Oliver J., Prato T. (1999). Thermo-Chemo-Mechanical Model for Concrete. II: Damage and Creep. *Journal Of Engineering Mechanics*; 125 (9): 1028-1039.

Cervera M., Agelet de Saracibar C., Chiumenti M. (2002). COMET: COupled MEchanical and Thermal analysis - Data Input Manual Version 5.0. CIMNE, Technical report IT-308.

Cervera M. (2003). Viscoelasticity and Rate-Dependent Continuum Damage Models. CIMNE, Monography Nº-79, Technical University of Catalunya, Barcelona, Spain.

Cervera M., Chiumenti M., Agelet de Saracibar C. (2003). Softening, localization and stabilization: capture of discontinuous solutions in J2 plasticity. *Int. J. Numer. Anal. Method Geomech*; 28: 373–393.

Cervera M., Chiumenti M., Agelet de Saracibar C. (2003). Shear band localization via local J2 continuum damage mechanics, *Computer Methods in Applied Mechanics and Engineering*; 193: 849–880.

Cervera M., Chiumenti M. (2006). Mesh objective tensile cracking via a local continuum damage model and a crack tracking technique. *Computer Methods in Applied Mechanics and Engineering*; 196: 304–320.

Cervera M., Chiumenti M. (2006). Smeared crack approach: back to the original track. *International Journal for Numerical and Analytical Methods in Geomechanics*; 30:1173–1199.

Cervera M. (2008a). A smeared-embedded mesh-corrected damage model for tensile cracking. *International Journal for Numerical Methods in Engineering*; 76: 1930–1954.

Cervera M. (2008b). An orthotropic mesh corrected crack model. *Computer Methods in Applied Mechanics and Engineering*; 197: 1603–1619.

Chaboche J.L. (1979). Le concept de contrainte effective appliqué à l'elasticité et à la viscoplasticité en présence d' un endommagement anisotrope. In: Comportement Méchanique des Solids Anisotropes, EUROMECH Colloque, Martinus, Nijhoff; 115: 737–760.

Chaboche J. (1988). Continuum Damage Mechanics part I. General Concepts. *Journal of Applied Mechanics*; 55: 59-64.

Chaboche J. (1988). Continuum Damage Mechanics part II. Damage Growth. *Journal of Applied Mechanics*; 55: 65-72.

Chaboche J.L. (1995). A Continuum Damage Theory with Anisotropic and Unilateral Damage. *La Recherche Aérospatiale*; 2: 139-147.

Clemente R. (2006). Análisis Estructural de Edificios Históricos mediante Modelos Localizados de Fisuración (in Spanish). Ph.D. thesis, Technical University of Catalonia, Barcelona, Spain.

Clemente R., Roca P., Cervera M. (2006). Damage Model with Crack Localization – Application to Historical Buildings. In: Lourenço P.B., Roca P., Modena C., Agrawal S., Editors, Structural Analysis of Historical Constructions, New Delhi, India.

Clemente R., Cervera M., Roca P. (2008). El modelo de daño localizado aplicado al análisis de estructuras de obra de fábrica (in Spanish). *Revista Internacional de Métodos Numéricos para Cálculo y Diseño en Ingeniería*; 24(1): 67-91.

Coleman B.D., Gurtin M.E. (1967). Thermodynamics with internal state variables. *Journal of Chemistry and Physics*; 47: 597–613.

Comi, C., Perego, U. (2001). Fracture energy based bi-dissipative damage model for concrete. *International Journal of Solids and Structures*; 38: 6427–6454.

Cook R.D., Malkus D.S., Plesha M.E., Witt R.J. (2002). Concepts and Applications of Finite Element Analysis. Fourth Edition, John Wiley & Sons.

Crisfield M.A. (1991). Non-Linear Finite Element Analysis of Solids and Structures. John Wiley & Sons.

Daniel I.M., Ishai O. (1994). Engineering Mechanics Of Composites Materials. Oxford University Press, Oxford.

Dhanasekar M., Page A.W., Kleeman P.W. (1985). The failure of brick masonry under biaxial stresses. *Proc. Intsn. Civ. Engrs.*; 79 (2): 295-313.

di Prisco M., Mazars J. (1996). Crush-crack: a non-local model for concrete. *Mechanics of Cohesive-Frictional Materials*; 1: 321–347.

Dragon A. and Mroz Z. (1979). A continuum model for plastic–brittle behaviour of rock and concrete. *International Journal of Engineering Science*; 1(17): 121–137.

Dragon A. (1985). Plasticity and ductile fracture damage: study of void growth in metals. *Engineering Fracture Mechanics*; 21: 875–885.

Drucker D. C., Prager W. (1952). Solid mechanics and plastic analysis for limit design. *Quarterly of Applied Mathematics*; 10 (2): 157-165.

Drysdale R.G., Hamid A.A. and Baker L.R. (1994). Masonry structures: Behavior and design. Prentice-Hall, Englewood Cliffs, New Jersey, USA.

Dutko M., Péric D., Owen D.R.J. (1993). Universal anisotropic yield criterion based on superquadric functional representation: part 1. Algorithmic issues and

accuracy analysis. *Computer Methods in Applied Mechanics and Engineering*; 109: 73–93.

Faria R., Oliver J. (1993). A Rate Dependent Plastic-Damage Constitutive Model for Large Scale Computations in Concrete Structures, CIMNE Monograph 17, Barcelona, Spain.

Faria R., Oliver J., Cervera M. (1998). A Strain-Based Plastic Viscous-Damage Model for Massive Concrete Structures. *International Journal of Solids and Structures*; 35 (14): 1533-1558.

Faria R., Oliver J., Cervera M. (2000). On Isotropic Scalar Damage Models For The Numerical Analysis Of Concrete Structures, CIMNE Monograph PI198, Barcelona, Spain.

Faria R., Oliver J., Cervera M. (2004). Modeling Material Failure in Concrete Structures under Cyclic Actions. *Journal of Structural Engineering*; 130(12): 1997-2005.

Feenstra P.H., De Borst R. (1996). A composite plasticity model for concrete. *International Journal of Solids and Structures*; 33(5): 707-730.

Gambarotta L., Lagomarsino S. (1997). Damage models for the seismic response of brick masonry shear walls. Part I: the mortar joint model and its applications. *Earthquake Engineering and Structural Dynamics*; 26: 423-439.

Gambarotta L., Lagomarsino S. (1997). Damage models for the seismic response of brick masonry shear walls. Part II: the continuum model and its applications. *Earthquake Engineering and Structural Dynamics*; 26: 441-462.

Ganz H.R. Thürlimann B. (1982). Tests on the biaxial strength of masonry (in German). Report No. 7502-3, Institute of Structural Engineering, ETH Zurich, Zurich, Switzerland.

GiD: the personal pre and post-processor, 2002. Available from: <http://gid.cimne.upc.es/>.

Govindjee S., Kay G.J., Simó J.C. (1995). Anisotropic modelling and numerical simulation of brittle damage in concrete. *International Journal for Numerical Methods in Engineering*; 38 (21): 3611–3634.

Green D. W. (2001). Wood: Strength and Stiffness. In: Encyclopedia of Materials: Science and Technology, pp. 9732-9736. Pergamon.

Guggisberg R., Thürlimann B. (1987). Experimental determination of masonry strength parameters (in German). Report No. 7502-5, Institute of Structural Engineering, ETH Zurich, Zurich, Switzerland.

Hankinson R.L. (1921). Investigation of Crushing Strength of Spruce at Varying Angles of Grain. Air Service Information Circular No. 259, U.S. Air Service.

Hansen E., Willam K., and Carol I. (2001). A two-surface anisotropic damage/plasticity model for plain concrete. Proc. FraMCoS-4 Conf., Cachan.

Hendry A.W. (1990). Structural masonry. Macmillan Education, London, UK.

Hill R. (1948). A Theory of the Yielding and Plastic Flow of Anisotropic Materials. *Proceedings of the Royal Society*, Series A, Vol. 193.

Hill, R. (1950). The Mathematical Theory of Plasticity. Oxford University Press, London.

Hilsdorf H.K. (1969). Investigation into the failure mechanism of brick masonry loaded in axial compression. In: Johnson F.H., editor, Designing, engineering and constructing with masonry products, Gulf Publishing Company, Houston, Texas, USA.

Hoffman O. (1967). The brittle strength of orthotropic materials. *Journal of Composite Materials*; 1: 200–206.

Hofmann P., Stockl S. (1986). Tests on the shear-bond behaviour in the bed-joints of masonry. *Masonry International*; 9: 1-15.

Janson J., Hult, J. (1977). Fracture mechanics and damage mechanics—a combined approach. *J. Méc. Appl.*; 1: 69–84.

Jansson S., Stigh, U. (1985). Influence on cavity shape on damage variable. *Journal of Applied Mechanics*; 52: 609–614.

Jirásek M. (1998). Nonlocal models for damage and fracture: comparison of approaches. *International Journal of Solids and Structures*; 35: 4133–4145.

Ju, J.W. (1989). On energy-based coupled elastoplastic damage theories: constitutive modeling and computational aspects. *International Journal of Solids and Structures*; 25 (7): 803–833.

Ju, J.W. (1990). Isotropic and anisotropic damage variables in continuum damage mechanics. *Journal of Engineering Mechanics*; 116 (12): 2764–2770.

Kachanov LM. (1958). Time of rupture process under creep conditions. *Izvestia Akademii Nauk, Otd Tech Nauk*; 8: 26-31.

Kachanov LM. (1986). Introduction to Continuum Damage Mechanics. Martinus Nijhoff Dortrecht, The Netherlands.

Krajcinovic D. (1984). Continuum Damage Mechanics. *Appl. Mech. Rev.*; 37: 1-6.

Krajcinovic D., Fonseka U. (1981). The Continuous Damage Theory of Brittle Materials, Part I and II. *Journal of Applied Mechanics*; 48: 809-824.

Krajcinovic, D. (1985). Constitutive theories for solids and structures with defective microstructure. *Damage Mechanics and Continuum Modeling, ASCE*; 39–56.

Krajcinovic D., Lemaitre J. (1987). Continuum Damage Mechanics Theory and Applications. CISM Lectures, Springer, Berlin Heidelberg, New York.

La Borderie C., Berthaud Y. and Pijaudier-Cabot G. (1990). Crack closure effects in continuum damage mechanics. Numerical implementation. Proc. 2nd Int. Conf. Comp. Aided Analysis Design Conc. Structures, Zell am See, 975-986.

Lee J., Fenves G. L. (1998). Plastic-damage model for cyclic loading of concrete structures. *Journal of Engineering Mechanics*; 124(8), 892–900.

Lemaitre J. and Chaboche J.L. (1978). Aspects phénoménologiques de la rupture par endommagement. J. Méc. Appl.; 2: 317–365.

Lemaitre J. (1984). How to use Damage Mechanics. *Nuclear Engineering and Design Journal*; 80: 233-245.

Lemaitre J. (1985). A continuous Damage Mechanics model for ductile fracture. *Journal of Engineering Materials and Technology* ; 107(1).

Lemaitre J. and Chaboche J.L. (1985). Mécanique des matériaux solides. Dunod, Paris.

Lemaitre J., Desmorat R., Sauzy M. (2000). Anisotropic Damage Law of Evolution. *European Journal of Mechanics - A/Solids*; 19: 187-208.

Lemaitre J., Desmorat R. (2005). Engineering Damage Mechanics. Springer-Verlag Berlin Heidelberg.

Lekhnitskii S.G. (1963). Theory of Elasticity of an Anisotropic Body. Holden day, San Francisco.

Liu S.I. (1982). On representations of anisotropic invariants. *International Journal of Engineering Science*; 20: 1099–1109.

Lofti H.R., Shing P.B. (1994). Interface model applied to fracture of masonry structures. *Journal of Structural Engineering*; 120 (1): 63–80.

Lourenço P.B., Rots J.G., Feenstra P.H. (1995). A “tensile” Rankine-type orthotropic model for masonry. In: Pande G.N. and Middleton J., editors, Computer methods in structural masonry - 3, Books & Journals International, Swansea, UK.

Lourenço P.B. (1996). Computational Strategy for Masonry Structures. Delft University Press, The Netherlands.

Lourenço P.B. Rots J.G. (1997). A multi-surface interface model for the analysis of masonry structures. Journal of Engineering Mechanics; 123 (7): 660–668.

Lourenço P.B., De Borst R., Rots J.G. (1997). Plane Stress Softening Plasticity Model For Orthotropic Materials. *International Journal for Numerical Methods in Engineering*; 40, 4033-4057.

Lourenço P.B., Rots J.G., Blaauwendraad J. (1998). Continuum model for masonry: parameter estimation and validation. *Journal of Structural Engineering*; 124(6): 642-652.

Lourenço P.B., Milani G., Tralli A., Zucchini A. (2007). Analysis of masonry structures: review and recent trends of homogenisation techniques. *Canadian Journal of Civil Engineering*; 34: 1443–1457.

Love AE. (1944). A Treatise on the Theory of Elasticity. Dover Publications, New York.

Lubarda V.A., Krajcinovic D., Mastilovic S. (1994). Damage model for brittle elastic solids with unequal tensile and compressive strengths. Engineering Fracture Mechanics; 49: 681–697.

Lubliner J., Oliver S., Oñate E. (1989). A plastic-damage model for concrete. *International Journal of Solids and Structures*; 25(2): 299–326.

Lubliner J. (1990). Plasticity Theory. Macmillan Publishing, USA.

Luccioni B., Oller S. (2003). A directional damage model. *Comput. Meth. Appl. Mech. Eng.*; 192: 1119–1145.

Luccioni B. (2003). Mecánica De Daño Continuo (in spanish). CIMNE Monograph M71, Barcelona, Spain.

Luciano R., Sacco E. (1997). Homogenization technique and damage model for old masonry material. *International Journal of Solids and Structures*; 34 (24): 3191-3208

Lurati F., Graf H., Thürlimann B. (1990). Experimental determination of the strength parameters of concrete masonry (in German). Report No. 8401-2, Institute of Structural Engineering, ETH Zurich, Zurich, Switzerland.

Magenes G., Della fontana A. (1998). Simplified Non-linear Seismic Analysis of Masonry Buildings. Proc. of the British Masonry Society, Vol. 8.

Mallardo V., Malvezzi R., Milani E., Milani G. (2008). Seismic vulnerability of historical masonry buildings: A case study in Ferrara. Engineering Structures; 30: 2223–2241.

Malvern L.E. (1969). Introduction to the Mechanics of a Continuous Medium. Prentice-Hall Inc., Englewood Cliffs.

Manzoli O.L. (2005). Simulação de propagação de fratura mediante modelos constitutivos locais combinados com técnica de construção progressiva da trajetória da descontinuidade. In: Congreso de Métodos Numéricos en Ingeniería, Granada, España.

Martínez G., Roca P., Caselles O., Clapés J. (2006). Characterization of the Dynamic Response for the Structure of Mallorca Cathedral. In: Lourenço P.B., Roca P., Modena C., Agrawal S., Editors, Structural Analysis of Historical Constructions, New Delhi, India.

Massart T.J., Peerlings R.H.J., Geers M.G.D. (2004). Mesoscopic modeling of failure and damage-induced anisotropy in brick masonry. *European Journal of Mechanics A/Solids*; 23: 719–735.

Massanas M., Roca P., Cervera M., Arun G. (2004). Structural analysis of Küçük Ayasofya Mosque in Ístanbul. In: Modena C., Lourenço P.B., Roca P., editors, Structural Analysis of Historical Constructions IV, Padova, Italy.

Maugin G.A. (1992). The thermomechanics of plasticity and fracture. Cambridge University Press.

Mazars J. (1982). Mechanical damage and fracture of concrete structures. Advances in Fracture research (Fracture 81), 4, 1499-1506. Pergamon Press, Oxford.

Mazars J., Pijaudier-Cabot G. (1989). Continuum damage theory. Application to concrete. *Journal of Engineering Mechanics*; 115(2): 345-365.

Milani G. (2004). Homogenization techniques for in- and out-of-plane loaded masonry walls. Ph.D. thesis, University of Ferrara, Italy.

Milani G., Lourenço P.B., Tralli A. (2006). Homogenised limit analysis of masonry walls. Part I: Failure Surfaces. *Computers and Structures*; 84 (3-4): 166–180.

Milani G., Lourenço P.B., Tralli A. (2006). Homogenised limit analysis of masonry walls. Part II: Structural Examples. *Computers and Structures*; 84 (3-4): 181–195.

Milani G., Lourenço P.B., Tralli A. (2007). 3D homogenized limit analysis of masonry buildings under horizontal loads. *Engineering Structures*; 29: 3134–3148.

Milani E., Milani G., Tralli A. (2008). Limit analysis of masonry vaults by means of curved shell finite elements and homogenization. *International Journal of Solids and Structures*; 45 (20): 5258-5288.

Möes N., Dolbow J., Belytschko T. (1999). A finite element method for crack growth without remeshing. *International Journal of Numerical Methods in Engineering*; 46: 131–150.

Molins Borrell. (1996). Characterization of the mechanical behaviour of masonry. In: Roca P., Gonzales J.L., Marí A.R. and Oñate E., Editors, Structural Analysis of Historical Constructions, CIMNE, Barcelona, Spain,.

Mosler J., Meschke G. (2004). Embedded crack vs. smeared crack models: a comparison of elementwise discontinuous crack path approaches with emphasis on mesh bias. *Computer Methods in Applied Mechanics and Engineering*; 193: 3351–3375.

Murakami S., Ohno N. (1980). A Continuum Theory of Creep and Creep Damage. 3º IUTAM Symposium on Creep in Structure.

Murakami S. (1988). Mechanical modelling of material damage. *Journal of Applied Mechanics*; 55: 281-286.

Murcia J. (2008). Seismic Analysis of Santa Maria del Mar Church in Barcelona. Master thesis, Technical University of Catalunya, Spain.

Ngo D., Scordelis A.C. (1967). Finite element analysis of reinforced concrete beams. *ACI Journal*; 64(14): 152–163.

Norris C.B. (1816). Strength of Orthotropic Materials Subjected to Combined Stresses. U.S. Forest Products Laboratory Rep., FPL, Madison, Wisconsin, 1955.

Odqvist F.K.G. and Hult, J.A.H. (1962). Kriechfestigkeit Metallischer Werkstoffe., Springer-Verlag, Berlin.

Oliver J. (1989). A consistent characteristic length for smeared cracking models. *International Journal of Numerical Methods in Engineering*; 28: 461–474.

Oliver J., Cervera M., Oller S., Lubliner J. (1990). Isotropic Damage Models and Smeared Crack Analysis of Concrete. Second International Conference on Computer Aided Analysis and Design of Concrete Structures.

Oliver J. (1995). Continuum modeling of strong discontinuities in solid mechanics using damage models. *Comput. Mech*.; 17: 277–296.

Oliver J., Cervera M., Manzoli O. (1999). Strong discontinuities and continuum plasticity models: the strong discontinuity approach. *International Journal of Plasticity*; 15: 319–351.

Oliver J. (2000). On the discrete constitutive models induced by strong discontinuity kinematics and continuum constitutive equations. *International Journal of Solids and Structures*; 37: 7207–7229.

Oliver J., Huespe A.E., Samaniego E., Chaves W.V. (2004). Continuum approach to the numerical simulation of material failure in concrete. *Int. J. Numer. Anal. Methods Geomech*; 28: 609–632.

Oliver J., Huespe A.E. (2004). Continuum approach to material failure in strong discontinuity settings. *Computer Methods in Applied Mechanics and Engineering*; 193: 3195–3220.

Oller S., Oñate E., Miquel J. (1993). Simulation of anisotropic elastic-plastic behaviour of materials by means of an isotropic formulation. In *2nd US National Congress on Computational Mechanics, Washington, DC*.

Oller S., Oñate E., Miquel J., Botello S. (1993). A finite element model for analysis of multiphase composite materials. In *Ninth International Conference on Composite Materials, Zaragoza, Spain*

Oller S., Botello S., Miquel J., Oñate E. (1995). An anisotropic elastoplastic model based on an isotropic formulation. *Engineering Computations*; 12 (3): 245–262.

Oller S., Oñate E., Miquel J. (1996). Mixing anisotropic formulation for analysis of composites. *Communications in Numerical Methods in Engineering*; 12: 471-482.

Oller S. (2001). Fractura Mecánica. Un Enfoque Global (in Spanish). CIMNE Monograph L52, Barcelona, Spain.

Oller S., Car E., Lubliner J. (2003). Definition of a general implicit orthotropic yield criterion. *Computer Methods in Applied Mechanics and Engineering*; 192: 895–912.

Oñate E. (1995). Cálculo de Estructuras por el Método de Elementos Finitos (in Spanish). Second Edition, CIMNE, Barcelona.

Ortiz, M. (1985). A constitutive theory for inelastic behaviour of concrete. *Mechanics of Materials*; 4: 67–93.

Owen D.R.J., Fawkes A.J. (1983). Engineering Fracture Mechanics. Pineridge Press, Swansea.

Page AW. (1981). The biaxial compressive strength of brick masonry. *Proc. Inst. Civil Engrs.*; 71(2): 893–906.

Page AW. (1983). The strength of brick masonry under biaxial tension–compression. *International Journal of masonry constructions*; 3(1): 26-31.

Papa E. A (1996). unilateral damage model for masonry based on a homogeneisation procedure. *Mechanics of Cohesive-Frictional Materials*; 1:349 –366.

Pelà L., Cervera M., Roca P., Benedetti A. (2008). An Orthotropic Damage Model for the Analysis of Masonry Structures. In: Sinha B. and Tanaçan L., editors, *Proceedings of 8th International Seminar on Structural Masonry*, Istanbul, Turkey.

Pelà L., Cervera M., Roca P., Benedetti A. (2008). An Orthotropic Damage Model for the Analysis of Historical Masonry Structures. *Proceedings of I Congreso Iberoamericano sobre construcciones históricas y estructuras de mampostería* (in spanish), Bucaramanga, Colombia.

Pelà L., Aprile A., Benedetti A. (2009). Seismic Assessment of Masonry Arch Bridges. Accepted for publication on *Engineering Structures*.

Pluijm, R. van der. (1993). Shear behaviour of bed joints. In: Hamid A.A. and Harris H.G., editors, Proc. 6th North American Masonry Conf., Drexel University, Philadelphia, Pennsylvania, USA.

Pluijm, R. van der. (1998). Overview of deformation controlled combined tensile and shear tests. Technical report TUE/BCO/98.20, Eindhoven University of Technology.

Rabotnov Y.N. (1969). Creep Rupture. Proc. XII Int. Congr. Appl. Mech., Stanford, Springer Berlin.

Rabotnov Y.N.. (1963). On the equations of state for creep. In: Progress in Applied Mechanics-The Prager Anniversary Volume, The Macmillan Company, New York, NY.

Raijmakers T.M.J., Vermeltfoort, A.Th. (1992). Deformation controlled tests in masonry shear walls (in Dutch). Report B-92-1156, TNO-Bouw, Delft, The Netherlands.

Rashid Y. (1968). Analysis of prestrssed concrete pressure vessels. *Nucl. Engrg. Des.*; 7: 334–344.

Resende, L. (1987). A damage mechanics constitutive theory for the inelastic behaviour of concrete. *Computer Methods in Applied Mechanics and Engineering*; 60: 57–93.

Roca P., Molins C., Marí A.R. (2005). Strength capacity of masonry wall structures by the equivalent frame method. *Journal of Structural Engineering*; 131(10): 1601-1610.

Rots J.G., Nauta P., Kusters G.M.A., Blaauwendraad J. (1985). Smeared crack approach and fracture localization in concrete. *Heron*; 30(1).

Rots J.G., Blaauwendraad J. (1989)Crack models for concrete: discrete or smeared? Fixed, multi-directional or rotating? *Heron*; 34 (1).

Samarasinghe W., Hendry A.W. (1980). The strength of brickwork under biaxial tensile and compressive strength. Proc. of the 7th Symposium on load bearing brickwork, London.

Shieh-Beygi B., Pietruszczak S. (2008). Numerical analysis of structural masonry: mesoscale approach. *Computers and Structures*; 86: 1958–1973.

Simó J.C., Ju J.W. (1987). Strain- and stress-based continuum damage models – I Formulation. *International Journal of Solids and Structures*; 23: 821–840.

Simó J.C., Ju J.W. (1987). Strain- and stress-based continuum damage models – II Computational Aspects. *International Journal of Solids and Structures*; 23: 841-869.

Simó J.C., Oliver J., Armero F. (1993). An analysis of strong discontinuities induced by strain-softening in rate-independent inelastic solids. *Comput. Mech.*; 12: 49–61.

Sobotka Z. (1969). Theorie des plastischen Fliessens von anisotropen Körpern. *Zeit. Angew. Math. Mech.*; 49: 25–32.

Soden P.D., Hinton M.J., Kaddour A.S. (2002). Biaxial test results for strength and deformation of a range of E-glass and carbon fibre reinforced composite laminates: failure exercise benchmark data. *Composites Science and Technology*; 62: 1489–1514.

Sutcliffe D.J., Yu H.S., Page A.W. (2001). Lower bound limit analysis of unreinforced masonry shear walls. *Computers and Structures*; 79: 1295–1312.

Sukumar N., Möes N., Moran B., Belytschko T. (2000). Extended finite element method for three-dimensional crack modelling. *International Journal of Numerical Methods in Engineering*; 48: 1549–1570.

Syrmakesis C.A., Asteris P.G. (2001). Masonry Failure Criterion Under Biaxial Stress State. *Journal of Materials in Civil Engineering*; 13: 58-64.

Talreja, R. (1985). A continuum mechanics characterization of damage in composite materials. Proc. R. Soc. London, A 399, 195–216.

Tong P., Pian T.H.H. (1973). On the convergence of the finite element method for problems with singularily. *International Journal of Solids and Structures*; 9: 313–321.

Tsai S.W., Wu E.M. (1971). A general theory of strength for anisotropic materials. *Journal of Composite Materials*; 5: 58–80.

Tzamtzis, A.D. (1994). Dynamic finite element analysis of complex discontinuous and jointed structural systems using interface elements. Ph.D. Thesis, Department of Civil Engineering, QMWC, University of London.

Von Mises R. (1928). Mechanics der plastischen Formänderung von Kristallen. *Zeitschrift Angewandte Mathematik Mechanik*; 8: 161–185.

Wang C.C. (1970). A new representation theorem for isotropic functions, Part I and II. *Arch. Rat. Mech.*; 36: 166–223.

Wu J.Y., Li J. (2008). On the mathematical and thermodynamical descriptions of strain equivalence based anisotropic damage model. *Mechanics of Materials*; 40: 377–400.

Yazdani S., Schreyer H.L. (1990). Combined plasticity and damage mechanics model for plain concrete. *Journal of Engineering Mechanics*; 116(7): 1435–1450.

Yokel F. Y., Fattal S. G. (1976). Failure hypothesis for masonry shear walls. *Journal of Structural Division*; 102(3): 515–532.

Zijl G.P.A.G., van. (2004). Modeling masonry shear-compression: the role of dilatancy highlighted. *Journal of Engineering Mechanics*; 130(11): 1289–1296.

Zucchini A., Lourenço P.B. (2002). A micro-mechanical model for the homogenisation of masonry. *International Journal of Solids and Structures*; 39: 3233–3255.

Zienkiewicz O. C., Taylor R.L. (2000). The Finite Element Method. Fifth Edition, Butterworth-Heinemann.

Życzkowski M. (2001). Anisotropic yield conditions. In: J. Lemaitre, Editors, Handbook of Materials Behavior Models, Academic Press, San Diego, 155–165.